Dissertation
submitted to the
Combined Faculties for the Natural Sciences and for Mathematics
of the Ruperto-Carola University of Heidelberg, Germany
for the degree of
Doctor of Natural Sciences

Put forward by
Dipl.-Phys. Jim Thieser
born in Merzig, Saarland

Oral examination: 07.02.2013

Atmospheric Reactive Nitrogen Chemistry via Cavity Ringdown Spectroscopy

From short-lived compounds to reservoir species

Referees: Prof. Dr. Ulrich Platt
Prof. Dr. Thomas Wagner

Zusammenfassung

Die vorliegende Arbeit untersucht die Einflüsse wichtiger Vertreter der Stickoxide (NO_y) auf die atmosphärische Chemie. Der Fokus der Arbeit lag sowohl auf den Nitratradikalen (NO_3), die zu den wichtigsten Oxidantien in der nächtlichen Troposphäre zählen, als auch auf den langlebigeren organischen Nitraten ($RONO_2 + RO_2NO_2$). Besonderes Interesse galt dabei den Alkylnitraten ($RONO_2$). Für die Messung der organischen Nitrate wurde im Verlauf dieser Arbeit ein neues Cavity Ringdown Spektrometer (CRDS) entwickelt. Die Detektion von NO_3 erfolgte mittels eines etablierten CRDS. NO_3-Messungen, die 2008 im Rahmen der DOMINO-Kampagne in Südspanien durchgeführt wurden, zeigten eine hohe Variabilität der NO_3-Konzentration und -Lebenszeit, die stark vom Luftmassenursprung beeinflusst wurden. Vergleiche von bodennahen mit vertikalausgedehnten NO_3-Messungen belegten einen Anstieg der NO_3-Konzentration mit der Höhe. Bodennahe NO_3-Messungen dürften demnach die mittlere NO_3-Menge in der nächtlichen Grenzschicht unterschätzen. Im Gegensatz zu den kurzlebigeren Nitratradikalen besitzen organische Nitrate in der Regel Lebenszeiten von mehreren Tagen bis Monaten. Daher spielen sie eine große Rolle beim Transport von NO_x zu abgelegenen Regionen der Erde. Die ersten Messungen von Alkylnitraten mit dem neuen CRDS wurden 2011 während der PARADE-Kampagne auf dem Kl. Feldberg durchgeführt. Es zeigte sich, dass der Anteil der Alkylnitrate an NO_y bei etwa 8-10 %, sowie an NO_z bei etwa 22 %, lag. Für die $RONO_2$-Ausbeute aus der OH-initiierten atmosphärischen Oxidation verschiedener VOCs wurde ein Wert von etwa 3-4% bestimmt.

Abstract

This thesis investigates the impacts of important members of the reactive nitrogen family (NO_y) on atmospheric chemistry. In particular, the short lived, reactive nitrate radical (NO_3), one of the most important nighttime oxidizing trace gases, and longer-lived organic nitrates ($RONO_2 + RO_2NO_2$), especially alkyl nitrates ($RONO_2$), were studied. Organic nitrates were measured via a newly developed Cavity Ring Down Spectrometer (CRDS). For the detection of NO_3 an established CRDS was used. NO_3 measurements, conducted in 2008 in Southern Spain in the framework of the DOMINO campaign, showed a high variability of NO_3 concentration and lifetime. Comparison between ground based and vertically distributed NO_3 measurements revealed a strong increase of NO_3 concentration and lifetime with height, suggesting that ground based measurements severely underestimate the mean NO_3 concentration within the nocturnal boundary layer. In contrast to the short lived NO_3 radicals, organic nitrates generally have lifetimes in the order of a few days up to several months and therefore they play a major role in the transport of NO_x to remote areas. The first total alkyl nitrates measurements using the newly developed instrument were carried out on the summit of Mt. Kl. Feldberg during the PARADE campaign 2011. These measurements showed the contribution of alkyl nitrates to total NO_y and NO_z of about 8-10 % and about 22%, respectively. Furthermore an effective branching ratio of about 3-4% for the formation of $RONO_2$ from the oxidation of VOCs by OH could be determined.

Contents

I. Motivation and Scientific Background 1

1. Introduction 3

2. Reactive Nitrogen chemistry in the Troposphere 7

2.1. Atmospheric chemistry of Nitrogen Oxides . . . 7

2.1.1. Sources of Nitrogen Oxides . . . 7

2.1.2. Sinks for Nitrogen Oxides . . . 10

2.1.3. Chemistry of Nitrogen Oxides in the Troposphere . . . 10

2.2. Chemistry of the Nitrate Radical . . . 12

2.2.1. Sources of NO_3 . . . 12

2.2.2. Direct sinks of NO_3 . . . 13

2.2.2.1. Photolysis of NO_3 . . . 13

2.2.2.2. Reaction of NO_3 with NO . . . 13

2.2.2.3. Reactions of NO_3 with VOC's . . . 13

2.2.2.4. NO_3 uptake on aerosol and deposition . . . 15

2.2.3. Indirect sinks of NO_3 . . . 16

2.2.3.1. Homogeneous reaction of N_2O_5 with water vapour 17

2.2.3.2. Heterogeneous reaction of N_2O_5 on aerosols and deposition . . . 18

2.2.4. Atmospheric importance of NO_3 and N_2O_5 . . . 18

2.2.4.1. NO_x losses and photochemical O_3 production . . . 18

2.2.4.2. Influence on organic species . . . 18

2.2.4.3. Impact on sulphur cycle . . . 19

2.2.4.4. Impact on HO_x and RO_2 cycle . . . 20

2.2.4.5. Formation of organic nitrate and SOA . . . 20

2.2.4.6. Formation of particulate nitrate . . . 20

2.2.4.7. Halogen activation by N_2O_5 . . . 21

2.3. Chemistry of Organic Nitrates . . . 21

2.3.1. Sources of Organic Nitrates . . . 21

2.3.2. Different types of Nitrates . . . 22

2.3.2.1. Peroxy Nitrates ($\sum$PNs) . . . 22

2.3.2.2. Alkyl Nitrates ($\sum$ANs) . . . 23

2.3.3. Sinks of Organic Nitrates 24
2.3.4. Atmospheric importance of Organic Nitrates 26
2.4. Relationship between NO_2, NO_3, N_2O_5, $\sum$PNs and $\sum$ANs 27

II. Instrumentation and Measurement Sites 29

3. Instrumentation for field measurements 31
3.1. Cavity Ring Down Spectroscopy (CRDS) 31
3.1.1. CRDS principle 31
3.2. CRDS for measuring NO_3 and N_2O_5 32
3.2.1. Data corrections 35
3.2.1.1. R_L ratio 35
3.2.1.2. Transmission efficiency of the cavities 35
3.2.1.3. Transmission efficiency of the filter 36
3.3. Newly developed thermal dissociation Cavity Ring Down Spectrometer (TD-CRDS) 37
3.3.1. General overview 37
3.3.2. Characterization of the instrument 42
3.3.2.1. Dilution effect by purge gas 42
3.3.2.2. Effective cross section and stability 43
3.3.2.3. Effects due to Rayleigh scattering 45
3.3.2.4. Additionally formed NO_2 during sample time . . . 47
3.3.2.5. Introduction to Thermal Dissociation method . . . 48
3.3.2.6. PAN measurements 49
3.3.2.7. AN measurements 52
3.3.2.8. Precision and uncertainty of the instrument 54

4. Campaign overview 59
4.1. DOMINO campaign 60
4.1.1. Scientific Question 60
4.1.2. Site descriptions and local surroundings 60
4.1.3. Meteorological conditions during the DOMINO campaign . 61
4.1.4. Instrumentation of the campaign 65
4.2. PARADE campaign 69
4.2.1. Scientific Question 69
4.2.2. Site description and local surroundings 69
4.2.3. Meteorological conditions during PARADE 70
4.2.4. Instrumentation 72

III. Results and Discussion 77

5. Results from DOMINO 2008 79

5.1. Instrument setup during DOMINO 79
5.1.1. NO_3 concentration from N_2O_5 and NO_2 measurements . . . 79
5.2. NO_3 Lifetime and steady state 81
5.2.1. NO_3 lifetimes 83
5.2.1.1. Direct losses to NO_3 83
5.2.1.2. Direct losses to N_2O_5 84
5.2.2. Validity of steady state approach during Domino2008 84
5.3. NO_3/N_2O_5 measurements 85
5.4. Lifetime of NO_3 during the campaign 87
5.4.1. NO_3 Losses 89
5.4.2. NO_3 lifetime dependence on wind sectors 92
5.5. NO_3 reactivity in different air masses 94
5.5.1. Sector A+B: 23-24 November (urban/industrial) 94
5.5.1.1. Heterogeneous loss of NO_3 and N_2O_5 96
5.5.1.2. Gas-phase reaction of NO_3 and N_2O_5 98
5.5.1.3. Unknown or undetermined reactions/loss processes 99
5.5.2. Sector B+C: 26-27 December (Continental/Rural) 101
5.5.2.1. Heterogeneous loss of NO_3 and N_2O_5 103
5.5.2.2. Gas-phase loss of NO_3 and N_2O_5 105
5.5.2.3. Possible explanation for the different behaviour . . 105
5.6. Overview of NO_3 reactivity 106
5.7. Comparison of the Oxidation capacity of NO_3, OH and O_3 109
5.8. Vertical gradients of NO_3 112
5.8.1. LP-DOAS measurements of NO_3 during DOMINO 112
5.8.2. Nocturnal profiles for the different layers 114
5.8.3. Dependence of gradients on wind sectors 115
5.8.4. Influence of the NBL height 116
5.9. Height dependent NO_x partioning and losses during the night . . . 118
5.10. Atmospheric importance of nitrate radical gradient 122
5.11. Comparison with other known NO_3 profiles 124
5.12. Summary of DOMINO results 127

6. Results from PARADE 2011 129

6.1. Set up of the instrument during the campaign 129
6.2. NO_2 measurements 130
6.2.1. Comparison of NO_2 instruments 130
6.2.2. Low NO_2 condition during HUMPPA 133
6.3. $\sum$PNs and $\sum$ANs measurements 136
6.3.1. Determination of $\sum$PNs and $\sum$ANs 136

6.3.2. Interferences of ∑PNs and ∑ANs during PARADE 137
6.3.3. Comparison of TD-CRDS with TD-CIMS 138
6.4. Time series of NO_2, ∑PNs and ∑ANs 139
6.5. Diel profiles 141
6.6. Wind Sectors 143
6.7. ∑PNs and ∑ANs contribution to NO_y 145
6.7.1. Contribution to NO_z 148
6.8. Comparison with previous PN measurements 149
6.9. Production of ∑ANs and Ozone 151
6.9.1. Contribution to the ∑ANs Production rate 156
6.9.2. Link between ∑ANs and Ozone 157
6.9.2.1. Comparison with calculated branching ratios . . . 160
6.10. Summary of PARADE 162

IV. Conclusion and Outlook 165

7. Conclusion 167

8. Outlook 169

Appendix 171

A. Abbreviations 173

B. DOMINO 2008 175
B.1. Steady state calculation 176
B.2. Timeseries 178
B.3. Nocturnal losses 180

C. PARADE 2011 185
C.1. Timeseries 186
C.2. Diurnal profile from NO_y contribution 192
C.3. Diel Profiles 193
C.4. O_x versus ∑ANs 196

Bibliography 203

Acknowledgements - Danksagung 225

Part I.

Motivation and Scientific Background

Chapter 1.

Introduction

Since the beginning of industrialisation, anthropogenic activities have dramatically altered the chemical state of the atmosphere with significant consequences for air quality and environmental sustainability. The impacts of anthropogenic activity on society and health were reported in the nineteen fifties. Increased levels of SO_2 and particles ('smoke') in the presence of dense fog and low inversion layer during winter time ('smog' = smoke + fog) led to the death of thousands of people in London (London smog Finlayson-Pitts and James N. Pitts (1999)). This phenomena mainly occurs in winter at low temperatures. In contrast, in 1940 a new air pollution problem was observed in Los Angeles [Middleton et al. (1950)] during hot summer days and bright sunshine (Los Angeles Smog or photosmog). In contrast to the London smog, the ambient air contained strong oxidizing, eye - watering and plant destructive pollutants which could lead to high levels of ozone. Contrary to stratospheric ozone, tropospheric ozone has harmful effects for health. Since the first investigation of Los Angeles smog, this phenomenon is recognized to be a world - wide problem in many major cities and the surrounding areas. The formation of photosmog is the consequence of large ejections of primary pollutions (NO_x=NO + NO_2) and VOCs (Volatile organic compounds) which are trapped in the inversion layer and undergo photochemical reactions in the sunlit atmosphere forming secondary pollutant species (such as ozone).

NO_x emissions are dominated by anthropogenic sources (e.g. car traffic) and have increased strongly in the last decades and are expected to increase further in the next decades. Total Nitrogen emissions of about 42 - 47 Tg N yr^{-1} were calculated for the year 2000. This amount is expected to increase to about 105 -131 Tg N yr^{-1} in the year 2100 [Lamarque et al. (2005)]. Consequently this extreme increase in nitrogen emissions will also impact the atmospheric importance of nitrogen related chemistry. Volatile Organic Compounds (VOC) play an important role in atmospheric processes. VOCs are emitted from both anthropogenic and natural sources, e.g. trees or other plants. VOCs play an important role in the formation of photosmog. During daytime the chemistry is mainly driven by reaction of the hydroxy radical OH. Hydroxy radicals initiate chain reactions by attacking VOCs. Beside the oxidation of VOCs, OH is one of the most important oxidants and

is responsible for the self cleaning of the atmosphere during the day. OH is also important in the oxidation of anthropogenic trace gases (like e.g. greenhouse gases) by converting them to non absorbing substances. The attack of a VOC by a hydroxy radical leads a formation of a secondary, organic peroxy radicals (RO_2). These peroxy radicals are directly linked to the NO_x cycle. The reaction of RO_2 with NO leads on one hand to the formation of NO_2 and subsequently to the formation of O_3 and on the other hand to a minor branch leading to a NO_x reservoir species ($RONO_2$).

In the early days of atmospheric chemistry it was expected that all processes were driven by photochemistry. This picture changed in the late 1970's. During that time it was found that oxidation processes occurred also during nighttime and were important in both polluted and clean environments [Platt et al. (1979)]. One of the major oxidants during nighttime is the nitrate radical NO_3 which was detected the first time in the troposphere by Platt et al. (1980) and Noxon et al. (1980). Following these first observations, NO_3 concentrations were measured in polluted and clean background air under continental and maritime conditions [e.g Brown and Stutz (2012); Crowley et al. (2010); Heintz et al. (1996); Martinez et al. (2000); Mihelcic et al. (1993); Platt et al. (1981)]. These studies showed that the nighttime chemistry driven by NO_3 as primary oxidant is very important and is involved in several processes. Nitrate radicals were found to act as important initiator of the nighttime degradation of many VOCs. The reaction of NO_3 with VOCs can lead to the formation of peroxy radicals (RO_2 and HO_2) [e.g. Geyer et al. (2003); Mihelcic et al. (1993); Platt et al. (1990)] and also to NO_x reservoir species ($RONO_2$) [Fry et al. (2011, 2009); Hallquist et al. (1999)]. Additionally the nitrate radical play an important role in the non - photochemical conversion of nitrogen oxides to HNO_3.

Hydrocarbon analysis from Penkett et al. (2007, 1993) suggested that the oxidation potential of NO_3 will increase in vertical distribution. Since the development of new measurement technique, compact design of instruments capable to measure NO_3 [Okeefe and Deacon (1988)] are available with the opportunity to deploy them on mobile platforms including aircraft. Since then several studies showed the vertical distribution of NO_3 [e.g. Brown et al. (2007a,b); Stutz et al. (2004, 2009); von Friedeburg et al. (2002)] and its for the oxidation capacity of NO_3. Therefore further investigation of the vertical distribution of NO_3 will extend the understanding of the role of NO_3 for the complete nocturnal boundary layer.

Beside the importance of nitrogen oxides for the nocturnal chemistry, nitrogen oxides play an important role in most of atmospheric chemical processes. Nitrogen oxides are mainly emitted as NO_x but undergo further oxidation. Depending on the nitrogen oxide the primary emitted NO_x can be stored in these oxides (reservoir species) or be lost due to wet deposition (HNO_3). The organic nitrates ($RONO_2$

and RO_2NO_2) act as reservoir species which are able to transport NO_x from the source regions to remote areas over the globe [Fischer et al. (2010); Kotchenruther et al. (2001)]. In particular alkyl nitrates ($RONO_2$) may have lifetimes of several weeks to months which allow them to transport NO_x to remote areas. Alkyl nitrates were first detected by Atlas (1988). Following these measurements and until the end of the twentieth century, alkyl nitrates derived from speciated hydrocarbons were measured [e.g. Buhr et al. (1990); Flocke et al. (1991); Kastler and Ballschmiter (1998)]. In several studies a large fraction of 'missing NO_y' was measured which could not be explained until first measurements of total alkyl nitrates [Day et al. (2003)]. This result showed that a relative large fraction of NO_y can be present in form of alkyl nitrates which can have a large influence on the NO_x distribution and also on the composition of NO_y globally.

Alkyl nitrates are formed via the reaction of RO_2 with NO with a small branching ratio compared to the forming NO_2. The branching ratio is strongly dependent on the VOC, ranging from about less than 1 % for small VOCs (e.g. Ethene) to about 35% for large VOCs. Depending on the precursor for the formation of $RONO_2$, the branching ratio can lead to significant impacts on a global scale. Since the branching ratios are small its determination for each individual hydrocarbon may lead to large uncertainties. This is reflected in the formation of nitrates derived from isoprene (4-15 %). Wu et al. (2007) showed that the global O_3 concentration can be changed by 10 % when increasing the branching ratio for the isoprene nitrates from 4 to 12 %. Therefore organic nitrates and in particular alkyl nitrates have a large contribution to the nitrogen oxides and significant influence on the NO_x distribution and consequently on ozone formation globally.

Outline of the Thesis

After the introduction this thesis starts with the description of the chemistry of the nitrogen oxides in which the importance of the role of the nitrogen oxides for atmospheric chemistry is shown and also further information of the sources and sinks of the individual oxides which will be discussed.
Chapter 3 gives an overview of the existing cavity ring down spectrometer for the detection of NO_3 and N_2O_5 which was deployed during the DOMINO 2008 campaign. The characteristics of the Cavity Ringdown Spectrometer developed in this thesis for the detection of NO_2, total peroxy nitrates and total alkyl nitrates are presented. This new instrument extended on the one hand the range of measurable nitrogen oxides and on the other hand it can directly link nocturnal nitrogen oxide chemistry and diurnal nitrogen oxide chemistry. Additionally, NO_2 is the direct precursor of NO_3 and is strongly linked to NO_3 and N_2O_5. The thermal dissociation technique allows the TD-CRDS instrument to characterize several trace gas sources which are necessary for the calibration of other instruments (e.g. CIMS).

Therefore, the development of this new instrument is an improvement for the understanding of nitrogen oxides in particular the organic nitrates.
In Chapter 4 the measurements sites from two campaigns (DOMNIO 2008 and PARADE 2011) and the meteorological conditions as well the instrumentation which were available at each campaign are described. The result from both campaigns will be discussed later on. The first campaign, DOMINO, took place in Southern Spain (close to Huelva) in November/December 2008. This campaign focussed on nighttime chemistry. The second campaign discussed in this thesis took place in August/September 2011 on top of Mt. Kleiner Feldberg in Central Germany. This campaign focussed on the longer lived nitrogen oxides. Additionally the newly developed CRDS instrument was deployed at an other campaign in Hyytiälä, Finland in the summer 2010.
Chapter 5 and 6 showed the measurement result of the each campaign and discussed these results. Whereas in Chapter 5 the analysis is focussed on the nighttime chemistry involving NO_3 and N_2O_5 the results discussed in Chapter 6 focus on the measurements of the new instrument (NO_2, total peroxy nitrates and total alkyl nitrates) and their importance in relation to total nitrogen oxides. Chapter 7 will give a short summary of the results of this thesis and chapter 8 an outlook for further research on this topic and instrumental improvements.

Chapter 2.

Reactive Nitrogen chemistry in the Troposphere

In this chapter an overview will be given of the most important reactive nitrogen species and their importance for tropospheric chemistry. The focus is on the trace gases which will also be discussed more in detail in this thesis, i.e. NO, NO_2, NO_3, N_2O_5 and the organic nitrates. There are also excellent overviews of NO_x, NO_3, N_2O_5 etc... (e.g. Finlayson-Pitts and James N. Pitts (1999); Seinfeld and Pandis (2006)).

2.1. Atmospheric chemistry of Nitrogen Oxides

The anthropogenic influence to the atmosphere can clearly be seen from the global distribution of nitrogen oxides. While in remote areas nitrogen oxide mixing ratios typically are in the range of 10 -20 pptv, in rural or urban areas the nitrogen oxides mixing ratios normally do not fall below several ppbv, in very large cities the mixing ratios can reach several hundred ppbv. Therefore, many atmospheric phenomena directly or indirectly involve reactions of nitrogen oxides [e.g. Finlayson-Pitts and James N. Pitts (1999)]. Important examples are the 'Ozone Hole' in the Stratosphere [Farman et al. (1985)], 'acid rain' in the lee of industrial areas and also 'Summer smog' [Middleton et al. (1950)] in urban centres. Nitrogen oxides play a very important role in atmospheric chemistry on the global scale as they are involved in the formation of tropospheric ozone and contribute to the formation of other atmospheric oxidants. In the following sections the sources and sinks of the nitrogen oxides and as well the most important reactions will be discussed.

2.1.1. Sources of Nitrogen Oxides

The sources of nitrogen oxides are both natural (soil emissions, natural wildfires and lightning) and anthropogenic (fossil fuel combustion, biomass burning). During the last decades many publications have discussed the sources and sinks of the nitrogen oxides [e.g. Logan (1983)]. The largest source of NO_x is fossil fuel combustion,

which together with the emissions form biomass burning and other anthropogenic activities dominates the NO_x budget. NO_x is predominantly emitted in the form of NO (typically $> 90\%$) whereas the direct contribution of NO_2 can vary between 1% and 30 % [Lenner (1987)]. The emitted NO is from processes taking place at temperatures high enough to dissociate the triple bond of the nitrogen (N_2) molecule. The process forming NO is known as the Zel'dovich Process [Zel'dovich and Raizer (1966)].

$$O_2 \longrightarrow 2\,O \tag{2.1}$$
$$O + N_2 \longrightarrow NO + N \tag{2.2}$$
$$N + O_2 \longrightarrow NO + O \tag{2.3}$$

For the back reaction similar high activation energies are required and therefore the NO concentration can be 'freezed' due to fast cooling. The highest NO concentrations can therefore be found in processes which occur at very high temperatures followed by fast cooling, e.g. burning in internal combustion engines. Similar conditions appear in nature during lightning and wildfires. Otherwise bacteria in the soil can emit NO and contribute to the natural emissions.
The main sources of nitrogen oxides in the troposphere are listed in table 2.1 [IPCC (2007)]. Global NO_x emissions are difficult to measure because the highly

Table 2.1.: *Estimate of global tropospheric nitrogen oxides emissions in Tg N yr^{-1} [from IPCC (2007) AR4]*

Sources	Emission Tg N yr^{-1}	Uncertainty Tg N yr^{-1}
Anthropogenic Sources		
Fossil fuel combustion	25.6	21.0 - 28.0
Biomass burning	5.9	6.0 - 12.0
Agriculture	1.6	0 - 4.0
Aircraft	0.6	0.5 - 0.8
Anthropogenic total	**33.7**	**27.5 - 44.8**
Natural Sources		
Lightning	1.1-6.4	3.0 - 7.0
Soils under natural vegetation	7.3	5.0 - 8.0
Stratosphere	< 0.5	
Natural Total	**8.9-14.2**	**8.0 - 15.0**
Total Sources	**42.6 - 47.9**	**35.5 - 59.8**

variable lifetime results in pronounced spatial and temporal variations in their distributions. The main contributors to the global NO_x emissions are from burning processes. Lightning, emissions from aircraft and transport from the stratosphere

to the troposphere are minor contributors to the total sources. However these 'minor' contributors can impact the O_3 production in the remote - and upper troposphere.
The pre-industrial values for the global NO_x emissions are estimated to be 12 Tg N yr^{-1} [Holland et al. (1999) and Galloway et al. (2004)]. So therefore the total emissions have almost quadrupled to about 42 - 47 Tg N yr^{-1} in the year 2000 (see Table 2.1). For the year 2100 total emissions in the range of 105 - 131 Tg N yr^{-1} are estimated [Lamarque et al. (2005)].
Estimates of tropospheric NO_2 columns from space by the Global Ozone Monitoring Experiment (GOME) and the SCanning Imaging Absorption SpectroMeter for Atmospheric CHartographY (SCIAMACHY) [Heue et al. (2005); Richter and Burrows (2002)] provide constraints to NO_x emissions [Leue et al. (2001)]. Figure 2.1 provides a comparison of the tropospheric NO_2 columns of three state-of-the-art retrievals from GOME for the year 2000 with model results from global atmospheric chemistry models. Due to the short lifetime of the nitrogen oxides compared to

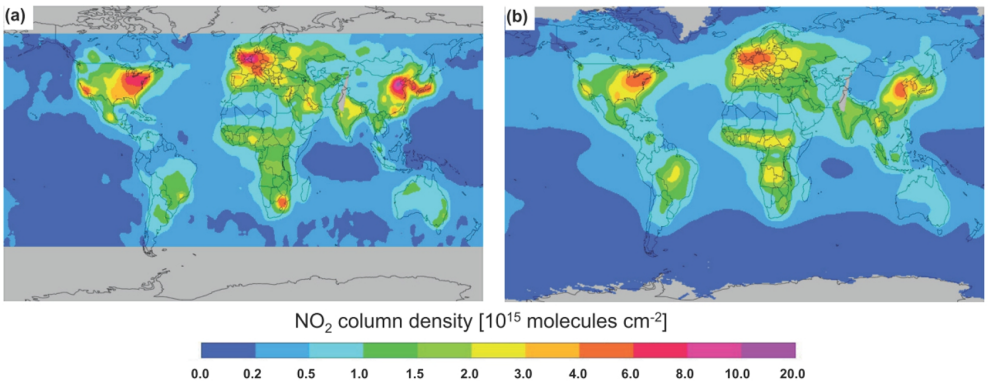

Figure 2.1.: *Tropospheric column NO_2 from (a) satellite measurements (GOME) and (b) atmospheric chemistry models. The maps represent ensemble average annual mean tropospheric NO_2 column density maps for the year 2000. (adapted from van Noije et al. (2006) and IPCC (2007)).*

timescale for global circulation, there is only a very little influence of vertical and horizontal transport. Therefore, since a large contribution of the global fossil fuel combustion is in urban or the vicinity of urban areas, region close to the urban centres are impacted the most. Figure 2.1 clearly shows this strong correlation of the NO_x distribution towards the major source region which is more pronounced in the northern-east USA, Europe and eastern Asia. There are also other regions mostly in South America, central Africa and southern Asia which are influenced by strong NO_x emissions, from biomass burning and bio-fuel use.

2.1.2. Sinks for Nitrogen Oxides

The atmospheric lifetime (defined here as turnover lifetime from steady state) of nitrogen oxides is in the range of hours to days. Therefore, there is a high degree of variability in tropospheric NO_x concentrations. Close to the Earth's surface the lifetime is relatively short (hours), however, it increases at higher altitudes (days). The lifetime of the nitrogen oxides is also season dependent, i.e. it is longer in winter than in summer due to the lower OH concentrations in the winter.
The main sink of NO_x in the troposphere is the conversion to water soluble species like nitric acid (HNO_3) or nitrous acid (HONO), which are removed by dry and wet deposition. 16% - 40 % of the total nitrogen flux to the surface is expected to be due to dry deposition of HNO_3 (e.g. adsorption on aerosols or the ground) as estimated by Russell et al. (1993) and Nielsen et al. (1996), respectively.
One of the main reactions leading to the formation of nitric acid is the reaction of nitrogen dioxide (NO_2) with the hydroxyl radical (OH):

$$NO_2 + OH \xrightarrow{M} HNO_3 \tag{2.4}$$

Comparable sink for NO_x is the hydrolysis of N_2O_5 during nighttime and subsequently the dry and wet deposition of the HNO_3 formed [Mentel et al. (1996)].

$$N_2O_5 + H_2O_{(l)} \longrightarrow 2\,HNO_{3\,(g)} \tag{2.5}$$

$$N_2O_5 + H_2O_{(l)} \longrightarrow 2\,HNO_{3\,(aq)} \tag{2.6}$$

In the northern hemisphere, reactions (2.5) and (2.6) and the adsorption of NO_3 on wet surfaces [Dentener and Crutzen (1993)] are responsible for about 50-90 % of the HNO_3 formation.
During nighttime HNO_3 can also be formed by the reaction of the nitrate radical (NO_3) with aldehydes and higher alkanes (H-abstraction):

$$NO_3 + RH \longrightarrow R\cdot + HNO_3 \tag{2.7}$$

$$NO_3 + RCHO \longrightarrow RCO\cdot + HNO_3 \tag{2.8}$$

2.1.3. Chemistry of Nitrogen Oxides in the Troposphere

NO, NO_2 and O_3 acquire a photochemical steady state in the sunlit atmosphere. The photolysis of NO_2 in sunlight, at wavelengths less than 424 nm, results in the formation of O_3:

$$NO_2 + h\nu \longrightarrow NO + O(^3P) \qquad (\lambda < 424nm) \qquad (JNO_2) \tag{2.9}$$

The photolysis rate of nitrogen dioxide (JNO_2) depends on the solar radiation which is strongly influenced by the solar zenith angle, clouds and aerosols. On sunny days typical noon photolysis frequencies at mid-latitudes are about $JNO_2 =$

$0.01s^{-1}$. The oxygen atom which is formed in reaction 2.9 reacts with oxygen molecule to form O_3.

$$O(^3P) + O_2 + M \longrightarrow O_3 + M \tag{2.10}$$

M represents a third molecule (N_2 or O_2) that stabilizes the formation of O_3 by absorbing excess energy. The above mechanism is believed to be the only significant source of O_3 production in the troposphere [Seinfeld and Pandis (2006)]. O_3 produced in reaction 2.10 can react with NO to regenerate NO_2:

$$O_3 + NO \longrightarrow NO_2 + O_2 \tag{2.11}$$

With enough actinic flux the reactions (2.9 to 2.11) will reach a point where NO_2 is destroyed and produced rapidly and as a result a steady state is maintained. Although O_3 is produced from the photolysis of NO_2 (reaction 2.9) and the subsequent titration of O_3 by nitric oxide (reaction 2.11) limits the O_3 formation and therefore results in a balance between O_3 production and titration. Therefore, if the coupling between NO and NO_2 only occurs through the photolysis of NO_2 and the reaction of NO with ozone, a null cycle is established during the day and therefore there is no net O_3 production.
The production rate of O_3 is determined by the photolysis of NO_2. Thus, the equilibrium between NO and NO_2 is an important factor for the O_3 production. The expression that results from the steady state of reactions 2.9 to 2.11 has been named the photo stationary state relation or the Leighton ratio (φ) [Leighton (1961)]:

$$\varphi = \frac{JNO_2[NO_2]}{k_{2.11}[O_3][NO]} \tag{2.12}$$

where $k_{2.11}$ is the reaction rate constant of reaction 2.11. Peroxy radicals ($RO_x = RO_2 + HO_2$) provide an alternative pathway to conversion of NO to NO_2 where R denotes an organic group. This leads to the conversion of NO to NO_2 without O_3 destruction in reaction 2.13 and 2.14, leading to the accumulation of O_3:

$$HO_2 + NO \longrightarrow NO_2 + OH \tag{2.13}$$
$$RO_2 + NO \longrightarrow NO_2 + RO \tag{2.14}$$

The Leighton ratio is used as a means of characterizing the photo stationary state and is approximately equal to unity in urban environments. [e.g. Carpenter et al. (1998); Thornton et al. (2002)]. In areas with low NO_x levels, the Leighton ratio is expected to deviate from unity [Hauglustaine et al. (1999, 1996); Mannschreck et al. (2004); Parrish et al. (1986); Volz-Thomas et al. (2003)]. This is due to the fact that low NO concentrations reduce the importance of reaction 2.13 and 2.14 as peroxy radical sink. Therefore, the peroxy radical levels increases and consequently reactions 2.13 and 2.14 compete with reaction 2.11. So in this case,

the photo stationary state depends not only on the NO and NO_2 concentrations but also on peroxy radical concentrations.
During nighttime, other processes become more important. The oxidation of NO to NO_2 with simultaneous ozone depletion (Reaction (2.11)) still takes place, but another reaction becomes important; the reaction with NO_2 with O_3 to form the nitrate radical (NO_3).

2.2. Chemistry of the Nitrate Radical

Free radicals play an important role in the self-cleaning of the atmosphere (i.e. removal of nitrogen oxides and organic trace gases from the atmosphere). Beside the Hydroxyl radical (OH) and ozone (O_3) the nitrate radical (NO_3) is one of the most important radicals. In 1881 Hautefeuille and Chappuis (1881) postulated such a molecule to explain absorption bands between 500 and 700 nm which could not be explained by ozone. The strongest of these absorption bands was found at 662nm. In 1978 the nitrate radical was first detected by Noxon et al. (1978) in the stratosphere and in 1980 by Platt et al. (1980) and Noxon et al. (1980) in the troposphere. While during daytime NO_x is removed mostly from the atmosphere by the oxidation of NO_2 by OH to form HNO_3 (see Reaction 2.4) [Seinfeld and Pandis (2006)], during nighttime the OH production from O_3 photolysis stops and its concentration is estimated to be below 2×10^5 $molecules\ cm^{-3}$. NO_2 is slowly oxidized by O_3 to form NO_3 (reaction 2.15), which can further react with NO_2 to form N_2O_5 (reaction 2.16). N_2O_5 decomposes thermally to form NO_3 and NO_2 (reaction 2.17) to establish a dynamic equilibrium between NO_2, NO_3 and N_2O_5.

$$NO_2 + O_3 \longrightarrow NO_3 + O_2 \tag{2.15}$$

$$NO_2 + NO_3 + M \longrightarrow N_2O_5 + M \tag{2.16}$$

$$N_2O_5 + M \longrightarrow NO_2 + NO_3 + M \tag{2.17}$$

In the following sections the sources and sinks of NO_3 and its atmospheric importance will be discussed more in detail.

2.2.1. Sources of NO_3

The most important source of nitrate radical in the troposphere is the reaction of NO_2 with O_3 as shown in reaction 2.15. Thus, the production rate of NO_3 can easily be determined from known concentrations of NO_2 and O_3:

$$P(NO_3) = k_{2.15}(T)[NO_2][O_3] \tag{2.18}$$

where $k_{2.15}(T)$ is the temperature dependent rate constant for reaction 2.15 [Atkinson et al. (2004)] with a value of 3.76×10^{-17} $cm^3\ molecule^{-1}\ s^{-1}$ for T=298 K.

Due to the fact that NO_3 and N_2O_5 are in a dynamic equilibrium, the back reaction from N_2O_5 to NO_3 is also a NO_3 source which can occur over N_2O_5 photolysis (only in the stratosphere) or decomposition (see reaction 2.17):

$$N_2O_5 + h\nu \longrightarrow NO_3 + NO_2 \tag{2.19}$$

2.2.2. Direct sinks of NO_3

In contrast to the sources of NO_3 which can be described almost completely by reaction 2.15 at night the sinks for NO_3 are much more complex. In the following the different sink terms will be described.

2.2.2.1. Photolysis of NO_3

During the day the lifetime of NO_3 is limited due to its photolysis to NO_2 or NO.

$$NO_3 + h\nu \longrightarrow NO + O_2 \qquad (\lambda < 700\,\text{nm}) \tag{2.20}$$

$$NO_3 + h\nu \longrightarrow NO_2 + O \qquad (\lambda < 580nm) \tag{2.21}$$

The quantum yields of these two reactions depend strongly on the wavelength. At the earth's surface the formation of NO_2 dominates (90%) with typical photolysis rates for noon time conditions are in the range of $0.17 - 0.19\ s^{-1}$ for reaction 2.20 and $0.016 - 0.02\ s^{-1}$ for reaction 2.21. [Johnston et al. (1996); Orlando et al. (1993)].

2.2.2.2. Reaction of NO_3 with NO

Another important NO_3 loss process is the reaction with NO

$$NO_3 + NO \longrightarrow 2\,NO_2 \tag{2.22}$$

With a room temperature rate constant of $k_{2.22}(298K) = 2.6{\times}10^{-11}\ cm^3\ molec^{-1}\ s^{-1}$ [Atkinson et al. (2004)] this reaction leads to short lifetimes of NO_3 in the presence of NO, i.e. in the presence of about 150 ppt NO the NO_3 lifetime is shortened to about 10s.

2.2.2.3. Reactions of NO_3 with VOC's

During nighttime when photolysis ceases and if no local NO emissions are present, NO_3 mixing ratios can build up several hundreds of pptv. The reaction with NO_3 are important nocturnal oxidation processes for many organic trace gases. The global estimate for anthropogenic VOC emission is believed to be in the range of 60 to 140 Mio. t/year and about 1150 Mio t/year from biogenic sources [Guenther et al. (1995); Lamb et al. (1996)]. Although the reaction constants for the reaction

of VOCs with OH are typically larger than those from the reaction of VOCs with NO_3, the nighttime concentrations of NO_3 are in the order of 100 times higher than the OH concentration. The total loss frequency via the reaction with VOC can be estimated by

$$f_{NO_3-VOC} = \sum_i [VOC]_i k_{NO_3-VOC} \tag{2.23}$$

where $[VOC]_i$ is the concentration of a certain VOC which is multiplied by the specific rate constant k_i.
The reaction of NO_3 with saturated hydrocarbons (alkanes) are typically slow. NO_3 reacts with alkanes by H abstraction as exemplified in Reaction 2.24.

$$CH_3CH_2CH_2CH_3 + NO_3 \longrightarrow CH_3CH_2CH{\cdot}CH_3 + HNO_3 \tag{2.24}$$

The reaction of NO_3 with unsaturated hydrocarbons (alkenes) and especially biogenics (e.g. terpenes) are fast enough to be significant for the overall hydrocarbon budget [Atkinson and Arey (2003)]. In rural areas the reaction of NO_3 with terpenes or isoprene contribute to the major sinks of NO_3 due to the high monoterpene emissions from forests [Geyer et al. (2001b); Gölz et al. (2001)]. The initial step is the addition of NO_3 to the carbon double bond as shown in Equation

$$NO_3 + R_1{-}C{=}C{-}R_2 \longrightarrow R_1{-}C{-}C(NO_3){-}R_2 \tag{2.25}$$

The resulting nitroxyalkyl radical can then rapidly react with oxygen forming a nitroxyalkyl - peroxy radical ($RH{-}ONO_2{-}O_2$). Beside the reaction with alkanes and alkenes NO_3 reacts efficiently with oxygenated hydrocarbons, such as aldehydes and phenolic compounds. For the marine boundary layer, reactions of NO_3 with reduced sulphur trace gases (e.g.DMS) plays an important role. Table 2.2 gives an overview of the rate constants for different classes of VOCs and a VOC lifetimes at a fixed NO_3 concentration.

Table 2.2.: *NO_3 rate constants at room temperature for selected VOCs and their lifetimes at a fixed NO_3 mixing ratio [taken from Brown and Stutz (2012)]*

VOC	k(NO_3) ($cm^3 molecule^{-1} s^{-1}$)	Lifetime (NO_3 = 20 pptv)
Anthropogenic hydrocarbons		
Alkanes	$< 5 \times 10^{-16}$	> 46 days
Aromatics	$< 2 \times 10^{-15}$	> 11 days
Ethene	2×10^{-16}	> 116 days
Linear alkenes	$1 - 2 \times 10^{-14}$	28-55 h
Internal, branched alkenes	$< 3 - 600 \times 10^{-13}$	0.5 min - 1.9 h
Biogenic hydrocarbons and sulphut		
Isoprene	7×10^{-13}	0.8 h
Monoterpenes	$2.5 - 12 \times 10^{-12}$	3-15 min
Sesquiterpenes	$7 - 1400 \times 10^{-13}$	14s - 0.8 h
DMS	1×10^{-12}	0.6 h
Oxygenates		
Formaldehyde	6×10^{-16}	39 days
Acetaldehyde	3×10^{-15}	7.7 days
Higher aldehydes	$0.7 - 3 \times 10^{-14}$	18 h - 3.3 days
Alcohols	$1 - 20 \times 10^{-16}$	11-230 days
Ketones	$< 6 \times 10^{-16}$	> 38 days
Phenol, cresols	$2 - 13 \times 10^{-12}$	3-17 min

2.2.2.4. NO_3 uptake on aerosol and deposition

Although the losses of NO_3 are dominated by gas phase reactions. NO_3 can potentially also interact with particles. The loss of NO_3 due to direct uptake on aerosols is proposed be of minor importance [Thomas et al. (1998)]. The loss frequency with respect to heterogeneous reaction of NO_3 with aerosols is determined by the uptake coefficient γ, which largely depends on the chemical composition of the aerosols and also on temperature. γ is defined as the probability that a molecule which collides with the surface of an aerosol is up taken by the surface. Generally the uptake coefficient $\gamma(NO_3)$ is small. Several laboratory studies have investigated the uptake of NO_3 on several types of aerosols, a short overview is shown in Table 2.3. The first order loss rate (s^{-1}) due to the reactions of NO_3 with aerosols can be estimated using the expression:

$$k_{het} = 0.25 \cdot \overline{c} \cdot \gamma \cdot A \tag{2.26}$$

with the temperature dependent mean molecular velocity $\bar{c}$ ($\frac{cm}{s}$), the total surface area density A ($\frac{cm^2}{cm^3}$) and the uptake coefficient γ. Equation 2.26 does not include corrections for the limitation of gas phase diffusion to the particle surface, but for uptake coefficients < 0.1 and a particle of $< 1\mu m$ diameter this simplified expression is adequate. For the correct expression the effective uptake coefficient must be considered which is approximated by [Fuchs and Sutugin (1970)]:

$$\frac{1}{\gamma_{effective}} = \frac{1}{\gamma} + \frac{0.75 + 0.283Kn}{Kn(Kn+1)} \tag{2.27}$$

where $Kn = \frac{3D_g}{\bar{c}r_{sw}}$, r_{sw} is the radius of the particle at the maximum of the surface area weighted size distribution and D_g is the gas phase diffusion coefficient of NO_3 or other molecules at the appropriate pressure and temperature ($D_g(NO_3) \approx 0.11 cms^{-1}$ [Geyer et al. (1999)]). Beside the loss due to the uptake on aerosol NO_3 can also be removed from the atmosphere via deposition on the ground depending on meteorological conditions. Assuming neutral to stable stratification, the loss rate via dry deposition, which depends on the height of the mixing layer, can be estimated from the wind speed [Haugen (1973)]:

$$f_{Dep} = \frac{1}{h[R_T + R_L + R_C]} \tag{2.28}$$

where h is the height of the mixing layer and R_L and R_T are the turbulent and laminar transport resistances, respectively. The chemical resistance R_C describes the rate of reactions on the ground. These reactions depend on the chemical and physical properties of the surface. Due to the fact that no observations of the surface resistance for NO_3 have been published, upper limits to dry deposition can be calculated assuming $R_C = 0$. Turbulent and laminar transport resistance can be estimated for neutral stratification using the friction velocity u* obtained from the wind speed. For typical values a calculated upper limit of the deposition loss rate is about $3 \times 10^{-4} s^{-1}$ ($u* = 15\ cm\ s^{-1}$, h=100m, $R_T \approx 1.9\ s\ cm^{-1}$ and $R_L \approx 1.1 scm^{-1}$)[Geyer et al. (2001b)]. Huff et al. (2011) presented measurements of N_2O_5 gradients in which they could estimate a deposition velocity for N_2O_5 in a range of $0 - 1.5\ cm\ s^{-1}$ with an average value of $0.6\ cm\ s^{-1}$.

2.2.3. Indirect sinks of NO_3

Loss processes of N_2O_5, which is in equilibrium with NO_3 (see Reactions 2.16 and 2.17), also lead to removal of NO_3 and may be considered 'indirect' routes to NO_3 loss. The Equilibrium between NO_3 and N_2O_5 is strongly dependent on temperature and as well on the NO_2 concentration. At low temperatures and low NO_2 mixing ratios the equilibrium is shifted to N_2O_5 like shown in equation 2.29:

$$[N_2O_5] = k_{eq}(T)[NO_2][NO_3] \tag{2.29}$$

Figure 2.2 shows the NO_3/N_2O_5 ratio against NO_2 mixing ratios for different

temperatures calculated after equation 2.29. The figure shows a clear dependence on temperature and NO_2 mixing ratios. The NO_3/N_2O_5 ratio decreases with increasing NO_2 mixing ratios linearly whereas the ratio increases even exponentially with increasing temperature. Due to the strong temperature dependence of the equilibrium constant (cold temperatures favours N_2O_5) the indirect sinks for NO_3 are most effective during the winter months.

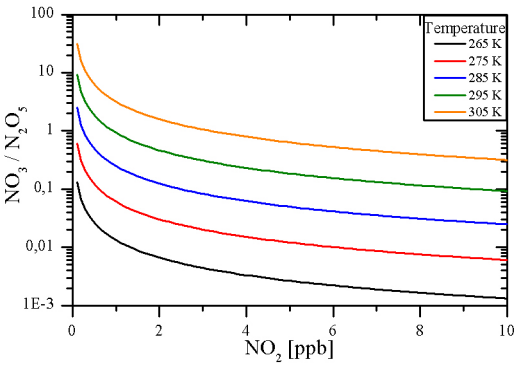

Fig. 2.2.: *NO_3/N_2O_5 ratio against NO_2 mixing ratios for different temperatures. The temperature dependent equilibrium constant was calculated based on Atkinson et al. (2004)*

This indirect degradation frequency for NO_3 can be calculated using Equation 2.30 where $f_{N_2O_5}$ is the loss frequency for N_2O_5:

$$f_{indir(NO_3)} = k_{eq}(T) \cdot [NO_2] \cdot f_{N_2O_5} \tag{2.30}$$

In the following the possible indirect sinks for NO_3 via losses of N_2O_5 are discussed.

2.2.3.1. Homogeneous reaction of N_2O_5 with water vapour

The homogeneous reaction of N_2O_5 with water vapour producing HNO_3 is a possible sink.

$$N_2O_5 + nH_2O \longrightarrow 2\,HNO_3 + (n-1)H_2O \tag{2.31}$$

Laboratory studies by Mentel et al. (1996) and by Wahner et al. (1998a) provided evidence for a slow reaction between N_2O_5 and H_2O, which, under certain circumstances (e.g. low aerosol concentration), can contribute to the loss of N_2O_5. The reaction was found to have a complex dependency on $[H_2O]$, the loss rate coefficient (k_{H_2O}) being described by $k_{H_2O} = 2.5 \times 10^{-22}\ [H_2O] + 1.8 \times 10^{-39}\ [H_2O]^2\ s^{-1}$. At high nighttime relative humidities this reaction could limit the N_2O_5 lifetime to about 20 minutes (at 80% relative humidity and 25 °C). Such a rapid hydrolysis would dominate the loss of NO_3 and N_2O_5 in many environments.
Results of recent field measurements show longer N_2O_5 lifetimes than calculated from the homogeneous hydrolysis. Brown et al. (2009b) determined N_2O_5 lifetimes that were up to a factor of 10 larger than the minimum lifetime due to homogeneous hydrolysis from aircraft measurements over Texas and Crowley et al. (2010) showed for a rural site in Germany that the actual rate constant is at least a factor

of 3 lower than the literature value. IUPAC [1] no longer suggest that this reaction should be incorporated in calculations of NO_3 or N_2O_5 losses in the atmosphere.

2.2.3.2. Heterogeneous reaction of N_2O_5 on aerosols and deposition

The loss of N_2O_5 is usually dominated by heterogeneous reaction on the surface of atmospheric particles. The degradation frequency for N_2O_5 on aerosol can be calculated after Equation 2.26 as described in section 2.2.2.4. The uptake of N_2O_5 to different sorts of aerosols has been extensively investigated in several laboratory studies. Table 2.3 gives a short overview of the uptake coefficients for different types of aerosol [for detailed description see Brown and Stutz (2012) and references therein]. However, uptake coefficients of N_2O_5 on ambient aerosols [Bertram et al. (2009a,b); Brown et al. (2009b, 2006)] are often a factor of 10 or more lower than the values used in the current large-scale model parametrizations, which are based on laboratory studies. The difference is related to the multi-component nature of atmospheric aerosols, which can reduce the heterogeneous hydrolysis of N_2O_5. The degradation frequency due to dry deposition can be estimated via Equation 2.28 in section 2.2.2.4. As already mentioned there is only one publications referring to a deposition velocity for N_2O_5.

2.2.4. Atmospheric importance of NO_3 and N_2O_5

The impact of NO_3 and N_2O_5 chemistry for the troposphere covers several aspects which will be shortly summarized in the following section.

2.2.4.1. NO_x losses and photochemical O_3 production

The nocturnal NO_x losses, which mainly occur over the reaction of NO_3 with VOCs or heterogeneous uptake from N_2O_5 on aerosols, have a direct impact on the NO_x budget itself but also influences on photochemical O_3 (and OH) production for the next day [Dentener and Crutzen (1993); Evans and Jacob (2005)]. Differences in nocturnal and diurnal NO_x losses depends strongly on the season and locations. The relative contribution of the nocturnal losses between the degradation of VOCs by NO_3 and the heterogeneous uptake of N_2O_5 by aerosols depend on the concentration of biogenic alkenes and DMS, the aerosol surface area, relative humidity and temperature [Geyer et al. (2001b)].

2.2.4.2. Influence on organic species

As discussed in section 2.2.2.3, the degradation processes for biogenic alkenes by the reaction with NO_3 are very important.As an example, Asaf et al. (2009) reported

[1] International Union of Pure and Applied Chemistry

Table 2.3.: *Summary of uptake coefficients of NO_3 and N_2O_5 on different kinds of aerosols [adapted from Brown and Stutz (2012)]*

Aerosol type	range of uptake coefficient	typical value	Reference from typical value
N_2O_5			
Water	$<$ 0.01 - 0.06	0.013	George et al. (1994)
H_2SO_4	0.02 - 0.2	0.02	Hallquist et al. (2000); Hu and Abbatt (1997)
NH_4HSO_4	0.017 - 0.085	0.02	Hallquist et al. (2003)
$(NH_4)_2SO_4$	0.017 - 0.085	0.02	Hallquist et al. (2003)
$NaNO_3$ or NH_4NO_3	0.002-0.003	0.002-0.003	Mentel et al. (1999); Wahner et al. (1998b)
NaCL	0.005 - 0.03	0.03	Zetzsch and Behnke (1992)
Dust	0.005 - 0.2	0.02	Tang et al. (2012)
Soot	$4 \cdot 10^{-6}$ - 0.006	0.003	Kamm et al. (1999)
Organics	$0.15 - 8 \cdot 10^{-3}$ type depending	$1.5 - 4 \cdot 10^{-4}$ $5 - 8 \cdot 10^{-3}$	Escorcia et al. (2010) Griffiths et al. (2009)
NO_3			
Water	$1.5 - 60 \cdot 10^{-4}$	$2 \cdot 10^{-4}$	Rudich et al. (1996)
H_2SO_4	$< 10^{-3}$		Fenter and Rossi (1997)
Dust (Saharan)	0.001-0.026	0.018	Tang et al. (2010, 2012)
Soot	$< 4 \cdot 10^{-4}$ - 0.33	0.33	Karagulian and Rossi (2007)
Dry Salts	0.002 - 0.49		Brown and Stutz (2012)
Organics	$4.5 \cdot 10^{-4}$ - 1.01		Brown and Stutz (2012)

from measurements in Jerusalem during the summer that the oxidation of total VOCs by NO_3 contribute to 70 % of the total oxidation capacity. The contribution was even 75 % considering only olefinic VOCs. In this case the oxidation potential of NO_3 was about twice of the oxidation potential of OH.

2.2.4.3. Impact on sulphur cycle

The reaction of NO_3 with DMS (CH_3SCH_3) has an impact on the sulphur cycle. The reaction occurs via the abstraction of an H-atom forming nitric acid and the CH_3SCH_2 radical [Butkovskaya and LeBras (1994)]. During nighttime, the ensuing peroxy radical can further react with NO_3 resulting in formation of SO_2, methane sulfonic acid (MSA) and ultimately H_2SO_4 [Barnes et al. (2006)]. DMS is the dominant natural source of sulphur in the atmosphere and therefore the oxidation of DMS impacts the sulphur budget and thus aerosol levels and cloud formation. Depending on the measurement location the reaction of NO_3 with DMS can be a

significant sink of NO_x [Platt and LeBras (1997)] and in many remote locations affects the NO_3 budget most.

2.2.4.4. Impact on HO_x and RO_2 cycle

The reaction of NO_3 with alkenes can lead to production of various types of radicals. Platt et al. (1990) proposed for the first time the link between NO_3 and RO_2, HO_2 and OH radicals. The presence of RO_2 at night with mixing ratios up to 40 pptv were observed in several studies [Andrés-Hernández et al. (2012); Cantrell et al. (1997, 1996); Carslaw et al. (1997); Emmerson and Carslaw (2009); Emmerson et al. (2005); Geyer et al. (2003); Mihelcic et al. (2003); Sommariva et al. (2007)]. Due to the fact that RO_2 can also be produced from ozonolysis of VOCs the direct link between NO_3 and RO_2 formation is often hard to demonstrate. Depending on the location the contribution of NO_3 to the formation of RO_2, HO_2 and OH is different (e.g. Emmerson and Carslaw (2009); Emmerson et al. (2005); Geyer et al. (2003)). Geyer and Stutz (2004) suggest that at night the $NO_3 + VOC$ reaction is the major source of RO_2 radicals due to the high NO_3 levels aloft that result from the suppressed mixing in the nocturnal boundary. From their modelling results they argued that NO_3 do not play a role in the formation of HO_2 and OH.

2.2.4.5. Formation of organic nitrate and SOA

Organic nitrates and also secondary organic aerosols (SOA) can be formed by reaction of NO_3 with biogenic VOCs such as isoprene or α - pinene [Fry et al. (2011); Ng et al. (2008); Perring et al. (2009b)]. The branching ratio for organic nitrate formation via the reaction of NO_3 with alkenes is variable. For example, the reaction of NO_3 with isoprene yields to $65 \pm 12\%$ organic nitrates, of which the majority are nitrooxy carbonyls [Perring et al. (2009b)]. Fry et al. (2011) studied the reaction of limonene with NO_3 with the result that the organic nitrate yield is about 30 %, while the SOA mass yield was observed to be 25 - 40 %. SOA yields from the oxidation of isoprene by NO_3 could be estimated during field measurements. During a summer campaign in the Northeast US Brown et al. (2009a) could determine a contribution of nocturnal oxidation of isoprene to SOA in the range of 1 - 17 %. The isoprene SOA mass derived from NO_3 was calculated to exceed that due to OH by approximately 50 %.

2.2.4.6. Formation of particulate nitrate

The uptake and hydrolysis of N_2O_5 on aqueous aerosol is a mechanism for formation of particulate nitrate. Also the reaction of NO_3 with DMS forming HNO_3 via H-atom abstraction can also lead to formation of particulate nitrate. For example Vrekoussis et al. (2006) observed during measurements in the eastern

Mediterranean that both processes are responsible for about 50 - 65 % of the total particulate nitrate formation.

2.2.4.7. Halogen activation by N_2O_5

In chloride containing aerosol N_2O_5 uptake can lead to the formation of $ClNO_2$ [Finlayson-Pitts et al. (1989); Roberts et al. (2008, 2009)], which will accumulate over the night. The photolysis of $ClNO_2$ is an early morning source of a Cl radical and NO_x that can initiate ozone formation. Osthoff et al. (2008) presented the first combined measurements of N_2O_5 and $ClNO_2$ along the US Golf Coast. They measured $ClNO_2$ in the ppb range. They estimated that all $ClNO_2$ production took place either form ship emissions within the marine boundary layer, or from coastal urban areas. Later Thornton et al. (2010) measured $ClNO_2$ in the mid of the US (1600 km distance from the coast). Phillips et al. (2012b) observed $ClNO_2$ concentration close to ppb range in central Europe (about 300-400 km distance from the coast). Both studies suggest that $ClNO_2$ is present not only in the marine boundary layer and could have a large influence on oxidation processes in the morning.

2.3. Chemistry of Organic Nitrates

Organic nitrates contribute substantially to the total reactive nitrogen species. In the following the sources and sinks of the organic nitrates will be discussed and also their atmospheric importance. In general organic nitrates are present in the atmosphere in the form of $RONO_2$ and RO_2NO_2.

2.3.1. Sources of Organic Nitrates

Organic nitrates have their origin in direct emissions from combustion and chemical processes and are formed from atmospheric photo oxidation of organic compounds in the presence of NO_x [Roberts (1990)]. Emissions of $RONO_2$ were observed from industrial activity and also from engines [Thompson et al. (1979)] but the importance of those sources is still uncertain. The following reaction scheme summarizes

the known gas - phase reactions resulting in the formation of $RONO_2$ and $ROONO_2$

$$RO_2\cdot + NO \xrightarrow{M} RONO_2 \tag{2.32}$$

$$RO_2\cdot + NO_2 \xrightarrow{M} ROONO_2 \tag{2.33}$$

$$\text{Alkene} + NO_3 \xrightarrow{M} R'ONO_2 \tag{2.34}$$

$$RC(O)OONO_2 \xrightarrow{M} RONO_2 + CO_2 \tag{2.35}$$

$$RO\cdot + NO_2 \xrightarrow{M} RONO_2 \tag{2.36}$$

where $RO\cdot$ are oxy - and $RO_2\cdot = ROO\cdot$ peroxy radicals. Both radicals are products of the OH, NO_3, O_3 initiated oxidation of organic compounds. The formation of organic nitrates via the reaction of $RO_2\cdot$ with NO (see Reaction 2.32) is only a small fraction of the total reaction, which is dominated by:

$$RO_2\cdot + NO \longrightarrow RO\cdot + NO_2 \tag{2.37}$$

which represents a key step in the production of ozone from photo oxidation of organic compounds. Because of the large number of hydrocarbons in the atmosphere hundreds of different organic nitrates can be formed but in principal all formation processes occur according to the reaction scheme above.

2.3.2. Different types of Nitrates

As already mentioned there are two major groups of organic nitrates. One in the form of RO_2NO_2 and the other in the form of $RONO_2$. In the following the sum of all peroxy nitrates is designated as $\sum$PNs (RO_2NO_2) and the sum of the alkyl nitrates as $\sum$ANs ($RONO_2$). Peroxy nitrates can be further divided into non-acyl and acyl peroxy nitrates. Non-acyl nitrates (e.g. Methyl nitrate $CH_3O_2NO_2$) are very unstable and play a significant role only in the upper troposphere. Therefore in the following sections $\sum$PNs are acyl peroxy nitrates.

2.3.2.1. Peroxy Nitrates ($\sum$PNs)

The peroxy nitrates ($\sum$PNs) are in the general form of $RC(O)O_2NO_2$. $\sum$PNs are formed during the photo-oxidation of VOC in the presence of NO_x. Acyl peroxy (AP) radicals ($RC(O)O_2$) are the direct precursors to $\sum$PNs and are generated through OH - initiated oxidation or photolysis of aldehydes, ketones and other organic VOC. The Acyl peroxy radical can further react with NO_2 to form PN but also can be lost through reactions with NO, HO_2 or RO_2. Thermal decomposition of the $\sum$PNs regenerates the peroxy radical and NO_2. Therefore the lifetime of $\sum$PNs depends on both the thermal decomposition and the subsequent fate of the peroxy radical. The lifetime of the PN's is inversely proportional to the NO/NO_2

ratio and decays exponential with increasing temperature.
The functional form of a PN will depend on its VOC precursor. The most abundant PN in the atmosphere is the peroxyacetyl nitrate, or PAN with (R=CH_3). PAN normally comprises $70-90\%$ of the total $\sum$PNs [Roberts (1990)]. PAN can be formed from a variety of anthropogenic and biogenic VOC, most notably acetaldehyde and methyl vinyl ketone (MVK) [LaFranchi et al. (2009)]. Peroxypropionyl nitrate (PPN, R=CH_3CH_2) is produced during the reactions of OH with propanal, an oxidation product of anthropogenic alkanes. In contrast to PPN, peroxymethacryloyl nitrate (MPAN, R=$CH_2C(CH_3)$) is formed due to the reaction of OH with methacrolein, which in turns is a first - generation oxidation product of isoprene, a ubiquitous biogenic VOC. PPN and MPAN are typically in the order of $5-20\%$ of PAN [Roberts et al. (2002, 2003); Williams et al. (1997)]. The relative abundances of PAN, PPN and MPAN are useful indicator for the relative roles of anthropogenic and biogenic VOC in oxidation chemistry [Roberts et al. (1998); Williams et al. (1997); Wolfe et al. (2007)]. PN mixing ratios can vary from a few ppts up to tens of ppbs [Roberts (1990); Singh and Salas (1989)]. The relative contribution of $\sum$PNs to the total nitrogen budget (NO_y=NO + NO_2 + PN + HNO_3 + $RONO_2$ + HONO + NO_3 + $2 \cdot N_2O_5$+...) is generally about $10-40\%$[Day et al. (2009); Murphy et al. (2006); Roberts (1990); Turnipseed et al. (2006)] but can be as much as 80 % of NO_y in aged air masses [Roberts et al. (2004)].

2.3.2.2. Alkyl Nitrates ($\sum$ANs)

Organic nitrates of the form $RONO_2$ are a product of reaction 2.32 and 2.34. First measurements of alkyl nitrates in the atmosphere were made by Atlas (1988), and subsequent calculations suggested that the atmosphere should contain a wide suite of individual alkyl and multifunctional nitrates [Atherton and Penner (1988); Calvert and Madronich (1987)]. Trainer et al. (1991) predict that organic nitrates, primarily hydroxy alkyl nitrates derived from isoprene oxidation, can constitute as much as 12-26% of atmospheric NO_y. Schneider and Ballschmiter (1999) demonstrated that at least nearly 100 different alkyl nitrates are present in the atmosphere. In several observation the total measured NO_y could not be explained by individual measurements of different nitrogen compounds (NO + NO_2 + PAN + HNO_3 + HONO + NO_3 + $2 \cdot N_2O_5$+...). The range of this 'missing' NO_y was about 10-20 %. In most of these observations the total alkyl nitrate content was not measured or only partially [e.g. Buhr et al. (1990); Fahey et al. (1986); Parrish and Buhr (1993); Ridley et al. (1990); Singh et al. (1996); Williams et al. (1997)]. In 2003 Day et al. (2003) applied a new thermal dissociation method to detect PAN's, AN's and HNO_3 via thermal conversion to NO_2, and derived contribution of total alkyl nitrates in the range of 10-20 % of total NO_y. Several studies with a similar technique could also measure a contribution of alkyl nitrates in the range

of the so called missing NO_y [e.g. Perring et al. (2009a)]
Alkyl nitrates are formed in the atmosphere following hydrocarbon oxidation as a minor product (1-35 %) of the reaction of an organic peroxy radical (RO_2) with NO.

$$RO_2 + NO \xrightarrow{M} RONO_2 \tag{2.38}$$
$$RO_2 + NO \longrightarrow NO_2 + RO \tag{2.39}$$

The branching ratio $\alpha = \frac{k_{2.38}}{(k_{2.38}+k_{2.39})}$ between reaction 2.38 and 2.39 depends on the number of carbon atoms in the peroxy radical precursor (e.g. 1 % for ethylperoxy to about 35% for C8 peroxy radical).The oxidation of an alkane by OH occurs via H-atom abstraction and leads to an alkyl nitrate whereas the oxidation of an alkene by OH (adding OH to the double bound) leads to a hydroxyalkyl nitrate.
Beside the production over the oxidation by OH, alkyl nitrates can also be formed during nighttime via the reaction of alkenes with NO_3. Here the NO_3 radical adds to the double bond of the alkene to form a alkyl nitrate. The yield for the nitrate formation in the NO_3 case is higher than for OH initiated nitrate formation and is reported to be up to 80 % [Fry et al. (2009); Hallquist et al. (1999)].

2.3.3. Sinks of Organic Nitrates

Organic nitrates can be removed from the atmosphere by gas - phase reaction or multi-phase processes [Roberts (1990)], including reactions with OH, photolysis and thermal decomposition can be responsible for the destruction of the organic nitrates. Additionally uptake by cloud water, aerosol or precipitation and deposition can also play a role. Depending on the type and class of nitrates and also on the location in the atmosphere these removal processes can have different relative importance.
The reaction with OH typically occurs via H abstraction of the alkyl group. This is not the case for nitrates, formed from NO_3 + terpene reactions, with a second double bound. There the OH can add to the second double bond. Typical rate constants for alkyl nitrates ($RONO_2$) are in the range of $0.023 - 3.82 \times 10^{-12} \frac{cm^3}{molecule\ s}\ for\ 298K$ [Atkinson et al. (1982, 2004)]. The rate constant for peroxyacetyl nitrate is about $0.1 \times 10^{-12} \frac{cm^3}{molecule\ s}$. Assuming a mean OH concentration of about $6 \times 10^5 \frac{mol}{cm^3}$ the lifetime of organic nitrates against OH reaction is between 5 days (3-octyl nitrate) and 2.3 years (methyl nitrate) and about 190 days for peroxyacetyl nitrate and plays therefore only a minor role [Orlando et al. (2002)].
The photolysis rates for $RONO_2$ and $ROONO_2$ are in the order of $10^{-8} - 10^{-5} s^{-1}$ depending on the number of carbon atoms, time of the year and latitude [Carbajo and Orr-Ewing (2010); Clemitshaw et al. (1997); Luke et al. (1989); Roberts and Fajer (1989); Talukdar et al. (1997, 1995); Turberg et al. (1990)]. Therefore the lifetime of the nitrates due to loss via photolysis is in the range of a few days up

to several years.
Thermal dissociation is an important process because it constitutes the most important atmospheric loss mechanism of RO_2NO_2 and can limit the extent to which $RONO_2$ compounds will survive in combustion sources. These reactions occur via the following pathways [e.g. Hendry and Kenley (1977, 1979)]

$$RONO_2 \xrightarrow{M} RO + NO_2 \tag{2.40}$$

$$ROONO_2 \xrightarrow{M} ROO + NO_2 \tag{2.41}$$

Figure 2.3 gives an overview of the loss rate for the main processes. The figure shows the atmospheric loss rate against height. Peroxyacetyl nitrate (PAN) [taken from Talukdar et al. (1995)] as an example for RO_2NO_2 and Methyl - (with R=CH_3) and Isopropylnitrate (R = i−C_3H_7) [adopted from Talukdar et al. (1997)] for $RONO_2$ are shown. The top x-axis additionally shows the equivalent lifetime of the nitrates in days. For $RONO_2$ the thermal decomposition is several orders

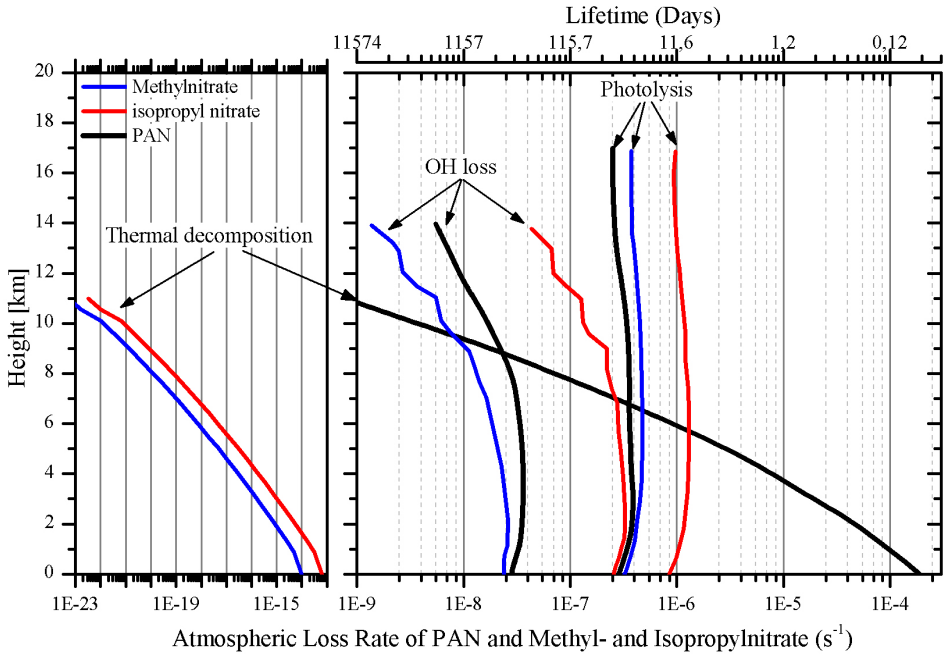

Figure 2.3.: *Loss processes for different types of organic nitrates [Figure adopted from Talukdar et al. (1997, 1995)]. The additional thermal decomposition rates for Methyl - and Isopropyl nitrate are calculated using the Arrhenius Equation after Roberts (1990) (here Temperatures are assumed to be 298 K at Ground and about 227 K at about 11 km height). For the photolysis rate and OH reaction averaged values for actinic flux andOH concentrations are used calculated for summer conditions and* 30° *N and standard temperature profile.*

of magnitude smaller than the decomposition of RO_2NO_2. Therefore, $RONO_2$ loss via thermal decomposition can be neglected. The loss rate due to the reaction of $RONO_2$ with OH can be significant for compounds with a high carbon number. The photolysis of $RONO_2$ is generally the most important loss process but as mentioned above the loss rate is dependent on the solar actinic flux and on the type of nitrate.
The major loss process for RO_2NO_2 is thermal decomposition, with a lifetime of several minutes to hours close to the surface, increasing to weeks in the cold upper troposphere. For higher altitudes the losses due to photolysis dominates and the reaction of OH with higher carbon number species (e.g. PBzN) will also be significant.

2.3.4. Atmospheric importance of Organic Nitrates

Total organic nitrates ($\sum$AN + $\sum$PNs) contribute in a large fraction to NO_y. Due to their different thermal stability the fate of both is different. Peroxy nitrates with a carbonyl group are quite stable in the mid-troposphere, which allows the compound to serve as a reservoir for reactive nitrogen, which can be transported to remote areas before decomposing to release NO_x [Fischer et al. (2010); Kotchenruther et al. (2001)], which can enhance ozone formation in those remote areas. Due to the fact that huge amounts of peroxy nitrates can be formed in oxidation processes especially in urban areas (up to several ppb Roberts (1990); Singh and Salas (1989)), the remote areas downwind of large urban centres can be influenced from the transport of peroxy nitrates. The anthropogenic influence, especially in NO_x emissions, shows a strong increase over the last decades as already mentioned in section 2.1.1. This increase is very pronounced in Eastern Asia where the NO_x emission doubled between 1985 and 1997 and is projected to more than double again by 2020 in the absence of improved mitigation strategies [van Aardenne et al. (1999)]. Modeling studies predict that e.g. the polluted air transported from Eastern Asia may contribute 4 -7 ppbv to the ozone background over the North Pacific Ocean [Berntsen et al. (1999)].
Alkyl nitrates can have an important impact on the NO_x distribution and the ozone budget. The lifetime and the formation yield of the organic nitrates with respect to their loss due to deposition and further oxidation processes, along with the fate of the products from oxidation, control the effect of alkyl nitrates on global NO_x distribution and local ozone formation [Beaver et al. (2012)]. Due to the fact that the branching ratios of the nitrate formation from the reaction RO_2 + NO are small and difficult to determine correctly, the influence on global tropospheric ozone can vary. Ito et al. (2007) and Wu et al. (2007) explained differences in global simulation of tropospheric ozone with different types or formation yields

of nitrates, especially from isoprene nitrates. Paulot et al. (2012) suggest that depending on the lifetime, formation yield and also NO_x recycling efficiency the ozone production behaviour can vary widely. The formation of alkyl nitrates can also have an influence on strategies to improve the air quality in large cities due to non-linear interaction between VOC and NO_x (see Farmer et al. (2011)). One of the most important nitrates is isoprene nitrate because of the huge amount of isoprene which is emitted to the atmosphere (about 440 - 660 Tg C yr^{-1} [Guenther et al. (2006)]). Also nitrates from monoterpenes or oxygenated VOC oxidation processes can be important. Isoprene lifetimes are typically about 3 h (assuming $1 \times 10^6 mol/cm^3$ OH). However, organic nitrates function to increase the spatial scale where relatively short-lived VOC (e.g. isoprene) can impact NO_x concentrations and ozone formation. The branching ratio for the formation of isoprene initiated organic nitrates varies between 4-15 % for the OH oxidation [Atkinson et al. (2004)] and even about 65-70% for the NO_3 oxidation [Perring et al. (2009b); Rollins et al. (2009)]. Isoprene nitrates have a significant influence on global O_3, which is sensitive to the yield of AN formed in the OH reaction. Wu et al. (2007) found a 10 % decrease in global ozone production rates by increasing the nitrate yield from 4.4 to 12 %. Beside this strong impact on the ozone budget nitrates can also influence the NO_x distribution. Horowitz et al. (2007) and Paulot et al. (2009) both showed that isoprene nitrates can be recycled back to NO_x in the range of 40-50% after further oxidation by OH.

2.4. Relationship between NO_2, NO_3, N_2O_5, $\sum$PNs and $\sum$ANs

Figure 2.4 reveals the central role of nitrogen dioxide in the atmosphere. Photolysis of NO_2 is the most important production process for ozone and is responsible for the formation of the nitrate radical. NO_2 together with temperature regulates the equilibrium between NO_3 and N_2O_5 which is important for nocturnal chemistry. NO_3 is the most important radical for nocturnal oxidation which sometimes even exceed the oxidation via OH (e.g. Asaf et al. (2009)). N_2O_5 which is in equilibrium with NO_3 can also significantly influence the NO_y/NO_x budget via e.g. uptake on aerosol as suggested by Dentener and Crutzen (1993); Evans and Jacob (2005). In recent studies a link between N_2O_5 and chlorine activation over aerosol interaction could be investigated [Osthoff et al. (2008); Phillips et al. (2012b); Thornton et al. (2010)] which gives additional oxidation capacity in the morning hours. NO_2 is also directly linked to the formation of peroxy nitrates and indirectly in the formation of alkyl nitrates both species can thermally dissociate to NO_2. NO_3 and alkyl nitrates are also connected. Alkyl nitrates can not only be formed via the reaction of peroxy radicals with NO but also by the oxidation of mainly alkenes by NO_3. The nitrate yields of the NO_3 oxidation is often much more efficient than for the oxidation

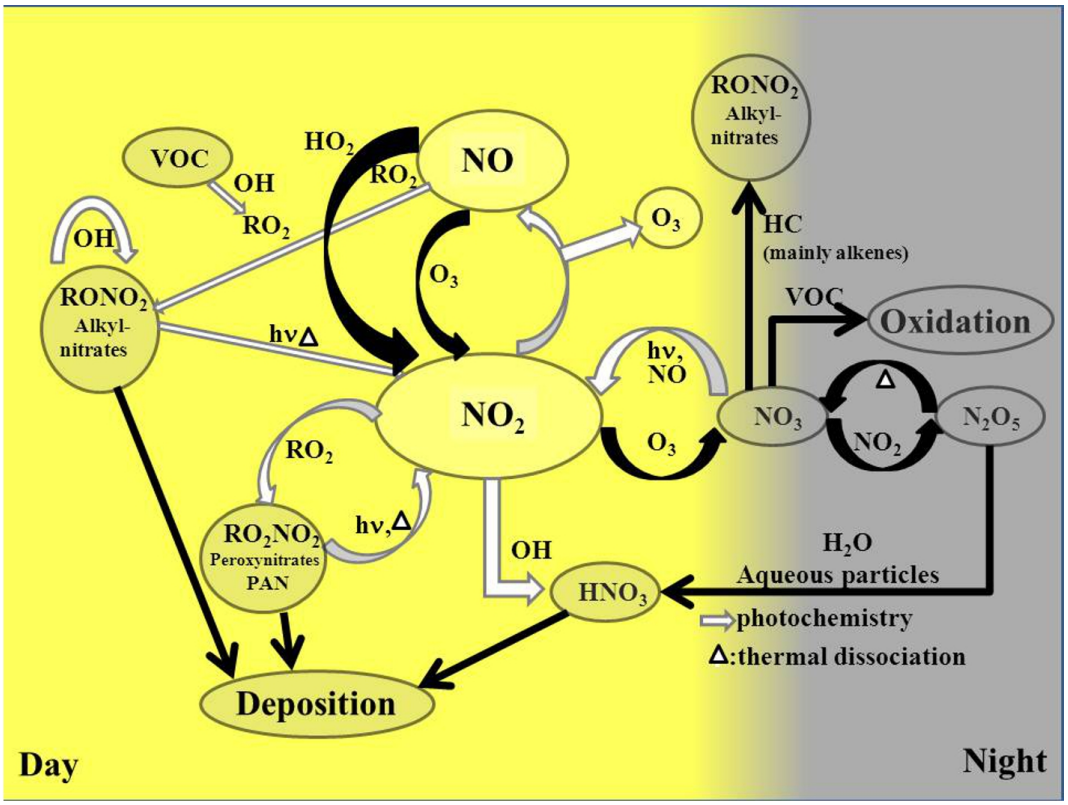

Figure 2.4.: *Schematic overview of day and night time chemistry of NOy in the troposphere adapted from Aldener et al. (2006)*

by OH. In order to enable thorough investigation of the chemistry outlined in section 2.4 a number of central trace gases must be accurately measured. At the beginning of this thesis an instrument for detection of NO_3 and N_2O_5 only was available. The major goal of this thesis was to develop a technique to measure NO_2, which could utilize the different thermal properties of alkyl - and peroxy nitrates also, to monitor the mixing ratios of $\sum$ANs and $\sum$PNs also, and provide information about the relative contributions of NO_2, NO_3, N_2O_5, PN's and AN's to the reactive nitrogen budget.

Part II.

Instrumentation and Measurement Sites

Chapter 3.

Instrumentation for field measurements

During the three campaigns NO_3 and N_2O_5 were measured by a Cavity Ringdown spectrometer which was built in our group [Schuster et al. (2009) and Crowley et al. (2010)]. In the following section a short description of this CRDS instrument will be given. During this work a new cavity ring down spectrometer was built which will be discussed more in detail in the following section. The general idea of CRDS and the basic principle will be explained in the following text.

3.1. Cavity Ring Down Spectroscopy (CRDS)

Cavity assisted extinction spectrometers use an optical cavity, built of two highly reflective mirrors in which photons propagate for a prolonged time, increasing the effective optical length by several orders of magnitude. The intrinsic loss of the resonator can be measured by the lifetime of the photons within the cavity. In a cavity pumped by laser pulses, the decay time of the light leaking out of the cavity yields the mean photon lifetime. This technique is named cavity ring down spectroscopy (CRDS) [Okeefe and Deacon (1988)]. Since this technique relates the extinction inside the cavity to decay times, it is insensitive to intensity fluctuations of the light source. The following section will describe the basic principles of optical absorption spectroscopy and the cavity ring down system.

3.1.1. CRDS principle

Cavity assisted absorption spectrometers make use of highly reflective mirrors with reflectivity R (typically $R > 0.9999$) to provide long paths for extinction spectroscopy (see Figure 3.1). A small fraction of the light focused on the entrance is transmitted into the resonator. The intensity of the transmitted light is given by the product of the light source intensity I_0 and the transmittance of the mirror $T = 1 - R$. Inside of the cavity the light with the intensity I_R propagates to the second (exit) mirror, distance L_0, where a tiny fraction, $I_R \cdot T$ leaves the cavity.

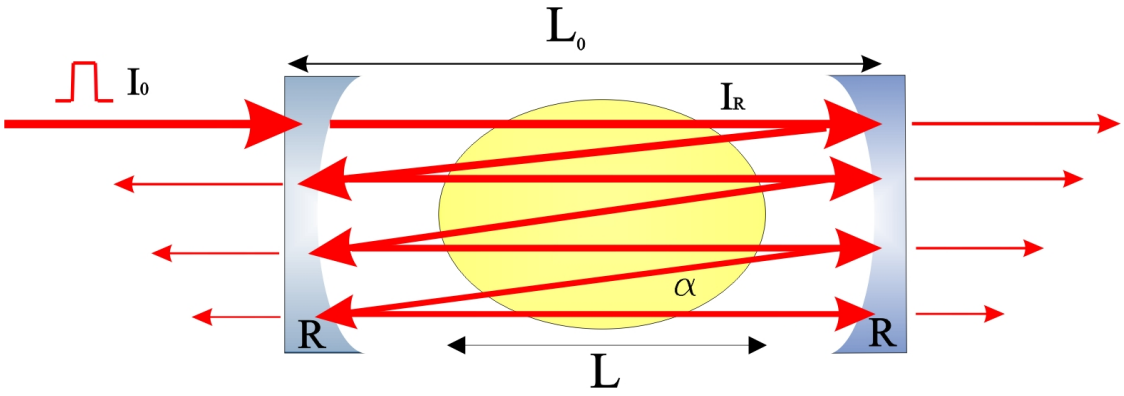

Figure 3.1.: *Scheme of a cavity assisted spectrometer. I_0: Incident pulsed light intensity. R: Mirrors with high reflectivity. L_0: mirror distance. L: Effective absorbing path. α: Absorbing and/or scattering species*

.

The fraction $I_R \cdot R$ is reflected back to the first mirror. The remaining fraction of the light inside the cavity propagates further between both mirrors until no light is left inside the cavity. If an absorber with the absorption coefficient α is present in the cavity, the light intensity inside is reduced by $\alpha \cdot L$ with each traverse. The light leaking out of the second mirror is detected at high time resolution by a photomultiplier (PMT) and describes an intensity decay which is related to the losses inside the cavity.

$$I(t,\alpha) = I_0\ exp[-\frac{c}{L_0}(\alpha L + |ln(R)|)\ t] = I_0\ exp[-\frac{t}{\tau}] \tag{3.1}$$

Equation 3.1 describes the decay of light inside a cavity. For direct application of this method the extinction loss is given by the comparison of a signal from the resonator with and without an absorbing or scattering species inside. So, if the decay of the empty (τ_0) and filled (τ) resonator is compared, the absorption coefficient can be determined by:

$$\alpha\ = \frac{R_L}{c}\ \ (\frac{1}{\tau} - \frac{1}{\tau_0}) \tag{3.2}$$

In Equation 3.2, $R_L = \frac{L_0}{L}$ is the ratio of total length to the length over which the absorber is present. This value is dependent on the design of the cavity and of the flow conditions inside the cavity and must be measured for each cavity design.

3.2. CRDS for measuring NO_3 and N_2O_5

The measurement of NO_3 and N_2O_5 in this work was performed with a two-channel CRDS, developed in our group. A schematic overview of the instrument is shown

in Figure 3.2. Instrument details regarding optical setup, gas flows and data acquisition were described in detail previously (Schuster et al. (2009); Crowley et al. (2010)) and thus only a brief description is given here. The instrument makes use

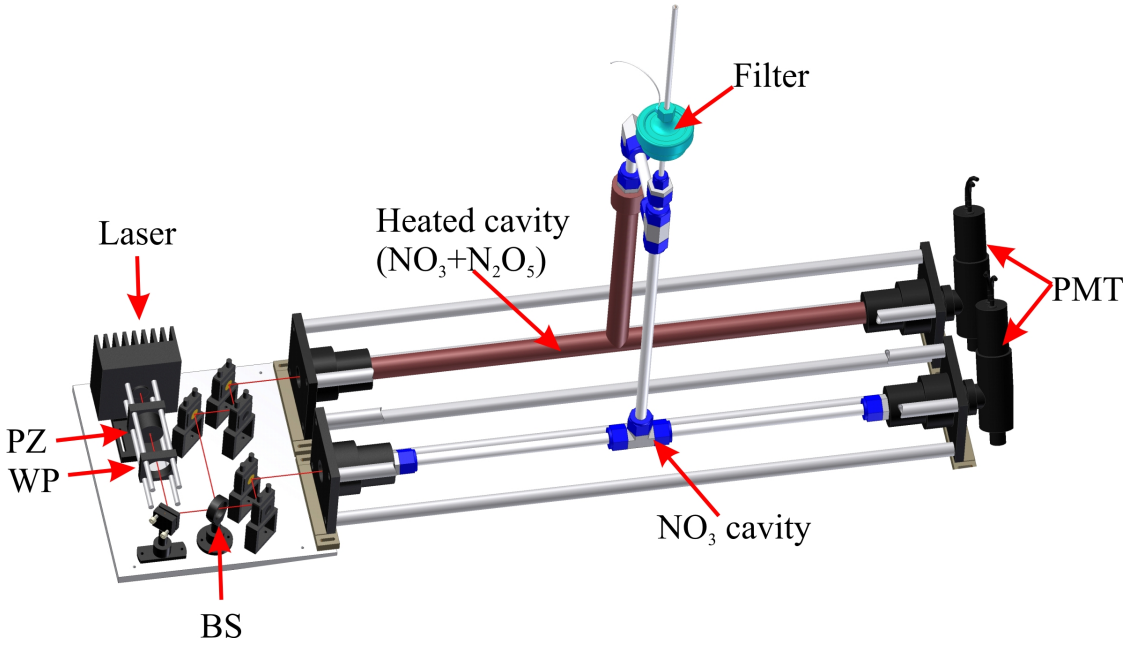

Figure 3.2.: *A schematic of the two-channel CRDS at 662 nm. Ambient air was sampled through the filter and then divided into the two channels. The NO_3 cavity is kept at room temperature, the $NO_3 + N_2O_5$ cavity and inlet is kept at 90 °. PZ: polarizer WP: quarter wavelength plate BS: beam splitter*

of the strong absorption band of NO_3 at around 662 nm (black line in Figure 3.3). The light source is a temperature stabilized laser diode square-wave modulated at approximately 200 Hz (Mitsubishi ML101 J27). The laser light is aligned on the axis of the two-mirror optical cavities with physical dimension of 70 cm length and with an inner diameters are 12.4 mm and 18.7 mm for the NO_3 cavity (volume: 79 cm^3) and the N_2O_5 cavity (volume: 180 cm^3), respectively.

Optical absorption length, depending of the reflectivity of the cavity mirrors, can reach up to 50 km. The change in ring-down constants ($\Delta\tau = \frac{1}{\tau} - \frac{1}{\tau_0}$) in the presence and absence of NO_3 is used to calculate the NO_3 concentration using eq. 3.2.

$$[\mathrm{NO_3}] = \frac{R_L}{\sigma_{\mathrm{NO_3}} \cdot c} \cdot \Delta\tau \tag{3.3}$$

To determine the ring-down constant in the absence of NO_3 a chemical zero method is used. The chemical 'zero' is achieved by adding 8 sccm NO (100 ppmv in N_2) to the sample flow to titrate the NO_3 after reaction 3.4:

$$\mathrm{NO} + \mathrm{NO_3} \xrightarrow{\mathrm{M}} 2\,\mathrm{NO_2} \tag{3.4}$$

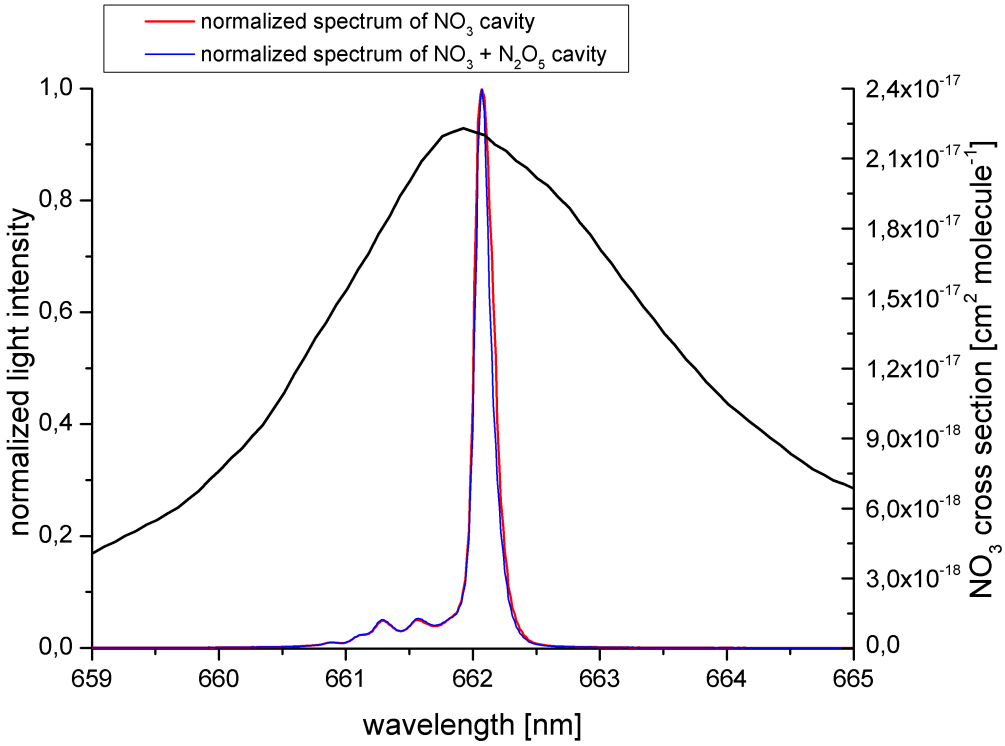

Figure 3.3.: *The cavity emission spectra from the two channels (red line: NO_3 cavity), blue line: NO_3+N_2O_5 cavity, both on left y-axis). Additionally the NO_3 absorption spectra (black line on right y-axis) at 298 K from Yokelson et al. (1994)*

The rate coefficient of reaction 3.4 is $2.6 \cdot 10^{-11} \frac{cm^3}{molecule \cdot s}$ at $25°C$ [Sander et al. (2006)]. At a NO concentration of $1.1 \cdot 10^{12} \frac{molec}{cm^3}$ the lifetime of NO_3, defined by $\frac{1}{k_{NO} \cdot [NO]}$, is 0.035 s (this is short compared to the NO_3 residence time in the inlet). While one of the two cavities is kept at ambient temperature (NO_3 cavity) the second cavity and a part of the inlet is kept at 90 $°C$. At this temperature N_2O_5 is thermally decomposed after Equation 3.5 to NO_3:

$$N_2O_5 + M \longrightarrow NO_2 + NO_3 + M \tag{3.5}$$

The rate constant at this temperature and 690 Torr is $k_{3.5} = 21.1 s^{-1}$. Using this rate constant, more than 99% of N_2O_5 is converted after 0.25 s. With a residence time of 0.5-1 s in the heated part the total N_2O_5 concentration is converted to NO_3. The difference in the measured concentration of both cavities determines the N_2O_5 concentration.
To determine the concentration from Equation 3.3 the effective cross section is needed. The temperature of the laser diode was chosen in such a way that the emission spectrum peak at the maximum of the NO_3 cross section, 662 nm as

shown in Figure 3.3. Convolution of the reported cross section of NO_3 [Yokelson et al. (1994)] with the measured laser spectra leads to the effective cross section of NO_3 for both cavities. For the NO_3 cavity, kept at ambient temperature, the effective cross section is $2.107 \cdot 10^{-17} cm^2\ molecule^{-1}$ [Yokelson et al. (1994)] whereas for the $NO_3 + N_2O_5$ cavity, kept at 90 °C, the effective cross section is $1.605 \cdot 10^{-17} cm^2\ molecule^{-1}$ [Yokelson et al. (1994) and Orphal et al. (2003)].

3.2.1. Data corrections

Owing to the high reactivity of the NO_3 radical the transmission efficiency of the inlet line and the filter must be determined and corrected for. An additional correction factor R_L has to be applied for the use of a purge flow. This purge flow is used to maintain mirror cleanliness. This purge flow reduces the effective absorption path length from the mirror distance L_0 to the real absorption length L. The ratio $R_L = \frac{L}{L_0}$ was measured in the laboratory.

3.2.1.1. R_L ratio

During ambient measurements, the purge flow of both cavities is typically set to 200 sccm for each cavity. To determine the value of R_L, measurements at different purge gas flows were made. For these experiments a total flow of about 10 SLM was typically used. 4 SLM for the NO_3 cavity and 6 SLM for the $NO_3 + N_2O_5$ cavity. Owing to its stability, NO_2 in high concentrations, instead of NO_3, was used as the absorber in these experiments. By changing the purge flow from 0 sccm up to 600 sccm R_L was determined to be 1.01 ± 0.01 and 1.02 ± 0.01 for the NO_3 channel (at 4 SLM total flow) and the $NO_3 + N_2O_5$ channel (at 6 SLM total flow), respectively when the purge flow was 200 sccm.

3.2.1.2. Transmission efficiency of the cavities

The high reactivity of NO_3 results in losses inside the optical cavities for which a correction must be applied. To determine the transmission efficiency a constant amount of NO_3 was measured in both cavities at different residence times inside the cavity. A constant NO_3 mixing ratio was generated via the gas-phase reaction 3.6.

$$NO_2 + O_3 \longrightarrow NO_3 + O_2 \tag{3.6}$$

O_3 was produced by photolysis of a small flow of synthetic air or oxygen by a low pressure Hg lamp. The flow of O_3 was mixed with a flow of NO_2 in a FEP-coated, blackened glass reactor (ID: 5.6 cm, length: 60 cm, volume: 6 l). The flow of the NO_3/N_2O_5 mixture was diluted after the glass reactor by a constant main flow of 11 SLM. Before dilution, the mixture was heated to 90 $°C$ to convert the N_2O_5

to NO_3. This constant flow of NO_3 was split between both cavities. A range of residence times within the cavities were obtained via changing the ratio of the flows within the cavities. A typical dataset of the measured NO_3 and N_2O_5 mixing ratios

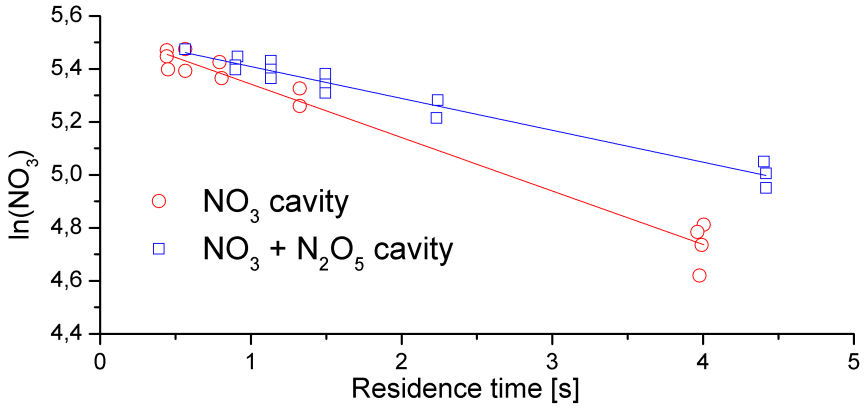

Figure 3.4.: *Graph of a typical measurement for determination of wall loss rates of the cavities*

as function of residence time is displayed in Figure 3.4. The loss of NO_3 and N_2O_5 is a pseudo first order process for each cavity. The averaged wall loss rates were measured to be $0.245 \pm 0.010\ s^{-1}$ for the NO_3 cavity and $0.181 \pm 0.010\ s^{-1}$ for the N_2O_5 cavity requiring corrections of $10 - 20\%$ for typical residence times of less than one second.

3.2.1.3. Transmission efficiency of the filter

To prevent aerosol entering into the cavities a 2 μm pore Teflon (PTFE) membrane filter (PALL Life sciences) held in a PFA filter-holder was placed in front of the cavities. The transmission efficiencies of NO_3 and N_2O_5 through these filter were determined by measuring the differences with and without the filter, shown in Figure 3.5. The transmission efficiency of clean filters was determined to be $86 \pm 3\%$ and $100 \pm 1.0\%$ for NO_3 and N_2O_5, respectively. Depending on the composition of the air masses the filter has be changed frequently to guarantee the measured transmission efficiency. Taking all these data corrections and errors into account, the detection limits for NO_3 and N_2O_5 are estimated to be several pptv in 5-6 s.

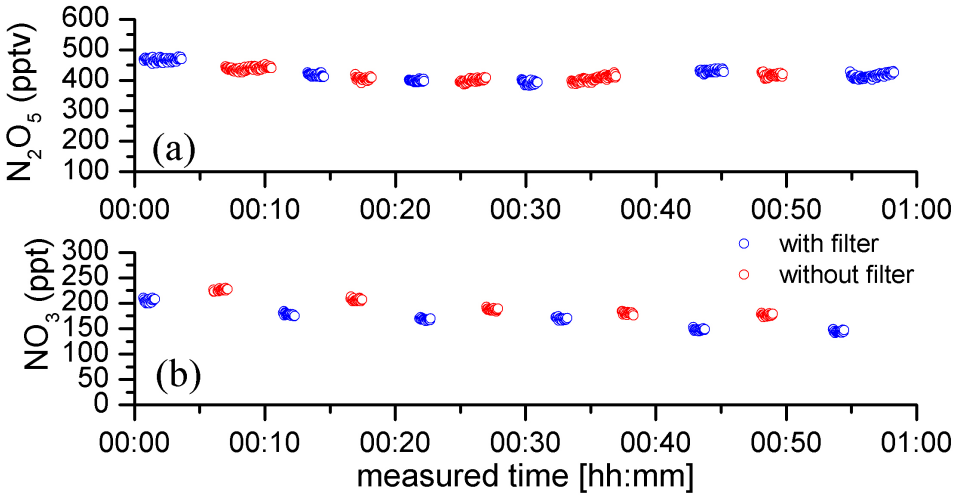

Figure 3.5.: *Typical data set for the determination of the loss rate of NO_3 and N_2O_5 on the filters. In the upper panel a) the measurement of N_2O_5 with and without filter is shown. In the lower panel b) the same measurement is shown for NO_3*

3.3. Newly developed thermal dissociation Cavity Ring Down Spectrometer (TD-CRDS)

During this work a new instrument based on cavity ring down spectroscopy was built to enable measurement of other reactive nitrogen species.
Apart from the fact that the analysis of NO_3 and N_2O_5 datasets require accurate NO_2 measurements, NO_2 is one of the key species in atmospheric chemistry and especially in the nitrogen cycle (see Figure 2.4). A number of temporary reservoir species of NO_x such as N_2O_5, $\sum$PNs, $\sum$ANs and HNO_3 can thermally dissociated to NO_2 at different temperatures (like shown in eq. (3.5)). One of the first instrument based on this thermal dissociation method converting $\sum$PNs, $\sum$ANs and HNO_3 to NO_2 detected by a laser induced fluorescence (LIF) technique is described in Day et al. (2002). In the following sections an overview of the instrument and its characterization will be shown.

3.3.1. General overview

A schematic overview of the main part of the instrument is shown in Figure 3.6. The instrument makes use of the strong NO_2 absorption spectrum at around 400 - 450 nm and the availability of blue laser diodes at around 405 nm (Blue ray Disc Player).Two continuous wave (cw) laser diodes (Lasercomponents, output power 120 mW) aligned on the axis of a two-mirror optical cavity, were modulated on/off. After the buildup of light intensity in the cavity during the on-time of

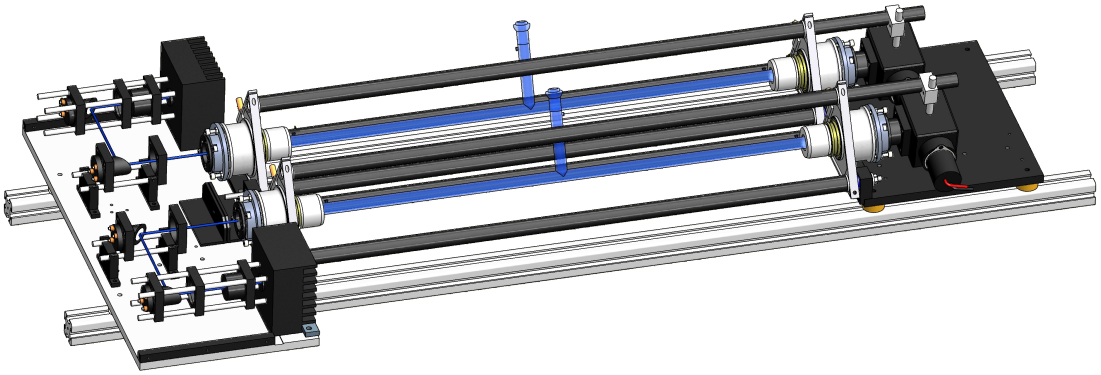

Figure 3.6.: *The new constructed Cavity Ring Down Spectrometer. Detailed information are explained in the text and in the schematic overview in Figure 3.7*

the laser, the time dependence of the light intensity which is transmitted through the rear mirror is observed after modulation of the source intensity to zero. The time constant of the exponentially decreasing intensity gives a direct extinction measurement. To calculate the number density of the absorber the time constant with (τ) and without (τ_0) absorber present in the cavity is used by

$$[\mathrm{NO_2}] = \frac{R_L}{\sigma_{\mathrm{NO_2}} \cdot c} \cdot \left(\frac{1}{\tau} - \frac{1}{\tau_0} \right) \tag{3.7}$$

where, $\sigma_{\mathrm{NO_2}}$ is the absorption cross section, c is the speed of light and R_L is the ratio of the total cavity length to the absorption length.
A schematic overview of the instrument and air sampling system is shown in Figure 3.7. Both laser diodes were temperature stabilized with a peak value of 405.25 nm and 408.5 nm (shown in Figure 3.8), respectively with a FWHM of about 0.75 nm. The diodes are modulated by a square wave signal (on/off) at a repetition rate of 1666 Hz with a duty cycle of 50%. The shut-off time of the laser ($< 1\mu s$) is much shorter than the observed times constants. The laser output was found to be relatively broad so that direct coupling into the cavity is possible without, for example, a requirement for an active matching of any mode structure present in the laser output to the resonant frequencies of the cavity or a scheme to increase the cavity mode density (Ayers et al. (2005), Baer et al. (2002)). This is an important simplification. The cavity mirrors reflectivity is 0.999965 (Advanced Thin Films) leading to typical ring down time constants of about 40 μs for a mirror separation of 70 cm in dry air at a pressure of 670 Torr and 35°C. This leads to optical absorption path lengths up to 12 km. Extinction due to Rayleigh scattering at this pressure is 24 ppm/pass, comparable to mirror reflectivity, necessitating measurements of temperature and pressure in each cavity to track variation in the

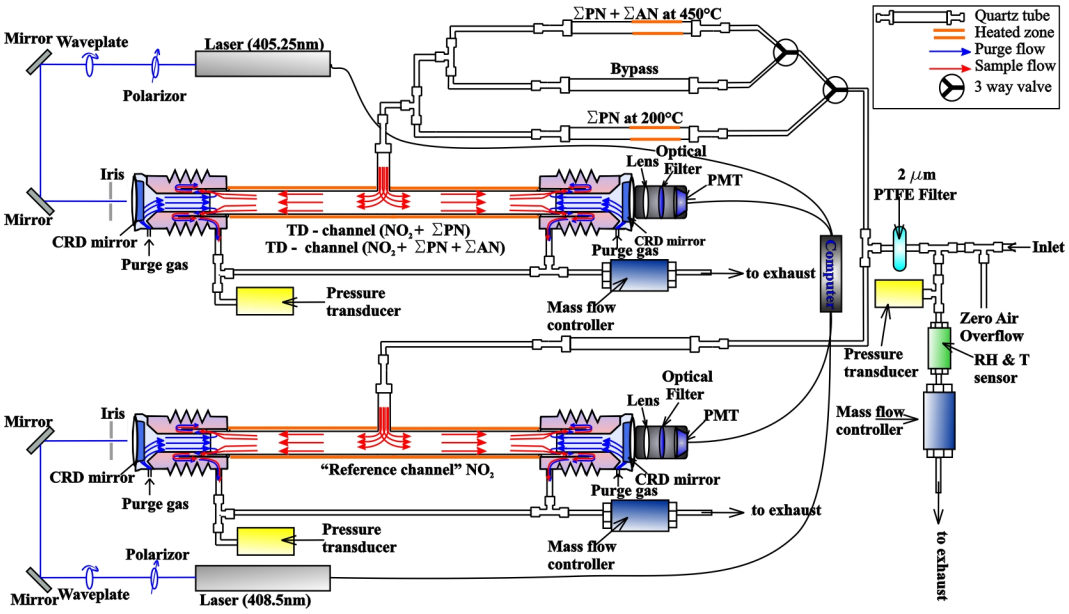

Figure 3.7.: *Schematic overview of the TD-CRDS two channel instrument. Details are explained in the text*

background ring-down time constants with the air sample number density.
The ring down time signals are acquired with a digital oscilloscope (Picoscope 3000, 12 bit vertical resolution, 5Mhz sampling rate), and 1344 decays are averaged in order to achieve a good signal to noise ratio. The time resolution is about 3-4 s. The averaged ring down traces and all needed input parameters are handled via a self-written Agilent Vee code. The ring-down time is determined by correcting for the baseline of the averaged signal followed by a linear exponential regression (time constant and amplitude are derived). This kind of averaged procedure offers no significant loss in accuracy compared to averaging fits of individual decays and is computationally more efficient [Brown et al. (2002)].
A small purge flow (100 sccm of zero air at each mirror) is used to maintain mirror cleanliness. A schematic view of the flow conditions inside the cavity is shown in Figure 3.7 [red and blue arrows]. Consequently, the ratio of total length to the length over which the absorber is present, R_L in eq 3.7, is larger than unity. This value was measured in the laboratory and is shown in detail in section 3.3.2.1.
Laser and turning optics are mounted on an aluminium plate which is directly coupled to the cavity. The front and the rear site of the cavity are fixed together with three carbon fibre rods (outer diameter 15 mm, length 70 cm) to minimize the thermal stress in order to reduce the sensitivity of the alignment to temperature changes of the environment. Both cavity and optics, are mounted on a transportable aluminium frame (MayTec) which also houses the laser diode drivers, electronic equipment to control valves, heated elements and pump.
Air is sampled through a Teflon line (approx. 4-5 L per minute) and filtered by a

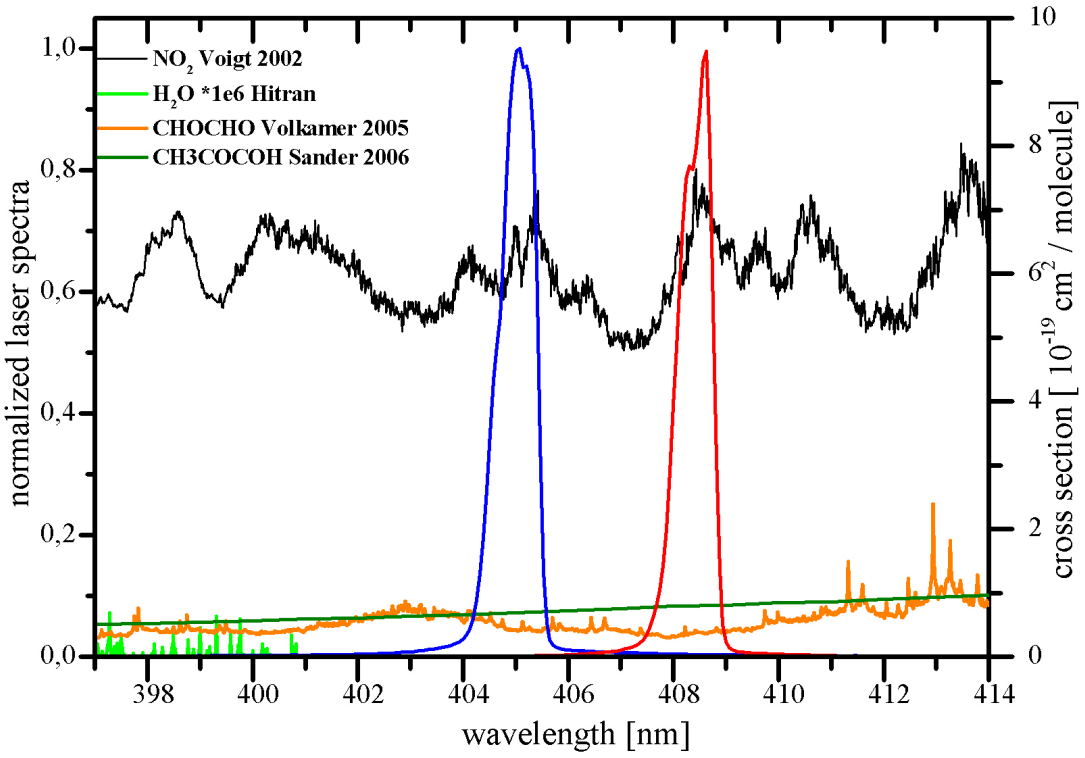

Figure 3.8.: *normalized laser spectra of both channels (red line: NO_2 reference cell, blue line: thermal dissociation channel, both on left y-axis). Additionally on the right y axis the NO_2 cross section from Voigt et al. (2002) is shown as well possible interference species in this wavelength range (H_2O calculated from the HITRAN database, Glyoxal from Volkamer et al. (2005b)) and methylglyoxal from Sander et al. (2006)*

Teflon filter (2 μm pore size) to remove particles. The main air flow is divided into two flows of approximately 2 $\frac{L}{min}$ for each cavity after the Teflon filter. Additionally a flow of approximately $0.5-1$ $\frac{L}{min}$ is passed over a further pressure transducer and a humidity sensor. This flow was regulated by a mass flow controller to keep the instrument at a constant pressure and both cavities were kept at 35 °C. These controlled conditions reduced the baseline variation. The importance of measuring the humidity of the sample air flow, as well as the pressure regulation was investigated in the laboratory and is explained in detail in section 3.3.2.3.
In the first cavity, NO_2 is measured directly and continuously. For the second, Thermal Dissociation (TD) cavity, the air sample can pass through one of three quartz tubes. Two of the quartz tubes are placed in commercial ovens (Carbolite, up to 1000°C). 15 cm of the quartz tube (42 cm length, 1.5 cm inner diameter) can be heated up to several hundred degrees. The third quartz tube is kept at ambient temperature to serve as a NO_2 reference. The heaters are set to 200 °C

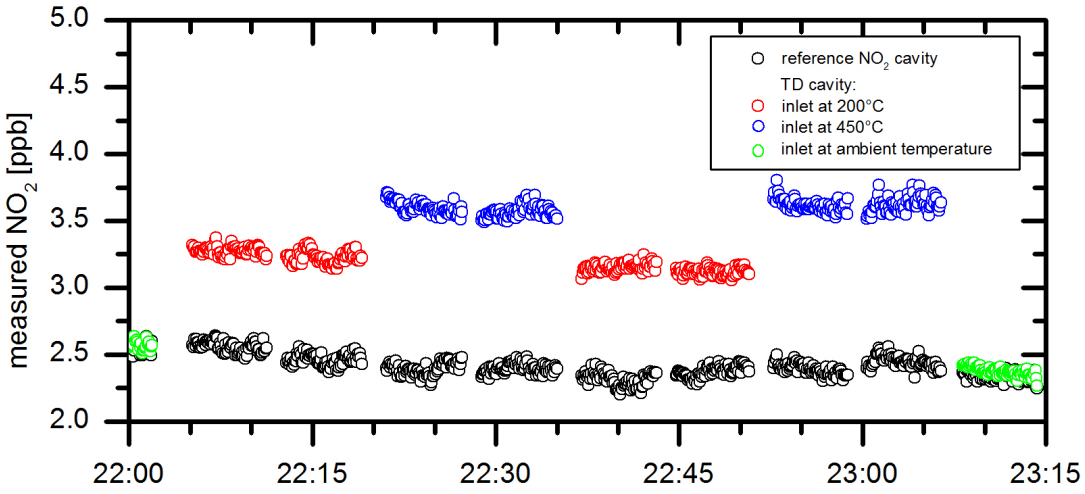

Figure 3.9.: *Sketch of a typical measurement during a field campaign: the black dots represent the NO_2 reference cavity, the red dots display the $\sum$PNs measurements at 200° C, the blue dots show the measured $\sum$PNs + $\sum$ANs and the green dots show the NO_2 concentration measured over the bypass of the TD cavity.*

and 450 °C, respectively. $\sum$PNs are converted to NO_2 in the tube heated to 200 °C, whereas $\sum$PNs and $\sum$ANs are converted to NO_2 in the 450 °C tube. Typically the sample flow is regulated by two three-ways valves to measure alternately $\sum$PNs and $\sum$PNs + $\sum$ANs at 10 minute intervals. To calculate only the $\sum$ANs concentration the 10 min intervals of the $\sum$PNs measurement are averaged and linearly interpolated. The difference from measured $\sum$PNs + $\sum$ANs to the interpolated $\sum$PNs concentration leads to total $\sum$ANs concentration. Approximately every two hours the sample flow is passed through the cold bypass quartz tube to compare the measured NO_2 concentration with the reference channel. Figure 3.9 shows a typical cycle for NO_2, $\sum$PNs and $\sum$ANs measurements during a campaign.

To determine the background ring down time constants an excess flow of zero air was added to the inlet for about 1-2 min every 5-10 min. This frequency of zero air measurements was found to be sufficient to track drifts in the zero air ring down times. Each time period of zero air measurement is averaged and then linearly interpolated. This interpolation is used to derive the correct number density of the measured NO_2 concentration between two zero air measurements.

In contrast to the NO_3/N_2O_5 instrument there is no other option to acquire zero air measurement aside from the use of synthetic air. Synthetic air may contain traces of NO_2 which can affect the accuracy of the measurement at low ambient NO_2. During this work several methods were applied to quantify these small amounts

of NO_2 in the synthetic air bottle. Using heated catalytic reactions of different metals a high efficiency for destroying NO_2 was observed but unfortunately only for higher NO_2 amounts. The best solution was use of a home-made blue light NO_2 converter (8 high power LEDs at 365 nm) with an efficiency of 80% conversion at a flow of 0.7 L min^{-1}. This way an upper limit to the NO_2 levels in the zero air could be obtained, which was defined by the precision of the instrument.
Using synthetic air for zero measurements makes the instrument vulnerable to interference due to any other species contained in the sampled air that absorbs at around 405-409 nm. The only species that are currently known to be of significant concern are water vapour, glyoxal and methylglyoxal . The absorption cross section of these three species are also included in Figure 3.8. In Hargrove and Zhang (2008) and Hargrove et al. (2006) a large water vapour interference of a CRDS instrument detecting NO_2 at 405 nm was reported, which is not consistent which the known absorption cross section of water vapor [Rothman et al. (2005)]. This possible interference was investigated carefully in the laboratory and is explained in detail in section 3.3.2.3. Glyoxal and methylglyoxal have absorption cross sections of approximately a factor of 10 smaller than of NO_2 in this wavelength range (Volkamer et al. (2005b),Washenfelder et al. (2008)). Glyoxal is a product of photo oxidation of VOCs, and mixing ratios up to 1.85 ppbv have been measured in highly polluted environments (Mexico City, Volkamer et al. (2005a)), although concentration were less than 10% of NO_2, this would lead to an artifact less than 1% of the reported NO_2 mixing ratios. In forested environments, smaller levels up to 200 pptv have been observed (Huisman et al. (2008)), which contribute up to 20 pptv interference for the observed NO_2 mixing ratios.

3.3.2. Characterization of the instrument

In the following sections the characterization of the instrument is discussed in more detail.

3.3.2.1. Dilution effect by purge gas

To maintain the cleanliness of the cavity mirrors a small purge flow of typically 200 sccm is used. A flow scheme is shown in Figure 3.7 in which the purge flow and also the sample flow is showed (blue arrows: purge flow, red arrows: sample flow). The effective absorption length was measured in the laboratory and the result is shown in Figure 3.10. A constant NO_2 flow was diluted in a constant flow of synthetic air. The sample flow to each cavity was $2\frac{L}{min}$. The purge flow varied between 0 and 200 sccm. As a reference value, the measurement with no purge flow was used. To confirm this value in comparison to the normal flow method the complete cavity was filled with the same NO_2 concentration. Both results agree within the uncertainty of the measurements. In Figure 3.10 the ratio of the NO_2

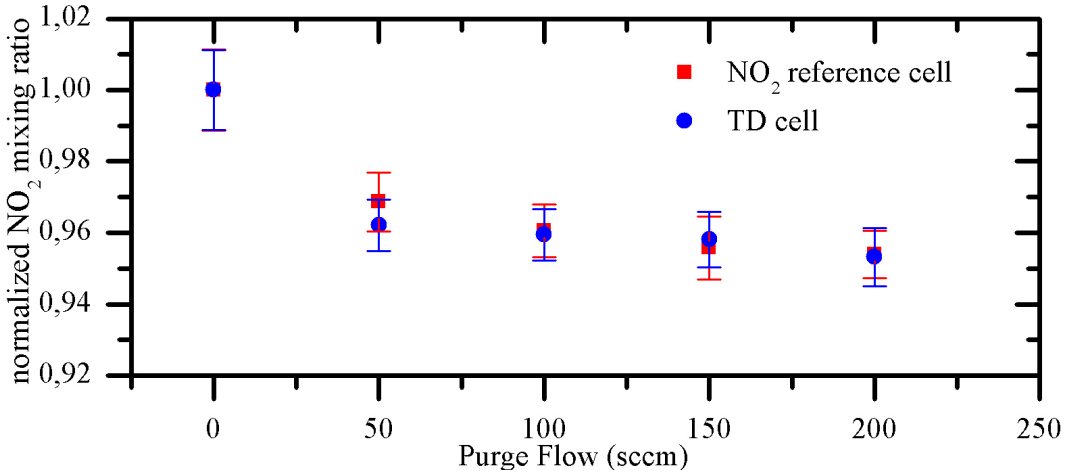

Figure 3.10.: *Ratio of the mirror distance L_0 to the effective absorption path length L depending on the purge flow derived from measurement of a constant amount of NO_2 diluted with a constant flow of zero air at different levels of the purge flow.*

concentration normalized to the value with no purge flow is plotted against the purge flow. Both cavities show a similar behaviour, which is expected owing to the same design and same flow conditions. A clear jump $(3 - 4\%)$ between no purge flow and 50 sccm purge flow indicates that the main sample flow will not reach the mirror and therefore maintain the cleanliness of them. So for a typical purge flow of 200 sccm the dilution effect is the inverse of the measured ratio R_L: 1.048 $\pm$ 0.008 for the NO_2 reference cavity and 1.049 $\pm$ 0.009 for the TD cavity.

3.3.2.2. Effective cross section and stability

The effective cross section for NO_2 in the wavelength range, 405.25 nm and 408.5 nm was determined by measuring the emission spectrum of each laser. The diode laser's peak wavelength and output power are dependent on the current driving the diode and also the temperature of the diode. The current of the laser diodes is modulated by a 6V square wave signal with a duty cycle of 50%. The laser diodes are placed in a commercially available laser diode head (Thorlabs) and controlled by a current - and temperature controller unit (Thorlabs ITC 510 and ITC 502). This combination of laser head and controller unit was chosen to be more flexible because almost every Fabry Perot laser diode can be installed in the laser head. Laser diodes at around 405 nm are commercially available although the exact peak wavelength can vary by several nm. By varying the current driving the diode, and its temperature the peak wavelength can be changed by up to 4nm. The peak wavelength of both diodes differ approximately 4 nm at the same current and temperature. The operating conditions of each diode were optimized to

maximize the overlay with the NO_2 cross section which is shown in Figure 3.8. The laser - diode temperature was kept at 50 °C for the NO_2 reference cell and 40 °C for the TD cell, respectively. The spectra were taken with a spectrometer

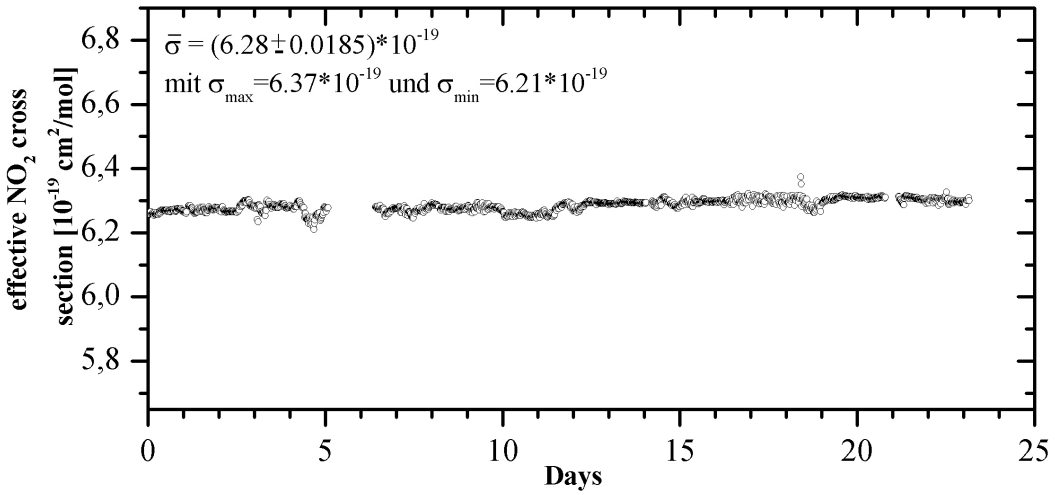

Figure 3.11.: *calculate effective cross section of a laser diode emission spectrum taken every 20 minutes during a measurement campaign*

(cooled back thinned CCD detector, OMT) which was calibrated using a mercury penray lamp. The emission spectra of both diodes are fairly broad, with a full width at half maximum of about 0.75 nm, an effective cross section was calculated to be $6.5 \cdot 10^{-19} \frac{cm^2}{molec}$ and $6.28 \cdot 10^{-19} \frac{cm^2}{molec}$ for the NO_2 reference cell and the TD cell, respectively. The temperature dependence of the NO_2 cross section is rather small and was measured from 273 K - 293 K without any significant change [Burrows et al. (1998)]. The uncertainty of the calculated effective cross section is determined by the uncertainty of the reference spectrum which is less than 4%. In comparison to this method, also a gas - phase titration method was applied. A known NO concentration (uncertainty $< 5\%$) was mixed with an high O_3 concentration to guarantee a complete conversion from NO to NO_2. This reaction was simulated using a FACSIMILE code [Curtis and Sweetenham (1987)] to optimize the reaction time before dilution and minimize further reaction forming NO_3 and N_2O_5. Applying the calculated effective cross section the determined NO_2 concentration is equal to the simulated NO_2 concentration within their uncertainty of both methods. Both methods agree well.
To check the stability of the emission spectra, spectra were measured a number of times over several months without any significant change. Figure 3.11 shows a time series of laser spectra measured, every 20 minutes over a period of 24 days, and the effective cross section determined automatically. The 1σ precision is better than 1% with a maximum variability of 2.5% compared to the mean value.

3.3.2.3. Effects due to Rayleigh scattering

Rayleigh scattering can affect extinction in the instrument cavity and thus must be considered and corrected for. The Rayleigh scattering cross section is highly dependent on the wavelength of light:

$$\sigma_{Ray} = \frac{24\ \pi^3}{\lambda^4\ N^2} \left(\frac{n^2-1}{n^2+2}\right)^2 F_K(\lambda) \tag{3.8}$$

where n is the refractive index of air, λ is expressed in units of centimetre, N is the number density in $\frac{molec}{cm^3}$ and F_K is the King correction factor for the depolarization. Differences in the Rayleigh scatter cross section and changes in the concentration of an air sample can lead to a different extinction

$$\alpha = \sigma_{Ray} \cdot N \tag{3.9}$$

where σ_{Ray} is the Rayleigh scatter cross section and N is the number density of the air sample. The Rayleigh scatter cross section at 405 nm of dry zero air is

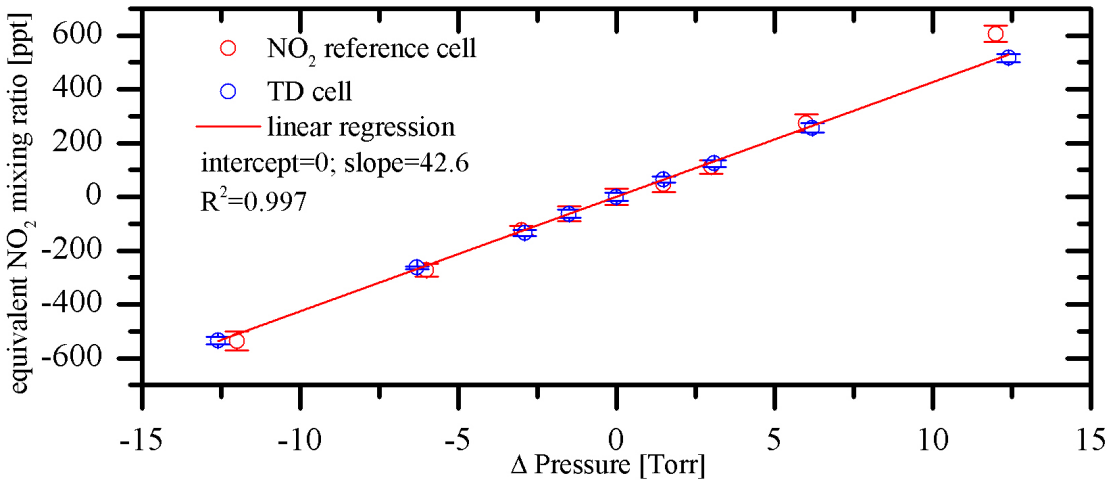

Figure 3.12.: *Dependency of measured equivalent NO_2 mixing ratios on different pressure changes*

$\sigma_{ray}(air) = 1.61\ 10^{-26} cm^2$ [Sneep and Ubachs (2005)] with a number density of $2.5479\ 10^{19}\ \frac{molec}{cm^3}$ (760 Torr ambient pressure and 15°C).
Due to the fact that background measurements are obtained with zero air it is important to minimize pressure changes when switching from ambient air sampling to zero air measurement. In Figure 3.12 equivalent NO_2 mixing ratios are plotted against pressure differences. Due to the different pressure inside the cavities the extinction in the cavity is changed according to Equation 3.9. The equivalent NO_2 mixing ratios can be calculated using the the effective laser cross sections. This result is consistent with the theoretical values using Equation 3.8 and 3.9, e.g. and

shows that a pressure difference of just 2.5 Torr requires a correction of about 100 pptv.
As previously noted, the use of synthetic air for measuring instrument zeros leaves the techniques vulnerable to interferences. Water vapour could one of the possible interfering species. In Figure 3.8 the dark blue line represents the H_2O absorption cross section [Rothman et al. (2005)]. Hargrove and Zhang (2008) report a high interference of water vapour in a similar instrument working at 405 nm. Therefore, this possible interference was investigated carefully here.

Zero air containing different water vapour levels (Relative humidity: 10-70 %)

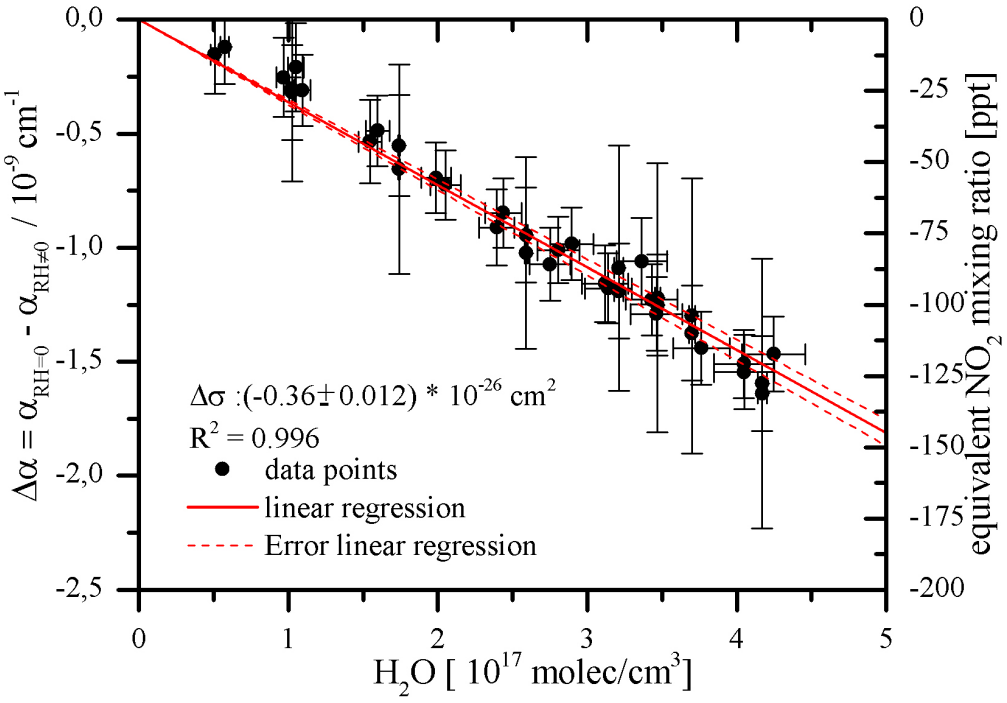

Figure 3.13.: *Dependence of measured extinction on different levels of water vapour. Additionally plotted the equivalent NO_2 mixing ratios on the right hand side. The resulting decrease in extinction with increasing water vapour concentrations is due to smaller Rayleigh scatter cross section of water compared to zero air.*

was sampled and the extinction measured. The difference between measured extinction at a dry air sample and for each level of water vapour was plotted against absolute humidity which is shown in Figure 3.13. The result clearly shows a linear decrease of extinction with increasing water vapour concentration which shows a clear contrast to the observation of Hargrove and Zhang (2008) in which they suggest an increasing signal with increasing water vapour due to absorption .The slope of the linear fit gives a cross section difference between water vapour and dry air of $(0.36 \pm 0.012) \cdot 10^{-26}\ cm^2$. This change leads to an approximately 77% smaller

Rayleigh scatter cross section for H_2O compared to dry air ($1.61\ 10^{-26}\ cm^2$ [Sneep and Ubachs (2005)]). This result is also consistent with theoretical calculations and measurements which suggest a smaller cross section of water vapor compared to dry air in the order of $70 - 80\%$ [Sutton and Driscoll (2004)].
This result indicates that an accurate correction is required to account for the difference in Rayleigh scattering between the dry air used for background measurements and the humid ambient air. The correction for an ambient relative humidity of 70 % at 22°C leads to a correction of 130 pptv using standard conditions of 610 Torr and 35 °C inside the cavity. The precision of the instrument should not be effected by this correction as the variations of ambient water vapour concentration in typical ground-based sampling conditions are on a time scale much longer than the repetition rate of CRDS measurements and that of instruments measuring the water content in the air.

3.3.2.4. Additionally formed NO_2 during sample time

During daytime, NO_2 formed via the reaction of $NO + O_3$ is an steady state with the photolysis of NO_2. Typically the formation of NO_2 via this reaction happens in a few minutes. Therefore, if NO levels are sufficiently high enough, a small amount of NO_2 can be formed in the instrument on the way to the detection unit. This interference was investigated in the laboratory and the result is shown in Figure 3.14. For this study the reaction at different NO mixing ratios with three different O_3 mixing ratios were investigated and compared with the theoretical values from the reaction $NO + O_3$ assuming a residence of about 3.5 s and the recommended rate constant [IUPAC (2010)]. The temperature dependence of this reaction leads to a faster reaction with increasing temperatures. Therefore the effect might lead to an even higher NO_2 production in the heated channels for the $\sum$PNs and $\sum$ANs measurements. As the real temperature profile and residence time in the heated area is different for both species and also not accurately known the same studies as shown in Figure

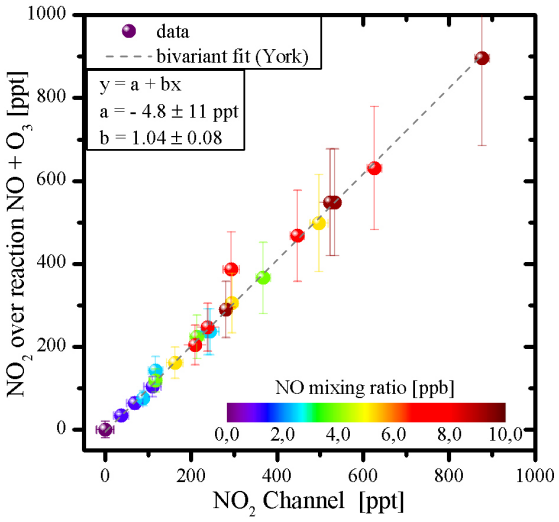

Fig. 3.14.: *Relation between measured and calculated NO_2 production within in the instrument*

3.14 are investigated also for the $\sum$PNs and the $\sum$ANs channel. These measurements allow to derive an effective rate constant assuming the same residence time for all channels. With this effective rate constant ($2.5 \cdot 10^{-14} \frac{cm^3}{molec\ s}$ for $\sum$PNs channel and $6.2 \cdot 10^{-14} \frac{cm^3}{molec\ s}$ for $\sum$ANs channel) these effects can be corrected.

3.3.2.5. Introduction to Thermal Dissociation method

Upon heating, some NO_y species thermally dissociate to yield NO_2 and a companion radical

$$XNO_2 + \text{heat} \longrightarrow x + NO_2 \tag{3.10}$$

where x = RO_2, RC(O)OO, RO, HO_2, OH, NO_3, ClO, BrO, Cl. Compounds that are detected by NO_y instruments but do not thermally dissociate to produce NO_2 include nitrites (HONO and RONO) and NO_3. N_2O_5 produces 1 NO_2 and 1 NO_3 upon heating. There are known interference species for the NO_y instruments, e.g. CH_3CN and NH_3. These compounds do not thermally dissociate to yield NO_2 without subsequent chemical reactions. The yield of the thermal dissociation of the NO_y species to NO_2 can be explained by a very simplified expression

$$\phi = \frac{[NO_2]_t}{[PAN]_0} = 1 - exp\left[-A \cdot exp\left(\frac{-E_a}{RT}\right) \cdot t\right] \tag{3.11}$$

where A and E_a are the Arrhenius parameters for thermal dissociation (TD) of organic nitrates (example are shown in Table 3.1), T is the temperature, R is the universal gas constant and t is the residence time in the converter. With this simplification only the general trend of the behaviour will be described, recombination reactions (loss of NO_2) are neglected. This simplification assumes a homogeneous temperature throughout the converter. An exemplary temperature profile is shown in Figure 3.15; the profile must be determined for each instrumental setup and these will be described in the following sections. Previously measured thermal decomposition rates of various compounds within two organic nitrate classes ($RONO_2$ and $RC(O)O_2NO_2$) exhibit little dependence on what constitutes the "R" group [Hao et al. (1994),Kirchner et al. (1999), Roberts (1990)]. Therefore only PAN

Organic nitrate	A ($10^{14}\ s^{-1}$)	E_a (kJ/mol)	Reference
$CH_3C(O)O_2NO_2$ (PAN)	250	113 ± 2	Bridier et al. (1991)
$(CH_3)_2CHONO_2$ (IPN)	≈ 160	≈ 158	Krause et al. (1989)

Table 3.1.: *Arrhenius parameters [$k = A\ exp(-E_a/(RT))$] for TD of selected molecules. R is the universal gas constant (8.314 J mol^{-1} K^{-1})*

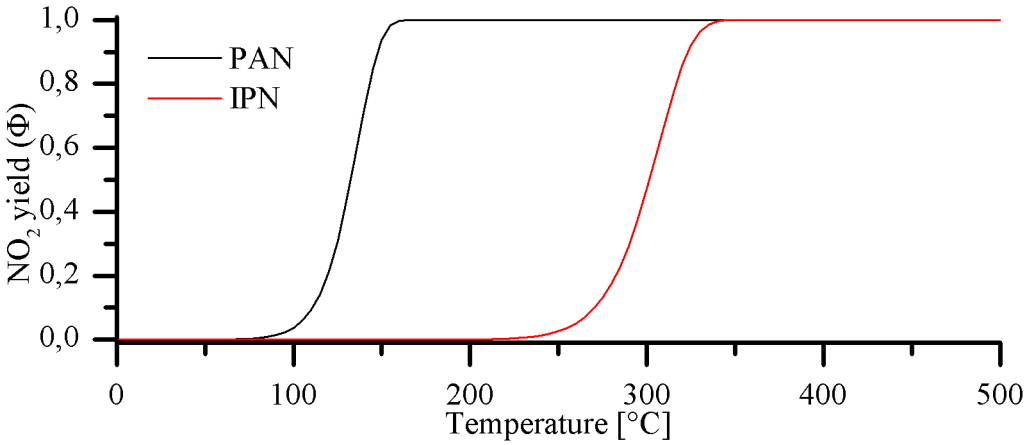

Figure 3.15.: *Result of a model run according to eq.3.11 and the used values of Table 3.1. The residence time in this simulation is 10ms: IPN is isopropyl nitrate*

generated from an acetone photolysis source and two alkyl nitrates (isopropyl nitrate and isobutyl nitrate) were used to determine the temperature profile and the characterization of the instrument which is shown in the following sections.

3.3.2.6. PAN measurements

A sample of peroxyacetyl nitrate (PAN) in zero air was generated by photolysis of acetone (Penray lamp at 285 nm) as described in the following equations [Flocke et al. (2005),Warneck and Zerbach (1992)].Formation of the peroxy radicals CH_3O_2 and $CH_3C(O)O_2$ in excess ensures that the NO is converted to NO_2 quantitatively.

$$CH_3COCH_3 \xrightarrow{h\nu} CH_3CO + CH_3 \quad (3.12)$$

$$CH_3CO + O_2 \longrightarrow CH_3C(O)O_2 \quad (3.13)$$

$$CH_3 + O_2 \longrightarrow CH_3O_2 \quad (3.14)$$

$$CH_3O_2 + NO \longrightarrow CH_3O + NO_2 \quad (3.15)$$

$$CH_3C(O)O_2 + NO_2 \longrightarrow CH_3COO_2NO_2 \quad (PAN) \quad (3.16)$$

The output flow of about 100 sccm was directly diluted by a large zero air flow of $5 - 10$ *slpm* depending on the expected mixing ratio. The amount of PAN generated is dependent on the NO concentration. The conversion efficiency of this photochemical PAN source should be at least 90 % according to several publications [Warneck and Zerbach (1992), Flocke et al. (2005)].
Beside the peroxyacetyl nitrate there are a number of less abundant homologous of PAN. The most important of these are:

- PPN ($C_2H_5C(O)OONO_2$, peroxypropionyl nitrate)
- PiBN ($((CH_3)_2CHC(O)OONO_2$, peroxyisobutyryl nitrate)
- MPAN (CH_2=$CHC(O)OONO_2$, peroxymethacryloyl nitrate)
- APAN (CH_2=$CHC(O)OONO_2$, peroxyacryloyl nitrate)
- PBzN ($C_6H_5C(O)OONO_2$, peroxybenzoyl nitrate)

The rate constant for thermal dissociation to NO_2 of each of these compounds is similar and all can therefore be detected as NO_2 molecules. The new instrument

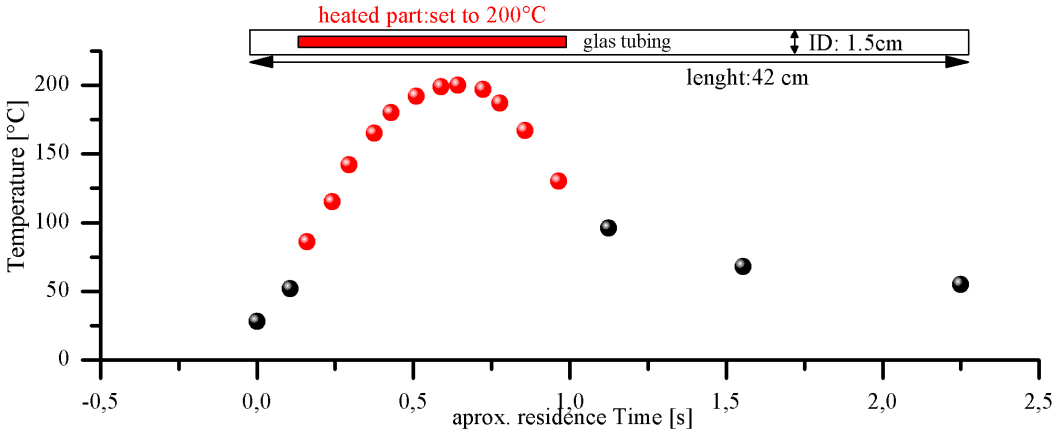

Figure 3.16.: *Temperature distribution of the heater under standard flow condition*

took advantage of the thermal instability of PANs and therefore it was necessary to determine the thermal dissociation properties of the particular setup. A quartz tube of about 42 cm length and inner diameter of about 1.5 cm is placed in the oven which can be heated up to about 1000 °C. In Figure 3.16 the temperature (measured by a thermocouple: J sensor) inside this heated quartz tube is plotted against the residence time of an air sample in the tubing. A typical flow of about 2000 sccm of zero air was flushed during this measurement to simulate real measurement conditions. The red dots in the Figure indicate the part of the tubing which is inside the oven. For this experiment the temperature of the oven was set to 200°C and this temperature was reached in a small section in the middle of the heated area.
Previous work [Day et al. (2002), Slusher et al. (2004)] suggests that complete dissociation occurs at temperature of about 150 to 200°C. However the optimum temperature is likely to be instrument dependent and therefore the dependence of the NO_2 yield on temperature was investigated. The result of this measurement is shown in Figure 3.17. A stable flow of PAN was generated using the photochemical source which is described above. Figure 3.17 shows the normalized PAN

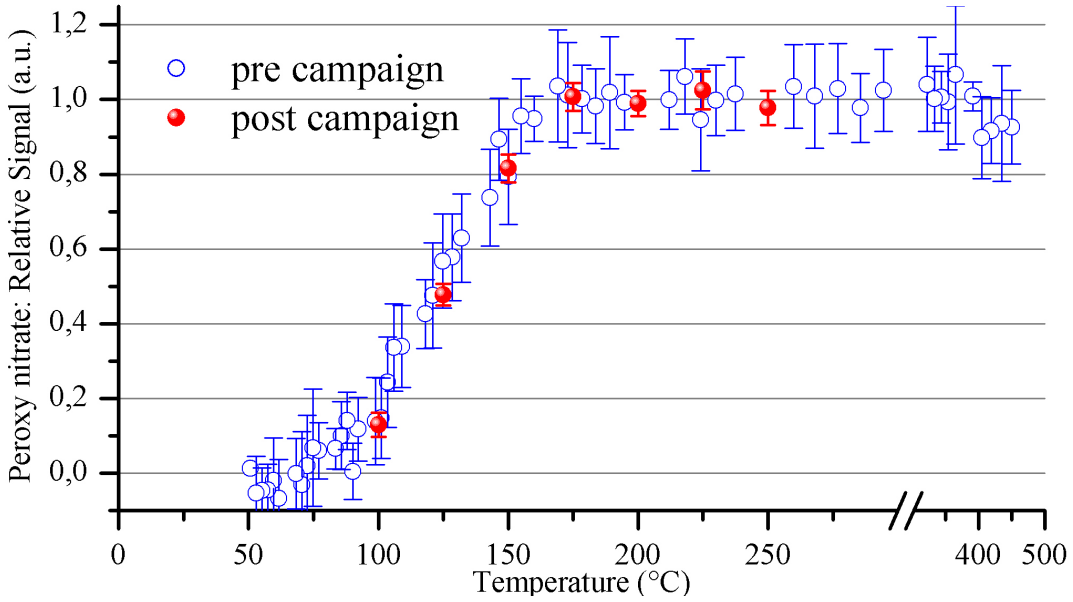

Figure 3.17.: *Temperature dependency of the thermal dissociation efficiency of peroxy nitrates*

signal in dependency of the temperature of the oven from two measurements. The temperature dependence of PAN dissociation was investigated both before (blue points, source output about 500pptv) and after (red points, source output about 1400 pptv) a field campaign. The thermal dissociation to NO_2 is apparent at 80°C and reaches complete conversion at about 180 °C and stays constant up to 500°C. This suggests in contrast to Paul et al. (2009) that no significant amounts of alkyl nitrate is formed in the photolytic PAN source. To suppress detection of any alkyl nitrates in the PAN measurements the heater was set to 200°C.
With the flows used, the efficiency of the conversion to NO_2 was independent of the residence time inside the heated volume. Changing the standard flow rate of $2\frac{l}{min}$ by $\pm 1\frac{l}{min}$ leads to no significant changes in the measured concentration of NO_2. The linearity to PAN was investigated in the laboratory and is shown in Figure 3.18. The result of this experiment shows that the instrument as well as the source itself stays linear over a range up to 1 ppb of PAN by a dilution of $7.7\frac{l}{min}$.
Summarizing all these lab studies it was found that:

- the photolytic PAN source works highly efficient with a conversion efficiency of about 90%.
- A heater temperature of 200°C is enough to convert PAN to NO_2 at flows between 1 and 3 $\frac{l}{min}$.
- Both instrument and source is highly linear up to 1 ppb and most likely for higher mixing ratios.

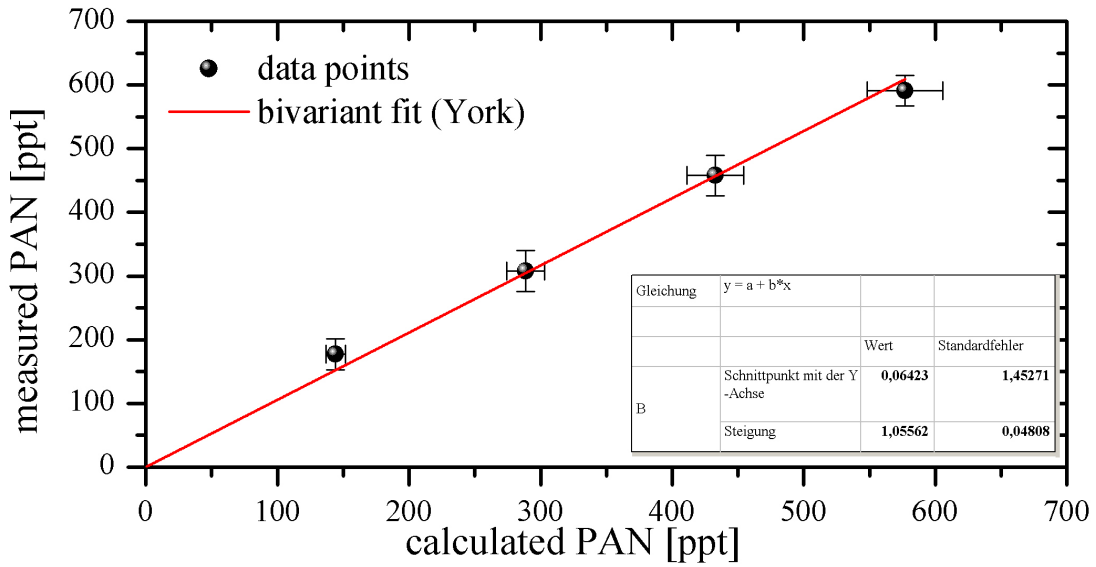

Figure 3.18.: *Linearity of instrument and as well of the PAN source. PAN concentration were calculated assuming* 90% *conversion efficiency of photolytic PAN source (NO mixing ratio of 617 ppb)*

Apart from these lab studies possible interference as shown in Paul et al. (2009) and Paul and Osthoff (2010) was not investigated during this work but should be performed in future work. According to the equations 3.16 and 3.15 these interferences can occur if high NO and NO_2 concentrations are present in the sampling air. High NO concentration leads to reformation of NO_2 whereas high NO_2 concentration leads to reformation of PAN.
Paul et al. (2009) showed a NO_2 dependence at high PAN mixing ratios. With higher NO_2 mixing ratios they measured less PAN. The instrument which is described in this thesis has currently been used only in environments which moderate or low PAN mixing ratios where the observation from Paul et al. (2009) has only very little influence. Paul and Osthoff (2010) also investigated the influence of NO mixing ratios on PAN mixing ratios; an artefact due to NO was observed at high NO mixing ratios.
Another well-known possible interference can occur during nighttime when N_2O_5 is present. As mentioned in section 3.2 N_2O_5 can also dissociate to NO_3 and NO_2 starting from 80°C and higher. So N_2O_5 is a possible interference for the PAN measurements via a TD-CRDS instrument on the basis of NO_2 detection.

3.3.2.7. AN measurements

Alkyl nitrates are measured in a similar manner to the peroxy nitrates and therefore the characterization of the instrument is also similar. Glass bulbs containing ppm

levels of two different alkyl nitrates (isopropyl nitrate and isobutyl nitrate) were prepared using standard manometric methods. A small flow from these samples was diluted dynamically and diverted into the CRDS instrument. Alkyl nitrate are converted to NO_2 and alkoxy radicals at high temperatures (see Figure 3.15). The dissociation of alkyl nitrates was investigated over a range of temperatures and the results are shown in Figure 3.19. The blue data points display a profile for iso-

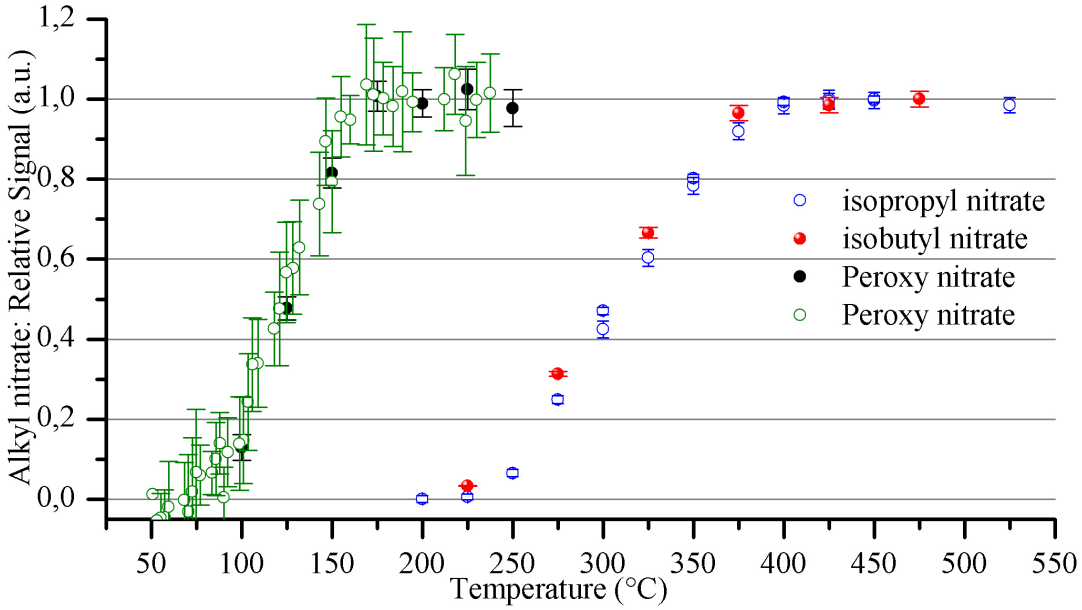

Figure 3.19.: *Normalized TD signals of PAN, isopropyl nitrate and isobutyl nitrate as function of heater temperature. Dissociation of $\sum$PNs ($\sum$ANs) is quantitative at $\sim$ 200°C ($\sim$ 450°C) with no overlap with the other species*

propyl nitrate and the red dots reflects the profile for isobutyl nitrate. The profiles of both alkyl nitrates are similar, reaching a plateau at about 450°C. Figure 3.19 also displays the normalized signals from PAN detection. Two distinct plateaus are observed in the measurements, one starting at about 200°C and the other starting at about 400-450°C. Thus, by choosing the appropriate heater temperature, one can differentiate between peroxy nitrates and alkyl nitrates.

The accuracy of the method was investigated using a well-known mixture of isopropyl nitrate.

In Figure 3.20 the result of this measurement is presented. The slope of this measurement is very close to unity and the intercept is almost zero. This indicates that at 450 °C the alkyl nitrates are converted with 100 % efficiency to NO_2. Possible interferences according to NO and NO_2 were not investigated during this work but in Paul et al. (2009). Interference due to NO_2 was not observed. A possible nighttime interference on the alkyl nitrate signal is nitryl chloride ($ClNO_2$), formed from the heterogeneous reaction of N_2O_5 with particle chloride. If $ClNO_2$ is present

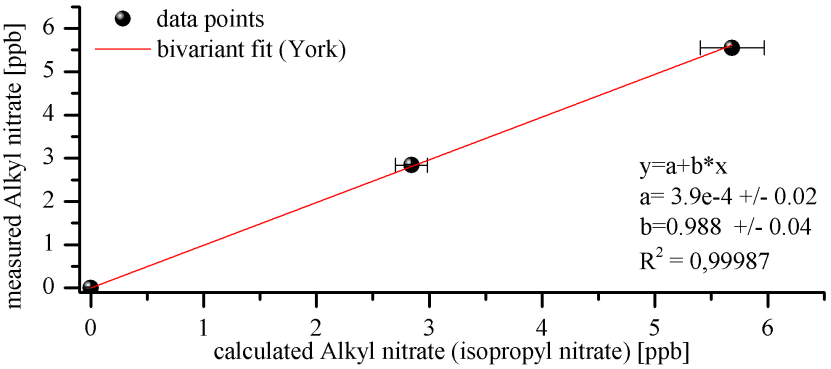

Figure 3.20.: *Qualitative measurement of alkyl nitrate: measured alkyl nitrate mixing ratios are plotted against calculated mixing ratios.*

during nighttime, an additional NO_2 signal beside the NO_2 signal coming from the PAN's and AN's dissociation in the TD-cavity will be measured. To correct for this additional NO_2 signal source a $ClNO_2$ standard was synthesized by passing Cl_2 over a mixture of $NaNO_2$ and NaCl crystals in a flow of humidified N_2. The concentration of the standard was determined using our new TD-CRDS in a similar manner to that described by Thaler et al. (2011). This standard was used to calibrate a CIMS (Chemical Ionisation Mass Spectrometer) which is capable to measure $ClNO_2$ directly. With this supplementary instrument it is possible to correct the nighttime measurements for possible $ClNO_2$ interferences. N_2O_5 interference as mentioned in section 3.3.2.6 have no influence on the alkyl nitrate concentration due to the fact that N_2O_5 dissociate at both temperatures (200°C and 450°C) to NO_2.
To derive alkyl nitrate concentrations the peroxy nitrate concentration has to be subtracted as they are also thermally decompose at 450 °C. During normal measurement routine the sample flow is switched to each temperature every 10 minute. The gap between two periods of peroxy nitrate measurements is linearly interpolated and afterwards subtracted from the sum of peroxy + alkyl nitrates (at 450°C).

3.3.2.8. Precision and uncertainty of the instrument

The baseline precision of NO_2 and AN measurements were investigated by continuous sampling of zero air. Equivalent mixing ratios were calculated for conditions of 670 Torr and 35°C. Figure 3.21 shows the 1σ precision for integration times between 1 s and 10 min for the NO_2 channel and 4s to 10 min for the TD channel. The precision approximately follows a square root dependency up to an integration time of 30-40 s (i.e., 28 pptv at 1 s and 5-6 pptv at 40 s). The baseline which is plotted for a two hour time interval here shows no long term trend, indicating that the zero measurements every 5-10 minutes are sufficient. Figure 3.21 also shows

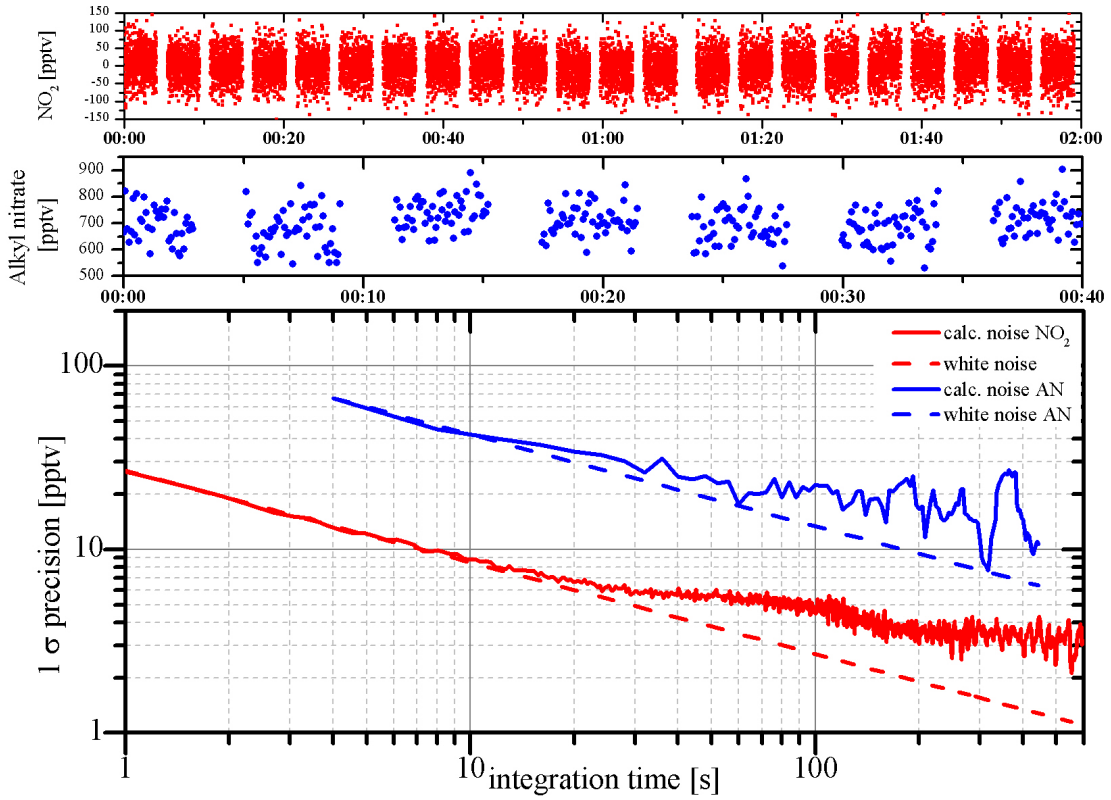

Figure 3.21.: *Dependence of 1 σ precision on integration time (Allan deviation plot) from a 2 h period of measurement of zero air. The upper panel shows the time series of the equivalent NO_2 mixing ratio. The middle panel shows a period of measurement of a constant alkyl nitrate mixing ratio of 700 pptv. The dependence of the calculated 1 σ precision on the integration time. The dashed line is the precision expected for purely random noise.*

the 1σ precision of an alkyl nitrate detection while sampling a constant mixing ratio of about 700 pptv in zero air. Again the precision follows a square root dependency up to 1 min of integration time. The precision increases from 65 pptv for 4 s integration time to about 20 pptv for 1 min integration time. The noise limited detection limit of the instrument can be taken as twice the 1 σ precision. For a measurement at 4 s time resolution this leads to a detection limit of about 30 pptv for NO_2 and about 130 pptv for PAN or PAN + AN, respectively according to Figure 3.21. The 1σ precision can vary depending on the conditions during the measurement period.

Inlet transmission and filter losses were also investigated in the laboratory for NO_2, PAN and AN. The response to concentration changes was nearly instantaneous, suggesting the absence of wall losses or memory effects on the Teflon inner walls of the sample tubing for all three species. PAN and AN mixing ratios did not change by varying the sample flow in the range of $1 - 3$ *slpm*. Transmission through the

Teflon filters (2 μm pore size) housed in a PFA filter holder was quantitative.
The NO_2 measurements are also independent of the laser output intensity. This was investigated by changing the laser output power by a factor of two without any significant changes. The quantum yield for the NO_2 photolysis is 20 % at 408 nm and is unity from 398 nm to shorter wavelengths. So with the laser diodes (405 and 408.5 nm) both of them are in a regime of 20 - 40 %.
The accuracy of the NO_2 measurements has to be considered for two different regimes. At high NO_2 mixing ratios the influence of the humidity correction is rather small due to a maximum correction of up to 170 pptv. The main factors to calculate the total accuracy are listed here:

- Error in determination the effective cross section σ_{Laser}: up to 4%
- Stability of laser spectra during measurement periods: up to 2.5%
- Error in determination the R_L: up to 1 %
- Error in pressure and temperature stability: up to 0.5 %
- Interfering species: dependent on the measurement environment
- NO_2 amount in synthetic air bottles: checked with Blue light converter (BLC): less than 20 pptv
- Error in humidity correction: 3.3 % error in the slope (Maximum error up to 6 pptv)

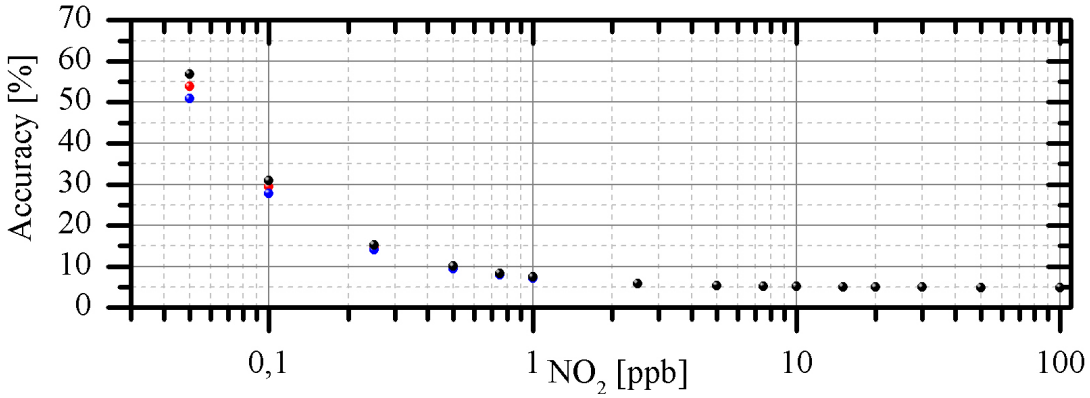

Figure 3.22.: *Uncertainty of the instrument as function of NO_2 mixing ratio (log scale) from 50 pptv to 100 ppbv including a maximum error for the humidity correction of 6 pptv (black dots: 95 % RH at 22 °C); 4pptv (red dots: 75 % RH at 22° C), 2 pptv(blue dots: 50% RH at 22° C) and 20 pptv of NO_2 possible in synthtetic air*

Figure 3.22 shows the calculated uncertainty as function of NO_2 mixing ratio for the NO_2 measurements. At low mixing ratios the effect of the humidity correction increases the uncertainty up to 60 % whereas for higher NO_2 mixing ratios the uncertainty reaches a constant value of about 4.1%.
Therefore the total uncertainty for the NO_2 measurement is the sum of the accuracy depending on NO_2 concentration and water content and the 1σ precision of this measurement. The uncertainty for the TD channel in which the sum of NO_2 and $\sum$PNs (or the sum of NO_2+ $\sum$PNs + $\sum$ANs) is measured is the same as for the reference cell. But to estimate the accuracy for $\sum$PNs ($\sum$PNs + $\sum$ANs) the influence of the synthetic air uncertainty is negligible because the background measurements for both cavities are equal. In Figure 3.23 the estimated accuracy is again plotted against NO_2 mixing ratios without the uncertainty of background bottle NO_2. Depending on the mixing ratio which is detected in the reference and the TD channel the absolute error of the $\sum$PNs (or $\sum$PNs + $\sum$ANs) measurement can be calculated using Gaussian error propagation as described where $\Delta_{TD}([NO_2])$ is the absolute error of the TD channel and $\Delta_{REF}([NO_2])$ the absolute error for the reference channel depending on the measured concentration in each channel as shown in Figure 3.23. As an example, assuming a NO_2 mixing ratio of 250 pptv and a $\sum$PNs mixing ratio of 250 pptv at 75% relative humidity, the total error of about 28.8 ppt which represents an relative error of about 11.5 % (4.96 % for TD channel and 5.86 % for the reference channel).

$$\Delta(\sum PNs) = \sqrt{(\Delta_{TD}([NO_2]))^2 + (\Delta_{REF}([NO_2]))^2} \tag{3.17}$$

The precision of the PAN measurement can be calculated after

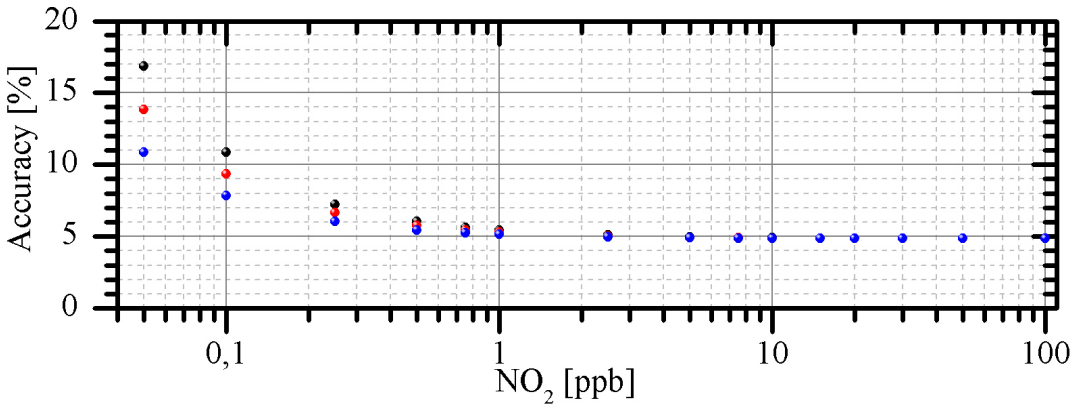

Figure 3.23.: *Accuracy of the instrument as function of NO_2 mixing ratio (log scale) from 50 pptv to 100 ppbv including a maximum error for the humidity correction of 6 pptv (black dots: 95 % RH at 22 °C); 4pptv (red dots: 75 % RH at 22° C), 2 pptv(blue dots: 50% RH at 22° C) and no influence of synthetic air for each of them*

$$\sigma(\sum PNs) = \sqrt{(\sigma(TD))^2 + (\sigma(REF))^2} \tag{3.18}$$

where $\sigma(TD)$ is the precision of the TD channel and $\sigma(REF)$ the precision of the reference channel. The total uncertainty is again the sum of the accuracy and the precision of the $\sum$PNs measurement. In contrast to the NO_2 measurement for small concentrations of $\sum$PNs the precision has a much larger influence on the total uncertainty.
The uncertainties of the alkyl nitrate measurements are very similar to the peroxy nitrate measurement. The only additional uncertainty of the determination of the $\sum$ANs is also dependent on the $\sum$PNs measurement due to the necessary interpolation between two $\sum$PNs intervals. The size of this uncertainty is to large extent, dependent on the variability of the $\sum$PNs signal.

Chapter 4.

Campaign overview

Beside the development of the TD CRDS instrument three measurement campaigns will be discussed. This chapter will give an overview of the scientific goals, description of the measurement site and the meteorological conditions. Figure 4.1 shows a map of Europe on which the three campaigns are marked via red stars. In this thesis only two of the three campaigns will be discussed more in detail in the following chapters.

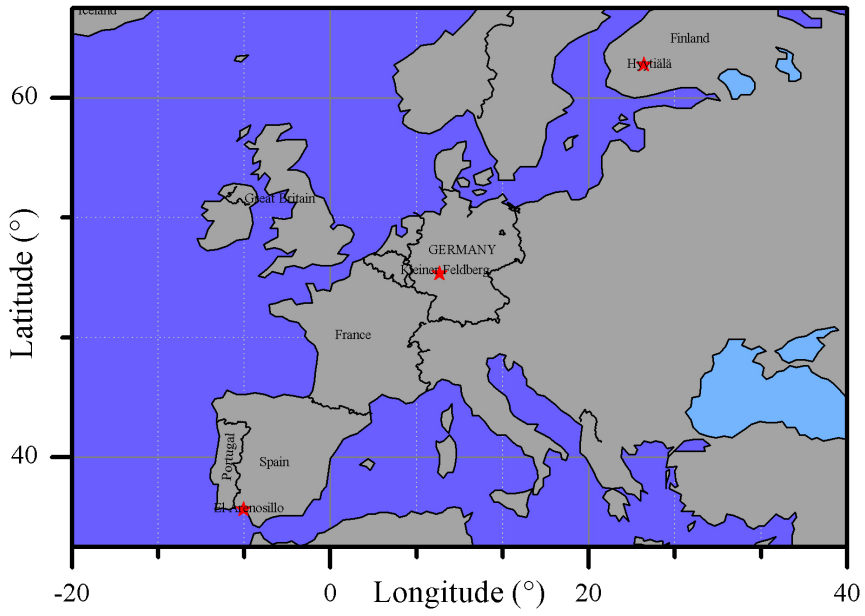

Figure 4.1.: *Map of Europe on which the red stars represents the locations of the different campaigns*

4.1. DOMINO campaign

The Domino campaign 2008 (Diel Oxidation Mechanism In relation to Nitrogen Oxides) took place in southern Spain from 21 November until 9 December. The measurements were performed on the site of an atmospheric research sounding station (Base de Arenosillo [1], 37°05'58"N,6°44'17"W), which is affiliated to the Spanish institute of aerospace technology (INTA).

4.1.1. Scientific Question

The goal of this campaign was to investigate the diurnal oxidation capacity within the planetary boundary layer at ground level. The focus of this thesis is in particular on the nighttime oxidation capacity. During nighttime the most important contributor to the tropospheric oxidation capacity is the NO_3 radical which is in equilibrium with the N_2O_5 molecule. Beside the measurement of NO_3 and N_2O_5 mixing ratios several other trace gases - and particle measurement were performed to characterize the loss processes and therefore the variability of the lifetime of the NO_3 radical depending on the meteorological conditions.
Additionally to the ground level in - situ measurement a LP - DOAS instrument was installed to investigate the vertical distribution of several trace gases including NO_3, NO_2 and O_3. With this combination of measurements the nocturnal oxidation at various altitudes within the boundary layer could be investigated.

4.1.2. Site descriptions and local surroundings

The El Arenosillo measurement station is located approximately 400 m north of the coast in a pine forest (see Figure 4.2). The surrounding trees are distributed irregularly on sandy ground. In the direct vicinity of the station there are only a few buildings and an infrequently used road. The measurements were performed on a 10 m high scaffold, the inlet lines of the instruments being attached to this scaffold at about 12 m height. The average height of the canopy, surrounding the station, is about 5-6 m. North west of the site in about 30 km distance, is the industrial centre, the city and the port of Huelva. The industrial area is dominated by oil refineries. To the east of the station a large National Park [2] is located. The more northerly region between Huelva and the National Park is neither influenced by the direct emissions of Huelva nor by emissions from Seville and is classified as "continental". The region to the north east of the station has been influenced from the city of Seville and surrounding industry of Seville at a distance of 90 km (city centre) and as well as by the pine - and eucalyptus forest which are located between the station and Seville.

[1] El Arenosillo
[2] Doñana National Park

Figure 4.2.: *Overview of the surrounding area during the DOMINO campaign. Part a) of the figure shows the measurement site in relation to the surrounding with Huelva in the north west and Seville in the north east. Part b) shows a closer look at the measurement site "Base de Arenosillo". Part c) shows a view from the measurement site of the surrounding canopy.*

4.1.3. Meteorological conditions during the DOMINO campaign

As shown in the last section the regions surrounding the measurement site, have different characters. Therefore it is important to classify the air masses arriving at the measurement site in different sectors. In Figure 4.3 different sectors are shown according to the on-site wind direction measurements. Sector A is strongly influenced by the industrial emissions of Huelva; sector B has a more continental/forested character. Sector C is influenced by the urban structure of Seville. Sector D is the clean sector with air masses coming from the Atlantic Ocean. The remaining southern sector (between C and D) was not characterized because no air masses were transported from this sector to the measurement site during the campaign.

Beside the on-site measurement of the wind direction a complete investigation of the air mass origin were performed by using the NOAA Hysplit model (Draxler and Rolph (2011)). 48 hours back trajectories were calculated for every two hours. A complete overview of this analysis is also shown in Diesch et al. (2012). Figure 4.4 shows the calculated back trajectories colour coded by the different sectors which are in good agreement with the in - situ measurement.

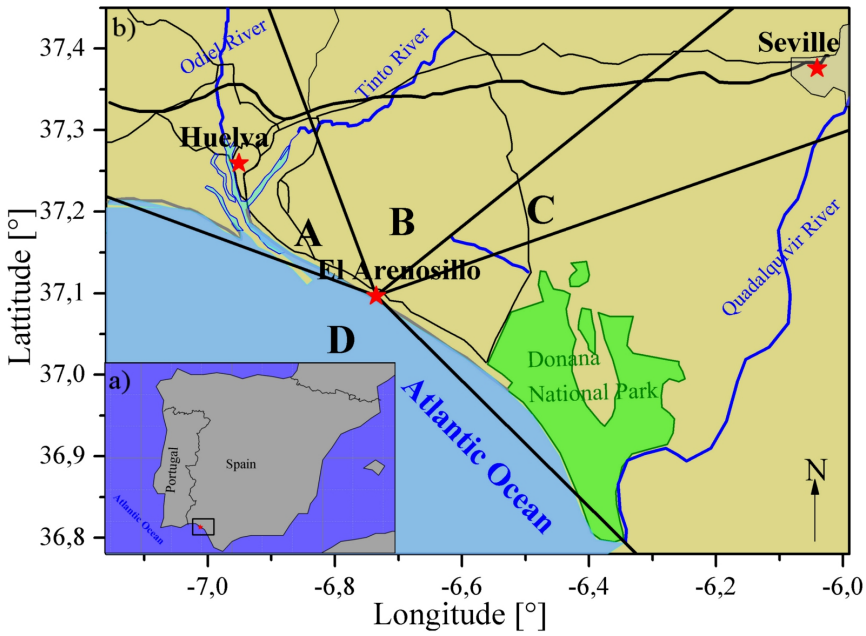

Figure 4.3.: *a) Map of Spain. b) is showing the location of the field measurements and the local surroundings.*

The following classification of the air masses depending on their origin derived from the combination of the on-site wind measurements and the back trajectories is used:

- Huelva and related industrial activity($\sim$ 30 km distance): dominated by industrial emissions coming from oil refineries (Sector A 290° - 340°). Sector A can be possibly divided into:
  - Huelva +maritime
  - Huelva +Portugal
- continental (sector B 340° - 50°)
- urban (Seville at a distance of 90 km) (Sector C 50° - 75°)
- maritime (Sector D 135° - 270°)

The long-term mean values of the wind direction during the measurement period November till December (of the years 1994 - 2007) indicated a predominance of air masses coming from the north-east direction (Seville). Based on this meteorological record one of the major goals of this campaign was to study the self-cleaning effect of the atmosphere when air masses influenced by urban emissions travelled along mainly forested environments before reaching the measurement site.

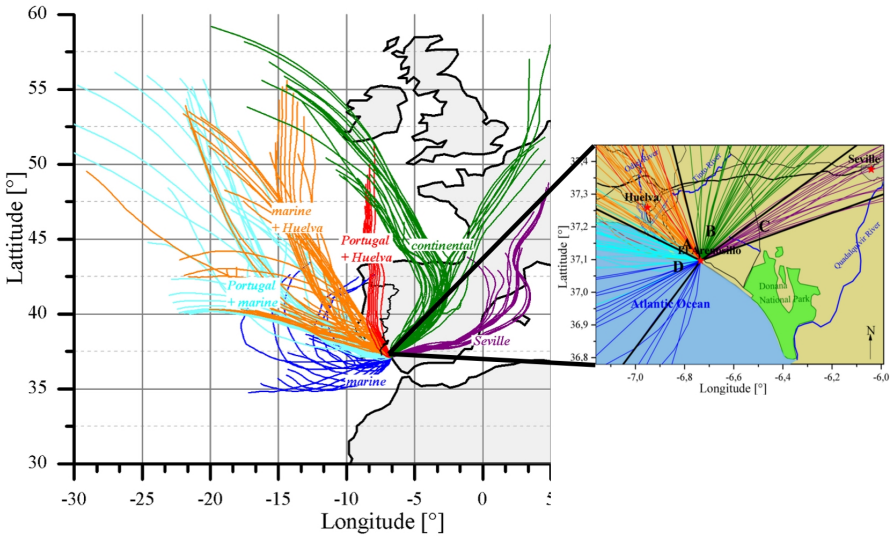

Figure 4.4.: *On the left side, a map of Western Europe with focus on the Iberian Peninsula is shown including 48 h backwards trajectories calculated for every 2 hours using the HYSPLIT model. The zoom-in on the right side shows the transport direction of the classified air mass types at the measurement site. 6 air mass categories corresponding to different source regions were separated: "Seville" (purple), "Continental" (green), "Portugal + Huelva" (red), "Marine + Huelva" (orange), "Portugal + Marine" (light blue) and "Marine" (blue)*

However air masses coming from northerly and westerly direction were the most dominant ones during the campaign (see Figure 4.5). Only a small fraction of the transported air masses reaching the site came from Seville. Less often, the wind came from the sea.
During nighttime (here defined roughly as 18 - 6 o'clock) the most pronounced wind direction was also the north - westerly direction as shown in Figure 4.5. Thus, during most nights of the campaign the measurement site was influenced by emissions of the industrialized Huelva region. When air masses came from the Atlantic Ocean the site was often influenced by clouds and occasionally rain. This influence is also clearly shown in the lower panel of Figure 4.6 (Photolysis frequency JNO_2). The temperature during the campaign varied between 1.9°C and 22.7°C with a mean

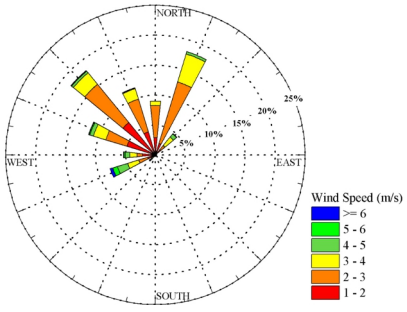

Fig. 4.5.: *Frequency distribution of the actual mean wind direction during the night (18:00 - 06:00)*

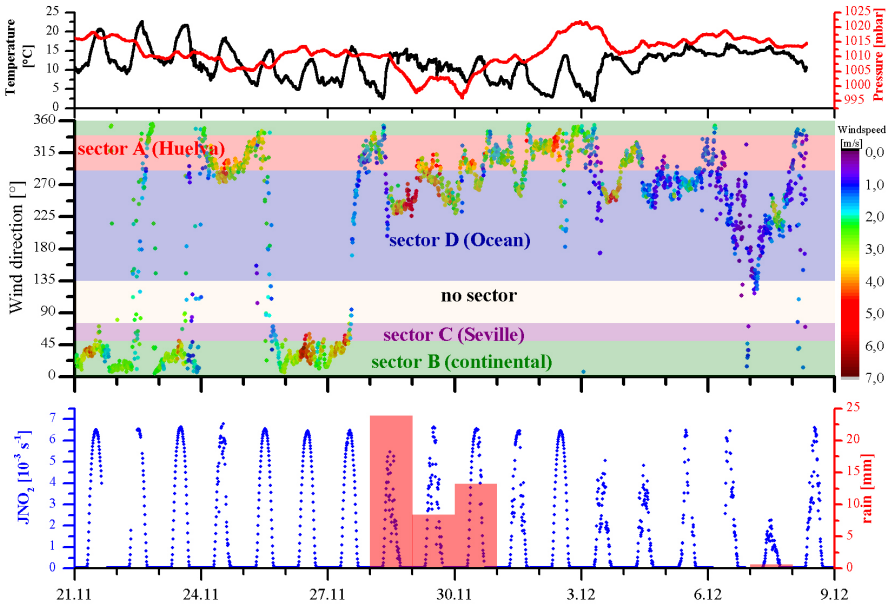

Figure 4.6.: *Meteorological overview during Domino 2008. The upper panel shows the temperature (black) and the pressure (red). The middle panel shows the wind direction colour coded by the wind speed. The regional influenced sectors are highlighted by different colours. The lowest panel shows the radiation during the campaign (blue dots) and the rainfall for each day (red bars)*

temperature of 11.6°C. The first period of the campaign was characterized with higher temperatures with pronounced diurnal variation. In between and during the last days of the campaign there was a less pronounced diurnal variation in temperature influenced by more air masses coming from the ocean.
The wind speed was relatively low during the campaign with an averaged wind speed of $2.5\frac{m}{s}$ with a minimum value of $0.15\frac{m}{s}$ and maximum values up to $6.8\frac{m}{s}$. For the nighttime values this pattern was similar. This results in an average transport time for the air masses from about 3.3 hours for air coming from Huelva and about 10 hours for air coming from Seville.

4.1.4. Instrumentation of the campaign

A large number of different instruments was installed at El Arenosillo, most with inlets about 12 m above the ground. A complete overview of the in - situ measurements is listed in table 4.2 including precision,accuracy and time resolution of each instrument. In addition to the on-site meteorological parameters; radiosondes were launched frequently to characterize the boundary layer. Beside the gas phase measurements, the chemical and physical properties of particles were investigated by the Mola instrument (see also Diesch et al. (2012)). In addition to the on-site mea-

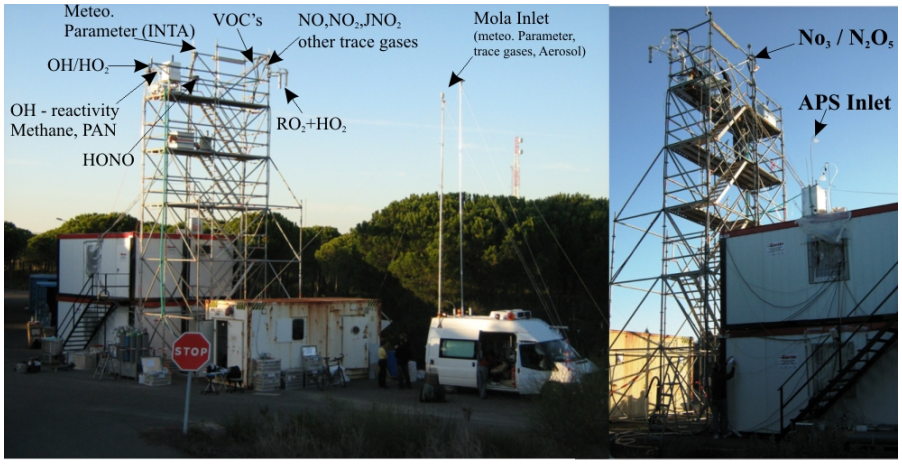

Figure 4.7.: *A huge set of different instrumentations. On the left side the front side of the measurement set up is shown with the different inlet location for each instrument. On the right side the back side of the container are shown with our NO_3/N_2O_5 and APS inlet*

surements, the horizontal and vertical distribution of different trace gases (NO_3, O_3, SO_2, NO_2, HCHO, HONO, BrO, O_4, CHOCHO, IO and H_2O) were performed with a LP-DOAS[3] instrument. These measurements were done by the University of Heidelberg. As a detailed comparison of NO_3 profiles between the LP-DOAS and the CRDS measurements will be made later, a description of the LP-DOAS set up and the profile retrieval is given here. The principle of these measurements is explained in detail in Platt and Stutz (2008). The LP-DOAS instrument applies the set-up from Merten et al. (2011) with a configuration described in Poehler et al. (2010). The absorption light path of this measurement was 9626 m. The LP DOAS telescope was located on top of the ESAt building at about 9 m height over ground. The ESAt building was about 1 km away from the in - situ measurements in northern direction. Figure 4.8 shows a overhead view of the measurement site in which the light path of the LP DOAS measurement is shown as well as the location of the measurement site. Three arrays of retro reflectors were mounted

[3]Long Path Differential Optical Absorption Spectroscopy

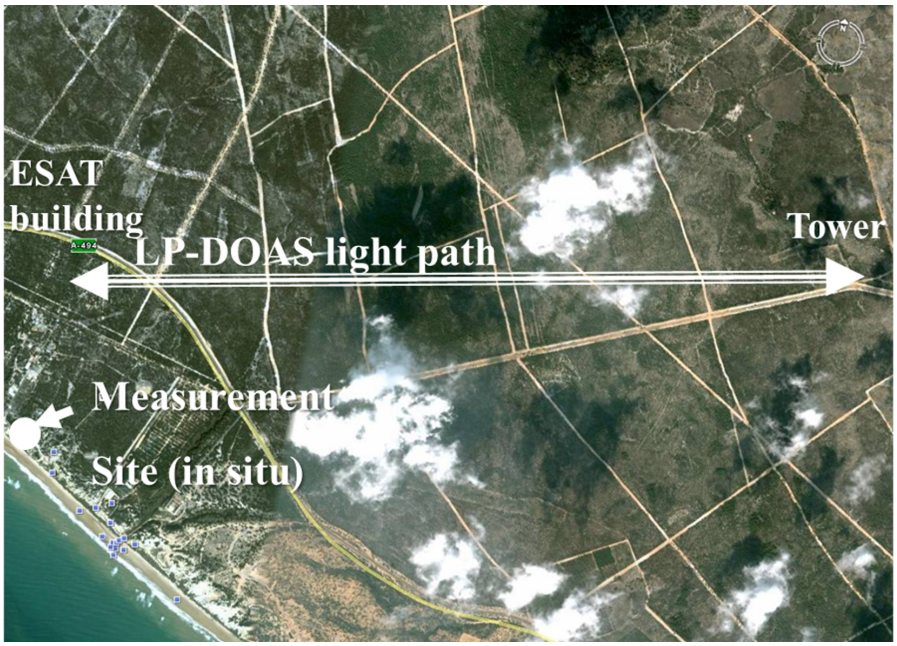

Figure 4.8.: *Set up of the LP-DOAS instrument. The telescope was mounted on the ESAT building and the retro reflectors are mounted to a Tower at 4.8 km distance*

on a tower (70 m height) facing east from the ESAt building in a distance of 4813 m at 20, 39 and 70 m above the ground.With this combination it was possible to retrieve horizontal and also vertical information of the different trace gases during the campaign.

The concentrations along the different light paths cannot be directly converted to profiles as the light path to the highest retro reflector also crosses air masses at lower altitudes. A plane parallel model with fixed layer heights (Veitel et al. (2002)) was applied to retrieve the concentration at different heights above the ground. In this model the boundary layer is divided into layers with limits defined by the retro reflector heights (see Figure 4.9). Using this model the profile concentration can be calculated by:

.

$$c_i = \frac{\overline{c_i} \cdot h_i - \overline{c_{i-1}} \cdot h_{i-1}}{h_i - h_{i-1}} \tag{4.1}$$

Where $\overline{c_i}$ is the measured concentration along the individual light path and h_i is the height of the associated retro reflector to $\overline{c_i}$ in relation to the lower most retro reflector. For the upper layer c_3, the layer height according to the plane layer height with $h_2 = 19m$ and $h_3 = 50m$ was used. The errors of the mean concentrations c_i can be calculated neglecting the errors of the reflector heights as these are

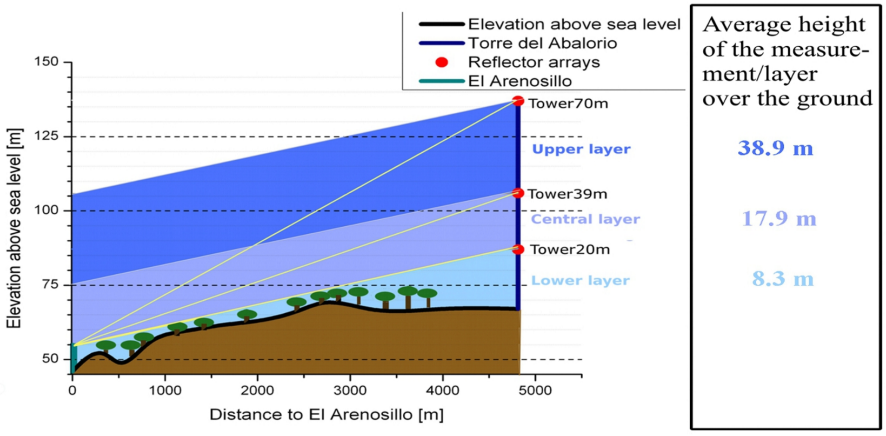

Figure 4.9.: *Schematic overview of the different light paths and the layers. The three different light paths are outlined in yellow. The blue boxes display the different layers. The box on the right side of the figure shows the average height of each layer above the ground.*

Table 4.1.: *Properties of layers*

	retro reflector height [m]	average altitude over ground [m]	lowest altitude over ground [m]	highest altitude over ground [m]
Layer 3 (upper)	70	38.9	26.5	70
Layer 2 (middle)	39	17.9	5.5	39
Layer 1 (lower)	20	8.3	2.3	20

determined with high precision:

$$\Delta c_i = \sqrt{\left(\frac{\Delta\overline{c_i}\cdot h_i}{h_i - h_{i-1}}\right)^2 + \left(\frac{\Delta\overline{c_{i-1}}\cdot h_{i-1}}{h_i - h_{i-1}}\right)^2} \tag{4.2}$$

The layer height does not represent the average height over the ground owing to the not absolutely plane parallel surface. Therefore the surface height derived from a high resolution map was used. The height of the telescope was about 9 m above the ground. The average altitude of the surface along the measured light path was 62.6 m above sea level. The resulting properties of each layer are summarized in table 4.1.

Table 4.2.: *Overview of the in - situ measured gas phase species, measurement technique, precision, accuracy and detection limit according to the time resolution. Abbreviations see Appendix A*

Species	Method	Precision [pptv]	Accuracy [%]	Detection Limit [pptv]	Time resolution [s]	Institute
NO_3	CRDS	2	14	2	5	MPIC
N_2O_5	CRDS	2	15	2	5	MPIC
NO_2	CLD	8.29	8		1	MPIC
NO	CLD	6.04	5		1	MPIC
OH	LIF	0.034	18	0.037	60	MPIC
HO_2	LIF	0.23	18	0.29	60	MPIC
O_3	UV Photometry		1000	< 1000	60	MPIC
SO_2	UV Fluorescence		1000	< 1000	60	MPIC
met. parameter	n/a	n/a	n/a	n/a	n/a	MPIC
Aerosol properties and chem. composition	n/a	n/a	n/a	n/a	n/a	MPIC
OH-reactivity	CRM		20	3.5 s^{-1}	12	MPIC
VOC	TD-GC-MS	n/a	n/a	100	2400	MPIC
Radon	n/a	2.28 [Bq/m^3]	n/a	n/a	3600	MPIC
PAN	GC-ECD	n/a	n/a	50	180	
HCHO	HPLC	19.1	16.3	21.1	3	MPIC
H_2O_2	HPLC	7.6	15.7	5.5	3	MPIC
JNO_2	Filterradiometer	n/a	n/a	n/a	0.5	MPIC
HONO	LOPAP	n/a	12	1-2	300	Uni Bayreuth

4.2. PARADE campaign

The Parade campaign 2011 (PArticles and RAdicals: Diel observations of the impact of urban and biogenic Emissions) took place on the summit of the Kleiner Feldberg in central Germany from 15 August until 9 September. The measurements were performed at the Taunus Observatorium (50°13'12"N, 8°27'E) which is affiliated to the Goethe University Frankfurt.

4.2.1. Scientific Question

The semi-rural location of the Kleiner Feldberg in Central Germany enables investigation of the effects of both biogenic and anthropogenic emissions on radical chemistry (both day and night) and also on the nucleation, growth, composition and aging of particles. This work focuses on the nitrogen cycle with special emphasis on NO_2 and the NO_y reservoir species peroxy nitrates ($\sum$PNs) and alkyl nitrates ($\sum$ANs). To date, alkyl nitrates have not often been measured although they may contribute significantly to NO_y. Therefore more measurements of $\sum$ANs and investigation of the contribution to NO_y compared to the other higher oxidized nitrogen species (like $\sum$PNs or HNO_3) are necessary.

4.2.2. Site description and local surroundings

The measurement site is located on top of the Kleiner Feldberg at 825 m height. Kleiner Feldberg is located in the Taunus region close to the Rhein Main Area as shown in Figure 4.10 a). Owing to its elevation, the station is known for its quite remote character for central Germany. A few main roads and some small towns lies within 5 km of the measurement site. A road passes a few hundred metres from and about 100 m below the observatory. The road is only lightly frequented, except during weekends, when the Taunus Range is used recreational purposes. This semi-rural location is impacted by pollution from the densely populated Rhein-Main area (pop. 2 million) including an extensive motorway system and large cities such as Frankfurt (pop. 700 000, 20 km SE), Wiesbaden (pop. 300 000, 23 km SW) and Mainz (pop. 200 000, 27 km SSW). The area 50-100 km north of the measurement site is lightly populated and devoid of major industry. The site has been described also by Handisides (2001) ,Crowley et al. (2010) and Phillips et al. (2012b). The area directly around the observatory is mainly coniferous forest. The hill top itself (about 50m radius) has been cleared of tress for meteorological measurements several times, the last time about 50 years ago and only a couple of willows and some birch trees remain between the cleared area and the spruce trees. The direct vicinity of the measurement containers is covered with low lying vegetation, which mainly consists of grasses and low blueberry bushes, with a few smaller trees. Wind flow pattern are influenced by the presence of two similar

sized mountains: Großer Feldberg (878 m asl; 1.3 km NE of Kleiner Feldberg) and Altkönig (798 m asl; 2.7 km ESE of Kleiner Feldberg). Figure 4.10 shows

Figure 4.10.: *Overview of the surroundings during the PARADE campaign. This figure is a composite of a) a google map figure of the measurement site in relation to the surroundings, b) a closer view of the Taunus Oberservatory of the Uni Frankfurt (google maps)*

additionally views of the site. Picture b) shows a closer google map zoom of the summit of Kleiner Feldberg in which the main measurement container is framed in red.

4.2.3. Meteorological conditions during PARADE

The weather during the campaign may be divided into different periods with three frontal systems and one thunderstorm passing the site. There were several periods with foggy conditions and several rainy periods. Figure 4.11 gives an overview of the meteorological conditions.The upper panel of the Figure shows the temperature (black line) and the pressure (red line) during the campaign. The temperature during the campaign varied from 5.1°C to 27.8°C with a mean temperature of 14.4°C. Apart from one longer period, influenced by a stable high pressure system, with rising temperature and sunny conditions, there were several days with heavy rain typically after a frontal system passed the site. The middle panel shows the wind direction colour coded with the wind speed. The local wind directions are divided into different sectors depending on the region as shown in the middle panel. The lower - most panel displays the radiation (JNO_2, blue dots) and the sum of rain per day (red boxes). Figure 4.12 a) indicates the different sectors according to the local surroundings. Sector A (rural) is the cleaner sector which is not that heavily influenced by emissions of large cities and industries. Sector B is a rural area

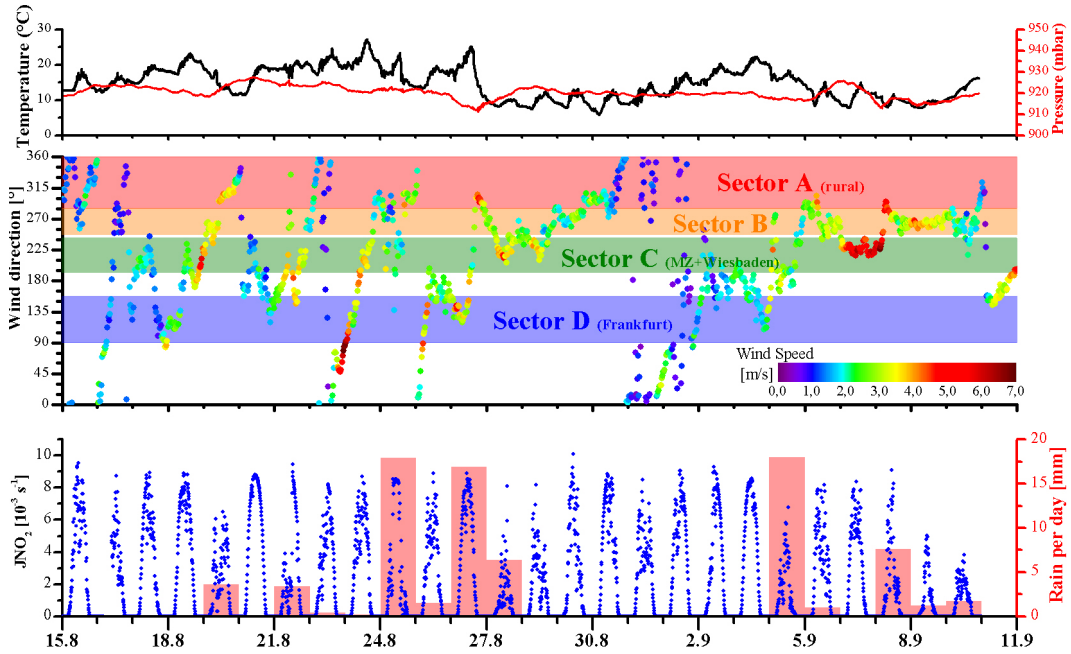

Figure 4.11.: *Meteorological overview during Parade 2011. The upper panel shows the temperature (black) and the pressure (red). The middle panel shows the wind direction colour coded by the wind speed. The regional influenced sectors are highlighted by different colours. The lowest panel shows the radiation during the campaign (blue dots) and the rainfall for each day (red bars)*

dominated by forest in the west of the measurement site. Sector C is influenced by the large cities Wiesbaden and Mainz which are about 20-30 km away from the site. Sector D is the area which is influenced by the largest city (Frankfurt am Main) in this region. Various industries and one of the world largest airports are located in this sector. In general the west to south-west direction dominated the wind patterns (see Figure 4.12 b)). The wind speed during the campaign measured by the HLUG varied in the range of $0.4 - 6.9 \frac{m}{s}$ with a mean velocity of $2.65 \frac{m}{s}$. This implies that, air masses e.g. from Wiesbaden/Mainz would need about 2.6 hours to arrive at the site. Owing to the difference in the elevation between the measurement site and the surrounding cities, direct emissions from these cities may however need longer to reach the site. To identify the air mass origin 48h back - trajectories were calculated using the Hysplit model (Draxler and Rolph (2011)). The origin of the air masses could be classified in five sectors as shown in Figure 4.12 b) (also see Phillips et al. (2012b)). The trajectories were consistent with the on - site wind direction measurements.
In general the campaign can be divided into three main parts. The first period

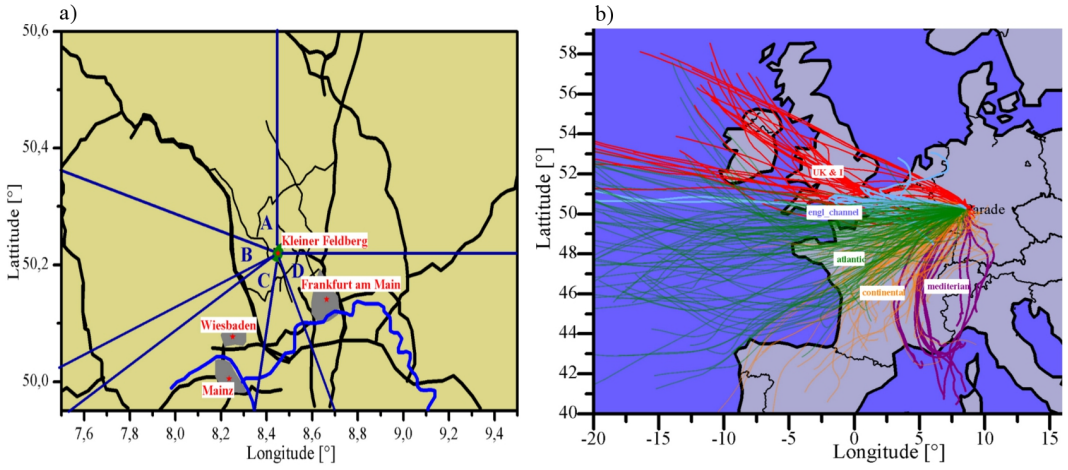

Figure 4.12.: *a) shows the surroundings of the measurement site with the different regional influenced sectors. b) Map of central Europe is shown including 48 hours backwards trajectories calculated for every 3 h using the HYSPLIT model. 5 air mass categories corresponding to different source regions were separated: "UK & I" (red), "English channel" (light blue), "Atlantic" (green), "Continental" (orange) and "mediterian" (purple)*

("Continental") was changeable, with the majority of air sampled from the 15th August to the 26th August having largely continental origin in the south to west wind sector. This period was interrupted by two shorter periods in which the air masses had their origin over the UK and over the English Channel, respectively. The second longer period ("UK-Marine"), from the 26th August to the 5th September, started with a cold front moving over the site from the west with an origin over the Atlantic. During the 29th August the air started to become influenced by the UK and the Benelux countries. The third and last longer period ("Atlantic") from the 5th September to the end of the campaign started again with a front moving over the site. In general this period was influenced by westerly winds with Atlantic origin.

4.2.4. Instrumentation

For the Parade 2011 campaign a large suite of instruments was installed on top of Kleiner Feldberg. The Taunus Observatory provided a two storey/4 - container setup with a two level platform on top. Beside the main container complex three additional measurement containers and the Mobile laboratory (Mola, MPIC Department particle chemistry) were placed close by. Table 4.3 gives an overview of the instrumentation with details of their performance. The Hessisches Landesamt für Umwelt und Geologie (HLUG) and the German weather service (DWD) use the station for monitoring. Figure 4.13 shows picture of the measurement site.

Beside the measurement of gas-phase species (see table 4.3) the chemical composition and properties of aerosol were investigated as well meteorological parameters with boundary layer characteristics from balloon launches and lidar measurements. During three days of the campaign aircraft based measurements were performed to support the ground based measurements and to gain chemical information about the inflow region. In addition to the NO_2 CRD instrument 7 other NO_2 instrument

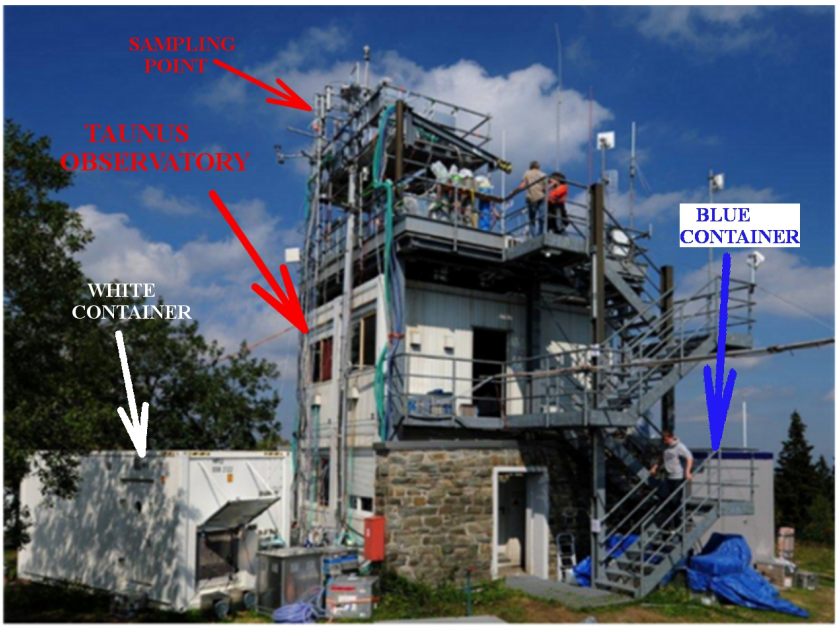

Figure 4.13.: *Picture of the Taunus Observatory with additional measurement containers around the observatory.*

(see Table 4.3) participate in the campaign which provides a unique opportunity to test the performance of the CRD-NO_2 instrument.

Table 4.3.: *Overview of the in - situ measured gas phase species, measurement technique, precision, accuracy and detection limit according to the time resolution. Abbreviations shown in Appendix A*

Species	Method	Detection Limit [ppt]	Accuracy [%]	Time resolution [s]	Institute
NO_x/NO_y					
NO_2	CRDS	50-60	5	4	MPI
$\sum$PNs	TD-CRDS	50-100	5	4	MPI
$\sum$ANs	TD-CRDS	50-100	5	4	MPI
NO	CLD	4	4 + 21 ppt	1	MPI
NO_2	CLD	55	10 + 105 ppt	1	MPI
PAN's+$CLNO_2$	TD-CIMS				MPI
HONO	LOPAP				FZJ
NO_2	CE-DOAS	300	5-10	30	Uni HD
NO_2	LIF	5/min	10	1	MPI
NO_2, NO	CLD				Uni Bremen
Radicals/Reactivity					
RO_2	PERCA	1-3	30		Uni Bremen
RO_2	PerCEAS				Uni Bremen
OH-reactivity	PTR-MS	$3s^{-1}$		60	MPI
OH-reactivity	GC-PID	$3s^{-1}$		120	MPI
OH and HO_2	LIF				MPI
NO_3	CRDS	2-3	20 + 2ppt	5	MPI
N_2O_5	TD-CRDS	5-6	15 + 2ppt	5	MPI

Table 4.3 continued

Species	Method	Detection Limit [ppt]	Accuracy [%]	Time resolution [s]	Institute
Organics					
VOCs	PTR-ToF-MS	330	5-7	60	Uni Wuppertal
terpenes	GC-MS	1	10-15	2100	MPI
HCs (C_2-C_{12})	GC-FID			1200	MPI
Peracetic acid	CIMS				MPI
HCHO	HPLC	25	14	3	MPI
H_2O_2	HPLC	32	14	3	MPI
Others					
CO_2	NDIR Abs.		1.5ppm	1	Uni Mainz
CO	QCL	3ppb	10	1	MPI
NO_x,CO,SO_2,O_3	Airpointer			4	MPI
NO_2,NO_3,SO_2,O_3...	LP-DOAS				Uni HD
NO_2,HCHO,HONO...	MAX-DOAS				MPI
SO_2	Fluorescence	1000		60	Uni Frankfurt
J values	Spec Rad				FZ Jülich

Part III.

Results and Discussion

Chapter 5.

Results from DOMINO 2008

5.1. Instrument setup during DOMINO

During the DOMINO campaign, NO_3 and N_2O_5 mixing ratios were measured using the two-channel CRD instrument as described in section 3.2 and also by long-path, differential optical absorption spectroscopy (LP-DOAS) as described in section 4.1.4. The CRD was located inside the upper container (see also Figure 4.7 right side) of a two - container stack. The air was sampled through 1/4 or 1/2" PFA-tubing with the inlet 7 to 12m above ground level ($\sim$ 1-5m above the adjacent canopy). In order to reduce the residence time when using the 1/2" tubing a additional bypass flow was used. A PFA filter holder containing a $2\mu m$ pore Teflon filter (replaced every hour) was located at the end of the inlet. The loss of NO_3 and N_2O_5 to the filter was characterized before and after the campaign and were determined to be $15 \pm 3\%$ and $< 2\%$, respectively. The loss of NO_3 to the Teflon coated (DuPont, FEP) glass cavities were also measured before and after but also during the campaign. The residence time in the cavity was 0.6 - 1 s depending on the flow rates and the pressure of the system.
The CRD noise-levels during the campaign varied between $\sim$ 3 and 7 pptv for N_2O_5 and between 2 and 5 pptv for NO_3. In both cases the integration time for one data point was about 5s. The detection limit of the instrument is partly defined by the accuracy of the chemical zero measurements (measured by adding NO (Equation 3.4) as described in detail previously (Schuster et al. (2009))) and was between 2-3 ppt v for NO_3 and 5-7 pptv for N_2O_5.
NO_3 was not detected during the campaign even at periods when N_2O_5 levels of several hundred pptv were present.

5.1.1. NO_3 concentration from N_2O_5 and NO_2 measurements

As shown in Equation 2.29, NO_3 and N_2O_5 concentrations are linked with those of NO_2 and the equilibrium constant K_{eq}, which is dependent on the temperature. The NO_2 levels were not sufficiently high and the temperature not sufficiently low to reduce NO_3 to below the detection limit, indicating a deviation of the NO_2-

NO_3-N_2O_5 chemistry from equilibrium. The average nighttime temperature was about 9°C with occasionally peaks up to 15°C. At this temperatures the equilibrium of this system should be established within a few minutes, suggesting that any processes that brings the system rapidly out of equilibrium must be very local otherwise N_2O_5 would also have been completely removed.
A potential reason for the dis-equilibrium between NO_2, NO_3 and N_2O_5 is the loss of NO_3 in the inlet line, which was not anticipated as a similar sampling strategy (long PFA line with about 1 s residence time) had been periodically deployed previously [Crowley et al. (2010)]
Replacing the inlet line by a new, fresh inlet line did not result in observation of NO_3, even temporarily. A NO_3 calibration source was used during the campaign on several occasions to measure the transmission of the inlet line and also of the cavities. NO_3 was generated by thermal dissociation of N_2O_5 at about 90 °C . N_2O_5 itself was generated by mixing NO_2 and O_3 in a FEP-coated, blackened glass reaction vessel as described in Schuster et al. (2009). The reaction time of NO_2 and O_3 was a few minutes. Typically the sample consists of about 200-400 pptv N_2O_5, 150 ppbv O_3 and 5 ppbv NO_2. The results of these transmission measurements were rather surprising as the initial transmission of the inlet line to NO_3 was very low even if the tubing was relatively fresh. Line conditioning with the calibration source over a longer time period (up to 1 hour) increases the transmission to a value of about $70 - 80\%$ which is consistent with the known loss rates of NO_3 in PFA tubing.
Simultaneously to the inlet transmission measurements, the transmission of the cavities themselves was measured. For the NO_3 cavity the loss rate was determined to be $1s^{-1}$, which is five times larger than loss rates determined in the laboratory. The loss rate in the hot cavity (NO_3 + N_2O_5) was determined to be 0.2 s^{-1} as measured in the laboratory.
These observations indicate that the PFA tubing rapidly became reactive to NO_3 when exposed to the air and this reactivity could be reduced by extended passivation with high NO_3/O_3 concentrations or by heating to 90°C. Post campaign laboratory tests also revealed high inlet reactivity to NO_3. All this suggest a complete loss of the ambient NO_3 in the inlet system, i.e. on a timescale of approximately 1s. This is considerably shorter than the lifetime of N_2O_5 (minutes), and consequently no loss of N_2O_5 in the inlet line is expected. Therefore it was possible to calculate the ambient NO_3 mixing ratios from the measured N_2O_5 and NO_2 and the equilibrium constant, K_{eq} via

$$[NO_3] = \frac{[N_2O_5]}{K_{eq}[NO_2]} \tag{5.1}$$

Possible losses of N_2O_5 due to coating of the wall of the inlet line with aerosol is not expected as the line was protected with a frequently replaced Teflon filter and itself was exchanged several times during the campaign.

The calculation of the ambient NO_3 mixing ratios decreases the accuracy of the values derived since the calculation relies on high quality (accurate, low noise) and preferably high time resolution NO_2 measurements. Also the equilibrium constant K_{eq} is associated with an uncertainty of about 20 % [Osthoff et al. (2007), Crowley et al. (2010)]. Using this indirect way of determine NO_3 mixing ratios the uncertainty will be considerably larger than via direct measurements and is estimated to be 35% for N_2O_5 mixing ratios $> 7pptv$. At lower levels of N_2O_5 the uncertainty in N_2O_5 ($\sim$ 40% at 5 pptv) dominates. For discussion of the results only NO_3 values are calculated for $[N_2O_5] > 7pptv$. The NO_3 measurements taken by the LP-DOAS instrument (see section 4.1.4) at similar height are however in good agreement with the CRD-NO_3 data derived from N_2O_5 and NO_2.

5.2. NO_3 Lifetime and steady state

The steady state approximation is commonly applied to calculate and interpret measured abundances of particular trace gases. It is based on the assumption that the rates of production and loss of a compound are roughly in balance, such that the rate of its concentration change is small compared to its formation rate (source term) and its loss rate (sink term). The continuity equation for the concentration, C, of a trace gas in a given volume is as follows [see, e.g. Ravishankara and Lovejoy (1994)]

$$\frac{dC}{dt} = P - L + F \tag{5.2}$$

where P stands for the production rate, L for the local loss rate and F=(F_{in}-F_{out}) for the net flux of the compound in the specific volume. Because of the chemical changes associated with the trace gases of interest in this chapter, namely NO_3 and N_2O_5, are likely to be rapid relative to transport, the flux terms will be assumed to be small small compared to the production and loss rates. Assuming that the total loss can be represented by a first-order process, the loss term in equation 5.2 becomes $L = k'C = C/\tau$, where k' is the total first - order rate coefficient for the loss of C and tau is thus its atmospheric lifetime:

$$\tau = \frac{C}{P - \frac{dC}{dt}} \tag{5.3}$$

For first - order loss processes such as gas-phase reactions with sink compounds that are in excess concentration, photolysis, etc, τ is equal to the inverse sum of the individual pseudo first-order reaction rate constants, i.e., $\tau = \frac{1}{\sum k_i}$. As noted above the steady state approximation is only valid when the time rate of the concentration change is negligible, i.e., dC/dt =0. In this case, the atmospheric

lifetime, τ, becomes the steady state lifetime (also referred to as steady state turnover lifetime), τ_{ss}, and has a simple form.

$$\tau_{ss} \equiv \frac{C}{P} \approx \frac{1}{\sum k_i'} \tag{5.4}$$

Under steady state, the first - order loss rate coefficient for a compound in the atmosphere may be obtained from the measurement of its concentration and production rate. This method is commonly used to infer the strengths of sinks for reactive compounds (e.g. OH, NO_3) or to estimate missing sinks. To use this steady state approach to analyse a data set, the effective first-order rate constant for the sink reaction must exceed that for the source reaction (when both can be described as first-order process), and the reaction must have proceeded for a period several times longer than the induction time determined by the inverse of the rate constant for the sink reaction [Seinfeld and Pandis (2006) and Holloway and Wayne (2010)]. Thus NO_3 would appear to be an ideal candidate for analysis via the steady state approximation. Indeed previous studies have taken advantage of these properties of NO_3 to draw conclusions about its sink chemistry from observations of its atmospheric abundance. In the following chapter the steady state approximation will be used extensively. NO_3 is formed predominantly in the reaction of NO_2 with O_3 (via reaction 5.5) and is converted to N_2O_5 via further reaction with NO_2 (via reaction 5.6). The thermal dissociation of N_2O_5 links the concentrations of NO_3 and N_2O_5 via the equilibrium constant, k_3 from reaction 5.7. Simultaneous measurements of NO_3 and N_2O_5 (Brown et al. (2003), Crowley et al. (2010)) confirm that (under most conditions) the timescales to acquire equilibrium are sufficiently short that the relative concentrations of NO_3 and N_2O_5 in the atmosphere are controlled only by the temperature and levels of NO_2. The short timescale to achieve equilibrium between NO_3 and N_2O_5 is also important for the steady state approximation. A steady state of NO_3 depends not only on its formation and loss, but also on its conversion to and reformation from N_2O_5, and the atmospheric sinks for the latter. The influence of N_2O_5 sinks on apparent steady state NO_3 lifetimes has been considered in the past [Allan et al. (1999); Geyer et al. (2001a,b); Heintz et al. (1996); Mihelcic et al. (1993); Platt et al. (2002); Platt and Heintz (1994); Platt and Janssen (1995); Smith et al. (1995)].

$$(R1) \qquad NO_2 + O_3 \longrightarrow NO_3 + O_2 \tag{5.5}$$

$$(R2) \qquad NO_3 + NO_2 + M \longrightarrow N_2O_5 + M \tag{5.6}$$

$$(R3) \qquad N_2O_5 + M \longrightarrow NO_3 + NO_2 + M \tag{5.7}$$

$$(R4) \qquad NO_3 + X \longrightarrow \text{Products} \tag{5.8}$$

$$(R5) \qquad N_2O_5 + Y \longrightarrow \text{Products} \tag{5.9}$$

where X and Y are gas phase or heterogeneous sink partners for NO_3 and N_2O_5.

5.2.1. NO_3 lifetimes

The production rate of NO_3 is given by $k_1[NO_2][O_3]$ (Reaction R1 5.5) so that its steady state turnover lifetime, $\tau_{ss}(NO_3)$, can be calculated from the observations of its concentration and those of O_3 and NO_2:

$$\tau_{ss}(NO_3) = \frac{[NO_3]}{k_1[NO_2][O_3]} \tag{5.10}$$

NO_3 can be removed directly from the air by e.g. reaction with organic trace gases (Wayne et al. (1991)) or indirectly via removal of N_2O_5 via e.g. heterogeneous loss to aqueous particles. The contribution of direct and indirect losses of NO_3 to its lifetime can, in principal, be evaluated if k_{eq} (the equilibrium constant $\frac{k_{R2}}{k_{R3}}$) and $[NO_2]$ are known. Therefore the lifetime can also be calculated as already described above by:

$$\tau_{ss}(NO_3) \approx \frac{1}{f_{ss}(NO_3)} \tag{5.11}$$

Where $f_{ss}(NO_3)$ is the overall loss frequency of NO_3 from steady state and is in general equal to $f_{ss}(NO_3) = k_x + k_{eq}\ k_y\ [NO_2]$ where k_x and k_y are the direct and indirect losses of NO_3 and N_2O_5 respectively as in Reaction R4 and R5. These rate constants are effective, pseudo-first-order rate constants for each of these reactions and are the sums of the first-order rate constants for the irreversible removal of these species.

5.2.1.1. Direct losses to NO_3

The total direct loss of NO_3 as here described as k_x is a composition of different loss processes:

- trace gas reaction: $\sum k_i[X_i]$
- Aerosol uptake : $0.25 \times \bar{c} \times \gamma(NO_3) \times A$
- Dry Deposition : f_{dd}

Where k_i $(cm^3/molecule^{-1}s^{-1})$ is the rate coefficient for reaction of NO_3 with trace gas i at concentration $[X_i]$ $(molecule/cm^3)$, A is the aerosol surface area density (cm^2/cm^3), $\bar{c}$ (cm/s) is the mean molecular velocity of NO_3 or N_2O_5, $\gamma(NO_3)$ is the dimensionless uptake coefficient for irreversible reaction with NO_3, $f_{dd}(s^{-1})$ is the first-order rate constant for dry deposition.

5.2.1.2. Direct losses to N_2O_5

The total direct losses to N_2O_5 (k_y) is the composition of the following processes:

- H_2O reaction: $k_{w1}[H_2O] + k_{w2}[H_2O]^2$
- Aerosol uptake : $0.25 \times \bar{c} \times \gamma(N_2O_5) \times A$
- Dry Deposition : f_{dd}

Where k_{w1+2} are the rate coefficients for the reaction of N_2O_5 with water, A and $\bar{c}$ as described above and $\gamma(N_2O_5)$ the uptake coefficient for N_2O_5.

5.2.2. Validity of steady state approach during Domino2008

Certain conditions must be fulfilled if equation 5.10 is used to examine NO_3 lifetimes and draw conclusions regarding direct and indirect loss routes. As already stated above in the text the application of a steady state analysis to NO_3 lifetimes is only suited to air masses where the chemical lifetime of NO_3 is sufficiently short that steady state is achieved with the transport time from the emission region to the measurement site (Brown et al. (2003)). To achieve steady state the time rate of concentration change must be negligible. In case of NO_3 and N_2O_5 that means:

$$\frac{dNO_3}{dt} = k_1[NO_2][O_3] + k_3[N_2O_5] - k_2[NO_2][NO_3] - k_x[NO_3] = 0 \tag{5.12}$$

$$\frac{dN_2O_5}{dt} = k_2[NO_2][NO_3] - k_3[N_2O_5] - k_y[N_2O_5] = 0 \tag{5.13}$$

The approximate time to achieve steady state thus depends on the production and loss rates of both NO_3 and N_2O_5 and is longer at high NO_2 mixing ratio and low temperatures. The time rates of the concentration change of NO_3 and N_2O_5 (dNO_3/dt and dN_2O_5/dt) were determined for an unfavourable case (i.e. high NO_2 mixing ratio of 10 ppb) by numerical simulation in a manner similar to that described previously (Brown et al. (2003)). The low N_2O_5 and NO_3 concentrations observed (implying short lifetimes) meant that steady was achieved within 1-2 hours after dusk and with the time of transport from the major source of NO_x (e.g. Huelva).
The code of the numerical simulation and as well a simulation run for the mean values of NO_2, O_3, k_x and k_y for the complete campaign are shown in the Appendix B.1. Equation 5.10 has been used to derive the direct and indirect contributions to NO_3 loss rates (Brown et al. (2009b), Crowley et al. (2010)) via the dependence of the observed lifetime on NO_2 mixing ratios. This approach however will break

down if the trace gases which react directly with NO_3 are correlated (e.g. have the same chemical source or spatial distribution of emissions) with NO_2. This in unlikely to apply to regions where NO_3 losses are dominated by e.g. reaction with biogenic volatile organic compounds (BVOC) in clean air masses, but might be the case where NO_3 reacts with trace gases resulting from combustion processes in which NO_2 is also generated. In a similar vein, if aerosol surface area also co-varies with NO_2, use of equation 5.10 to separate the contributions of homogeneous and heterogeneous loss rates of N_2O_5 to the NO_3 lifetime is not possible.

5.3. NO_3/N_2O_5 measurements

NO_3 and N_2O_5 were measured almost every night except from the 28th to the 29th of November due to bad weather. Owing to the rapid photolysis of the NO_3 radicals during daytime very low concentration of NO_3 radicals are expected in the air therefore the measurements started every day at about 6 pm shortly before sun set and ended about 8-9 am in the morning when the sunlight was strong enough to photolyse all of the NO_3 radicals. During the nights the measurements were performed continuously with hourly breaks of several minutes when the Teflon filter was changed. In Figure 5.1 the time series of the measured N_2O_5 and the calculated NO_3 is shown as are NO_2 and O_3. The NO_3 data are generally in good agreement with the DOAS measurements of the lowermost light path considering the differences in location and heights of inlet (CRD) and optical path (LP-DOAS). A comparison of both measurements will be discussed later on in this chapter.
The production rates of NO_3 and N_2O_5, as shown in Reactions (R1-R2 5.5+5.6) are governed by the NO_2 and O_3 mixing ratios. During the campaign, nighttime mixing ratios of NO_2 were highly variable, varying from local background levels of about 1 ppb to more than 15 ppb. Typically the highest levels of NO_2 were associated with air masses that had passed over the Huelva sector, often arriving in plumes with duration of about 1-2h. Sub ppb levels of NO_2 were usually associated with the Atlantic sector. The nighttime values of NO were close to zero apart from infrequent NO spikes presumably from traffic using local roads. At some nights NO levels from 5-10 pptv were however present for a prolonged duration. The lifetime of NO in the presence of O_3 (>15ppb) is a few minutes, the presence of NO thus implies a local source. An averaged nighttime wind speed of about 2.8 m/s implies that this local source of NO is within 500 m of the measurement site. The surrounding woodland soil is one possible NO source. Apart from the occasionally plumes from the Huelva Sector, non-zero levels of NO were not associated with any single wind direction which argues against a local, continuous point emission source (i.e. instrument exhaust-line) .
The nighttime O_3 mixing ratios were strongly anti - correlated with NO_2 and thus also showed significant variability, with typical levels of 15-40 ppbv. Air masses

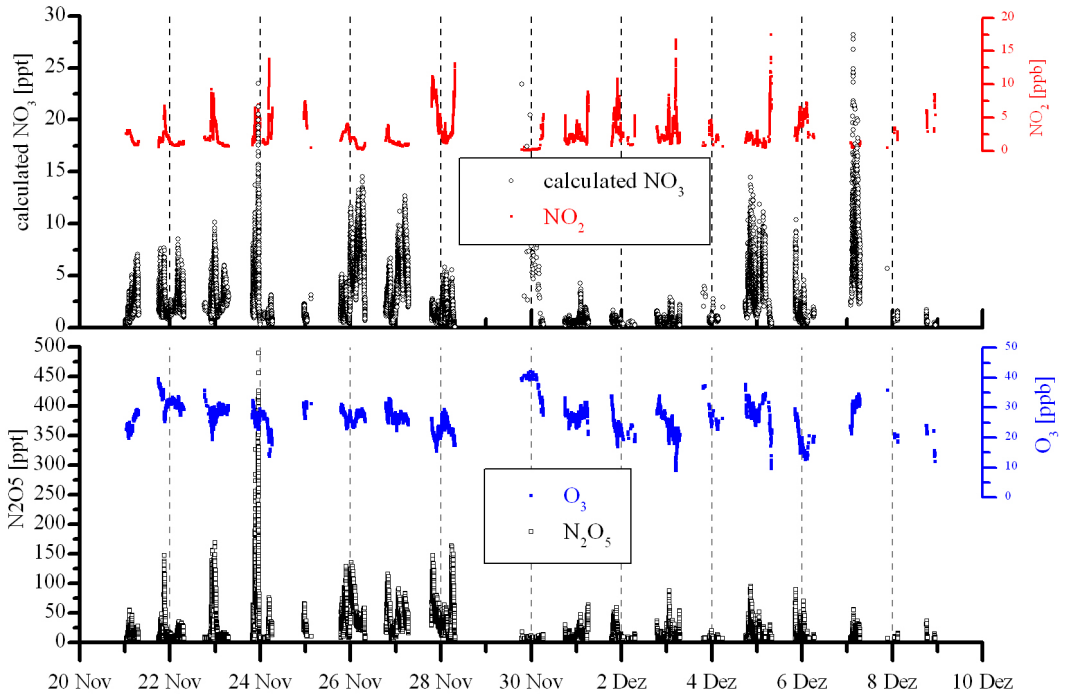

Figure 5.1.: *Timeseries of the NO_3 and N_2O_5 mixing ratios. Additionally the NO_2 and the O_3 mixing ratios are plotted owing to their direct coupling to NO_3 and N_2O_5*

reaching the site from the Huelva and coastal region often contained SO_2, with maximum levels up to 25 ppbv during nighttime in plumes originating from the port or Huelva areas. The SO_2 plumes were always correlated with high NO_2 levels which had a similar temporal profile, indicating a common process as source. One possible reason for the high SO_2 levels might be petrochemical industry activities and flaring at the petrochemical complex in Huelva which was frequently visible at night. A further possible source of SO_2 were ship emissions, either at sea or entering the harbour at Huelva. SO_2 was not measured above the detection limit in air masses reaching the site from the more continental or Seville sector. The presence of both SO_2 and NO_2 in a plume nearly always meant low levels or non-detection of N_2O_5, despite high NO_3 production rates. This particular aspect of the NO_3/N_2O_5 chemistry will be discussed more in detail later in this chapter.
Beside the trace gases, particles which can play an important role for the loss processes were also measured at the site . The number size distribution of the measured particles typically showed mode diameters of between 40 and 80 nm. The organic fraction was generally dominant but with a significant sulphate component with short term increases that correlated with SO_2 plumes. The ammonium to sulphate mole ratio was always less than unity during the campaign, indicating that the aerosol was acidic (ratio of 2: neutral aerosol). A complete overview of

the trace gases measured is shown in the Appendix B.2
The average nocturnal profile of NO_3 (see Figure 5.2 a)) over the entire campaign does not show any dominant features and is more or less constant during the night with only a smaller rise starting at around midnight till about 4 am. At sunrise, the concentrations of NO_3 dropped to zero within one hour, this long timescale indicated that N_2O_5 thermal lifetimes were about this order of magnitude. Compared to NO_3 the N_2O_5 profile (see Figure 5.2 b)) is more structured with N_2O_5 levels up to 35 pptv for the mean values. The maximum N_2O_5 concentration is reached at about 21:00 - 22:00. The median values are less than 20 pptv except from a large peak around 21:00 - 22:00 with values up to 45 pptv.

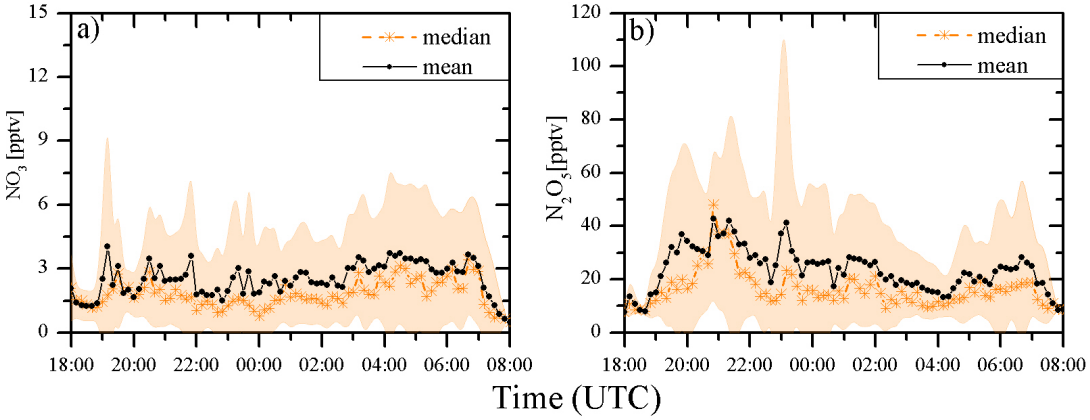

Figure 5.2.: *Nocturnal profile of calculated NO_3 (a) and measured N_2O_5 (b) mixing ratios*

5.4. Lifetime of NO_3 during the campaign

The mean NO_3 lifetime during the campaign was only about 2 min, the median value about 1 min. Maximum lifetimes of about 30 min were reached on one night (6.12-7.12.08) for the air masses with their origin over the Atlantic Ocean. The time series of the NO_3 lifetimes are shown in Figure 5.3. There are four nights were no lifetime values are shown. On the night from the 28.11-29.11.08 no measurements were performed due to a local thunderstorm. On the other nights (24.11-25.11, 25.11-26.11 and 29.11-30.11) no accurate NO_2 measurements were available to calculate the production rate of NO_3 and derive the steady state lifetime. Beside the very long lifetimes in the night from the 6.12-7.12 there are two more nights with lifetimes longer than 10 min. The night from the 26.11-27.11 was influenced by air masses coming from the continental region. On the local scale these air masses coming from the Seville region. The second night with elevated

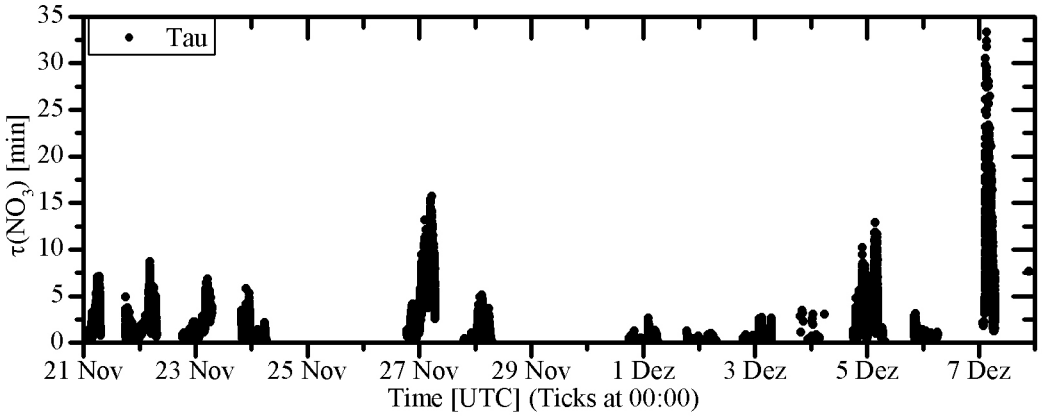

Figure 5.3.: *Timeseries of the NO_3 lifetime*

lifetimes is the night from the 4.12-5.12. The local wind direction during this night was predominantly the Huelva sector (normally dominated by very short lifetimes) but influenced also by the maritime sector. A nocturnal 10 min average profile of the complete lifetimes dataset is shown in Figure 5.4. The Figure shows the mean (black dots) and the median (orange crosses) values from 18:00 to 8:00. In the first half of the night mean and median values are similar with a more or less constant value of about 40-60 s whereas in the second part of the night (beginning at about midnight) the lifetime is longer (factor 2-3). Also the mean and median values deviate, which is likely due to the three nights with the very high lifetimes compared to the rest of the campaign.

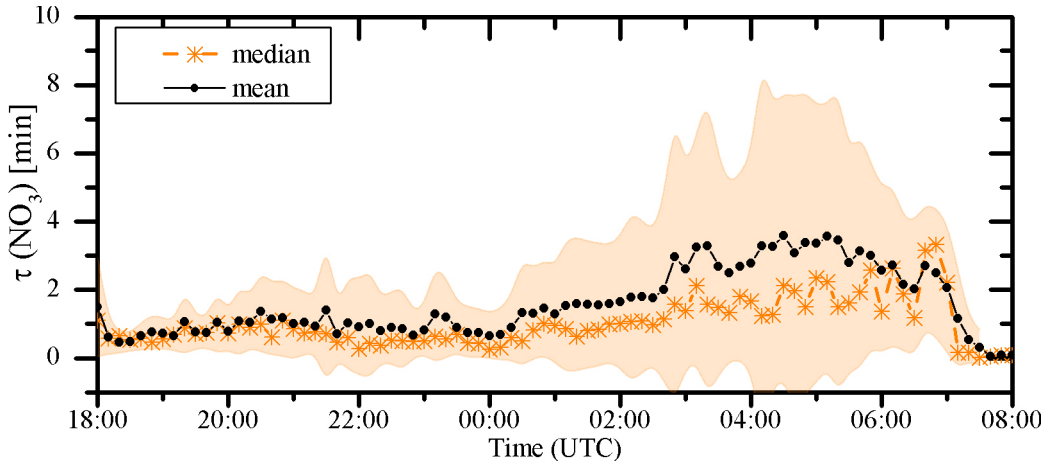

Figure 5.4.: *Mean nocturnal profile of the NO_3 lifetime*

5.4.1. NO_3 Losses

As mentioned in section 5.2.1 the steady state lifetime enables the overall loss to NO_3 to be estimated, which can be compared with the measured parameters which contributed to the total loss. Several VOCs which contribute to NO_3 loss by trace gas reaction were measured by GC-MS (Song et al. (2011)) . The measured trace gases and their rate constants for reactions with NO_3 are listed in table 5.1. From these measured VOCs only isoprene, α- pinene and limonene have fast rate constants so only these three compounds contribute significantly to the loss of NO_3. Compared to the sum of these three VOC's the sum of the rest of the measured VOC's are negligible ($\sum Isoprene + \alpha - pinene + limonene / \sum Rest\ of\ VOCs > 1000$).
Apart from its reaction with different VOC's, NO_3 can be removed directly from the atmosphere via uptake on aerosol. To calculate the loss to aerosol the surface area of the aerosol has to be known. Therefore data from an APS (Aerodynamic Particle Sizer) and an FMPS (Fast Mobility Particle Sizer) were used to determine the surface area (Diesch et al. (2012)). The APS measures the surface area from particles with diameters between $0.37 - 20\ \mu m$ and the FMPS from particles with diameters between 7-523 nm. During the nights of the campaign the mean aerosol surface area was about 80 $\mu m^2/cm^3$. Maximum values reached up to 295 $\mu m^2/cm^3$. To estimate losses of NO_3 and N_2O_5 due to the uptake to aerosols, the dimensionless uptake coefficient γ has to be corrected to take into account concentration gradients close to the surface. This requires modification of the simple expression for the heterogeneous loss rate, in Equation (5.11), so that the effective uptake coefficient ($\gamma_{effective}$) is given by Equation 2.27. For N_2O_5, D_g is $0.085 \frac{cm^2}{s}$ at atmospheric pressure and 298 K (Wagner et al. (2008)). During the nights of the campaign, the dominant contribution to aerosol surface area was by particles with diameters less than $\approx$ 200 nm. In this case, only uptake coefficients close to unity require significant correction. For example, an uptake coefficient of ~ 0.1 would be reduced by transport limitations to ~ 0.09, whereas a γ of 1 would be reduced to ~ 0.5. Therefore 0.5 is an approximate maximum value of $\gamma(N_2O_5)$ or $\gamma(NO_3)$, which can be used in estimating NO_3 lifetimes using Equation (5.11). The uptake coefficient for hydrolysis of N_2O_5 on aqueous, sulphate containing, tropospheric aerosol has been measured using laboratory surrogate aerosol (Hu and Abbatt (1997), Kane et al. (2001), Folkers et al. (2003), Griffiths et al. (2009), Griffiths and Cox (2009)) and a value of $\gamma \sim 0.04$ at high relative humidity has been recommended (IUPAC (2010)). This is consistent with the largest values of γ derived from calculations using field observations of NO_3 and N_2O_5 (Allan et al. (1999), Aldener et al. (2006), Ambrose et al. (2007), Bertram et al. (2009a), Brown et al. (2009b)). To estimate the losses from the uptake of N_2O_5 to aerosol the recommended γ was used in this study. However, the uptake coefficient can be much smaller than the recommended ones in the presence of organic components or nitrate, although the

Table 5.1.: *Measured trace gases with their reaction constant towards NO_3 and their mean, median and maxima measured values*

Trace gas	Reaction constant @ 298 K IUPAC (2010) or Wayne et al. (1991)	Mean nighttime values	Median nighttime values	Maximal nighttime values
Unit	$\frac{cm^3}{molec*s}$	pptv	pptv	pptv
NO	2.6e-11	6	2	620
HCHO	5.5e-16	488	360	2200
Isoprene	7e-13	15.6	10	137
α - pinene	6.2e-12	8.8	6.5	47
limonene	1.22e-11	7.5	5.5	61
Benzene	$\leq$ 3e-17	201	111	3461
Toluene	7e-17	174	108	2708
p-xylene	5e-16	13.2	9	167
o-xylene	4.1e-16	11.6	8	184
m-xylene	2.6e-16	39	23	766
Ethylbenzene	$\leq$ 6e-16	17.5	12	219
Camphor	$\leq$ 3e-16	12	8	47
1,8-Cineole	1.7e-16	11	9	37
p-cymene	9.9e-16	2.8	1.9	23
RO_2	2.3e-12	14.3	11.2	102

presence of chloride can offset the nitrate effect (Bertram and Thornton (2009), Mentel et al. (1999), Riemer et al. (2009)). Riemer et al. (2009) showed that the uptake of N_2O_5 on a pure inorganic aerosol depended on the sulphate to nitrate ratio with maximum values of $\gamma(N_2O_5) = 0.02$ on pure sulphate, which reduced to ~ 0.01 when sulphate and nitrate masses were equivalent. Bertram and Thornton (2009) measured N_2O_5 reactivity on ambient aerosol and found for one air sample a maximum value of γ between 0.03 and 0.04 when the ratio of organic to sulphate particle mass was ~ 2.5. This decreased to 0.01 with an organic-to-sulphate ratio of 10. During most of the nights the organic to sulphate ratio was less than 10 like shown in Figure 5.5 [AMS data from Diesch et al. (2012)].Therefore a γ value of 0.04 for the uptake of N_2O_5 to aerosol is used to determine losses. Figure 5.6 shows the average nocturnal profiles of the different species which are responsible for NO_3 loss. Figure 5.6 a) shows the water concentration during the night which was in general between 1.5 and $3 \times 10^{17} molec/cm^3$ this contributes to a N_2O_5 loss due to reaction 2.31 of about 0.00002 s^{-1}. In Figure 5.6 b) the nocturnal NO profile is shown. In general the NO concentration was close to zero except a few nights where the site was influenced by local emissions which are apparent from the mean values. The median values show the general trend. The photochemical formation of NO (e.g. by NO_2 photolysis) starts rising from 7 am. In Figure 5.6 c)

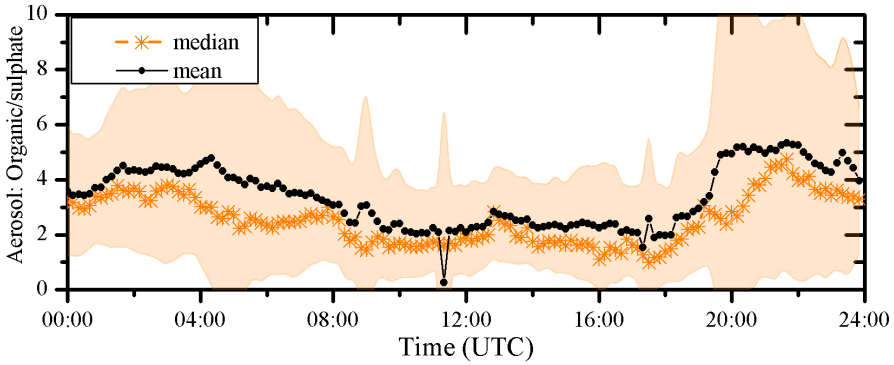

Figure 5.5.: *Mean diel profile of the organic to sulphate fraction of the aerosols*

the aerosol surface area (ASA) is shown with a range of 25 to 150 $\mu m^2/cm^3$ with a relatively constant mean value of about 100 $\mu m^2/cm^3$ during the night. Assuming a γ of 0.04 for the uptake of N_2O_5 to aerosol this average aerosol surface area leads to a loss rate of about 0.0002 s^{-1} for N_2O_5. The nocturnal profiles of the most

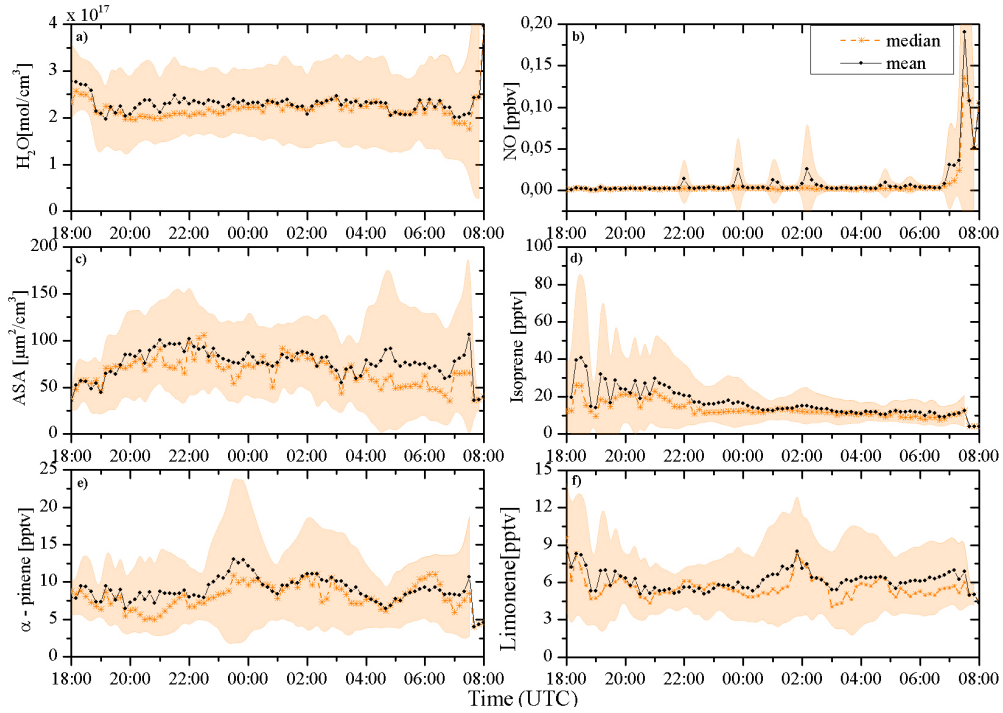

Figure 5.6.: *Nocturnal profile of the different loss processes: a) H_2O concentration, b) NO mixing ratio, c) aerosol surface area, d) Isoprene mixing ratio, e) α - pinene mixing ratio and f) limonene mixing ratio*

important VOCs in relation to direct NO_3 loss, which were measured at the site, are shown in Figure 5.6 d) - f). The Isoprene mixing ratio (Figure d)) decreased during the night from about 20-30 pptv to about 10 pptv after 22:00. The mixing

ratio of alpha - pinene (Figure e)) showed a relative constant values of about 10 pptv, where limonene (Figure f)) showed a similar behaviour with similar mixing ratios.

5.4.2. NO_3 lifetime dependence on wind sectors

The air mass origin varied during the campaign which is shown in Figure 4.5 in section 4.1.3. The most dominant wind direction (almost 50 %) during nighttime was the north - west direction which was influenced by the city and industrial centre of Huelva. As shown in Figure 5.7, where the NO_3 lifetime is plotted in a wind rose, the lifetime is highly dependent on the wind direction. The complete data set can be separated into four different wind sectors as mentioned in section 4.1.3. Figure 5.8 shows a 10 min average nighttime profile for the four different wind sectors. Each of these four plots shows the inverse NO_3 lifetime (black dots) of each wind sector compared with the measured loss processes for NO_3. The classification of the four wind sectors is based on the local measured wind direction and was also supported by back trajectories analysis as shown in Figure 4.4. Therefore, the range of these sectors was chosen as shown in Figure 4.3. Sector A is strongly influenced by the City and the industrial complex of Huelva, sector B is influenced by continental air masses, sector C is affected partly by air masses with continental origin or which are travelled a pronounced time over the Mediterranean Sea before reaching the site. For this sector back trajectories suggest that these air masses were also influenced by the city of Seville or its surroundings. Sector D displays air masses with their origin in the Atlantic Ocean.

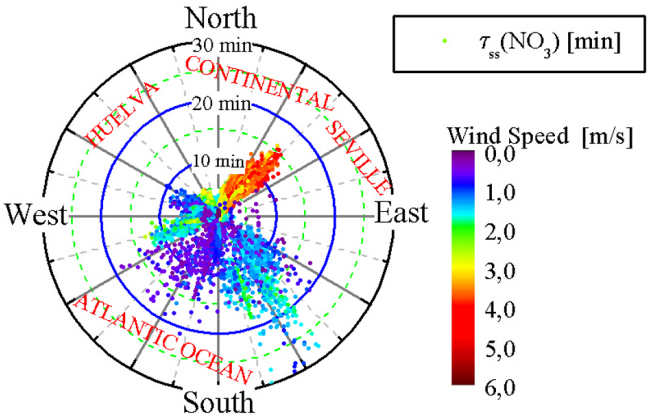

Fig. 5.7.: *Wind-direction dependency of NO_3 lifetimes (nighttime only). Almost 50% of the airmasses encountered at night came from the Huelva sector or was at least influenced by this sector, and were associated with very short NO_3 lifetimes*

Differences in the magnitude and variability of the inverse lifetime are clearly seen from sector to sector. The discrepancy between measured loss processes and the inverse lifetime is much higher in the Sectors A and B compared to the sectors C and D which indicate that air masses from these sectors contain reactive species towards NO_3 which are not measured (y-axis from plots A and B 10 times larger than for C and D). Along with the large oil refinery in Huelva several other indus-

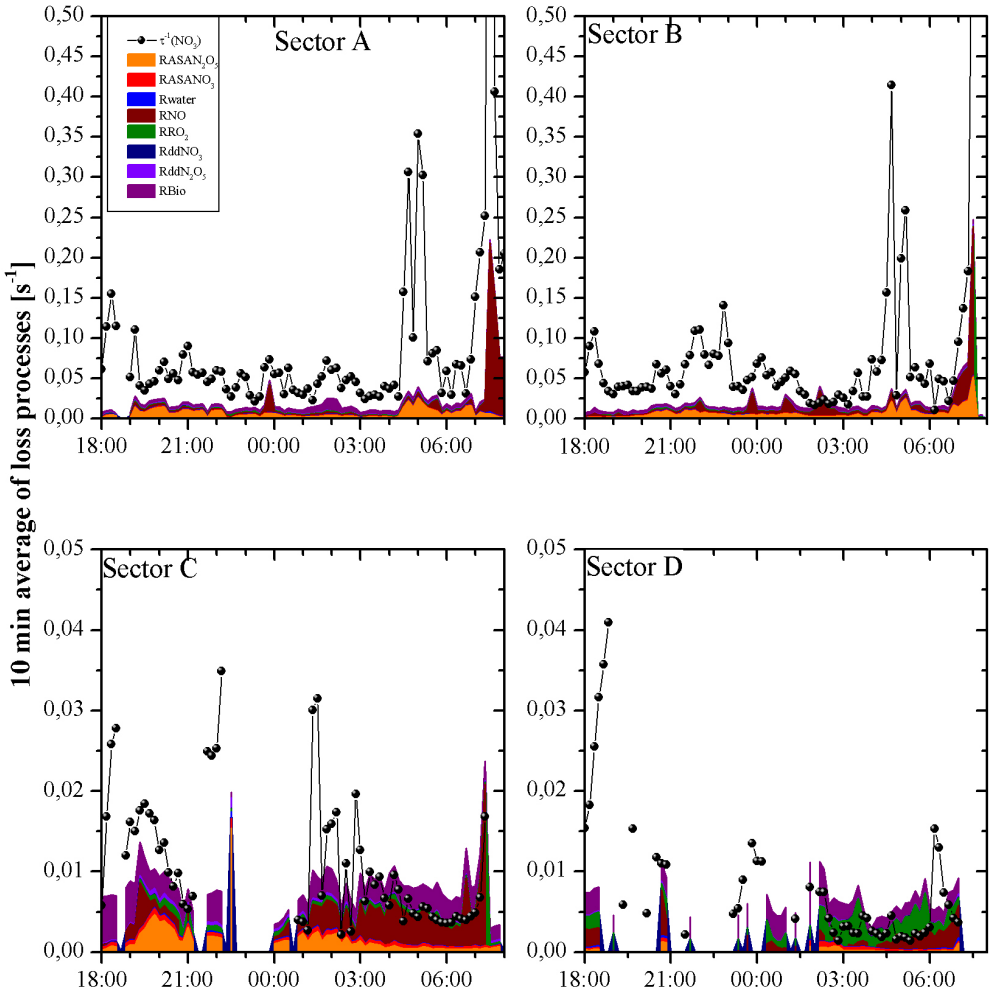

Figure 5.8.: *Averaged nocturnal profile of the inverse NO_3 lifetime compared with the calculated measured losses divided in four different wind sectors*

tries, e.g. Spain's largest pulp/paper mill and also the port of Huelva, could emit reactive species which were not directly measured at the site. In the nocturnal profile of sector B a similar behaviour to sector A is observed. The discrepancy between inverse lifetime and the measured loss processes is also significant but not as pronounced as in sector A. This also indicates that unmeasured trace gases react significantly with NO_3 in these air masses. Sector C and D have much longer NO_3 lifetimes which are broadly consistent with the measured loss processes.

5.5. NO_3 reactivity in different air masses

In the following, two days will be discussed more in detail to highlight the difference in NO_3 reactively air masses arriving at the measurement site. Therefore the nights from the 23.-24.11.2008 and 26.-27.11.2008 will be inspected more closely.

5.5.1. Sector A+B: 23-24 November (urban/industrial)

In this section an example for air masses reaching the site which are affected by the Continental and Huelva Sector (B and A) will be discussed. On this night the measurements of N_2O_5 started at 20:00 UTC, about 2.5 h after sunset. The complete dataset, with meteorological parameters and trace gases and particle properties is displayed in Figure 5.9. During the first half of the night (until midnight) the dominant wind direction was the north (continental) direction. For the rest of the night the air masses travelled over the Huelva sector before reaching the measurement site. Following a sunny, cloud free day, the night of the 23-24 November was characterized by low wind speeds and a strong temperature inversion (temperature at 50 m was about $7°C$ higher than at the inlet height), implying a highly stratified nocturnal boundary layer. Back trajectories (Figure 5.10) suggest that the air had travelled over the Atlantic before spending one day over central Spain with the last 6-12 h within the boundary layer.

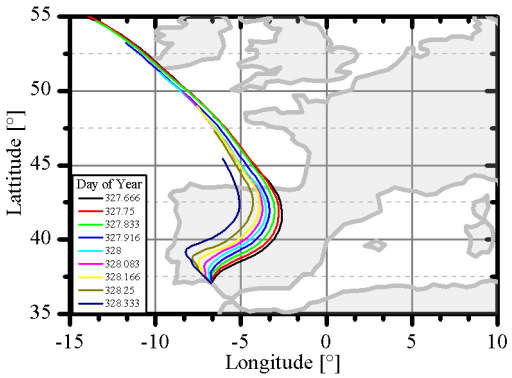

Fig. 5.10.: *48 h Back trajectories calculated every hours using the Hysplit model.*

During this night the NO_2 levels showed a large variability with mixing ratios from 1 to 13 ppbv, whereas the NO levels were always close to zero ($< 2pptv$) until about 04:30 when a few pptv were observed. This night was impacted by several plume - like NO_2 features. These were accompanied by plumes of similar duration in SO_2 (up to about 3 ppbv), HCHO (up to about 1.5 ppbv) and increases in the overall aerosol surface area, implying common, likely combustion related sources. This is especially apparent in two plumes (midnight and 05:00). There are several other NO_2 plumes which are not correlated with SO_2, HCHO or aerosol surface area. With these NO_2 plumes at about 20:00, 21:30 and 23:00 a significant increase in the N_2O_5 mixing ratios were observed, caused by an increase in the NO_3 production rate. In contrast, N_2O_5 remains close to the detection limit for the entire NO_2 plume at midnight and reaches only low N_2O_5 values during the second NO_2 plume

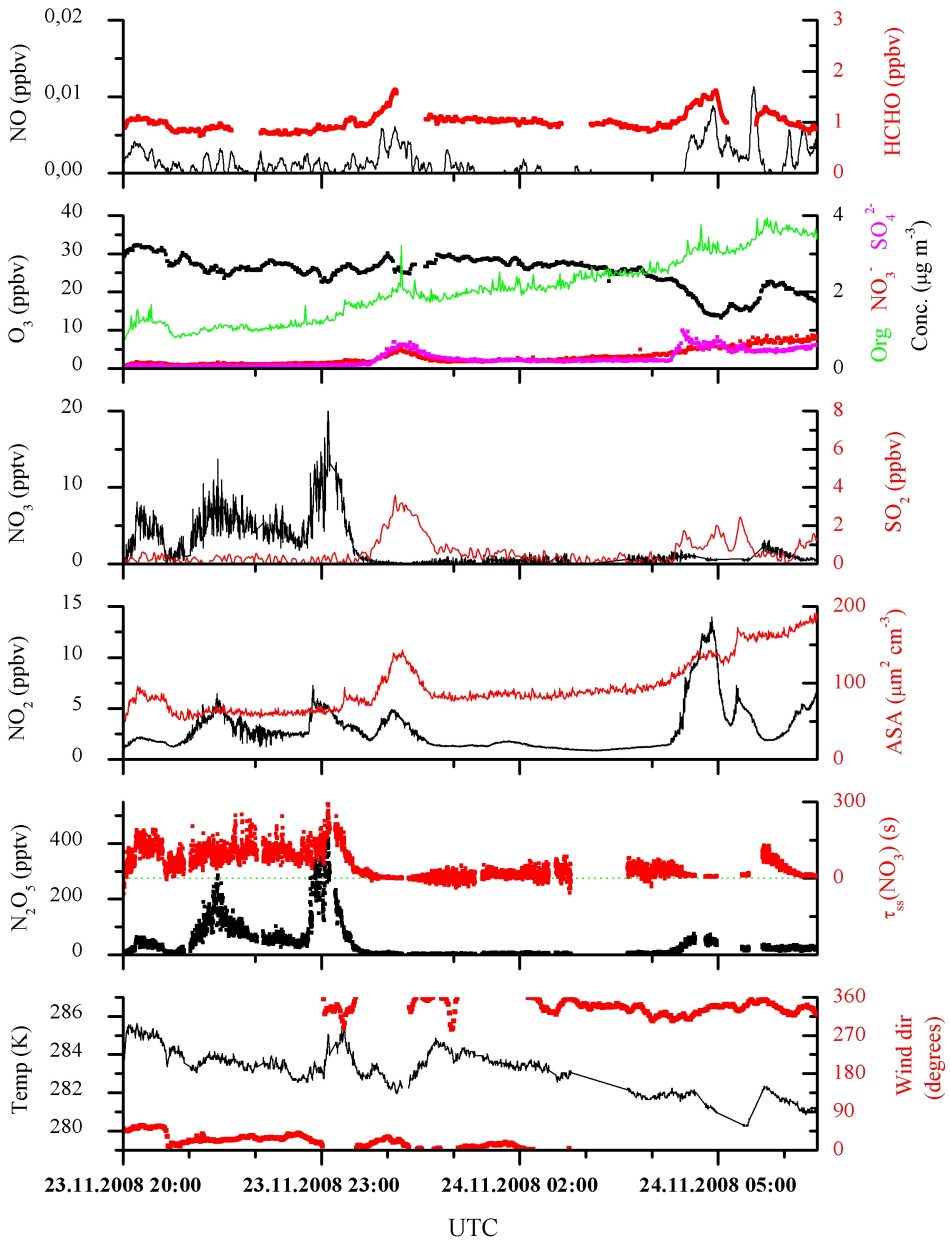

Figure 5.9.: *Overview of measurements on the night 23rd - 24th in which the wind direction swung form the continental to the Huelva sector*

at 05:00. The NO_2 plume at 23:00 (when SO_2 was close to zero) was accompanied by a positive gradient in the temperature (T(25m) - T (10m) gets smaller during this plume), whereas the NO_2/SO_2 plume at midnight shows a negative gradient in the temperature. Similarly the NO_2/SO_2 plume after 04:00 were accompanied by drops in temperature. The NO_2/SO_2 were also accompanied by an increase in the aerosol surface area, caused by an increase in mainly the sulphate and nitrate content, but also the organic fraction of the aerosol.

The production rate of NO_3 (N_2O_5) in the first part of the night (prior to midnight) was relatively high (up to 0.12 $pptvs^{-1}$) due to NO_2 mixing ratios between 1 and 6 ppbv and ozone levels greater than 25 ppbv. The N_2O_5 mixing ratios reached the highest measured values during the entire campaign in this night (up to 500 pptv). The high NO_2 levels and the moderately cold temperatures (283 K) meant that N_2O_5 was usually in greater than tenfold excess of the calculated NO_3 mixing ratio, and up to a factor of 50 greater than at the peak of the NO_2 plumes.
The NO_3 lifetime was fairly constant prior midnight with lifetimes of about 75-150 s but was essentially zero for the NO_2/SO_2 plume period between midnight and 01:00. During this night several the presence of malodorous gases at the site was reported.
Figure 5.11 displays the dependence of the NO_3 lifetime on the NO_2, SO_2 mixing ratio and the aerosol surface area (ASA). The shortest lifetimes are clearly associated with large NO_2 concentrations (upper panel in Figure 5.11). High values of SO_2 (greater 1 ppbv) were also associated with very short NO_3 lifetimes (middle panel of Figure 5.11). Also a weak anti - correlation of the lifetime with the measured aerosol surface area is visible. The observed NO_2 and aerosol surface area

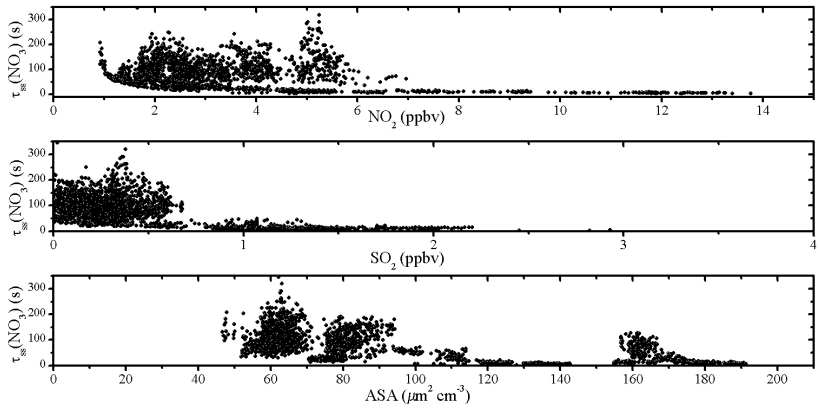

Figure 5.11.: *Dependence of $\tau_{ss}(NO_3)$ on NO_2 and SO_2 mixing ratios and the aerosol surface area (ASA).*

dependence on the NO_3 lifetime would seem to indicate that heterogeneous loss of N_2O_5 is important.

5.5.1.1. Heterogeneous loss of NO_3 and N_2O_5

The aerosol surface area available for interaction of aerosol with N_2O_5 and NO_3 was in the range of 45 to 190 $\mu m^2/cm^3$ and significantly larger in this night than the first night of this discussion (a factor of 2 - 3). The high NO_2 mixing ratios during the night and also the moderately low temperatures favours the production of N_2O_5 compared to NO_3, so that heterogeneous losses would be expected to be

more important for N_2O_5 than for NO_3. The aerosols during this night contained a very high fraction of organic component (up to 85 % of the aerosol mass (see Figure 5.12) with an organic to sulphate ratio of about 15 until midnight and lower values for the rest of the night but also larger than 3. The sulphate to (sulphate + nitrate) ratio was generally low (between 0.3-0.7).

This would suggest that the $\gamma(N_2O_5)$ on these particles would be expected to be

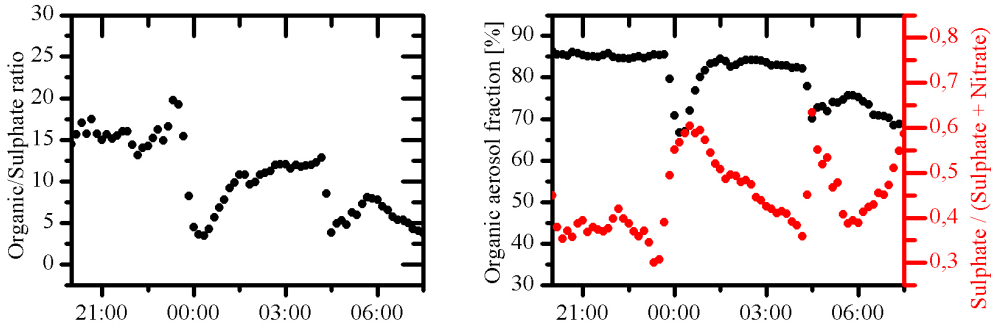

Figure 5.12.: *Overview of the aerosol content for the night of the 23rd to 24th November. The left plots shows the organic to sulfate ratio. The plot on the right site showed the organic fraction of the aerosol (left y-axis) and the sulphate to sulphate + nitrate ratio (right y-axis)*

less than 0.04. The uptake coefficient for NO_3 is poorly defined but potentially a factor of 10 larger (Tang et al. (2010)). An absolute upper limit to the sum of direct and indirect NO_3 loss rates via heterogeneous uptake to aerosol was thus calculated using uptake coefficients of 0.04 for NO_3 and 0.5 for NO_3, the later representing diffusion limited uptake. This provides an estimate of the maximum contribution of heterogeneous reactions on aerosols to NO_3 lifetime.

Figure 5.13 provides an overview of the relative importance of the constrained, direct and indirect loss processes for NO_3 on this night. Even though the uptake coefficients employed were upper limits, the calculated loss of N_2O_5 ($RASAN_2O_5$ in Figure 5.13) and NO_3 ($RASANO_3$) to aerosols does not account for the observed NO_3 loss frequency (black dots) before 23:30 on the 23rd. Despite the much larger uptake coefficient used for NO_3, its contribution to the total heterogeneous loss was similar to that of N_2O_5 as the NO_3-N_2O_5 partioning was shifted towards N_2O_5 on this night with high NO_2 mixing ratios.

When the first NO_2/SO_2 plume arrives on this night the NO_3 lifetime was drastically shortened and heterogeneous processes contribute an upper limit of about 10 % to the overall measured loss frequency of NO_3 ($RASAN_2O_5$ + $RASANO_3$). Similarly, the summed effect of dry deposition of NO_3 and N_2O_5 (using the dry deposition rates listed above) can be disregarded as a major loss of either NO_3 ($RddNO_3$) or N_2O_5 ($RddN_2O_5$).

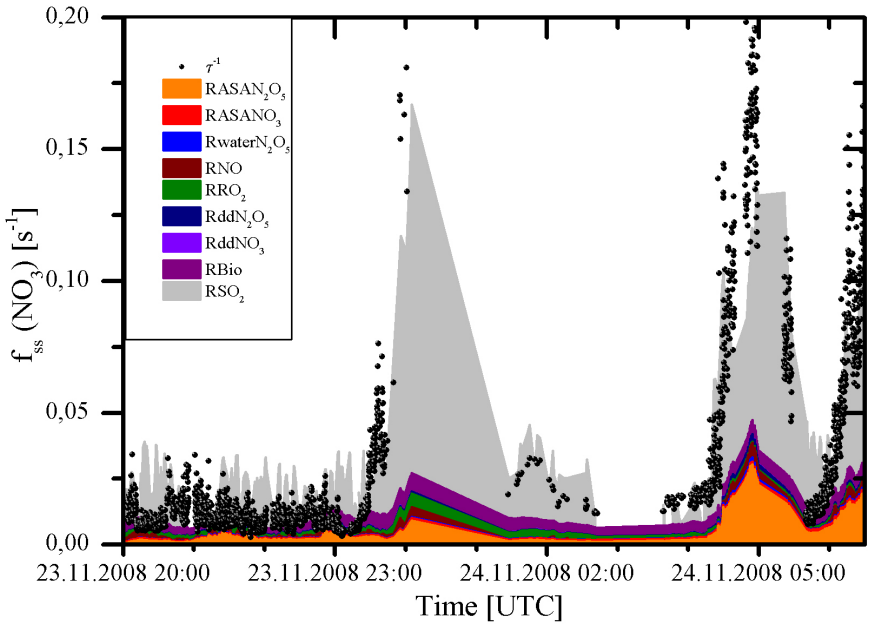

Figure 5.13.: *Apportioned NO_3 loss rates on the night 23-24 November. The various contribution are: $RASAN_2O_5$ = uptake of N_2O_5 to aerosol, $RASANO_3$ = reaction of NO_3 to aerosol, $RwaterN_2O_5$ = homogeneous hydrolysis of N_2O_5 with water, RNO = reaction of NO_3 with NO, RRO_2 = reaction of NO_3 with RO_2, $RddNO_3$ and $RddN_2O_5$ = Dry deposition of NO_3 and N_2O_5, RBio = reaction of NO_3 with isoprene, limonene and α - pinene, RSO_2 is the missing reactivity which has been scaled to correlate with SO_2 mixing ratios. The black dots are the calculated loss frequency of NO_3.*

5.5.1.2. Gas-phase reaction of NO_3 and N_2O_5

From the measured reactive gas-phase species towards NO_3 at the beginning of the night (until 23:00) the reaction with the BVOC was the dominant loss process. The homogeneous hydrolysis of N_2O_5 is again not an important loss process in this air mass, contributing less than 1% to the NO_3 reactivity (see $RwaterN_2O_5$ in Figure 5.13). The NO levels during most of the night were close to zero therefore no significant impact of these reactions to the total losses (RNO in Figure 5.13). Until 23:00 the calculated inverse lifetime of NO_3 can be described by the measured loss processes. But in this night the inverse lifetime was drastically shortened during two large SO_2 plumes. Also in this night, unusually high nighttime values of peroxy radicals (RO_2) were measured (up to 80 pptv). RO_2 (formed e.g. from NO_3 initiated oxidation of CH_3SCH_3 or ozonolysis of BVOC) has been shown to contribute to NO_3 loss (Sommariva et al. (2009)). This high RO_2 values were measured between midnight and 04:00 (Andrés-Hernández et al. (2012)). In the absence of speciated RO_2 measurements a loss rate of NO_3 due to reaction with RO_2 was calculated assuming a rate coefficient of $2.3 \times 10^{-12} \frac{cm^3}{molecule\ s}$ taken from

evaluated kinetic data (Atkinson et al. (2006)). Further measured trace gases which can react with NO_3 are HCHO and aromatics. The rate coefficients of these trace gases are relatively low compared to the rate coefficient of NO, isoprene, limonene and α - pinene (see Table 5.1) and also their concentrations are low. They do not significantly contribute to the total loss of NO_3.
Clearly, the sum of constrained indirect and direct losses of NO_3 does not explain the short lifetimes observed during the SO_2 plumes (see Figure 5.13). The heterogeneous losses cannot contribute more to the total loss, since for the calculation of their losses the upper limits for the uptake coefficients $\gamma(NO_3)$ and $\gamma(N_2O_5)$ were used. Therefore other trace gas reaction which were not constrained by measurements at the site might be responsible for these short NO_3 lifetimes during the SO_2 plumes.

5.5.1.3. Unknown or undetermined reactions/loss processes

During this night two significant plumes of SO_2 were measured at the site (see Figure 5.9). During these periods the extremely short lifetimes of NO_3 cannot be explained by the measured loss processes. A clue to the missing reactivity may be provided by the very short NO_3 lifetimes (or absence of N_2O_5) when SO_2 was present at levels above 1 ppbv (Figure 5.9 and 5.11 (middle panel)).
Whilst SO_2 itself does not react with NO_3 directly, it may be co-emitted or co-located with emissions of more reactive traces gases. Two scenarios are considered below in which reduced sulphur species or unsaturated VOCs are responsible for the short NO_3 lifetimes during the SO_2 plumes.

Reduced sulphur species
Especially in this night but also in some other nights strongly malodorous air was present at the site. Malodorous, reduced sulphur compounds (RSC) are often associated with oil refining, pulp/paper mill and waste treatment activities (Nunes et al. (2005), Toda et al. (2010), Pal et al. (2009)). Note that Spain's largest pulp/paper mill is located in Huelva. RSC with high reactivity to NO_3 are CH_3SCH_3 (dimethyl sulphide,DMS), CH_3SSCH_3 (dimethyl disulphide, DMDS) and CH_3SH (methanethiol). The lifetime of NO_3 can be strongly influenced by the reaction with DMS in marine air masses (Allan et al. (2000), Aldener et al. (2006), Sommariva et al. (2009)) but a large contribution to NO_3 loss in urban air masses has also been reported (Shon and Kim (2006)). The oxidation of RSC by NO_3 results in formation of SO_2, HCHO and RO_2 (Jensen et al. (1992a), Jensen et al. (1992b)) with (modelled) RO_2 levels often exceeding those observed during daylight (Sommariva et al. (2009)). The reaction of DMS, DMDS and CH_3SH with NO_3 are similarly fast with rate coefficients close to $1 \times 10^{-12} \frac{cm^3}{molecule\ s}$, so that a total mixing ratio of these RSC of about 4 ppbv would provide an equivalent

reactivity of $0.1s^{-1}$. Unfortunately no RSC measurements were available during the campaign to support their potential role, but ppbv mixing ratios of RSC are not unrealistic as RSC emitted into a shallow, highly stratified boundary layer at night have no gas - phase loss mechanism apart from the reaction with NO_3.
In order to capture the NO_3 lifetime dependency on SO_2, a reactive term, considering the presence of a reactive trace gas at a constant fraction of the SO_2 mixing ratio and reacting with NO_3 with a rate constant of about $1 \times 10^{-12} \frac{cm^3}{molecule\ s}$ (i.e. like RSC) was added to Equation (5.11). In Figure 5.13 this additional loss is showed in grey (RSO2). The RSC to SO_2 ratio was adjusted (about a factor of 2) to approximately capture the large NO_3 loss rate at midnight, bringing the measured and modelled steady state lifetime in rough agreement.
As also seen in Figure 5.11 (upper panel) the NO_3 lifetime in this night is also anti correlated with the NO_2 mixing ratios. During this night NO_2 plumes were present when SO_2 plumes were also present. Interaction between NO_x and reduce sulphur provide an interesting but highly speculative explanation for some of the observations on this and other nights during the campaign, including short NO_3 lifetimes, high RO_2 levels and formation of HCHO and SO_2, though the simultaneous plume like increase in SO_2 and HCHO.

Unsaturated VOCs
In this second scenario it is considered that the plumes of SO_2, NO_2 and HCHO are formed in a common combustion source, either related to ship or oil-refinery activity. During this night the wind direction changed slowly from the continental sector to the Huelva sector with the plumes of NO_2 reflecting emissions from various point sources in the Huelva region. The short NO_3 lifetimes after midnight reflect highly reactive air masses towards NO_3 reaching the site from the Huelva sector. Hydrocarbon emissions related to the petrochemical industry, include unsaturated VOC such as 1,3 butadiene (Roberts et al. (2003)) which are reactive to NO_3 could be responsible for the short NO_3 lifetimes. In this case the source of the observed peroxy radicals in this night would be reaction of unsaturated hydrocarbons with either NO_3 or O_3. The reaction of NO_3 with unsaturated, petrochemical-related hydrocarbons is at least a factor of 10 slower (e.g. the rate coefficient for NO_3 with 1,3 butadiene is $1 \times 10^{-13} \frac{cm^3}{molecule\ s}$) than with RSC so that mixing ratios of several tens of ppbv of the alkene would be necessary to explain the short NO_3 lifetimes. In summary, air masses reaching the site from the Huelva region were typically highly reactive towards NO_3 resulting in very short lifetimes which were controlled by gas-phase reactions and a diminished role for heterogeneous processes (either for NO_3 or N_2O_5). Whilst RSC and unsaturated hydrocarbons were proposed as potential reaction partners for NO_3 they were not constrained by measurements and for longer periods of these night (especially when SO_2 was observable) much of the reactivity is not accounted for.

5.5.2. Sector B+C: 26-27 December (Continental/Rural)

During this night the local wind directions indicated air masses originating from continental Spain partly avoiding large local cities and industrial centres especially in the first half of the night. Back trajectories suggest that the air masses during this night had spent the last two days over central Spain and France before reaching the site. In the second part of the night the trajectories also indicating that the air masses travelled over Seville before reaching the site (see Figure 5.14).

The 48 h trajectories also suggests that the air masses has spent only the last 4-6 hours in the lower part of the boundary layer (lower than 500 m) whereas the starting points of these trajectories were located at 2500 to 3500 m. The wind speeds during this night were between 2.5 *and* $5\frac{m}{s}$ which would lead to about 5-10 hours transport time for air masses from Seville. A general overview of the measured parameters is shown in Figure 5.15. During this night the NO_2 levels were quite low with less than 2 ppbv most of the night except from a plume-like increase (up to 4 ppbv) at the beginning of the night (20:00). Beside the low NO_2 levels, NO mixing ratios were close to the detection limit (2pptv) during the whole night except from some spikes due to very local emissions (most likely vehicular). The constancy of the NO values strongly suggests that the true value of the measurements during this night is zero and the 2 pptv is a residual from zero correction of the instrument. The O_3 mixing ratios were also quite constant at about 25 to 30 ppbv. Biogenic emissions were about 10 pptv during this night as also on other nights of the campaign.

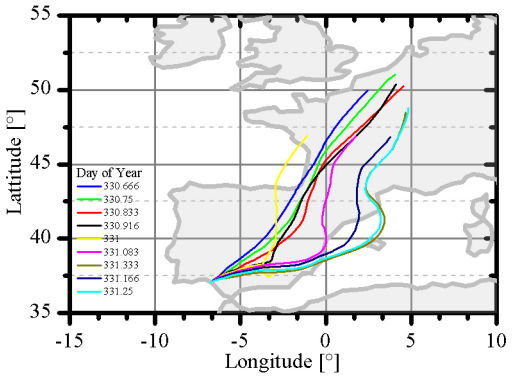

Fig. 5.14.: *48 h back trajectories for the night 26th to 27th of November calculated with the Hysplit model*

The temperature during this night was between 279 K and 281 K, with short-term fluctuations in temperature occurring in both directions. This might be an indicator for air masses from higher altitudes being sampled occasionally during this night and will be discussed later.

N_2O_5 could be measured above the detection limit at almost all times during this night, in a range of 7 to 100 pptv. The calculated NO_3 mixing ratios reached up to 12 pptv during this night with maximum steady state lifetimes of about 900s. Intermediate to those observed for the Huelva and Marine sector.

Figure 5.16 shows correlation plots of the steady state lifetime of NO_3 with NO_2, aerosol surface area (ASA) and wind direction. Also the correlation of NO_2 with

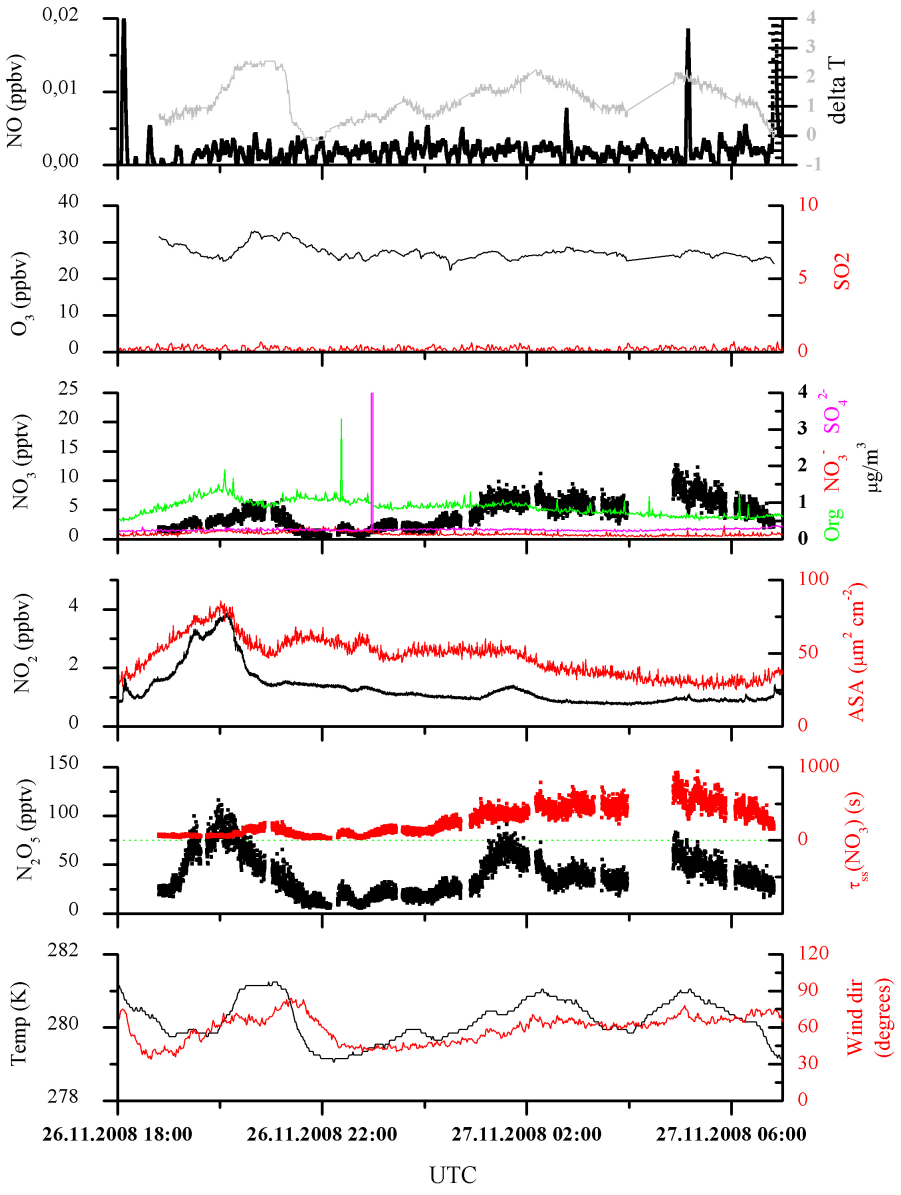

Figure 5.15.: *Overview of measurements on the night 26-27 November*

the aerosol surface area (ASA) is shown.
The steady state lifetime is anti correlated with NO_3 and with the aerosol surface area (ASA) which normally suggest a dominant loss via the indirect loss path way. The correlation between the lifetime and the wind direction especially for the second half of the night (see colour coding in Figure 4 right down panel) is quite

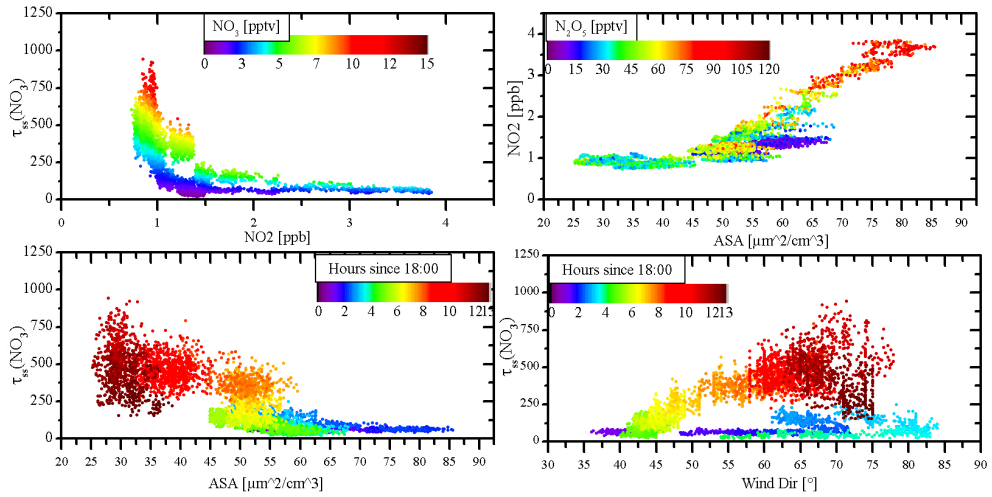

Figure 5.16.: *26-27 November: Dependency of $\tau_{ss}(NO_3)$ on NO_2, the aerosol surface area (ASA) and the wind direction. Additionally the dependency of NO_2 on the aerosol surface area is shown.*

interesting due to the fact that from about midnight the local wind direction is changing more to the east. Compared to the beginning of the night, where the local wind direction was also partly dominated by easterly winds, only short lifetimes were measured. This indicates that the air mass origin or at least the air mass transport between the first and the second half of the night is different which is also shown in Figure 5.14. In the first half of the night the trajectories suggest that the air masses travelled completely over central Spain whereas in the second half of the night the air masses reaching the site from the east with a few hours spent over the Mediterranean Sea.

Figure 5.17 shows the comparison of the inverse steady state lifetime (black dots) with the measured loss processes for NO_3 for that night. In general this night was clearly divided in two parts where not only the lifetimes of NO_3 were different also the composition of the measured loss rates was different.

5.5.2.1. Heterogeneous loss of NO_3 and N_2O_5

The available aerosol surface area for interaction during this night was between 25 and 80 $\mu m^2/cm^3$ and was correlated with NO_2 (see Figure 5.16). The moderately low NO_2 mixing ratios and the cold temperatures favours the production of N_2O_5 compared to NO_3, so that heterogeneous losses might be expected to be important. Also the anti-correlation of the steady state lifetime with NO_2 and the aerosol surface area support this.
The aerosol during this night was acidic with a dominant organic fraction of about 70 % during the whole night (see Figure 5.18). The organic to sulphate ratio was

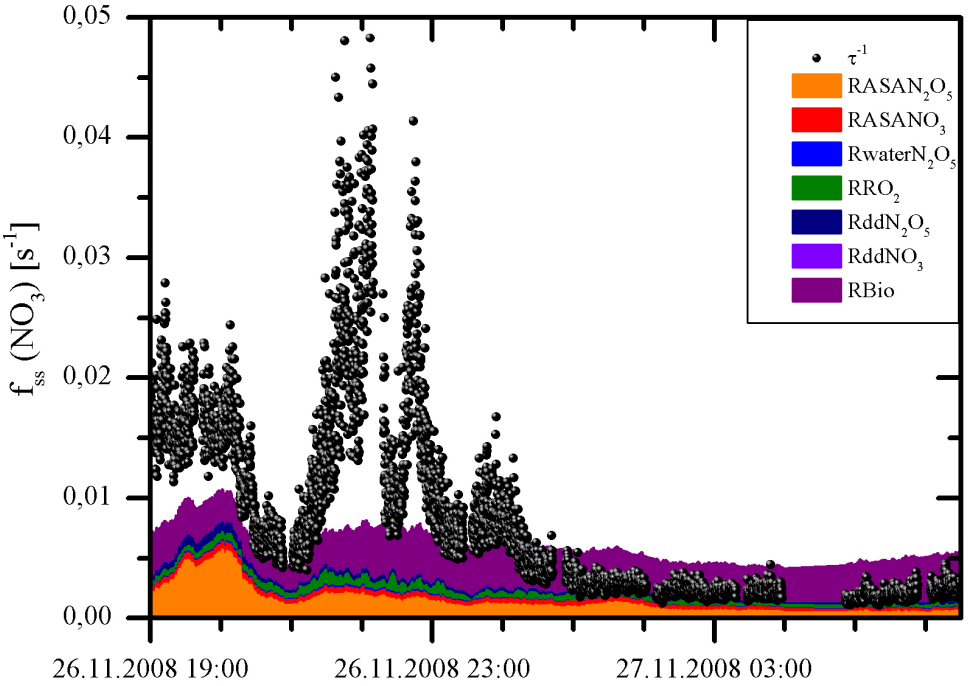

Figure 5.17.: *Apportioned NO_3 loss rates on the night 26-27 November. The various contribution are: $RASAN_2O_5$ = uptake of N_2O_5 to aerosol (using γ = 0.04), $RASANO_3$ = uptake of NO_3 to aerosol (using γ = 0.1), $RwaterN_2O_5$ = homogeneous hydrolysis of N_2O_5 with water, RRO_2 = reaction of NO_3 with RO_2, $RddNO_3$ and $RddN_2O_5$ = Dry deposition of NO_3 and N_2O_5, RBio = reaction of NO_3 with isoprene, limonene and α - pinene. The black dots are the calculated loss frequency of NO_3.*

between 2 and 4 beginning with a higher organic to sulphate ratio at the beginning of the night and decreasing to a value of two at the end of the night. The sulphate to (sulphate + nitrate) ratio was between 0.5 and 0.7 as shown in Figure 5.18. This implies a more likely value of γ (N_2O_5) of about 0.01 (Riemer et al. (2009)).

In the first half of the night the indirect losses reflects at least 50 % (until 21:00 to 22:00) of the measured losses whereas in the second part of the night they become less important compared to the other measured losses ($RASAN_2O_5$ in Figure 5.17). Despite of the large percentage of the indirect losses of the total measured loss frequency the measured total loss cannot explain the short lifetime at the beginning of the night. The lifetimes in the first half of the night (until midnight) were much shorter and highly variable with loss rates up to 0.05 s^{-1} (lifetime of just 200s) compared to the second half of the night were the lifetimes were very constant with small loss rates down to 0.0011 s^{-1} (lifetime of up to 900s).

It is barely conceivable that the increase in the NO_3 loss frequency is due to a change in reactivity of the aerosol toward either N_2O_5 or NO_3. Neither the aerosol

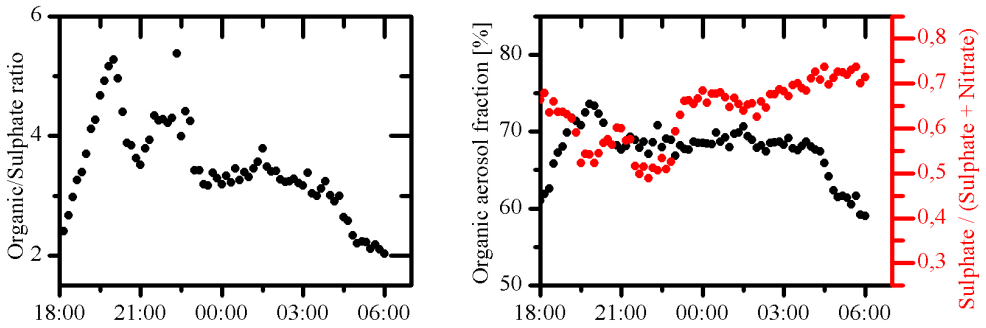

Figure 5.18.: *verview of the aerosol content for the night of the 26-27 November. The left plots shows the organic to sulfate ratio. The plot on the right site showed the organic fraction of the aerosol (left y-axis) and the sulphate to sulphate + nitrate ratio (right y-axis)*

composition (i.e. the organic, nitrate and sulphate fraction see Figure 3) nor the relative humidity changed significantly during the night so a large change in γ is not anticipated. Also the variability in the loss frequency cannot be explained by changes in the aerosol surface area.

5.5.2.2. Gas-phase loss of NO_3 and N_2O_5

In the first hours of the night the calculated loss frequency due to gas-phase reaction using the measured trace gases was similar to that of the indirect losses. Again the homogeneous hydrolysis of N_2O_5 is unimportant compared to the other gas phase losses. The reaction with NO is assumed to be zero. A small fraction of the total loss frequency is due to the reaction with RO_2 (RRO_2 in Figure 5.17).The main fraction of the gas-phase losses is again the reaction with the BVOC (isoprene + limonene + α - pinene) (RBio in Figure 5.17). The fraction of the gas-phase losses compared to the heterogeneous losses increases over the night and reaches about 80% at the end of the night.
The discrepancy between measured loss frequency and the short lifetimes cannot be explained by missing gas-phase reaction related to the presence of SO_2 as described for the night of the 23rd to 24th of November. During this night the SO_2 levels was under the detection limit of the instrument. Also other gas-phase reactions which were measured can be ruled out for contributors to the missing reactivity.

5.5.2.3. Possible explanation for the different behaviour

A possible explanation for the high variability could be associated with fluctuations in rates of vertical mixing within a highly stratified nocturnal boundary layer. The upper panel of Figure 5.19 shows a temperature difference (actual temperature - minimum temperature of the night). This temperature difference was also highly

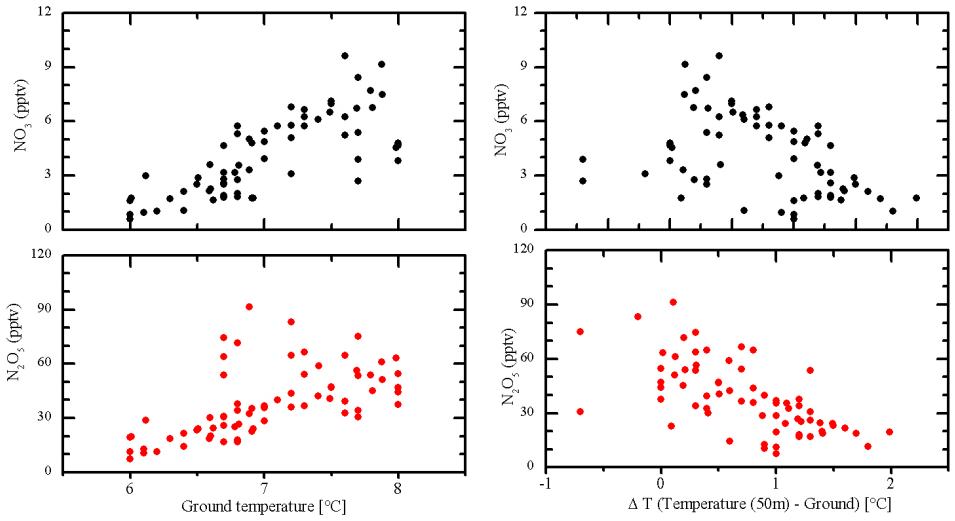

Figure 5.19.: *Temperature dependence of the N_2O_5 and NO_3 concentrations. The left shows the correlation between ground temperature and NO_3/N_2O_5 mixing ratios. Right shows the anti correlation of both species against temperature difference of 50m and ground level*

variable during the night with differences up to 4 °C.
Figure 5.19 shows a significant correlation of NO_3 and N_2O_5 mixing ratios with the ground level temperature (left site of the figure). The right side of the Figure, in which a clear anti correlation between the NO_3 and N_2O_5 mixing ratios and the temperature difference of the measured temperature in 50 m height and the ground level temperature is shown, is supporting the hypotheses that warmer air masses from higher altitude occasionally reach the measurement site. This suggests that the NO_3 and N_2O_5 mixing ratios at higher altitudes are much higher than at ground level. This hypothesis will be discussed more in detail in the section (5.8).

5.6. Overview of NO_3 reactivity

During the Domino 2008 campaign, N_2O_5 was measured via CRD in late autumn in Southern Spain. NO_3 could be calculated from the equilibrium between NO_3 and NO_3, and the steady state lifetime of NO_3 was calculated. All were highly variable and showed stark differences according to the air masses encountered. The longest lifetimes of about 30 min were encountered with air masses coming from the Atlantic Ocean whereas only very short lifetimes were encountered with air masses from the Huelva urban (petrochemical and industrial) sector. Figure 5.20 shows a summary of the median nocturnal lifetimes and the measured loss frequency day by day on the left hand site and depending on the different wind sectors on the right hand site of the Figure including median values of the entire campaign. During

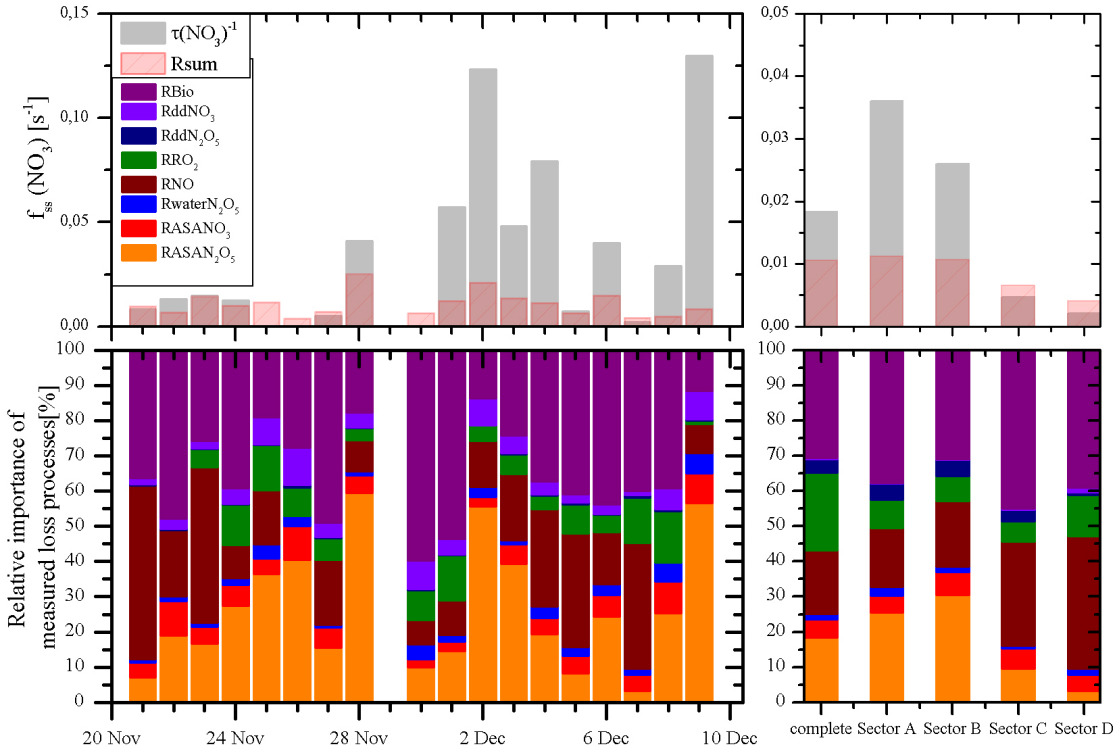

Figure 5.20.: *Overview of the nocturnal median lifetimes and loss processes with their different portioning to the entire measured losses (left site) and a comparison of the entire campaign median values with the median values for the different sectors. Appendix B.3 the nocturnal profiles for each night.*

the first half of the campaign (21.11 - 28.11.2008) the calculated lifetimes of NO_3 could be approximately explained by the measured loss processes despite from the 28th of November. During that period the loss processes due to the reactions with biogenics and NO dominate. For the 28th of November the heterogeneous reactions of N_2O_5 with aerosols are the dominating ones. The losses for NO_3 due to the direct uptake of NO_3 and the indirect uptake of N_2O_5 to aerosol were both calculated with upper limits for γ. Therefore, the fraction due to uptake losses might be in general smaller. The lifetimes in the first half of the campaign were much longer than in the second half except from the night with air masses coming from the Atlantic Ocean. In the second half of the campaign (30.11 - 9.12.2008) the lifetimes were much shorter and could not be explained by the measured trace gases which contribute to NO_3 losses. Averaged over the entire campaign, the heterogeneous losses could contribute with 30-35 % to the complete measured loss processes. For the sectors C and D the contribution of the heterogeneous losses was less than 20 %.
The short averaged lifetimes for the entire campaign (about 1 min) could only

be explained by about 50 % for the measured loss frequencies. Compared to this for the Huelva Sector (A) the median lifetime was calculated to be only about 30 sec and only about a third could be explained by the measured species. For the more continental Sector (B) the median lifetime was about 40 sec and in this case about 40 % of this lifetime could be explained by the measured losses. For the sectors C (Seville) and D (Atlantic Ocean) much longer lifetimes were observed. For the Seville sector a median lifetime of about 210 s was observed which could be explained by the constrained measurements. Also for the sector D the long lifetimes (mean: ca. 370 s) could be explained by the measurements. In both sectors the overestimated loss rate might be an indication that the measured NO - or VOC levels might be too large or the estimated γ values are too large. The relationship between the NO_3 lifetime, SO_2, NO_2 and aerosol surface area over the course of the entire campaign is shown in Figure 5.21. The relationship between the lifetime and these species clearly indicates that polluted air masses (NO_2 or SO_2 larger than 2 ppbv) do not support long NO_3 lifetimes.

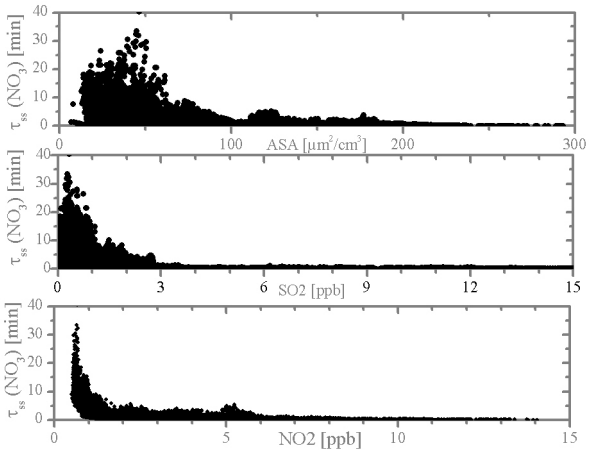

Fig. 5.21.: *Relationship between NO_3 lifetimes, $\tau_{ss}(NO_3)$ and the mixing ratios of NO_2, SO_2 and aerosol surface area (ASA) during the entire campaign.*

As mentioned in section 5.5.1 where the very short NO_3 lifetimes were observed at high SO_2 mixing ratios the median SO_2 levels were different for the different sectors. In Sector A the median SO_2 mixing ratios were in the order of 2-3 ppbv. For the continental sector B the SO_2 levels were also elevated (about 1 ppbv) but not as high as for sector A. For the two remaining sectors C and D the SO_2 levels are very low in the order of the detection limit of the instrument (less than 0.5 ppbv).

This relationship also indicates that the very high reactivity of the air masses towards NO_3 from the Sectors A and B is due to reaction with RSC or due to common or co - located emissions (e.g. combustion) source of other reactive trace gases.

5.7. Comparison of the Oxidation capacity of NO_3, OH and O_3

Since simultaneous measurements of NO_3, OH and O_3 were available during the campaign, it was possible to calculate the ground level oxidation capacity for each radical and to compare the results. This study was limited to the measured VOCs (see also Table 5.1) and methane. CO which is also an important reaction partner for OH was not measured during the campaign.
The oxidation capacity of a radical X (=NO_3, OH, O_3) was calculated as the sum of organic traces gases Y_i getting oxidized by the radical:

$$OC = \sum_{i=1} k_{Y_i - X}[Y_i][X] \tag{5.14}$$

To calculate a 24h-integral of the oxidation capacity of NO_3, daytime levels were calculated using the known production rate of NO_3 and the two major sinks during daytime. The reaction of NO_3 with NO is a very fast reaction and beside the photo

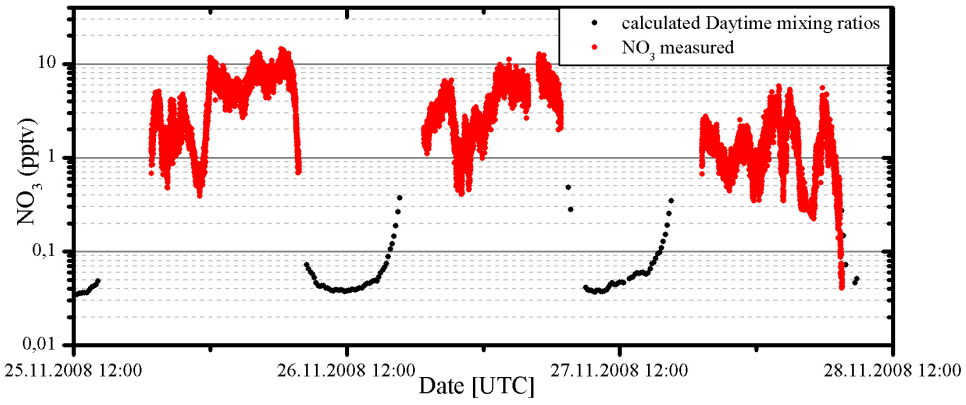

Figure 5.22.: *Extract of the time series of calculated daytime NO_3 levels including the measured NO_3 levels during night,*

dissociation the most important sink term during daytime. To calculate the loss due to the dissociation, JNO_3 values were calculated from the measured JNO_2 values and scaled with the TUV model [1]. The degradation of NO_3 due to other losses can be neglected during daytime. Figure 5.22 is an extract of the time series with measured NO_3 during nighttime and calculated NO_3 day time levels shown. A mean calculated daytime concentration of NO_3 ($JNO_3 > 5 \times 10^{-4} s^{-1}$) was about 0.1 pptv. For the oxidation capacity of OH only daytime values can be calculated due to the fact that only daytime OH measurements are available. The nighttime oxidation capacity of NO_3 varied from $3.5 - 32 \times 10^4$ *molec* $cm^{-3} s^{-1}$

[1] TUV = Tropospheric Ultraviolet & Visible Model

(average of one night) with a mean value during the entire campaign of 1.96×10^5 $molec\ cm^{-3}s^{-1}$. For the daytime NO_3 oxidation capacity a mean value of 0.4×10^4 $molec\ cm^{-3}s^{-1}$ was calculated. This results in a mean 24h oxidation capacity of NO_3 of $1.16 \times 10^5 molec\ cm^{-3}s^{-1}$. The uncertainty of this average value which is calculated from the error of the NO_3 measurements (about 15% accuracy) and the error of the rate constants for each reaction of NO_3 with the different VOCs (e.g. $\Delta k_{NO_3+limonene} \approx 35\%$) is about 35% corresponding to about 4.0×10^4 $cm^{-3}s^{-1}$.
Ozone was responsible for the depletion (on average) of 4.3×10^4 $cm^{-3}s^{-1}$ with a maximum oxidation capacity of $6.8 \times 10^4 cm^{-3}s^{-1}$ on one day. The influence of the reaction of NO_3 and O_3 with methane can be neglected. The mean oxidation capacity of OH was $3.5 \times 10^5 cm^{-3}s^{-1}$ during the campaign, at one day it reached a maximum value of 7.85×10^5 $cm^{-3}s^{-1}$. Figure 5.23 shows the comparison of the

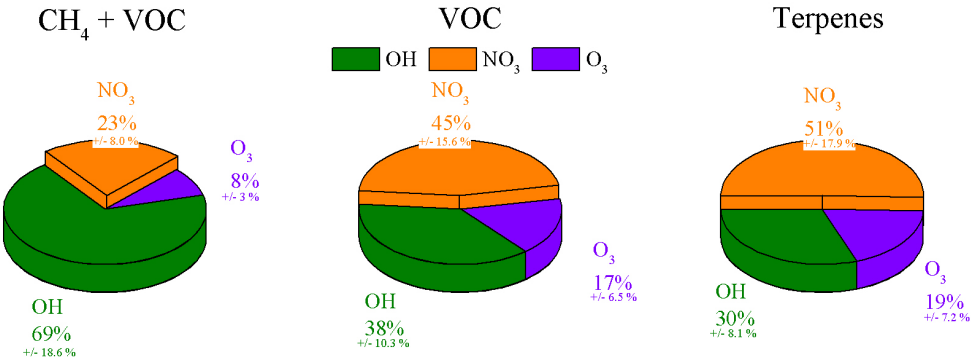

Figure 5.23.: *Comparison of the relative contribution of NO_3, OH and O_3 to the oxidation capacity. The oxidation capacity was calculated dor the oxidation of VOCs and methane (left), VOCs (middle) and terpenes (right).*

oxidation capacities of NO_3, OH and O_3. Since OH is the dominant oxidant agent for methane in the troposphere, OH was responsible for $69 \pm 18.6\%$ of the oxidation capacity regarding methane and VOCs (see left site of Figure 5.23). The oxidation capacity of OH decreased to about 0.95×10^5 $cm^{-3}s^{-1}$ with a relative contribution of $38 \pm 10.3\%$ when only the measured VOCs were used for the calculation (middle of Figure 5.23). Focusing only on the terpenes the oxidation capacity of the OH decreases further with a relative contribution of $30 \pm 8.1\%$ corresponding to 0.69×10^5 $cm^{-3}s^{-1}$ (right site of Figure 5.23). The relative contribution of NO_3 and O_3 to the oxidation of terpenes is $51 \pm 17.9\%$ and $19 \pm 7.2\%$ corresponding to 1.2×10^5 $cm^{-3}s^{-1}$ and 4.3×10^4 $cm^{-3}s^{-1}$. The averaged oxidation capacity of NO_3 leads to a 24 h integral of 1.04×10^{10} molecules per cm^3 (≈ 0.4 ppb).
For this analysis only measured VOC could be taken into account. As the main loss processes for NO_3 were none of the measured compounds, in Sector A and B, the total oxidation capacity is clearly underestimated. The NO_3 mixing ratios which were used for this calculation could be reduced by e.g. reaction with RSC,

as speculated in section 5.5.1.3. But the calculated loss for reaction with RSC was not taken into account due to absence of RSC measurements. The rate constant of typical RSC (e.g. DMS or methanethiol) with respect to OH and NO_3 are in the same order of magnitude which favours the oxidation capacity for NO_3 due to the higher mixing ratios. Therefore, the distribution of the total oxidation capacity for the three different oxidant agent might be changed if more auxiliary measurements would be available.

5.8. Vertical gradients of NO_3

In recent years several measurements have shown that NO_3 mixing ratios are height dependent (Brown et al. (2007b); Stutz et al. (2004, 2009); von Friedeburg et al. (2002); Wang et al. (2006)). These measurements indicate that NO_3 measurements near the surface are not completely representative for the nocturnal boundary layer. For this reason, in addition to the ground based NO_3/N_2O_5 measurement, NO_3 was measured in horizontal and vertical extent via a LP-DOAS system. The measurements with the LP-DOAS instrument were performed by the University of Heidelberg. A short description of the instrument and the measurement site is given in section 4.1.4. In the following the ground based measurements and the LP-DOAS measurements will be compared and the differences will be discussed.

5.8.1. LP-DOAS measurements of NO_3 during DOMINO

The LP-DOAS measurements allow investigation of the vertical distribution of the nitrate radical and several other trace gases during the DOMINO campaign. Beside NO_3, NO_2 and O_3 were also measured with the LP-DOAS instrument and therefore the production rate for NO_3 can be determined as function of height (see equation (5.5)). In addition, the steady state lifetime of the nitrate radical can be determined via equation (5.10).
The rate constant to determine the production rate for NO_3 (k_1) and as well the equilibrium constant (k_{eq}) to calculate N_2O_5 from NO_3 and NO_2 or vice versa are temperature dependent. Therefore the temperature for the mean height of each layer was used to determine the rate constants. The temperatures of these heights could be estimated from a linear interpolation from three different temperature measurements at 25m, 50m and 100m.
An Overview of the measured and calculated LP-DOAS data are shown in Figure 5.24. The ground based data (averaged to 1 h data) are also shown for comparison. In most of the nights during the campaign a clear NO_3 gradient between the different layers could be observed. NO_3 mixing ratios varied from close to zero to about 50 pptv (for the highest layer). Gradients in O_3 could also be observed, whereas gradients in NO_2 were weak. In one part of the campaign (325-333 DoY (Day of Year)) a clear difference in ground based O_3 and LP-DOAS measured O_3 could be observed. During this period, not only a difference between ground-based and LP-DOAS measurements, but also a strong difference between the layers themselves was observed. Vertical gradients in O_3 were accompanied by strong vertical gradients in NO_3 and its lifetime on these nights, which might indicate a shallow nocturnal boundary layer.
In the second part of the campaign the NO_3 mixing ratios were on average smaller than in the first part and also the vertical gradients were less pronounced. In this period only on one night could NO_3 mixing ratios greater than 30 pptv be observed

in the highest layer.
The gradient in O_3 was less obvious and the differences between the ground based O_3 data and the LP-DOAS measurements were much less than during the first period of the campaign. The calculated steady state lifetime of the nitrate radical

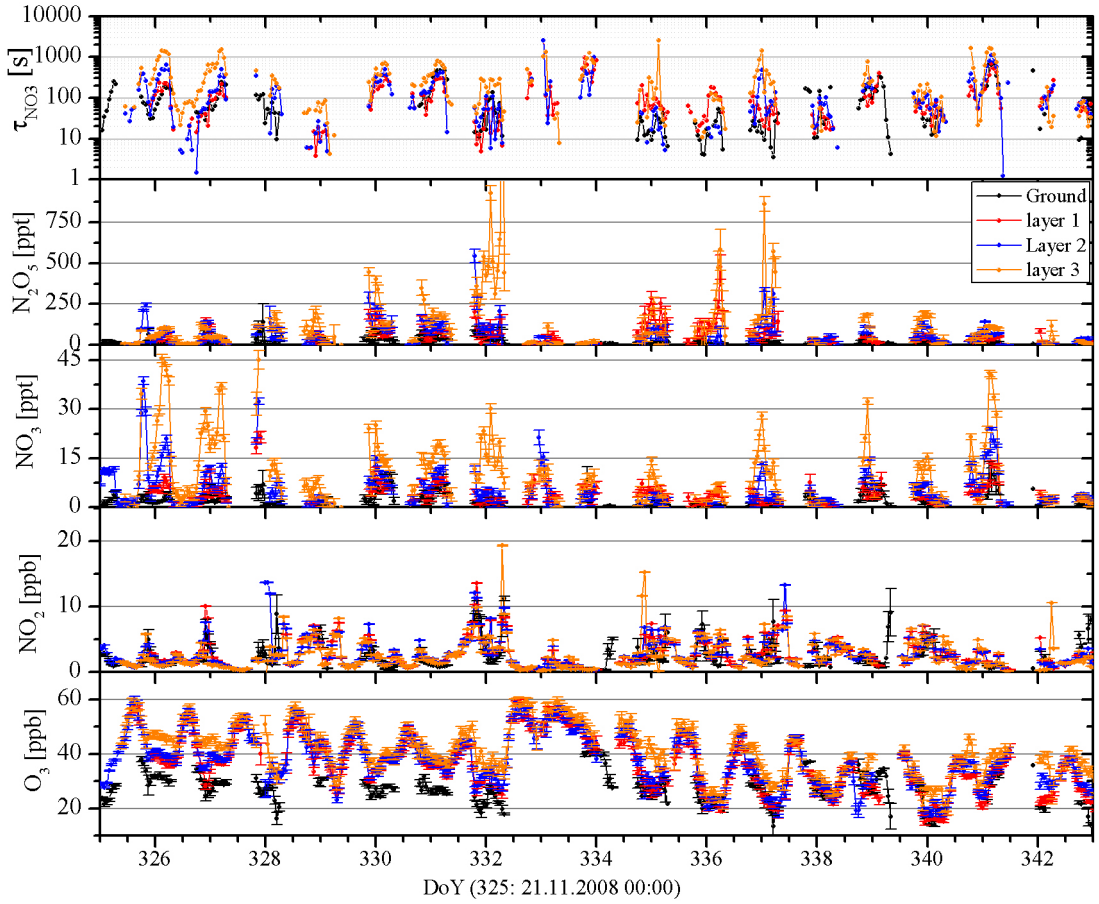

Figure 5.24.: *Overview of the measured profile from the LP-DOAS measurements and the in-situ measurements. Each panel shows the comparison of the in-situ measurement (black) with the the three layers from the LP-DOAS measurements (red: Layer 1, blue: Layer 2 and orange: Layer 3). Shown are the calculated NO_3 lifetime (upper panel) followed by N_2O_5, NO_3, NO_2 and O_3*

.

was also variable in general but differed between the different layers. The average over the entire campaign varied between 100 s for the ground based measurements and 340 s for the highest layer. The maximum lifetime during the campaign was surprisingly similar for the LP-DOAS measurements with a maximum value of about 2500 s for each layer whereas for the ground based measurement only about 700 s (for a one hour average) were observed.

5.8.2. Nocturnal profiles for the different layers

To compare time series of the different layers, nocturnal profiles (18:00 - 08:00) of the 1 hour mean values (DoY[2] 325-342) were calculated. Figure 5.25 shows the

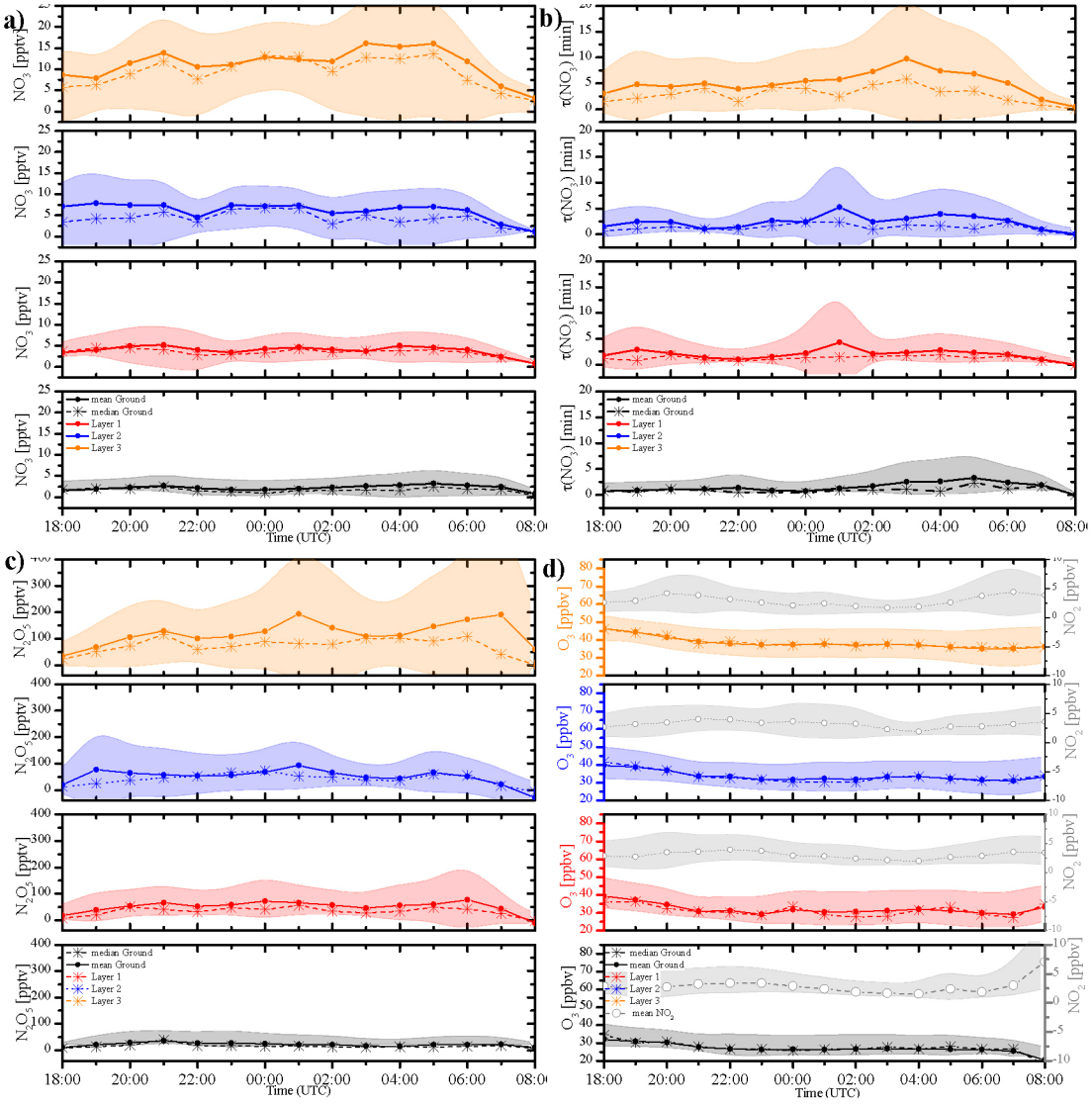

Figure 5.25.: *Averaged nocturnal profile (18:00 - 08:00) of NO_3, N_2O_5, NO_2, O_3 and the steady state lifetime τ_{NO_3}. In-situ measurements are shown in black, Layer 1 is in red, Layer 2 in blue and Layer 3 in orange.*

nocturnal profiles of NO_3 (a)), τ_{NO_3} (b)),N_2O_5 (c)), O_3 and NO_2 (d)) which are colour coded for each layer height.
The dots in the plots represent the mean values where the crosses represent the median values. The shaded area shows the $1-\sigma$ standard deviation. A clear

[2]DoY: Day of Year 325 := 21.11.2008

gradient in NO_3 mixing ratios were observed between the different layer. For the ground based measurements the NO_3 mixing ratio was on average only 2.3 pptv and showed no clear structure during the night. Compared to this, the LP-DOAS measurements constantly showed larger mixing ratios in NO_3. The shaded area in Layer 2 is more expanded than the shaded area of Layer 1 due to greater variability, possibly due to the influence of higher and cleaner air masses. Layer 1 and Layer 2 have on average NO_3 mixing ratios of 4.1 pptv and 5.9 pptv, respectively and show no pronounced structure during the night.
Layer 3 shows significantly higher levels of NO_3 than all the other layers. On average 11.1 pptv were measured which corresponds to approximately twice that measured in Layer 2. This is due to a large increase in the average height above the ground when going from Layer 2 to Layer 3 (see Figure 4.9 on page 67). Similar to the other layers, there is no obvious diurnal trend but the variability (shaded area) is increased in comparison. The reasons of these differences between the 4 layers will be discussed in the next sections.
Part b) of Figure 5.25 shows the NO_3 lifetimes. Similar to the NO_3 mixing ratios, a clear gradient between the various layers is recognizable. On average the lifetime changed from about 100 s for the ground based measurements to approximately 340 s for the highest layer. As the NO_3 production rates varied less than the NO_3 concentration or the lifetime between the layers, the loss processes must decrease with height. Part c) shows a similar trend for N_2O_5 mixing ratios. For the LP-DOAS measurements N_2O_5 could not be measured directly but was calculated via the measured NO_3 and NO_2 mixing ratios. As the NO_2 mixing ratios and the equilibrium constant varied only little between the layers the gradient in N_2O_5 is similar to the gradient of NO_3. On average N_2O_5 mixing ratios varied from about 23 pptv (at ground) to approximately 130 pptv in the top layer, whereas the mixing ratios in the two middle layers are very similar. To complete the chemical system, part d) shows the mean nocturnal profiles of O_3 and NO_2. While no vertical gradient was observed for NO_2, that for O_3 was quite pronounced.

5.8.3. Dependence of gradients on wind sectors

As shown in section 5.4.2 the ground - based measurements were highly influenced by wind direction. To aid comparison, the measurements of the LP-DOAS instrument were also divided in the different wind sectors (see Figure 5.26). Note that the ordinates in Sector A + B in Figure 5.26 are scaled differently to those of Sector C + D. In general the LP-DOAS measurements show similar trends to the ground - based measurement. The nocturnal mean values for Layer 1 and 2 increase constantly from wind sector A to wind sector D similar to the in-situ measurements. Layer 3 increases from sector A to B but did not show a clear increase to the wind sectors C and D. This is an indication that the upper most layer is less influenced by the origin of the air masses and thus wind-direction dependent

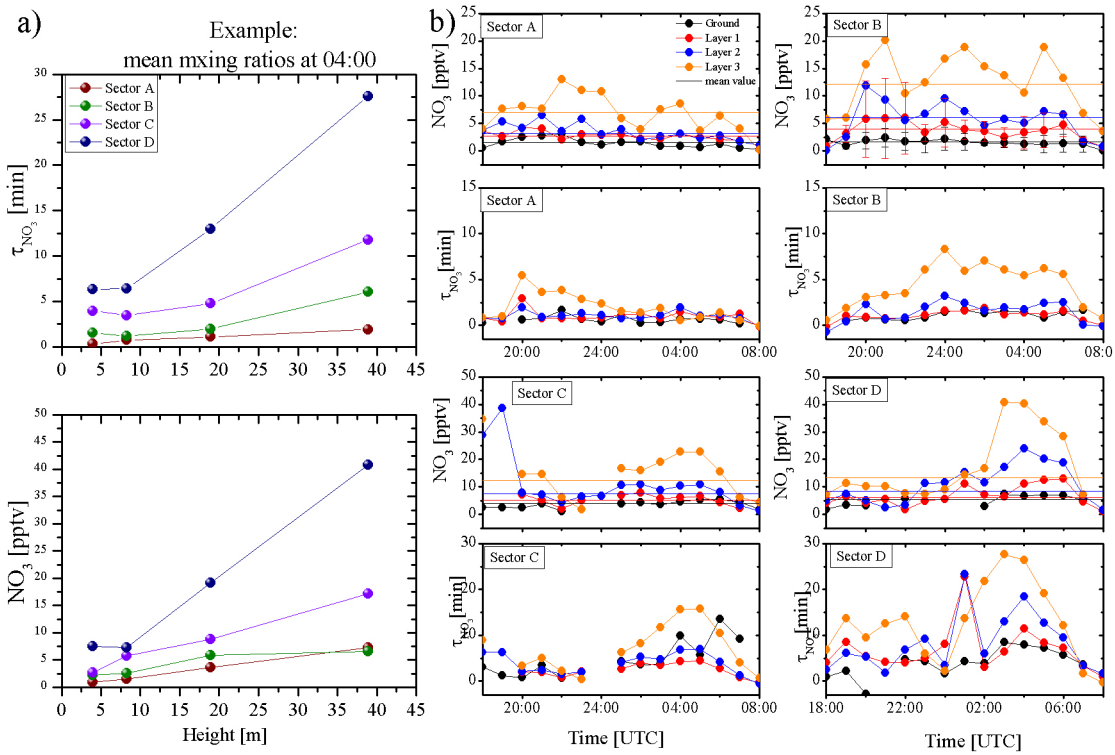

Figure 5.26.: *Height dependency of NO_3 and τ_{NO_3} for the different wind sectors. a) shows an example for NO_3 and τ_{NO_3} profil at 04:00.*

emissions of reactive trace gases compared to the lower layers. The top layer can also be influenced by cleaner air masses from higher altitudes.

5.8.4. Influence of the NBL height

A first impression of the importance of the stability of the nocturnal boundary layer with respect to the development of NO_3 is given in Figure 5.27. This shows a comparison of the temperature change ($\frac{\Delta Temp}{\Delta z}[\frac{°C}{m}]$), calculated from measurements at a 100 m Tower where meteorological parameters were measured at three different heights (25m, 50m and 100m), and the change of NO_3 mixing ratios ($\frac{\Delta NO_3}{\Delta z}[\frac{pptv}{m}]$)), calculated from the LP-DOAS measurements at the highest and lowest layer in respect to their averaged height above ground level.
On most of the nights a good correlation between the change in temperature and the change in NO_3 is visible (i.e. strong temperature increase with height = strong vertical NO_3 gradient). This is not the case on the nights 339, 340 and 341 in which air masses arrived from the Atlantic. In several nights Layer 1 and Layer 2 are however quite similar and only the difference between Layer 2 and 3 is obvious. Some information on the boundary layer structure can be gained from radio sondes. On two nights radio sondes were launched hourly. On further 7 days, a profile at mid-

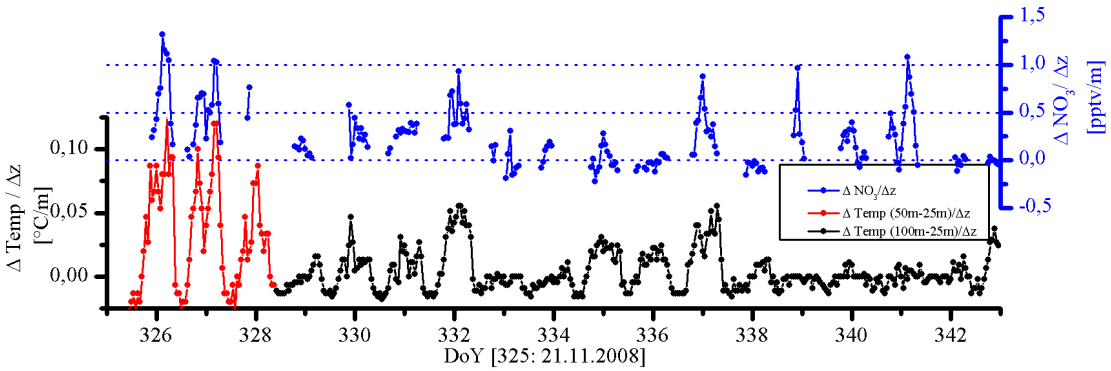

Figure 5.27.: *Comparison of the temperature change with height to the change of NO_3 mixing ratios in respect to height. Temperature changes were calculated from the temperature measurements on a 100 m Tower. The black line shows the temperature change from 25 m to 100 m whereas the red line shows the change from 25m to 50m due to no available 100 m measurements during this time period. For the change in NO_3 mixing ratios (blue) the LP-DOAS measurements from Layer 1 and 3 were used in respect to their averaged height above ground (a.g.l.)*

night was recorded to give an approximate height of the nocturnal boundary layer. An example of one of these nighttime balloon launches is shown in Figure 5.28.

In this night the Nocturnal Boundary Layer (NBL) was approximately between 25m and 100m above the ground. The profiles which were taken during nighttime are variable but most of them suggest that the typical height of the NBL during the campaign is about 100-150m. The vertical gradients in mixing ratio and lifetime of NO_3 clearly indicate that reactive emissions into the lower layers significantly contribute to NO_3 removal. The highest layer of the DOAS measurements is more influenced by the residual layer, which is decoupled from nocturnal emissions. This decoupling was strongest when the nocturnal boundary layer was most strongly stratified, and the nocturnal inversion strongest.

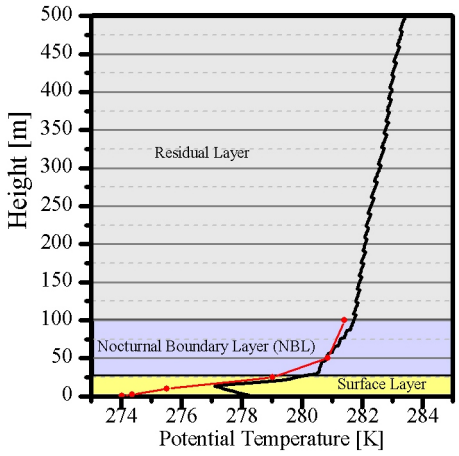

Fig. 5.28.: *Example of a balloon launch on midnight of the 3rd December. The red dots illustrate the potential temperature measured at the 100 m Tower.*

5.9. Height dependent NO_x partioning and losses during the night

The conversion of NO_2 to NO_3 and N_2O_5 followed by reactive losses either with gas-phase species or with aerosols and other surfaces represents a conversion of gas-phase NO_x trace gases to NO_z[3] in both gas phase and particle phases. If no NO is present in the atmosphere the fraction of nitrogen oxides (FNO_x) which is present in reactive form (i.e. as NO_3 or N_2O_5) at night can be expressed as:

$$FNO_x = \frac{[NO_3] + 2[N_2O_5]}{[NO_3] + 2[N_2O_5] + [NO_2]} \tag{5.15}$$

This simplified expression ignores the longer lived NO_x reservoir species such as HNO_3, $\sum$PNs, $\sum$ANs or halogenated nitrogen oxides, which unlike NO_3 or N_2O_5 are not in rapid equilibrium with NO_2. The contribution of NO_3 and N_2O_5 to the complete reactive nitrogen oxides (NO_y, which also include species such as HNO_3, $\sum$PNs or $\sum$ANs) is, of course smaller. The partioning of NO_x to NO_3 and N_2O_5 is favoured by large O_3 concentration and low losses of NO_3 and N_2O_5. During nighttime a positive O_3 gradient is typically observed (partly due to less deposition) which favours the partioning to NO_3 or N_2O_5 with height. Figure 5.29 shows a time series of FNO_x over the entire campaign (lower panel) and the height dependent nocturnal average in the upper panel FNO_x was very variable during the campaign with maximum values of almost 30 % for the highest layer. For the ground based measurements values up to 20 % could be measured. On average as shown in the upper panel of Figure 5.29 the fraction of reactive nitrogen oxides is low for the ground based measurement and increases with height. Short lifetimes of NO_3 result in low values of FNO_x at ground level and indicate that every oxidised NO_2 by O_3 represents an irreversible loss of NO_x. However, the relatively low partioning and also the relative short lifetime, even for the top layer, lead to the conclusion that all NO_2 oxidised by O_3 at night represents a sink for NO_x.
The loss rate of NO_x (LNO_x) is then given by:

$$LNO_x \approx n \cdot k_{2.15}[NO_2][O_3] \tag{5.16}$$

where the factor n is 1 if the loss is dominated by direct NO_3 loss (reaction with VOC) and is 2 if the loss is dominated by indirect processes (N_2O_5 uptake) due to the reason that two NO_2 molecules are necessary to form a N_2O_5 molecule. For this campaign the dominant losses at least for the ground based measurements could be identified as direct losses. Typically, relative humidity and also the amount of available aerosols decrease with height, so that the importance for the indirect losses should also decrease with height. Therefore, for the entire campaign and at

[3] NO_z = NO_y - NO_x

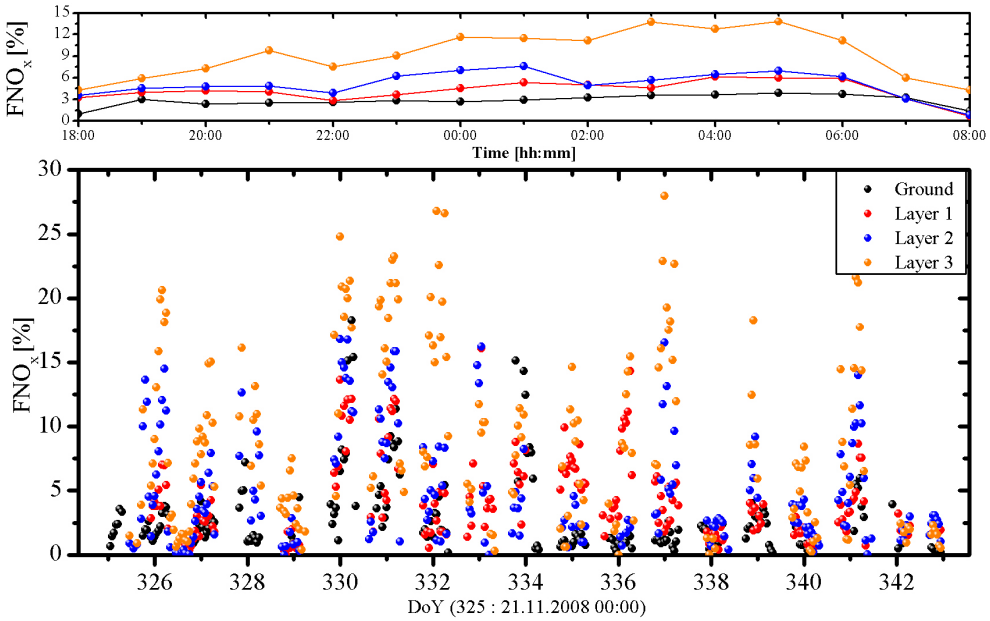

Figure 5.29.: *Timeseries of the partionioning depending on the measurement height. The upper panel shows the nocturnal profile of the partioning*

all altitudes, the nocturnal loss rates were calculated using n=1.
The daytime loss of NO_x is dominated by the reaction of NO_2 with the OH radical to form nitric acid.

$$OH + NO_2 + M \longrightarrow HNO_3 + M \tag{5.17}$$

The NO_x loss rate is approximately given by $k_{5.17}[OH][NO_2]$, which is also the production rate of HNO_3. For temperature and pressure prevailing during the campaign, the rate constant for reaction 5.17 is about $1.2 \times 10^{-11} \frac{cm^3}{molecule\ s}$. OH was measured using a LIF [4] instrument with typical maximum concentration of about 0.15 ppt during noon.
Figure 5.30 displays calculated rate of NO_2 loss (in ppb/hr) for both reaction with OH and O_3 for the ground based measurements. The nighttime losses were calculated between 18:00 and 08:00 local time where the radiation was too low to photolyse NO_2. For the OH measurements data were available from sunrise til sunset (about 08:00 - 17:00). The losses during day and nighttime were rather similar over the entire campaign, with maximum values of the order 0.7 ppb/hr. The upper panel of Figure 5.30 shows the mean diurnal profile for both loss processes. As shown in the Figure for the nighttime losses the variability is rather small with an overall average nighttime loss rate of about 0.11 ppb/hr. In contrast the day time losses via the reaction of NO_2 with OH shows more variability with two pronounced peaks at about 9 in the morning and about 12. However, the over-

[4]LIF: Laser Induced Fluorescence

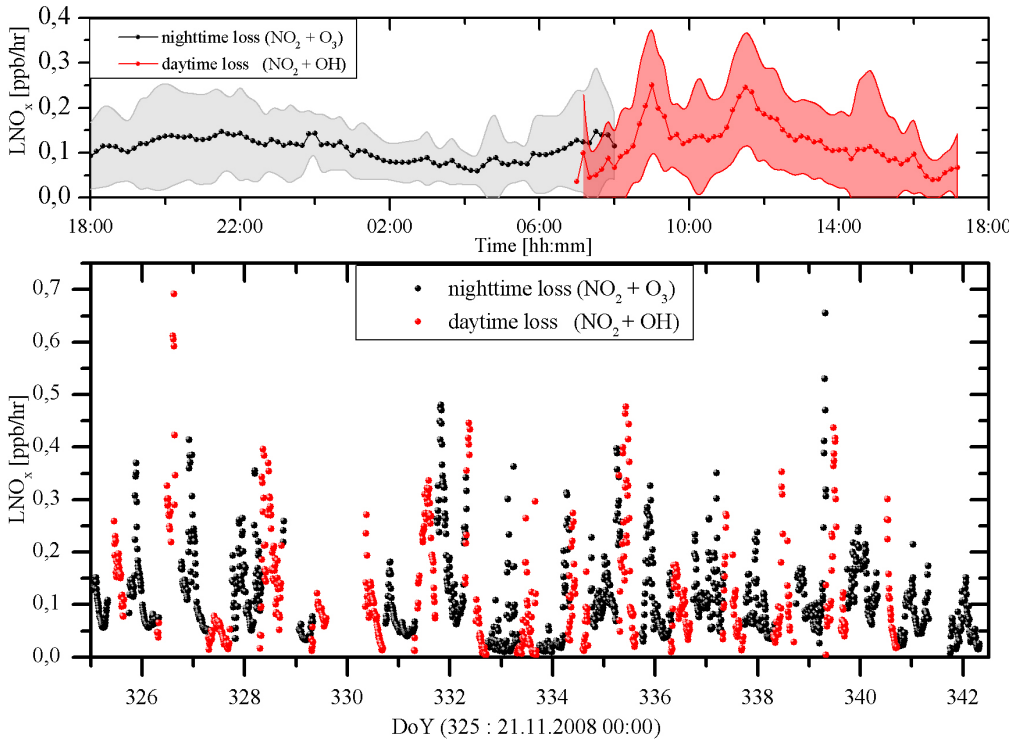

Figure 5.30.: *Daytime and nocturnal LNO_x calculated using Equation 5.16 and 5.17. The upper panel shows the mean daily profile for both (nocturnal losses in black and daytime losses in red). The lower panel shows the entire time series for both losses*

all averaged daytime loss rate is about 0.12 ppb/hr and therefore almost identical to the nighttime losses. The campaign average for the integrated daytime NO_2 loss was about 1.4 ppb with a standard deviation of about 0.8 ppb. This can be compared to the nighttime loss of NO_2 which varied between 0.7 and 2.8 ppb. Over a 24 h period the nocturnal chemistry thus contributes between 28 %, as observed on the 24.11.2008, and 80%, as observed on the 23.11.2008, to the removal of NO_x for the ground based measurements.
The same calculations of LNO_x were also applied for the LP-DOAS measurements. Figure 5.31 shows the result of this calculation for Layer 3 compared to the ground measurements. The lower panel of the Figure shows the entire time series for the 1 h averaged data for the ground level (black) and the highest layer (orange). Layer 1 and 2 are not displayed in the Figure to present a clearer view. Typically the calculated values for those both layers are in between the ground based and the highest layer values. The variation of layer 3 is more significant than the variation of the ground based calculation with maximum values up to 1.3 ppb/hr. The upper panel shows the nocturnal mean of the ground based and layer 3 values compared with the average of all layers (brown bars) and with the diurnal mean (green bars).

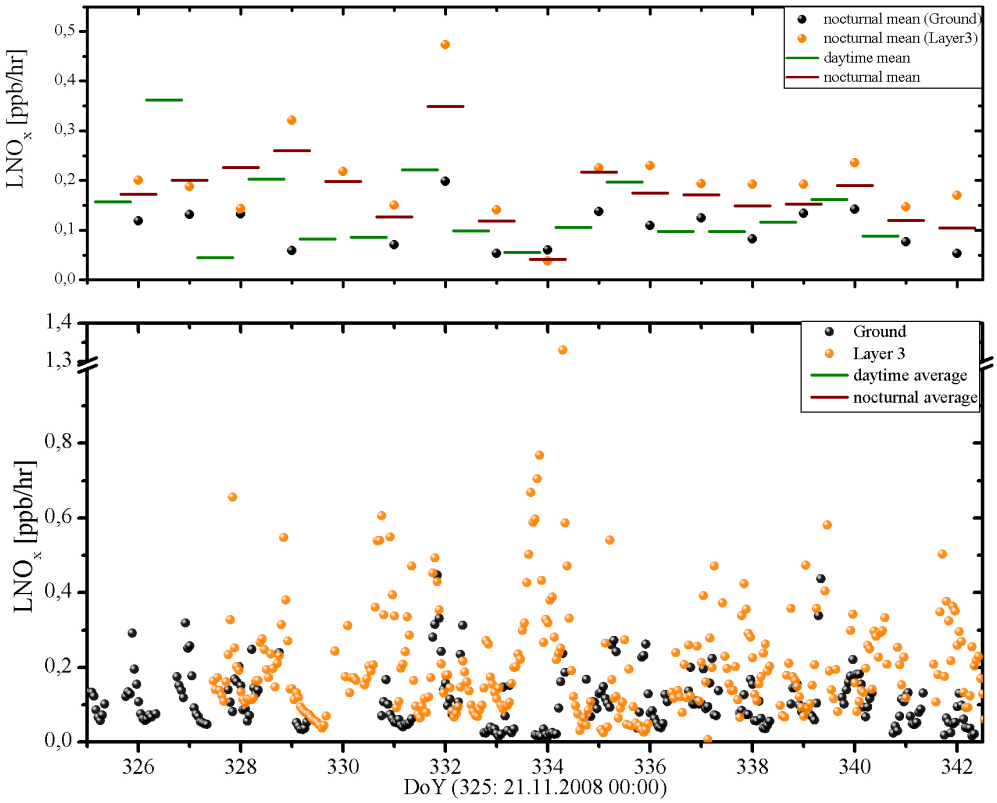

Figure 5.31.: *LNO_x-timeseries shown for ground based and all LP DOAS Layer. The upper panel shows the nocturnal mean for each Layer compared with the mean average of the daytime loss and the average of the ground based and all Layer is also displayed in the upper and as well in the lower panel. The lower panel shows additionally the 1 hours averages of all data.*

On average, the removal of NO_x in the upper layer is twice as large than at ground level which a maximum ratio of about 2.5 at one night. Comparing the mean values of all layers over a 24 h period, the nocturnal loss of NO_2 becomes more important. Therefore, the nocturnal chemistry contributes between 43%, as observed on the 22.11.2008, and 87 %, as observed on the 23.11.2008, to the removal of NO_x. On average 65% for the entire campaign of the complete NO_x removal was due to nocturnal chemistry.
The simple calculations above showed that, for this campaign the nocturnal removal of NO_x at ground level is comparable to the daytime loss but it is increasing with height. However, as the ratio of nighttime to daytime losses depends on the insolation at the site, nighttime losses will be favoured still more in the colder months as O_3 photolysis and OH production rate drop significantly.
The fact that the nighttime boundary is shallower than the daytime boundary layer will however have the converse effect and favour daytime oxidation. During the

Domino campaign typical daytime boundary were in the order of about 1500 m for sunny days [van Stratum et al. (2012)] whereas the nocturnal boundary layer height is somewhat in the range of 100-300m but the NO_3 concentrations above level 3 are likely to be even higher which will increase the importance during nighttime again.

5.10. Atmospheric importance of nitrate radical gradient

Several studies have shown that the vertical distribution of NO_3 and N_2O_5 can influence the photo chemistry of the following day. Here, a simple analysis of the measured vertical NO_3 distribution will be performed in terms of oxidation capacity .
Figure 5.32 shows the evolution of the planetary boundary during the day. During

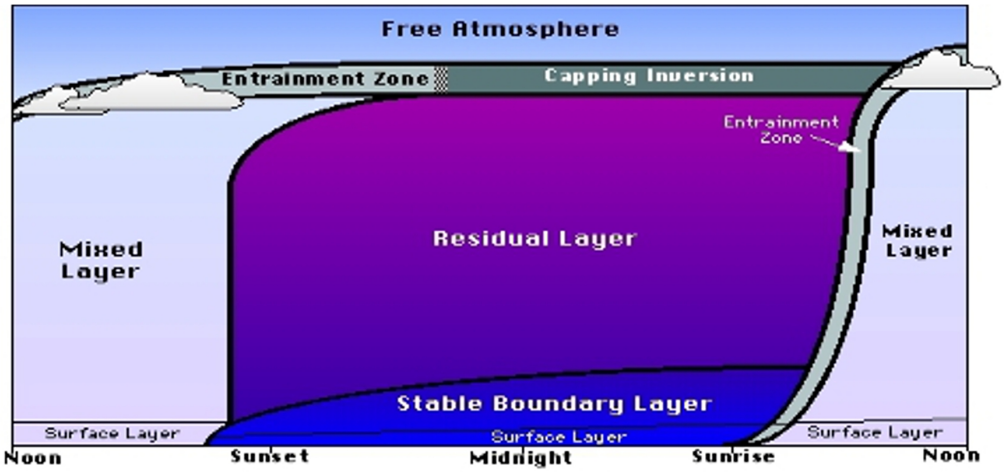

Figure 5.32.: *Planetary boundary evolution adapted from Stull (1988)*

daytime a very well mixed layer is established due to turbulence. After sunset the boundary layer becomes more stratified due to less turbulence in the absence of the surface heating by sunlight, and therefore, during night a stable nocturnal boundary layer is formed in which almost no mixing take place. On top of this nocturnal boundary layer a residual layer, which contains the longer lived trace gases from the day, is established. During nighttime typically also an inversion layer is established in which the emissions from the surface are trapped due to the very slow mixing. For the following analysis it is assumed that all measured VOCs which were present at the end of the day will stay in the residual layer and may therefore influence the higher altitudes of our measurements. NO concentrations which are emitted at the surface will remain in the surface layer and will not act as loss process for the higher altitudes. Also, it is assumed the possible indirect

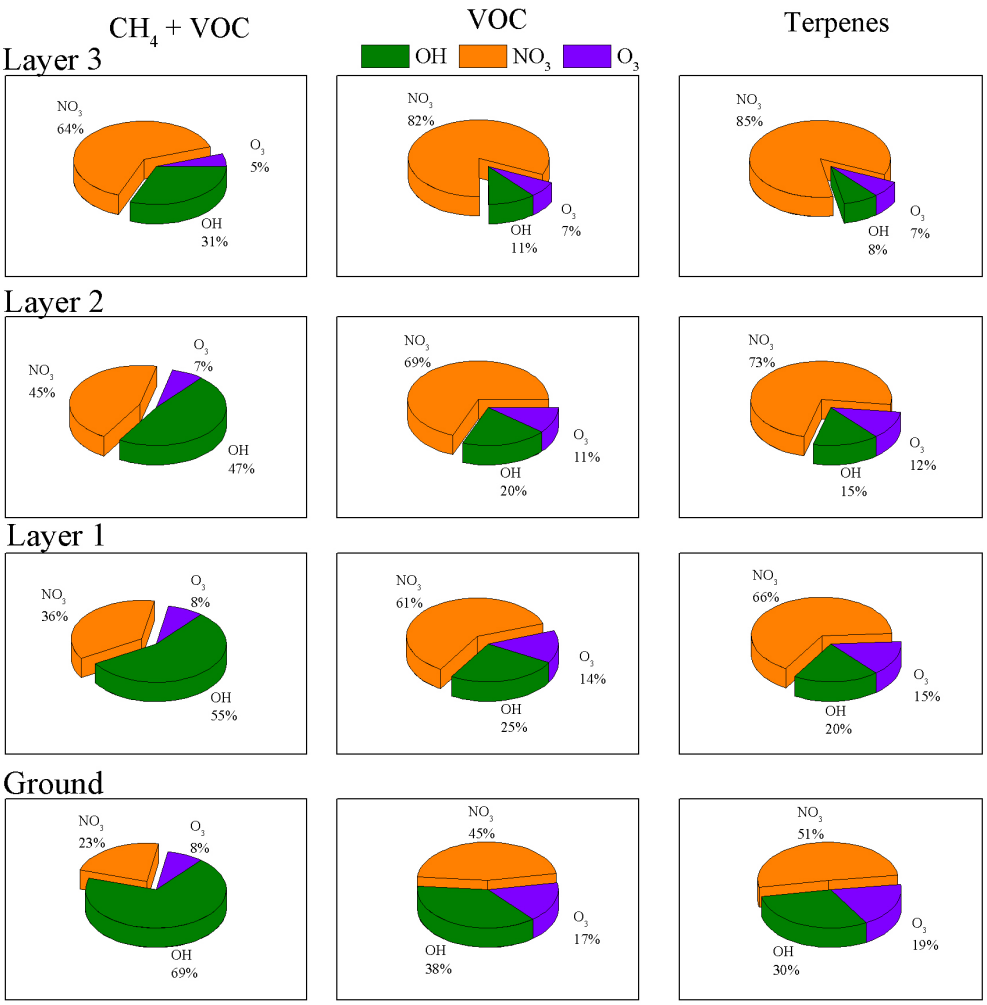

Figure 5.33.: *Overview of the Oxidation capacity depending on the vertical NO_3 concentration and different classes.*

losses via uptake of N_2O_5 on aerosol will have a much smaller impact with higher altitudes due to lower aerosol loading and lower relative humidity of the air masses. With these assumptions the oxidation capacity (see section 5.7) was calculated for the altitude dependent NO_3 and O_3 concentration assuming homogeneously distributed VOCs. The daytime OH oxidation capacity was compared to all height dependent nighttime measurements assuming no gradient of OH within the boundary layer. Figure 5.33 shows the comparison of the oxidation capacity for OH, NO_3 and O_3 depending on altitude and also on oxidizable trace gases. OH is the dominant oxidant for methane, and was responsible for 69 % of the oxidation capacity regarding methane and VOCs (left upper site of the figure). With increasing NO_3 concentration with height the oxidation capacity for OH dropped down to only about 31 % for the highest layer. Considering only VOCs and especially only terpenes (here: isoprene, limonene and α-pinene) the influence of height is much more

significant. For terpenes the oxidation capacity of NO_3 increases from 51 % for the ground based measurements up to 85% for the upper layer. For this calculation only a small set of VOC (see table 5.1) was available at this site.
Clearly, the role of NO_3 as nighttime oxidant and its effect on VOC removal cannot be gauged solely by ground level measurements. Still, the data from DOMINO shows that NO_3 will be the dominant oxidizer of terpenes at all heights.

5.11. Comparison with other known NO_3 profiles

While most measurements of NO_3 have been made at ground level, there are several studies apart from this one which suggest a significant vertical gradient. Penkett et al. (1993) measured NMHCs in the free troposphere and via a hydrocarbon clock type analysis concluded that NO_3 must be present at much larger mixing ratios in the free troposphere. Following this, several groups measured the vertical distribution of NO_3 using different techniques. Aliwell and Jones (1998) used a zenith sky spectrometer to measure the scattered light during sunrise in summer 1995 over Cambridge. They used a qualitative modelling study to test the feasibility of their measurements. This model approach was a somewhat idealized model, to describe the boundary composition and evolution, due to insufficient meteorological data. The result of this modelling study is shown in Figure 5.34 a).
Allan et al. (2002) measured NO_3 profiles at different remote locations in the Northern and Southern Hemisphere using also a zenith sky spectrometer. The measurements were performed at Mace Head (Ireland), Tenerife, the Weybourne Atmospheric Observation (WAO) (UK), Cape Grim (Tasmania) and in Andøya (Norway). The measurements indicate that a significant fraction of the tropospheric NO_3 exists above the nocturnal boundary layer. The averaged concentrations for the different locations are shown Figure 5.34 c). The highest NO_3 concentrations were observed around 2 km altitude which values between 3 - 25 pptv which are consistently higher than the ground levels concentrations.
From measurements during spring/summer 1999 in the urban area of Heidelberg made by von Friedeburg et al. (2002) NO_3 profiles could be derived by spectroscopy of scattered sunlight in off-axis geometry during sunrise. These measurements show a better vertical resolution than the measurements provided by the zenith sky spectrometers and therefore, they derived a peak value of about 140 ppt at about 350m above the ground. Figure 5.34 e) shows a model result which was consistent with the measurement values.
During a campaign in July/August 2004 in the north-eastern United States Brown et al. (2007a) used a CRDS instrument on board of an aircraft to study the vertical distribution of NO_3 with a high vertical resolution. These measurements could be compared with ground based NO_3 measurements which were done by LP-DOAS and by CRDS in-situ measurements on a ship. In their study they showed the

role of different sinks for NO_3 and N_2O_5 in different environments. Because the campaign took place in a coastal area, effects of both terrestrial and marine meteorology and emissions were observed. Figure 5.34 g) shows the averaged vertical distribution for all nighttime flights. They measured the maximum NO_3 mixing ratios of about 65 ppt, on average, at about 250 m.
In the same year (October 2004) Brown et al. (2007b) installed a CRDS instrument on a 300 m high Tower located in Erie, 25 km east of Boulder and 35 km north of Denver. The instrument was mounted on a movable carriage and could be moved up - and downwards with a resolution of about 1 m/s. Beside the NO_3 distribution with height they measured the stratification of the boundary layer and could distinguish between a surface - , nocturnal boundary - and residual layer. Figure d) shows the average profile on one night. On average they found maximum mixing ratios at about 300 m. The increasing rate of NO_3 with height is different in the different layers. In the surface layer ($\sim$ 20 m above ground) only a very small increase is visible. The increase in the nocturnal boundary which reaches typically up to 100 - 120 m was more distinct (0.144 ppt/m). In the residual layer the increase was most pronounced with about 0.165 ppt/m for the average profile.
Several studies used a LP-DOAS system, similar to the measurements described in this thesis, to derive vertical profiles of different trace gases. Stutz and Co-workers deployed a LP-DOAS system in Houston, Texas [Stutz et al. (2004)]. They set up five different light paths to cover a vertical range of about 115 m. Figure b) shows the average of four selected profiles during their measurement. The increase in NO_3 mixing ratio with height is approximately constant with a slightly stronger increase above 85m. A 1-D nocturnal chemistry and transport model (NCAT) was developed and the model results could represent the general behaviour well, allowing conclusions about the different mechanisms which are responsible for the change of trace gas concentrations with altitude to be made.

Six years later Stutz and Co-workers measured again the vertical distribution in Houston, Texas. During this measurement period from mid August to mid September 2006 Stutz et al. (2009) measured at three different altitudes up to 300 m. During this campaign NO_3 chemistry was strongly impacted by industrial emissions. The profiles from this night were also analyzed with the NCAT model. Figure f) shows an average of three modelled profiles during one measurement night. Several modelling studies predict a pronounced vertical gradient in NO_3 mixing ratios. [Fish et al. (1999); Galmarini et al. (1997); Geyer and Stutz (2004); Riemer et al. (2003)].
Figure h) shows several profiles obtained during the DOMINO campaign. The Figure shows the average over the complete campaign (black) compared to the average of two nights and to just one single profile. On most nights a constant increase in the NO_3 mixing could be observed with height, though the vertical gradient was very dependent on the meteorological. On some nights no gradient

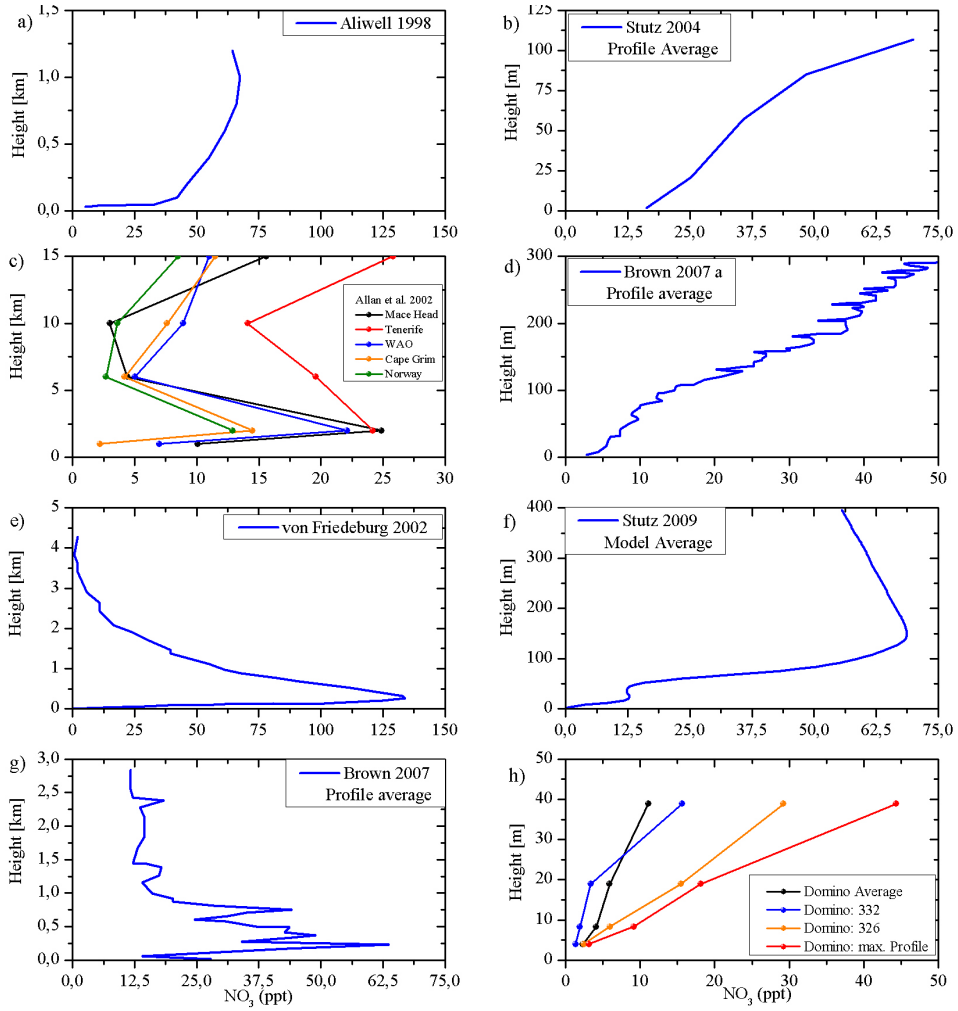

Figure 5.34.: *Comparison of different vertical NO_3 profiles.The different figures are taken or adapted from: a)Aliwell and Jones (1998), b) Stutz et al. (2004), c) Allan et al. (2002), d) Brown et al. (2007b), e) von Friedeburg et al. (2002), f) Stutz et al. (2009), g) Brown et al. (2007a), h) this thesis*

was observed or as shown in Figure h) Day 332 shows only a strong increase between the second and third layer and only a very small increase from the ground based measurements to the second layer. Compared to the other profiles the height dependent measurements during Domino were limited on average to about 50m. Therefore, assuming typically nocturnal boundary layer height of about 100-150 m, the increase between nocturnal and residual layer which could be shown partly in the other studies is difficult to estimate in our data set.
In general all shown vertical profiles have the same trend showing a clear increase with height. The absolute NO_3 concentration depends on the location of the measurement site and the meteorological conditions during these measurements periods. As also clearly visible is that the profile are not constantly pronounced. High

variabilities on already short time and spatial scale were observed leads to the conclusion that only ground based measurements underestimates the importance of nocturnal chemistry for the Oxidation Capacity during nighttime and therefore the influence of the daytime chemistry for the following day. Also the high variability can be important input for modelling studies.

5.12. Summary of DOMINO results

Ground based measurements of NO_3/N_2O_5 were performed by cavity ring down spectroscopy. A LP-DOAS system was also deployed at the site to investigate the vertical distribution of NO_3 and other trace gases. The results of our findings are summarized here:

- The ground based NO_3 measurements showed in general low concentration and low lifetimes which were strongly dependent on air masses.
- Very short NO_3 lifetimes which were associated with urban air masses could not be constrained by calculated NO_3 losses whereas longer lifetimes associated with continental/rural were constrained by the calculated losses.
- The very short NO_3 lifetimes in urban/industrial air are potentially caused by emission of reduced sulphur compounds or alkenes from the petrochemical industries.
- NO_3 showed a clear increase with height, which was strongly influenced by the meteorological conditions during the campaign. The mean concentration for the entire campaign was about 5 times higher in the uppermost layer compared to the ground based measurements. A clear positive gradient in O_3 was also observed whereas almost no gradient was observed for NO_2, implying a change in lifetime (on average four times longer lifetime in the uppermost layer compared to the ground).
- The nocturnal removal of NO_x calculated from the ground based measurements was derived to be about 0.1 ppbv/hr with a relatively constant distribution over the entire night. The strong vertical NO_3 gradient suggests that the mean NO_x loss in the nocturnal boundary layer is higher than calculated from the ground based measurements alone.
- The role of NO_3 as nighttime oxidant and its effect on VOC removal cannot be gauged solely by ground based measurements. The analysis showed that NO_3 is the dominant oxidizer of terpenes at all altitudes. For the uppermost layer nighttime oxidation of VOCs + CH_4 occurred roughly equally via NO_3 and OH. Therefore, height dependent NO_3 and VOC measurements would be helpful to understand the nocturnal chemistry and its influence on the photochemistry for the next day better.

Chapter 6.

Results from PARADE 2011

In this chapter the results of the PARADE campaign will be presented and discussed. The measurement site, the instrumentation and the meteorological conditions were described in section 4.2.

6.1. Set up of the instrument during the campaign

During the PARADE campaign NO_2, total peroxy nitrates ($\sum$PNs) and total alkyl nitrates ($\sum$ANs) were measured using a two-channel TD-CRD instrument as described in section 3.3. NO_2 was additionally measured by several other measurement techniques which allow an intercomparison between them. Speciated peroxy nitrates were measured using a different technique (TD-CIMS) [1]. The TD-CRDS was located in the ground floor container of the Taunus Observatory (see Figure 4.13). The air was sampled using a 3/8 " PFA tubing bypass flow with a inlet sampling height of about 10-12 m above the ground. The bypass flow was used to reduce the residence time in the inlet, which was in the order of 1 s. The bypass was shared with two other instruments during the campaign, the MPI-CIMS which is able to measure speciated PAN's, PAA [2] and also $ClNO_2$, and the CE-DOAS [3] instrument from the University of Heidelberg which measures NO_2. A $2\mu m$ Teflon filter was placed in front of the bypass, which was replaced every 2-3 days, to reduce possible contamination of the inlet line by aerosols. A second Teflon filter was placed directly in front of the instrument. The Teflon filters have no effect on the NO_2, $\sum$PNs and $\sum$ANs concentrations. The residence time from the bypass to the detection unit was about 3-4 s. In front of one cavity three quartz cells were mounted (about 42 cm length and inner diameter of 1.5cm) which could be alternatively used by switching two valves. Two of the quartz cells were placed in commercial ovens which had a length of about 20 cm. An additional piece of Teflon tubing was added to the NO_2 reference so that the volume and residence times were the same in all cavities. The time resolution of the measurement was about 4 sec.

[1] CIMS : Chemical Ionisation Mass Spectrometer
[2] peroxyacetic acid
[3] Cavity Enhanced DOAS

6.2. NO_2 measurements

NO_2 was measured during the campaign from the 16.08.2011 until the 08.09.2011 with a typical duty cycle of 80:20. Background measurements were performed by overflowing the inlet with zero air. The zero air bottles used, were compared against a 'standard' bottle which was checked postcampaign using a self built BLC [4]. The efficiency of the BLC to destroy NO_2 was determined in the laboratory to be about 80 % at 0.7 $\frac{l}{min}$. The amount of NO_2 in the zero air bottles was found to be below the detection limit of $\sim$ 20 pptv. Additional uncertainty due to the use of synthetic air for the background measurements, which leads to differences in the Rayleigh Scattering between ambient and background measurements, were corrected as described in section 3.3.2.3. The data coverage of the NO_2 measurements was about 75 % mostly due to the periodical background measurement. The precision of the NO_2 channel during the campaign varied between 10 and 100 pptv with a mean precision of 24.4 ± 8.4 pptv. Therefore a detection limit (2σ) of about 50 pptv for 4 sec data could be achieved.

6.2.1. Comparison of NO_2 instruments

During the Parade campaign, a total of 8 NO_2 instruments were deployed at the site, which were based on five different techniques. Therefore, the campaign was a good opportunity to evaluate the instrument. Figure 6.1 shows the correlation of the CRD with 6 other instruments (one CLD device did not report data). Beside the CRD technique described in this thesis, four instruments used the chemiluminescence technique (AG Fischer, AG Drewnick (Mola), University of Bremen and HLUG [5]), one instrument used laser induced fluorescence (LIF [6]) (AG Harder) and two instrument were based on the DOAS Principle [7] (LP-DOAS and CE-DOAS). Apart from the LP-DOAS instrument all others were point (in-situ) measurements. The inlets of five instrument were located on the main platform of the observatory whereas the measurements of the HLUG and the Mola instrument were about 10 m distant. The averaged NO_2 concentration from the LP-DOAS was derived from the light path between the Kleiner and Großer Feldberg (about 1.2 km distance). Whereas the CLD [8] and the LIF instruments have to be calibrated (CLD by known concentration of NO and a known conversion efficiency of NO_2 to NO; LIF by known concentration of NO_2), the DOAS based (LP-DOAS and CE-DOAS) and the CRD instruments are absolute measurements which rely only on absorption cross sections. Whereas the LP-DOAS instrument uses a defined path length, the

[4] BLC = Blue Light Converter
[5] HLUG: Hessisches Landesamt für Umwelt und Geologie
[6] LIF = Laser Induced Fluorescence
[7] DOAS: Differential Optical Absorption Spectroscopy
[8] CLD: Chemiluminescence Detector

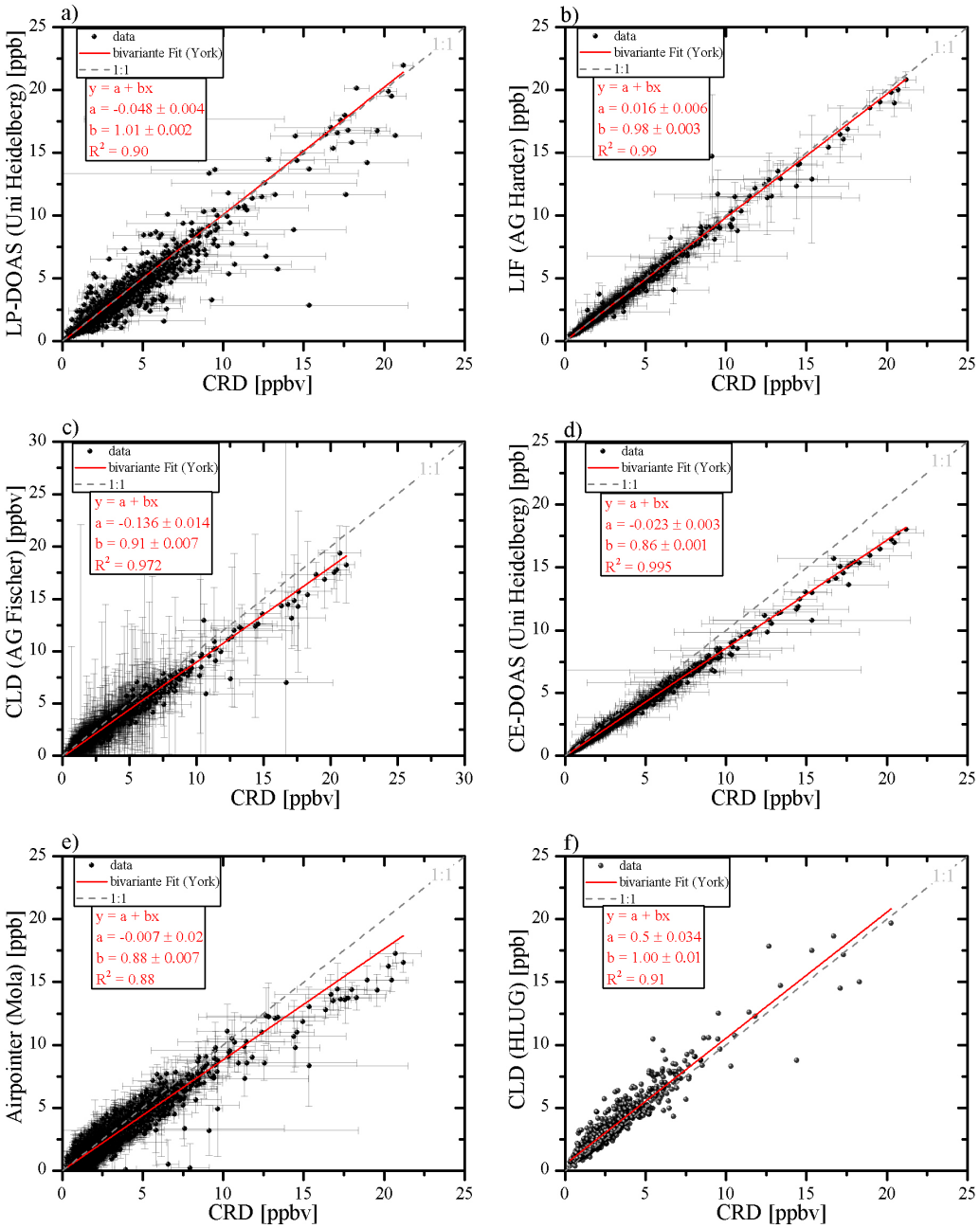

Figure 6.1.: *Correlation plots of the 10 min averaged data between 7 different instruments. Each panel shows the correlation of one instrument against the CRD instrument: a) LP-DOAS, b) LIF, c) CLD (AG Fischer), d) CE-DOAS, e) CLD (Mola), f) CLD (HLUG).*

path length of the cavity based CE-DOAS instrument must be determined via an additional measurement (typically comparison of different scattering by nitrogen and Helium).

The reported uncertainties of the instruments varied between 2 and 10 % (total uncertainties for the HLUG and the Mola instrument were not available). Panel a) of the figure shows the comparison of the CRD with the LP-DOAS instrument. The correlation between both instruments is very good. A few outliers are evident,most occur with high NO_2 levels measured by the CRD and lower levels measured by the LP-DOAS which might indicate local emissions around the measurement site. Removing these data points improves the correlation coefficient between these instruments to $R^2 = 0.95$. The uncertainty of the LP - DOAS instrument is mainly determined by the uncertainty of the NO_2 absorption cross section and was specified for this campaign with 2%.
Panel b) shows the comparison of the CRD instrument with the LIF instrument. The uncertainty of the LIF is reported to be 4.5 % during the campaign. The correlation between both instruments is very good ($R^2 = 0.99$) with almost a unity slope and an intercept within the noise range of both instruments.
Panel c) shows the comparison with one of the CLD instruments (AG Fischer). The accuracy of the CLD instrument is given as 10 %. The correlation between both instruments is still good ($R^2 = 0.972$) but the slope is only about 0.91 which, however, is still in the range of the accuracy of the instruments. Similarly, the comparison with the CE-DOAS instrument (Panel d)) shows an excellent correlation ($R^2 = 0.995$; both instrument share a inlet line), however the concentrations differ by about 14%. The accuracy of the CE-DOAS instrument is given by 5-10%. Therefore, it seems that there is a systematic differences. Panel e) shows the comparison with an commercial CLD instrument (Airpointer). The correlation with this instrument is the worst, but still high ($R^2 = 0.88$). The slope differs by about 12 %. The plot shows clearly that for lower concentrations (< 10 ppbv) both instruments agree well but differ at higher concentrations. The total uncertainty of this CLD instrument is not known. The last plot (panel f) shows the comparison with the CLD instrument from the HLUG. From the HLUG only half hour average values are reported. The correlation between the CRD and the HLUG instrument is also good ($R^2 = 0.91$). The slope is unity but the in-

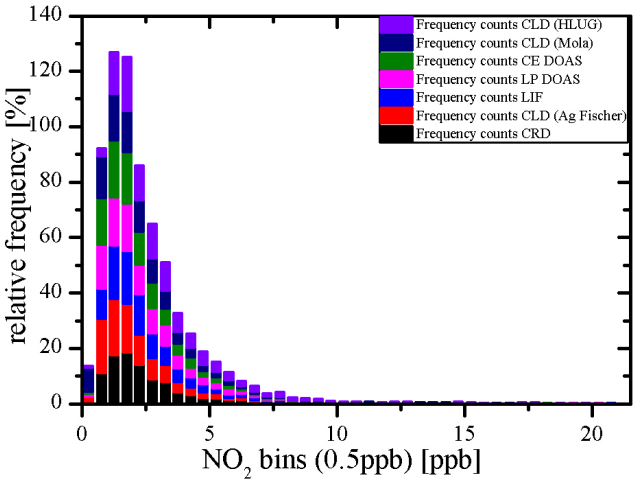

Fig. 6.2.: *Stacked column plot of the relative frequency distribution of the NO_2 concentration collected in 0.5 ppbv bins*

tercept is almost 0.5 ppbv which is very high compared to the other instruments. The accuracy of this instrument is also not known and the detection limit of the HLUG CLD is reported be 1 ppbv. The result of the comparison of the different instruments and techniques showes clearly that the instruments agree very well in the range of their uncertainties for an environment with on average low - medium NO_2 levels and occasionally also higher levels. For three of the 8 instruments (LIF, CE-DOAS and CRD) this comparison was quite useful as these instruments are relatively new compared to the well established LP-DOAS system and the CLD instruments. For the CRD developed as part of this thesis, the results of the intercomparison confirm that the corrections made and assessment of potential errors were appropriate. Figure 6.2 shows a stacked column plot of the relative frequency distribution of the NO_2 mixing ratios in 0.5 ppbv bins. All instruments show a maximum in the range of 1-2 ppbv. Thus, only a small fraction of the measurements were higher than 10 ppbv and most of the time the concentrations were less than 5 ppbv.

6.2.2. Low NO_2 condition during HUMPPA

The first application of the new TD-CRDS instrument was during the HUMPPA-COPEC campaign 2010 in Hyytiälä, Finland. An overview of this campaign is given in Williams et al. (2011). For the CRDS instrument this campaign was the first deployment under real atmospheric conditions. Although some problems with the instrument were encountered, part of the data set was of sufficient quality to use it for a comparison at low NO_2 concentrations and also to optimize the instrument for further field campaigns. Figure 6.3 shows a composite of the NO_2 time series from the CRD and the CLD (AG Fischer) instrument for a 20 day period of the campaign. At the beginning of the time series both instruments measured similar mixing ratios whereas in the middle of the campaign (29.7 - 3.8) the CRD suffered unexpected problems. At the end of the campaign the measurements were in reasonable agreement though some differences remained which could not be explained in detail.
Panel a) (29.7.10 - 03.08.10) shows a period in which both cavities of the CRD measured ambient NO_2 simultaneously. As clearly seen in this figure a significant difference between both channels occurred. The laboratory studies conducted during this thesis showed that this effect is not due to absorption by H_2O [Hargrove et al. (2006)] but rather due to most likely surface effects on the mirrors. Therefore, after the Humppa campaign the design of the mirror holder and the supporting structure of the purge gas of the mirrors was changed. After these modifications, decreasing Rayleigh scattering with increasing water vapour (see section 3.3.2.3) was the only measurable effect of water vapour.
Panel b) shows a closer look to the period 04.08.10 - 08.08.10. The lower panel shows the difference between both NO_2 instruments (CLD-CRD). In some periods

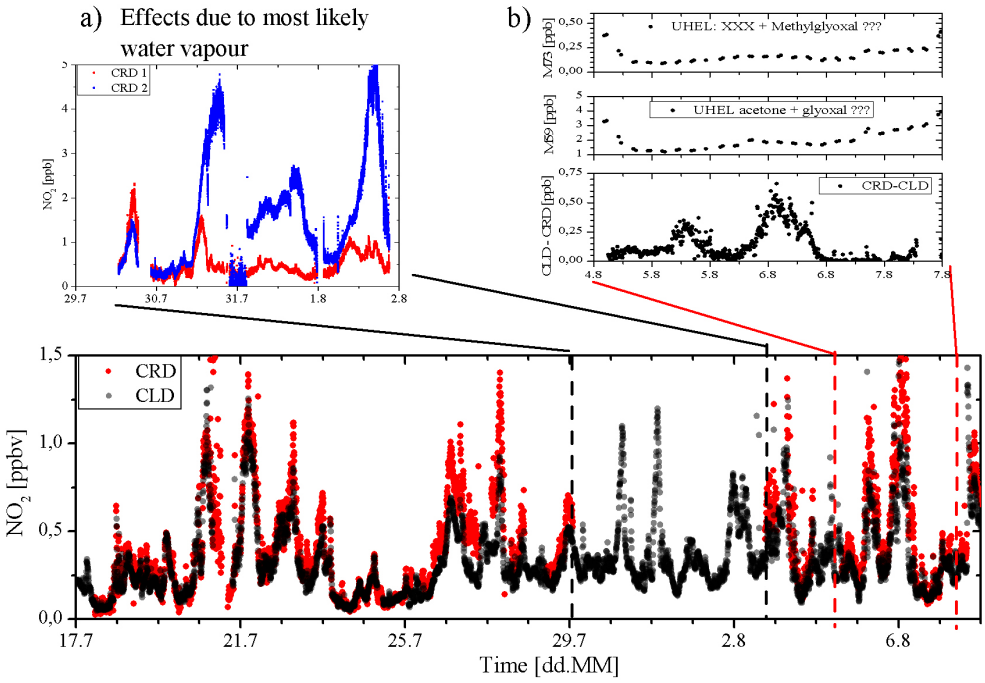

Figure 6.3.: *Composite of the time series of the NO_2 measurements from the CRD and CLD instruments (lower panel) and a) unexpected behaviour during the campaign and c) possible interference by Glyoxal or Methylgloxal*

both instruments measured equal concentrations (Difference = 0) but on two days there were significant differences. One possible explanation would be high levels of glyoxal or methylglyoxal which both absorb at 405 nm (Glyoxal: CHOCHO (m=58); Methylglyoxal: $CH_3C(O)CHO$ (m=72)). The two upper panels shows measurements of a PTRMS [9] instrument at masses 59 and 73 during this period. Mass 59 is mainly acetone but glyoxal would also be detected at this mass as well if present in the atmosphere at significant levels. Methylglyoxal can be detected at the mass 73. Therefore, both time series are plotted to compare them with the NO_2 differences of the CLD and CRD instrument . There is no correlation between the difference in the NO_2 signals and the PTRMS measurements and it is unlikely that the differences between CRD and CLD can be explained by absorption of glyoxal or methylglyoxal in the CRD instrument.
During the Humppa campaign about 80 % of the measured NO_2 concentrations were below 500 pptv and about 5 % were smaller than 100 pptv as shown in the frequency distribution plot in Figure 6.4. The Boreal forest in Hyytiälä can be classified as remote except from occasional anthropogenic influence. Therefore, this campaign was a good opportunity to test the new instrument under very low NO_x levels. As already mentioned in section 3.3.2.8 (see Figure 3.22)

[9]PTRMS: Proton - Transfer - reaction mass spectrometry

the accuracy of the CRD instrument at low NO_x is strongly influenced by the background measurements. The determination of the NO_2 concentration in a synthetic air bottle used for zeroing is difficult, and leads to an decrease of the accuracy at lower NO_2 mixing ratios (at 100 pptv the accuracy is about 30 %).

Figure 6.5 shows the comparison of 5 min mean data between the CRD instrument and the CLD measurements (AG Fischer), which reported an accuracy of about 6 % during the campaign. The left site of the Figure (a)) shows the comparison of the entire data set whereas panel b) shows the comparison for values below 0.4 ppbv. The correlation between both instruments for both cases is very good (R^2 = 0.91), and both cases the intercept of the linear regression is very low (< 10 pptv). This indicates that the background measurements are not strongly influenced by higher NO_2 mixing ratios in the synthetic air bottle. The slope of the regression is for the entire data set 1.18 (note that this is now CLD/CRD. The ratio CLD/CRD during PARADE was 1.1), which, taking the low NO_2 mixing ratios and also the problems which occur during the campaign into account, is in good agreement. Focusing only on the values below 400 pptv the slope becomes even closer to unity. Therefore, the result of the first measurement under real atmospheric low NO_x condition for the newly developed CRD instrument shows a very good agreement with a well-established instrument and furthermore the results could be used to improve the instrument as shown in comparison during the Parade campaign. The comparison between the CRD and CLD during both campaigns (Humppa and Parade) showed that the ratio CLD/CRD did not change even though the operational environments were very different. It can be concluded that the CRD is intrinsically more accurate than the CLD due to the necessary calibration of the CLD.

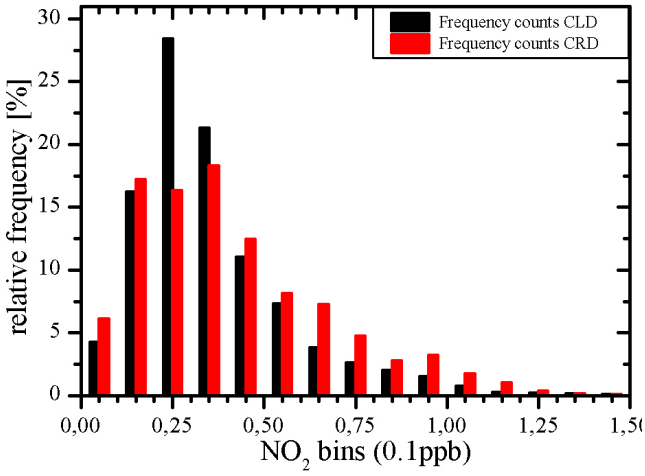

Fig. 6.4.: *Relative frequency distribution of the NO_2 concentration summarized in 0.1 ppbv bins*

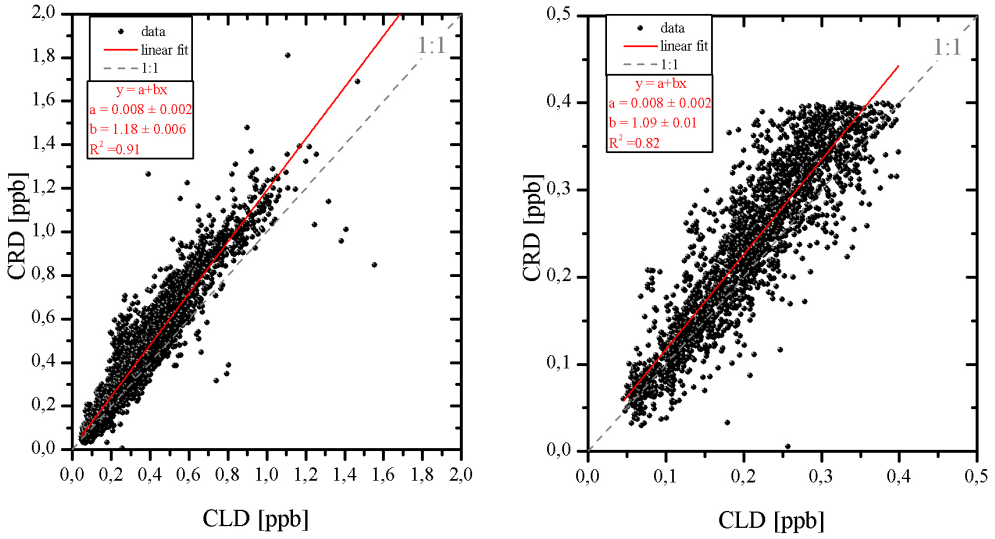

Figure 6.5.: *Comparison of a CLD instrument against CRD instrument during the HUMPPA-COPEC campaign 2010. Panel a) shows the the correlation of the entire data set except periods of instrumental problems and b) only for values lower than 400 pptv*

6.3. ∑PNs and ∑ANs measurements

The second cavity of the instrument was used to measure the sum of ambient NO_2 and the additional NO_2 from the thermal decomposition either from peroxy nitrates or from peroxy and alkyl nitrates. The precision of these measurements were similar to that of the NO_2 reference channel with a mean precision of about 22.7 ± 8.1 pptv . Therefore the detection limit either for the total peroxy nitrate or the sum of both nitrates can be calculated from the precision of both channels ($\sigma_{PAN} = \sqrt{\sigma_{Ref}^2 + \sigma_{TD}^2}$) and was about 70 pptv (2σ).

6.3.1. Determination of ∑PNs and ∑ANs

As described in section 3.3.2.6 and 3.3.2.7 the thermal dissociation of ∑PNs and ∑ANs to NO_2 occurs at different temperatures. Therefore, to detect all three species simultaneously a three channel instrument must be used. However, with the existing two channel instrument ∑PNs and ∑ANs could at least be measured by switching the air stream periodically prior reaching the cavities either through a quartz cell heated up to 200 °C (∑PNs + NO_2) or to one heated up to 450 °C (∑PNs + ∑ANs + NO_2). As described previously, this technique does not measure specific ∑PNs or ∑ANs but a sum (∑PNs, ∑ANs). During the campaign ∑PNs + NO_2 and ∑PNs + ∑ANs + NO_2 were measured for about 10 minutes alternately. Additionally every two hours the heated quartz cells were bypassed by a

third quartz cell which was held at ambient temperature to measure ambient NO_2.

These measurements were necessary to identify possible differences in the ambient NO_2 concentrations detected by both channels. $\sum$PNs and $\sum$PNs + $\sum$ANs concentrations are derived by subtracting the ambient NO_2 levels measured simultaneously in the reference channel. Therefore the NO_2 concentrations must be measured accurately in both channels. Figure 6.6 shows the comparison of the NO_2 measurements when bypassing the TD channels (i.e. both inlets at ambient temperature). After applying all corrections for both channels the comparison shows an excellent correlation with a slope of 0.9997 and an intercept of 0.8 pptv ($R^2 = 0.999$). To derive $\sum$ANs the $\sum$PNs mixing ratios must be subtracted from the overall signal. Due to switching between both heated channels the $\sum$PN measurements must be interpolated to calculate the $\sum$ANs mixing ratios. Due to their relatively long life time the changes in between switching the measurement modes is estimated to be small and therefore this interpolation method can be applied, under most conditions unless there is a very rapid air-mass change or local emissions.

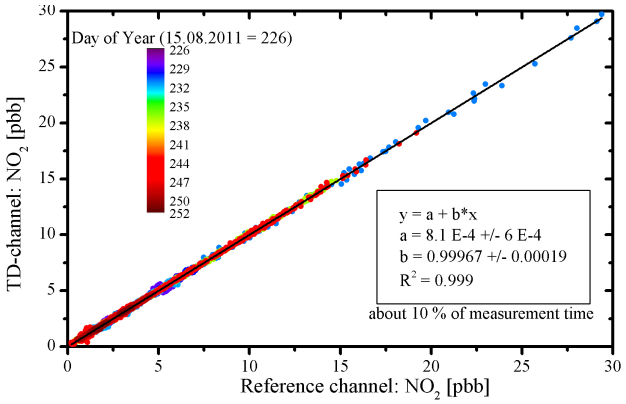

Fig. 6.6.: *Correlationplot between NO_2 mixing ratio of the TD-Channel using the bypass and the NO_2 reference channel*

6.3.2. Interferences of $\sum$PNs and $\sum$ANs during PARADE

As a consequence of the thermal dissociation method, the dissociation of N_2O_5 to NO_3 and NO_2 during nighttime, as described already in section 3.2, could lead to an additional NO_2 signal. A complete dissociation of N_2O_5 occurs in less than 1s at 90 ° C. In principle, if the TD-CRDS is located close to an instrument which measures N_2O_5 a direct correction for N_2O_5 is possible. However in practise N_2O_5 did not survive the long inlet tubing completely and accurate correction could not be applied for even though N_2O_5 measurements were available in PARADE. This affects mainly the $\sum$PNs measurement and less the $\sum$ANs measurement as any residual N_2O_5 would be present equally in both cavities. Only on one or two nights when the N_2O_5 mixing ratios were several ppbs and very variable it was not possible to derive $\sum$ANs mixing ratios. Therefore, no $\sum$PNs measurements are reported if the N_2O_5 levels exceed 150 pptv.

Beside N_2O_5 there are other trace gases with can thermally decompose to NO_2 at higher temperatures. Among there are trace gases like $BrONO_2$ and $ClONO_2$ which thermally decompose to NO_2 at 200 $°C$. Neither $BrONO_2$ or $ClONO_2$ are expected to be present in significant concentrations at the Feldberg, but may be regarded as potential interferences in environments heavily impacted by halogens and NO_x such as the Dead Sea.
For the ∑ANs additional species (like e.g. $ClNO_2$, $BrNO_2$, $IONO_2$) can also thermally decompose to NO_2 at 450 °C and therefore act as interference for the ∑ANs measurements. During the campaign, $ClNO_2$ was measured by a TD-CIMS instrument (shared same inlet line). Therefore when $ClNO_2$ was present, the additional NO_2 from its thermal decomposition to NO_2 could be corrected for.

6.3.3. Comparison of TD-CRDS with TD-CIMS

During PARADE, speciated PANs were measured using a TD-CIMS. The CIMS instrument is able to distinguish between different acyl peroxy nitrates such as PAN, PPN, MPN, while the TD-CRD measures the sum of all the individual nitrates. The TD-CIMS requires an in-situ calibration using a photochemical source of PAN. This PAN calibration source was characterized using the TD-CRDS instrument. As a consequence, it is expected that both instruments measure the same amount of PAN. Peroxyacetyl nitrate (PAN) is the most abundant PN in the atmosphere and contributes usually to about 70-90 % of the total [Roberts (1990)]. Figure 6.7 shows the comparison between the PAN measurements by CIMS and ∑PNs measured by the TD-CRD. The correlation between both measurement is very good (R^2 = 0.922) with a slope of 0.865 and and an intercept of 17 pptv which is consistent with the noise levels of the instruments. Assuming that PAN was measured equally sensitively in both instruments, this slope indicates that the sum of the other individual peroxy nitrate species (PPN, MPAN, APAN) is 13-14 %.

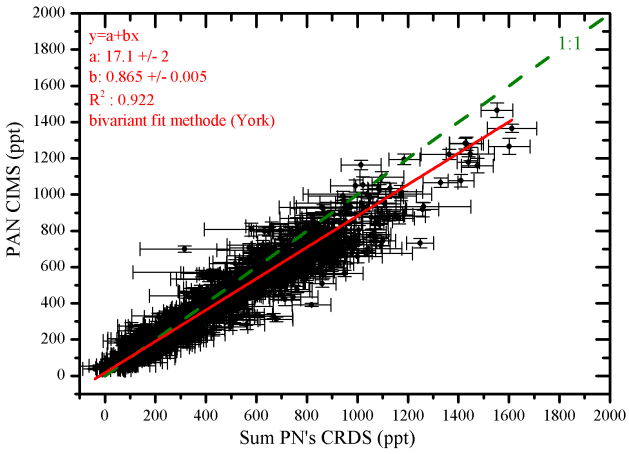

Fig. 6.7.: *Correlationplot between PAN measurements made by the MPI-CIMS and the sum of peroxy nitrates measured by the TD-CRDS*

6.4. Time series of NO_2, $\sum$PNs and $\sum$ANs

The measurements during the Parade campaign were performed from the 15.08.2011 to 10.09.2011. The NO_2 measurements started at the 16.08.2011 til the 09.09.2011 whereas the measurements of the $\sum$PNs and $\sum$ANs were recorded from the 17.08.2011 to 09.09.2011. The data coverage for all three species is very good with only a few interruptions due to inlet problems or instrument tests. An overview

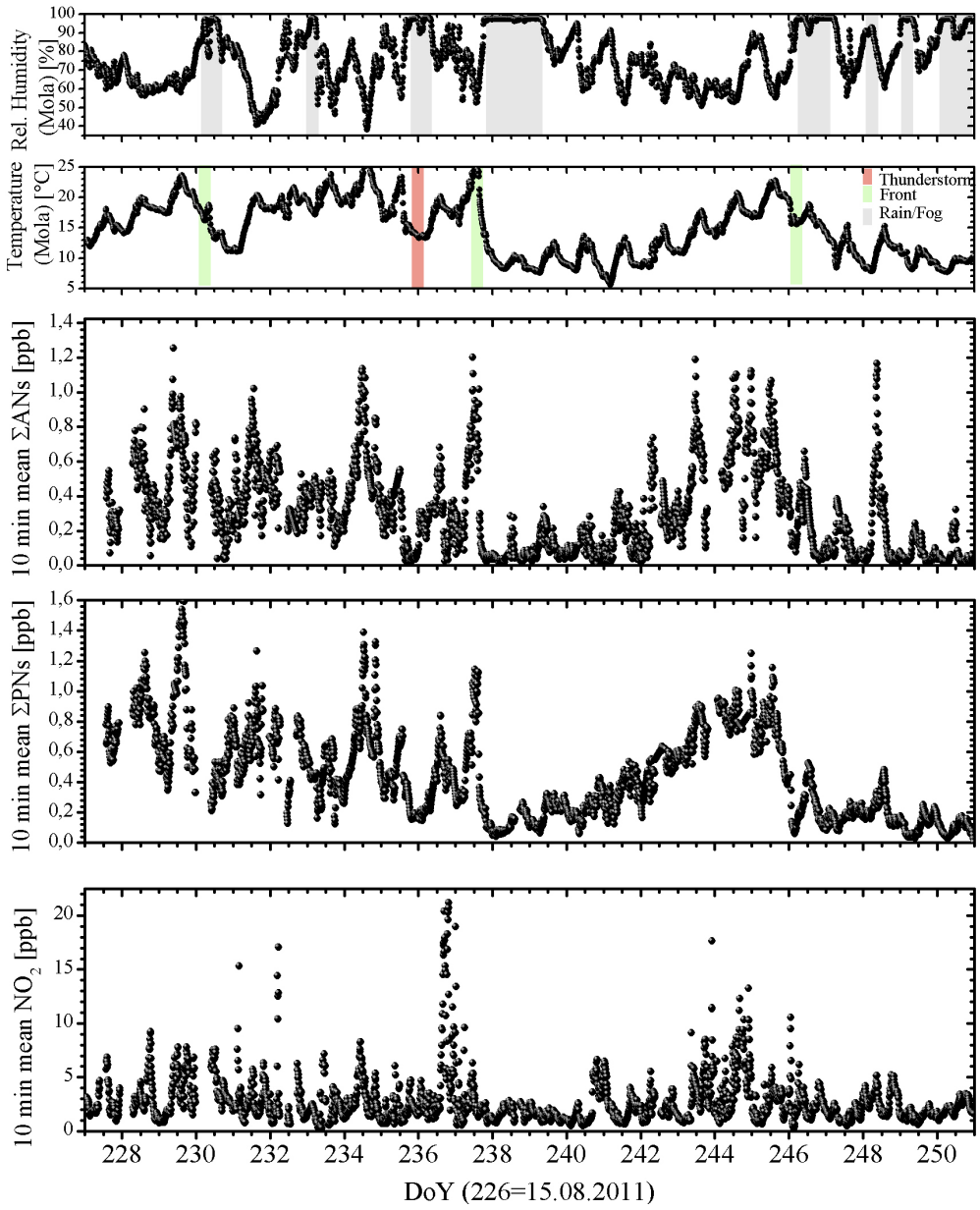

Figure 6.8.: *Timeseries of 10 min average of the NO_2, $\sum$PNs, $\sum$ANs, Temperature and relative humidity*

of the measurements is shown in Figure 6.8. $\sum$PNs varied from less than 0.1 to 1.8 ppbv with maximum values occurring during sunny periods. Similar mixing ratios of $\sum$ANs were measured (<0.1 - 1.6 ppbv). Both $\sum$PNs and $\sum$ANs showed pronounced variability. The two upper panels show the time series of temperature and relative humidity, providing a simple overview of the meteorological conditions during the campaign. The first week of the campaign was influenced by a warm and unsettled weather system with temperature up to 24 ° C. After a frontal system passed the site on the 19.08 the second week was influenced by a high pressure system with warm temperatures (maximum temperature up to 28 ° C). At the end of this warm period a thunderstorm hit the site at the 24/25.08 followed by a cold front on the 26.08. After this cold front the temperature decreased to about 10 ° C and less. The negative trend in the temperature is seen in several trace gases which are driven mostly by photochemistry such as O_3 or $\sum$PNs and $\sum$AN. After the cold front passed the site the third week was influenced by a stable high pressure system with increasing temperatures again. At the end of this stable high pressure system a further cold front passed the measurement site (04.09.11). A cold unsettled weather system followed this front with lower temperatures.
NO_2 was much less influenced by the meteorological conditions compared to $\sum$PNs or $\sum$ANs. Most of the time NO_2 mixing ratios were below 10 ppbv except of one day on which the mixing ratios increased to more than 20 ppbv. These higher NO_2 concentrations were typically associated with a wind direction from the south east where the Frankfurt region is located. The NO_2 mixing ratios varied during the campaign between 0.27 and 20.2 ppbv with a median concentration of about 2.1 ppbv.
The temporal behaviour of the $\sum$PNs and $\sum$ANs were similar, but not identical. Both species are formed via the reaction of peroxy radical via the reaction with either NO_2 ($\sum$PNs) or NO ($\sum$ANs). Therefore both species are closely related to photochemical activity. At the beginning of the campaign the $\sum$PNs were relatively variable with maximum values up to 1.6 ppbv. The passage of a frontal system was associated with a decrease in the $\sum$PNs mixing ratios. But on the other hand in the third week after the second front passed the site the $\sum$PNs mixing ratios increase again constantly during the high pressure system with increasing temperature. Therefore the $\sum$PNs mixing ratio are well correlated with temperature.
$\sum$ANs showed similar behaviour to the $\sum$PNs but with less pronounced correlation to temperature. The lifetime of alkyl nitrates can be much longer than the life time of the peroxy nitrates under these conditions depending on the class of nitrate. $\sum$ANs formed by OH addition have a hydroxyl group and are soluble. In this case the deposition velocities are large which shorten the lifetime of these kind of alkyl nitrates. Therefore, although $\sum$PNs and $\sum$ANs have similar formation processes due to the different lifetime of both species the temporal distribution of

both do not have to be totally similar.
In addition to the trace gases, temperature and relative humidity are also shown. Periods of rain or fog (Gray shaded areas in relative humidity) are highlighted as well the passing of a frontal system (green shaded areas) and a thunderstorm (red shaded area). The temperature during the campaign varied between very cold temperatures (about 5 °C) and very warm temperatures (up to 25 °C). Several periods during the campaign were influenced by rain or at least fog but in between also sunny and warm periods occurred. Additionally the time series of several other measured trace gases during the campaign are shown in Appendix C.1.

6.5. Diel profiles

Diel profiles were calculated for various atmospheric compounds and also for the meteorological parameters. A overview of some of these compounds are shown in Figure 6.9. They were obtained by averaging the individual profiles for all 26 days during the campaign. The process of averaging the diel profiles over a sufficiently long time interval amplifies features which are dependent on the relative time of day, such as ozone production or other photochemical related reactions. Features caused by factors which operate on time scales longer than 24 hours are averaged out, therefore their effect essentially disappears for a sufficiently large data set. For example the weather pattern can act as such a factor. Although it can cause e.g. large changes in the ozone concentration, it is independent of the time of day, so that the average profile should essentially be free of its influence. The trace gases in the figure show all a pronounced diel profile.
The diel profile of ozone shows a slow decrease in its level overnight with the minimum concentration around 07:00 to 08:00 UTC. This is followed by an increase of approximately 11 ppbv during the day until a maximum is reached in the afternoon for about 1-2 hours. After about 16:00 UTC the ozone mixing ratios decrease constantly again. The daytime increase in ozone is due its photochemical production via VOC oxidation and also advection from other areas.
The diel profile for $\sum$ANs is different to that of ozone. During the night the alkyl nitrates show a relative constant level of about 250 pptv. Between 05:00 and 06:00 UTC the mixing ratios increased constantly to reach a maximum of about 500 pptv at about 11:00-12:00. After this relatively short maximum period the mixing ratios decreased constantly until about 18:00-19:00 UTC to acquire the nearly constant nighttime levels. This diel pattern is similar to the profile of radiation or NO.
The diel profile of $\sum$PNs is more similar to the ozone profile but with a slight shift of the maximum. The profile of the $\sum$PNs also showed a long drop in the mixing ratio overnight with the minimum (about 330 pptv) around 05:00 to 06:00. This is followed by an increase of about 300 pptv during the day until a maximum is reached in the early afternoon (13:00 - 15:00). This maximum is reached approxi-

mately one hour before the ozone maximum. From about 15:00 the ∑PNs mixing ratios decreased constantly again. The diel profile of NO_2 is more complex due

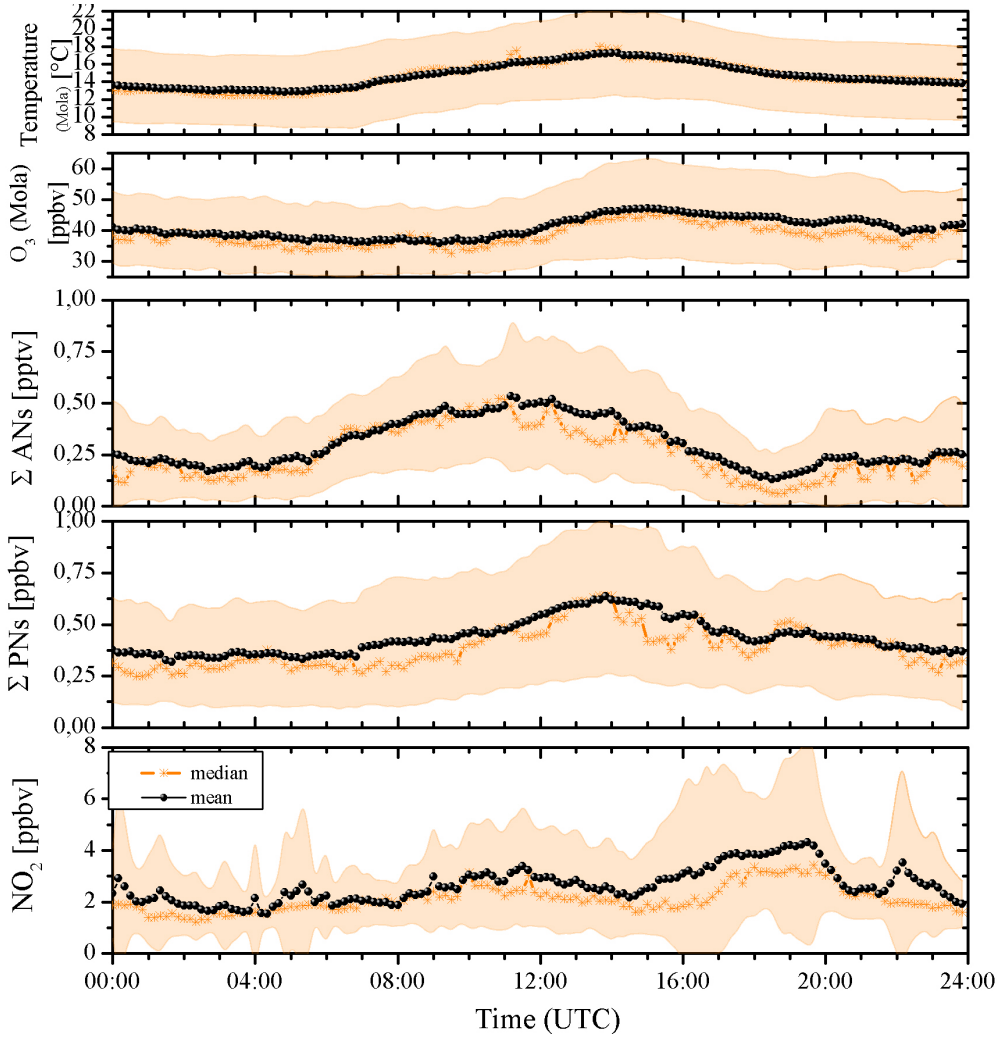

Figure 6.9.: *Diel profile of NO_2, ∑PNs, ∑ANs, O_3 and Temperature for an average of 26 days*

to its involvement in several chemical processes. The minimum of NO_2 is about 03:00 to 04:00 in the morning. This is followed by a slow increase of NO_2 until about 12:00 except a period of about one hour between 05:00 and 06:00 which is mainly related to the morning rush hour. After this first maximum at about 12:00 the NO_2 mixing ratios decreased again until about 14:00 to 15:00. The decrease is again followed by an increase until about 20:00 which is also influenced by the traffic situation. From 20:00 onwards the NO_2 mixing ratios decreased constantly.

6.6. Wind Sectors

As already mentioned in section 4.2 the measurement site is located at the summit of a mountain but still influenced by the surroundings. In the south east of the site lie Frankfurt and its industrial complex at $\sim$ 20 km distance. From the south-west, the site is influenced by the large cities of Wiesbaden and Mainz (with a distance of about 25 km). The area 50-100 km north of the measurement site is lightly populated and devoid of major industry. Figure 6.10 shows the wind distribution during the campaign. As clearly seen the site was mostly influenced by air masses from the SW - NW direction. The Kleiner Feldberg is close to the Großer Feldberg and the Altkönig which are mountains of similar height. Due to this relatively complex topographical environments the meteorological conditions (especially the wind pattern) on top of the mountains are quite difficult to interpret. However, four different wind sectors were selected to distinguish between the different influences of the surroundings. These four sectors were shown in Figure 4.11 of section 4.2.3. Sector A (North Forest: 285-300 °) indicates the northern sector which will be least influenced by anthropogenic emissions. Sector B (Western Forest 247-285 °) is also less influenced by higher anthropogenic emissions. Both sectors should reflect the more rural character of the measurement site. Sector C (Mainz-Wiesbaden 192-242 °) covers the cities of Mainz and Wiesbaden. Assuming a distance of about 25 km and an averaged wind speed of about $3.5\frac{m}{s}$ a typical transport time of about 2h. The last sector which was chosen according to the local wind direction and the environment is sector D (Frankfurt: 90-157 °). The average wind speed of this sector was about $4\frac{m}{s}$ resulting in a typical transport time of about 1.4 h.

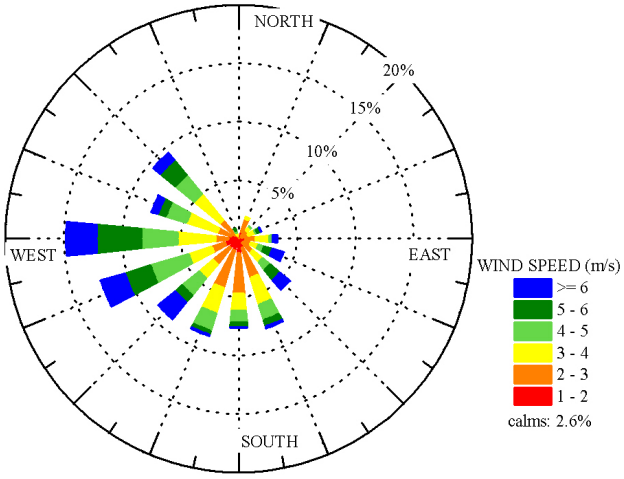

Fig. 6.10.: *Frequency distribution of the actual mean wind direction during the campaign*

The measured trace gases in this thesis showed also a dependence on wind direction. Figure 6.11 shows windrose plots of NO_2, $\sum$PNs, $\sum$ANs and additionally CO. CO was chosen as an anthropogenic tracer. As clearly seen in the CO plot the site is influenced from more polluted air masses when the air reached the site from more southern direction which includes the urban structures of Frankfurt and Mainz/Wiesbaden. Similar to the CO plot also the plots of NO_2, $\sum$PNs and

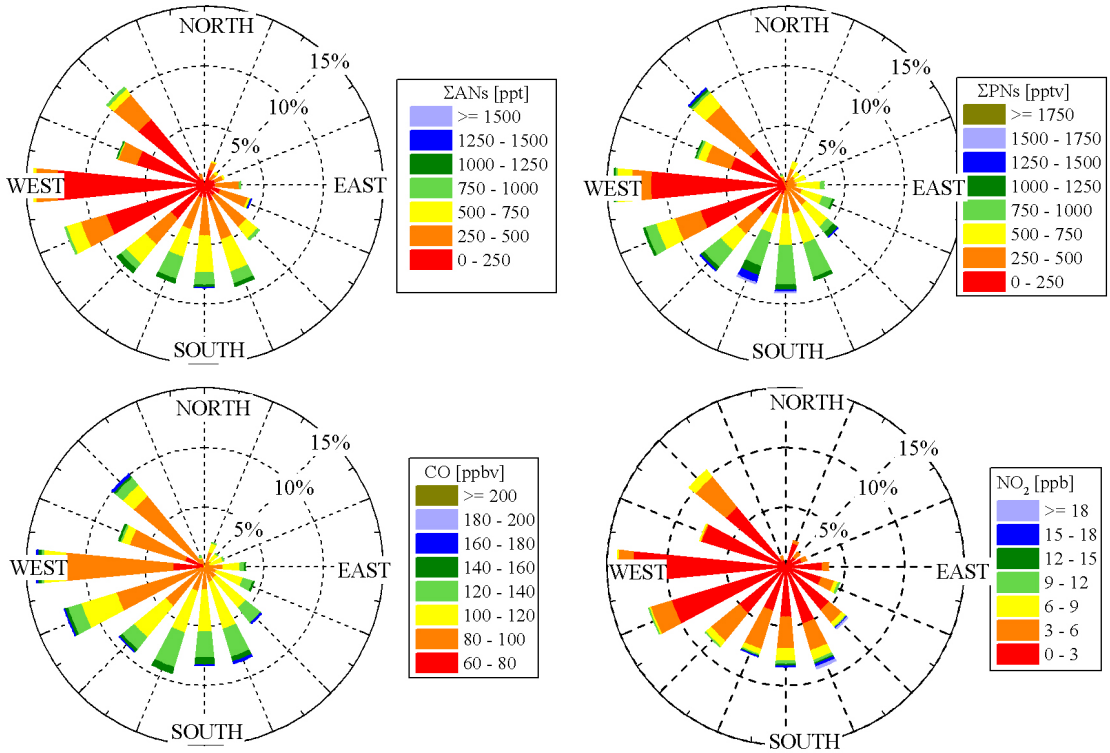

Figure 6.11.: *Frequency distribution for NO_2, CO, $\sum$PNs and $\sum$ANs during the campaign*

$\sum$ANs showed higher mixing ratios from the more urban areas. All of these plots showed that the west to northern direction is much less polluted compared to the southern urban influences. For Sector A the NO_2 mixing ratios varied between 0.3 to 7.6 ppbv with a mean of about 2.4 ppbv. The $\sum$PNs varied between the limit of detection and about 1.3 ppbv whereas the $\sum$ANs varied between the limit of detection and about 1 ppbv. The mean mixing ratios for $\sum$PNs and $\sum$ANs were 320 pptv and 180 pptv, respectively. For Sector B the value are a bit lower than in Sector A. NO_2, $\sum$PNs and $\sum$ANs showed only a mean mixing ratio of about 1.6 ppbv, 230 pptv and 140 pptv respectively. Compared to the more rural sectors A and B, Sectors C and D showed clearly increased mixing ratios in NO_2 but also in $\sum$PNs and $\sum$ANs. The mean NO_2 mixing ratio is about 3 ppbv for both sectors. The $\sum$PNs mixing ratio increased slightly from 530 pptv in Sector C to 580 pptv in Sector D. For the $\sum$ANs the values are very similar with a slightly lower mixing ratio in Sector D (380 pptv and 400 pptv in Sector C). An analysis based on local wind directions as shown in the results from the DOMINO campaign is interesting for short lived compounds but it is difficult for typically longer lived traces gases such as $\sum$PNs or $\sum$ANs. The data suggest that the $\sum$ANs are shorter lived than the $\sum$PNs (higher variability and more obvious diel variations) indicating that hydroxyalkyl nitrates contribute substantially to the $\sum$ANs.

6.7. $\sum$PNs and $\sum$ANs contribution to NO_y

In the last 30 years, total NO_y and several contributing nitrogen oxides have been measured. Most of these studies showed that the sum of all individual NO_y species (typically $NO+NO_2+PN+HNO_3+HONO$) are less than the total measured NO_y, hence the term 'missing NO_y' was used [Buhr et al. (1990); Fahey et al. (1986); Parrish and Buhr (1993); Ridley et al. (1990); Singh et al. (1996)]. The missing NO_y was often related to instrumental artefacts but model results from Trainer et al. (1991) suggested that alkyl nitrates can contribute a large fraction. In 2003, Day et al. (2003) showed, that the fraction of total alkyl nitrates to the total NO_y is in the order of 10-20%.
As shown in section 2.3.2.2, while the mechanism of formation of alkyl nitrates is understood, the individual branching ratio for each VOC are poorly known. For example the branching ratio for isoprene is reported to be in the range 4 - 15 %. This suggests that further studies of alkyl nitrates are important for the understanding of the nitrogen related atmospheric processes.
During this campaign many individual NO_y species were measured with the important exception of nitric acid. On the Kleiner Feldberg only two datasets of HNO_3 have been reported. Fuzzi et al. (1994) reported HNO_3 values of about 0.1 - 1 ppbv in November 1990. The second data set for HNO_3 was measured in summer 2012 [INUIT campaign 2012, Phillips et al. (2012a)]. HNO_3 mixing ratios varied in this summer between about 0.2 - 2.5 ppbv with an averaged daytime maximum of about 1.2 ppbv. However, the summer 2012 was a warmer and drier summer than 2011 and it is expected that photochemical production of HNO_3 was greater and that losses due to deposition, especially wet deposition is smaller.
For this reason, the diurnal profile for HNO_3 was taken from the mean diurnal profile derived from the INUIT campaign 2012 (daytime maximum of about 1.2 ppbv) scaled down by 25 %. Figure 6.12 shows the averaged diurnal profile of the relative fraction of each species for the entire campaign. This Figure includes only daytime data with a global radiation larger than $20\frac{W}{m^2}$. The upper panel of the Figure shows the diurnal NO_y profile. The averaged NO_y mixing ratios varied between less than 4 ppbv and about 7 ppbv with an averaged value of about 5.3 ppbv. The lower panel is a stack plot for the individual fraction to the total NO_y. The contribution of NO increased from about zero during nighttime to about 10-15 % at noon and decreased monotonically til dawn. The NO_2 fraction is dominant, varying between 45% up to 75% with an average contribution of about 50%. The fraction of NO_2 is relatively constant til about 15:00 and increased constantly tiil 18:00. The contribution of peroxy nitrates to NO_y is about 10 % with no significant variations during the day. Similar to the peroxy nitrates the alkyl nitrates showed less variations during the day. In the early morning hours a strong, but short increase is followed by a longer fairly constant period. In the late afternoon the fraction of alkyl nitrates decreased again. The contribution varied between 4

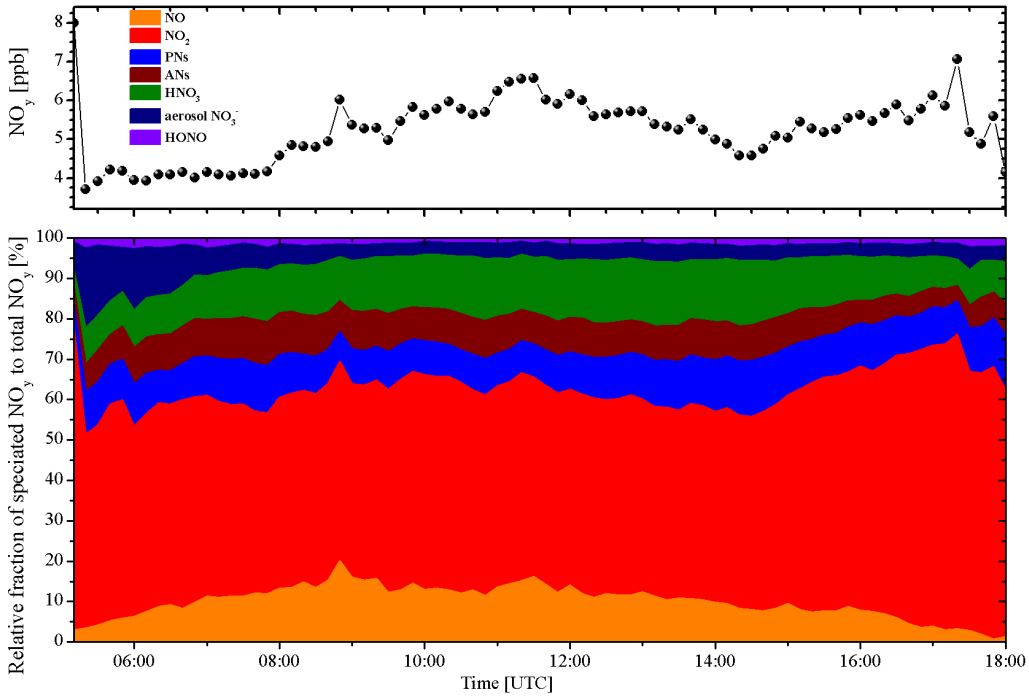

Figure 6.12.: *Averaged diurnal profile of total NO_y (upper panel) and the relative fraction of individual NO_y species to the total amount of NO_y (lower panel). HNO_3 data are an estimate based on measurements in 2012. Orange represent the NO fraction, red: NO_2, blue: total peroxy nitrates, brown: total alkyl nitrates, navy blue: aerosol NO_3 and purple: HONO*

and 11 % with an averaged value of about 8-9%. The estimated HNO_3 contribution (HNO_3 maximum estimated to be about 750 pptv) increased during the day from about 8 % to about 16 % at about 14:00-15:00. That increase followed a rapid decrease to about 7-8%. On average HNO_3 contributed to about 12-13 % to the total NO_y. The fraction of HONO contributed only a $\sim$ 2%. The fraction of particulate nitrates are less important to the total NO_y budget during the day than compared to the night. During the day the fraction is in the order of 3-5 %. An overview of diurnal profiles contributing to total NO_y is shown in Appendix C.2.

The contribution of alkyl nitrates is thus of the order of 10 % during the day which is in good agreement with several other publications [e.g. Day et al. (2003, 2009)]. Figure 6.13 shows a time series for the entire data set of total NO_y and the measured contribution from the individual species. This Figure focusses only on the measured NO_y species and does not include HNO_3. The variation of the NO contribution showed a clear diurnal pattern whereas that of NO_2 has no clear pattern as already known from the NO_2 time series itself and low variability. The organic nitrates showed both similar trends in which a diurnal pattern is visible but less

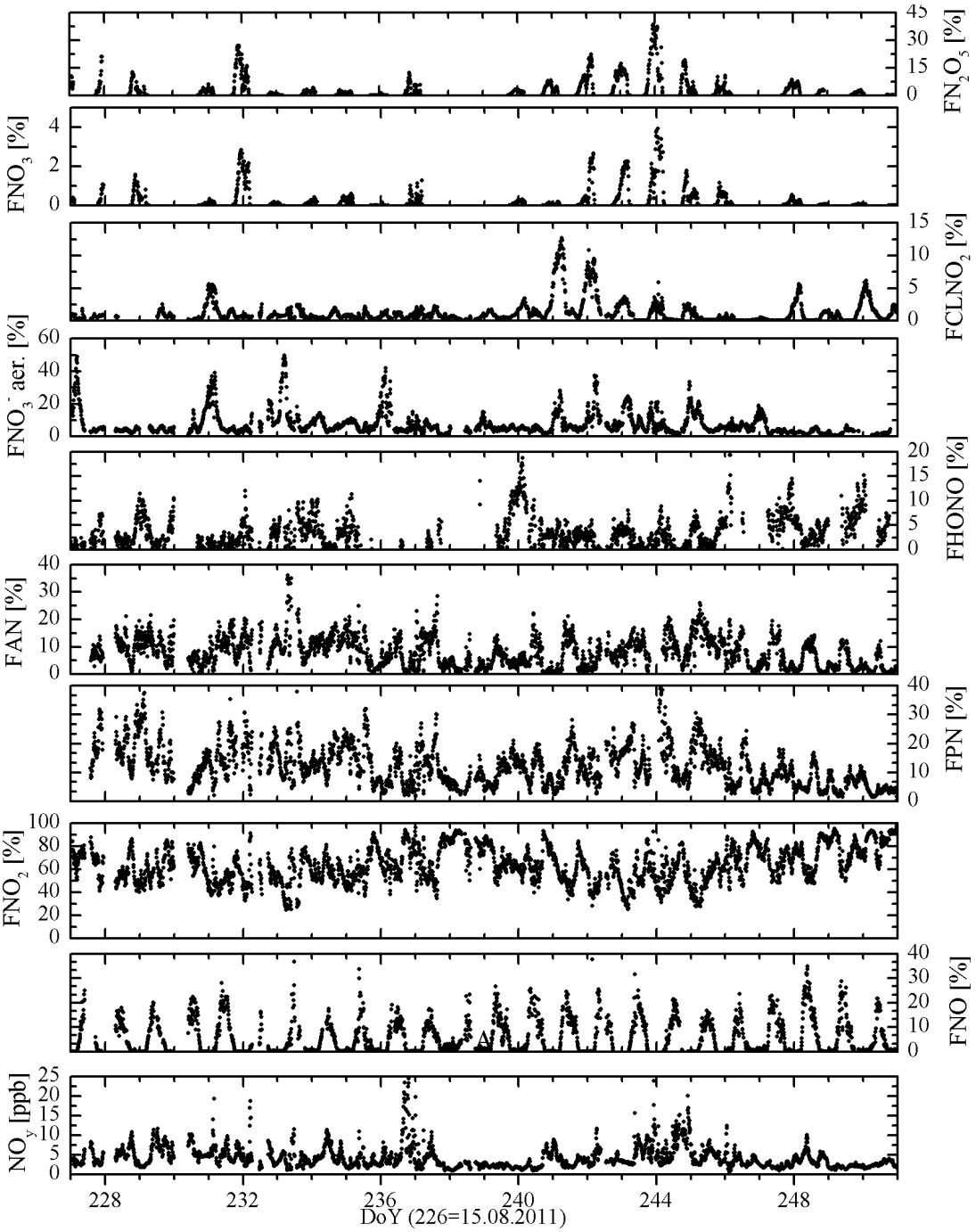

Figure 6.13.: *Time series of total calculated NO_y (bottom) and the contribution of the different measured individual NO_{yi} (e.g. FNO: Contribution of NO).*

pronounced NO. The variation is quite large for both, with a variation between 2 and 40 % for the peroxy nitrates and about 1 to 36 % for the alkyl nitrates. Both showed in general larger fraction during the beginning of the campaign when it was warmer and a lesser contribution during the rainy periods.

During nighttime the contribution of the individual species is different to the daytime contribution. The formation of the alkyl nitrates during nighttime via the reaction of RO_2 with NO is suppressed due to the absence of NO, so that they can be formed only by NO_3 reaction with alkenes. Additional species which contribute to NO_y which are present in the absence of light (e.g. NO_3, N_2O_5). During this campaign NO_3, N_2O_5 and $ClNO_2$ were present in the atmosphere on most nights. Therefore total NO_y is a composite of NO, NO_2, ∑PNs, ∑ANs, HNO_3, HONO, aerosol NO_3^-, NO_3, 2*N_2O_5 (two nitrogen containing molecules) and $ClNO_2$. Unfortunately no HNO_3 data were available but are expected to be small due to partioning to the particle phase as NO_3^-. The averaged nocturnal NO_y mixing ratios varied between 3 and 5.8 ppbv. NO_2 is the dominant fraction during nighttime with a relatively constant decrease from about 79 % at beginning of the night to about 50% at the end of the night, whereas NO is insignificant. For the organic nitrates the difference between day and night depends on the nitrate. Whereas the peroxy nitrates showed only small variations from day to night, the alkyl nitrates are on average almost a factor of 2 less during night than during day. Both nitrates have their smallest contribution at the beginning of the night with about 8% and about 3% for the peroxy and alkyl nitrates respectively. Both increase slightly during night to about 10 % for the peroxy nitrates and about 6 % for the alkyl nitrates. HONO and particulate nitrate have a much larger contribution during night. On average HONO contributed to about 3-4 % to NO_y and the particulate nitrate covered, although $ClNO_2$ had peak contributions of up to 15 %, about 10-11%. NO_3 and $ClNO_2$ have only a smaller contribution to the budget. N_2O_5 had on average a contribution of about 7 % but with maximum contribution of about 14%.

To summarize, during the PARADE campaign NO_2 was the dominant NO_y fraction (50-60%). The organic nitrates contributed about 20 % to NO_y (∑PNs = 12% and ∑ANs = 8%). The peroxy nitrates showed only little day to night variation whereas the alkyl nitrates showed a clear day to night variation. Therefore a significant amount of NO_y is stored in organic nitrates which can act as reservoir species for NO_x.

6.7.1. Contribution to NO_z

It is sometimes useful to consider NO_x (reactive, short lived nitrogen oxides) separately from the longer lived ones (NO_z). The higher oxides of nitrogen NO_z (NO_z = NO_y - NO_x) are formed via reactions including NO_x and the odd hydrogen radicals ($HO_x \equiv OH + HO_2 + RO_2$). The more oxidized NO_z species may act as reservoirs (e.g. ∑PNs and ∑ANs) or sinks (e.g. HNO_3) for the NO_x radicals. Due to their potential importance as reservoir species (depending on the kind of alkyl nitrate), the contribution of alkyl nitrates to NO_y but also to NO_z is an important issue in the nitrogen related chemical processes. Therefore, measurements of the alkyl

nitrates are necessary in terms of understanding what the fate of the higher oxides of nitrogen are. Figure 6.14 shows the contribution between the NO_z species as an

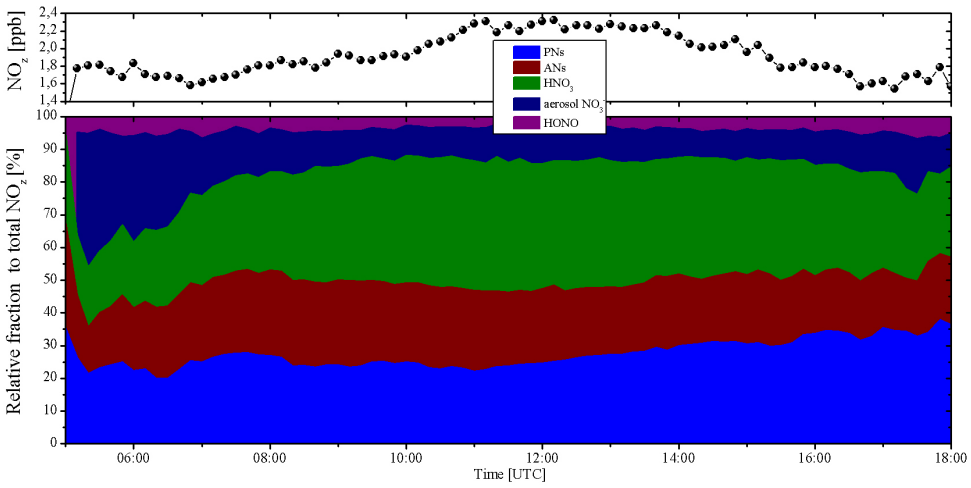

Figure 6.14.: *Averaged diurnal profile of total NO_z (upper panel) and the relative fraction of individual NO_z species to the total amount of NO_y (lower panel). HNO_3 data are an estimate based on measurements in 2012. blue: fraction of total peroxy nitrates, brown: total alkyl nitrates, navy blue: aerosol NO_3 and purple: HONO*

averaged diurnal profile for the sunlit atmosphere. The major contribution to NO_z is on average HNO_3 with about 33%. Note that this diurnal profile of HNO_3 was not measured during the campaign and it is an estimate based on measurements performed in summer 2012. Due to its relatively short lifetime HNO_3 is considered to be a sink for NO_x. The second most important components of NO_z are the peroxy nitrates with a contribution of about 27 %. The alkyl nitrates represent the third most important fraction of NO_z with about 22 % on average. The contribution of alkyl nitrates increased from about 14% in the early morning up to about 26 % at about 09:00 UTC. From 09:00 to dawn the alkyl nitrate contribution decreased constantly again to about 15-17 %. Particulate nitrate and HONO contributed only insignifcantly to the total NO_z.
This result indicates an important contribution of alkyl nitrates to the total higher oxides of nitrogen (NO_z) with implications for the transport of NO_x to remote areas and the associated ozone production and also photochemical production of O_3 in the NO_x source region.

6.8. Comparison with previous PN measurements

During the summer 1998 and 1999 an intensive measurement campaign focussing on peroxy radicals and ozone production was performed by the University of Frankfurt at the Taunus Observatory on the summit of Mt. Kleiner Feldberg. Beside

measurements of ozone and peroxy radicals, peroxyacetyl nitrate (PAN) was also monitored using the conventional GC approach. A complete overview of these measurements can be found in the Phd thesis of G. Handisides [Handisides (2001)]. Figure 6.15 shows the diurnal variation of the measurements performed during the Parade campaign (upper panel) and the measurements during the summers 1998 and 1999 (bottom panel). In addition to the measurements of Handisides the PAN measurements during PARADE performed by TD-CIMS is shown (red). The di-

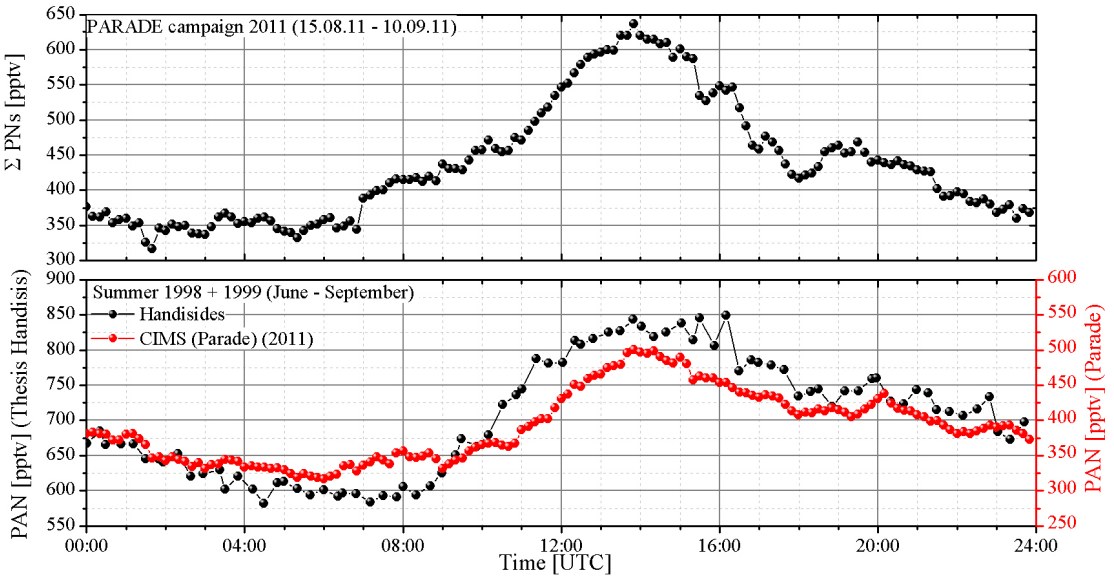

Figure 6.15.: *Diurnal profile of total peroxy nitrates druing PARADE (upper panel) and the profile of PAN from measurements during summer 1998 and 1999 [bottom panel]*

urnal trend is very similar for all profiles. They have their maximum at about 14:00 UTC and showed a similar difference between the minima and maxima values (about 250-300 pptv). The only significant difference between the profiles is reflected in the absolute mixing ratios. Whereas during the PARADE campaign the averaged maximum mixing ratios were in the order of about 600-650 pptv, during the measurements in the summer 1998 and 1999 the averaged maximum levels were in the order of about 800-850 pptv. However, in deriving this diurnal profile Handisides considered only days with high RO_x mixing ratios and sunny conditions. Therefore this diurnal profile will not be representative for the entire measurement period. Excluding daily profiles from the Parade data set during less sunny conditions increases the mean mixing ratios by about 100-150 pptv. The differences to Handisides is thus explained by the chosen data sets and the prevailing meteorological conditions.

6.9. Production of $\sum$ANs and Ozone

As discussed in section 2.3.1 the production of $\sum$ANs and ozone have very similar chemical pathways involving oxidation of NO. AN are produced during the day via the reaction of an peroxy radical with NO, the peroxy radicals being mainly formed by oxidation of VOCs by OH. The reaction mechanism for the formation of alkyl nitrates and ozone is:

$$\mathrm{OH + RH + O_2 \longrightarrow RO_2 + H_2O} \tag{6.1}$$
$$\mathrm{RO_2 + NO + M \longrightarrow RONO_2 + M} \tag{6.2}$$
$$\mathrm{RO_2 + NO \longrightarrow RO + NO_2} \tag{6.3}$$
$$\mathrm{RO + O_2 \longrightarrow R'C(O) + HO_2} \tag{6.4}$$
$$\mathrm{HO_2 + NO \longrightarrow OH + NO_2} \tag{6.5}$$
$$\mathrm{NO_2 + h\nu \longrightarrow NO + O} \tag{6.6}$$
$$\mathrm{O_2 + O + M \longrightarrow O_3 + M} \tag{6.7}$$

The RO_2 radical reacts primarily with NO to form either an alkyl nitrate (reaction 6.2) or an alkoxy radical and NO_2 (reaction 6.3) where the branching ratio for the alkyl nitrate formation is given by $\alpha = \frac{k_{6.2}}{k_{6.2}+k_{6.3}}$. The alkoxy radical produced in reaction 6.3 reacts with O_2, in most cases producing an aldehyde or a ketone and HO_2 (reaction 6.4). HO_2 then oxidizes NO producing OH and a second NO_2 (reaction 6.5). Via the photolysis of NO_2 ozone can be formed (reactions 6.6 and 6.7).
Therefore, the net alkyl nitrate production from the series 6.1 - 6.2, which terminates the catalytic chain, is:

$$\alpha(\mathrm{RH + OH + NO + O_2 \longrightarrow H_2O + RONO_2}) \tag{6.8}$$

For the ozone production the net reaction for the series 6.1 - 6.3 - 6.7 is:

$$(1-\alpha)(\mathrm{RH + 4\,O_2 + h\nu \longrightarrow H_2O + R'C(O) + \gamma O_3}) \tag{6.9}$$

where γ represents the number of O_3 produced and is two for many hydrocarbons. Since the reactions 6.2 - 6.7 are fast and nearly quantitative, the instantaneous AN or O_3 production rate is the weighted sum of the contribution from the individual hydrocarbons to reaction 6.1.

$$P_{\sum \mathrm{ANs}} = \sum_i \alpha_i k_{OH+RH_i}[OH][RH_i] \tag{6.10}$$
$$P_{\mathrm{O_3}} = \sum_i \gamma_i(1-\alpha_i) k_{OH+RH_i}[OH][RH_i] \tag{6.11}$$

Therefore the use of equations 6.10 and 6.11 along with the observed hydrocarbon mixing ratios, the rate constants and the alkyl nitrate branching ratios enables

the ∑ANs observations to be interpreted. During the campaign, in addition to the biogenic VOCs a large set of NMHC which act as precursor for the ∑ANs production were measured. These are listed in Table 6.1 together with their mixing ratios, rate constants and branching ratios. The rate constants and the branching ratios were taken from Rosen et al. (2004) and references therein. For the major compounds laboratory studies for the branching ratio α are known but still carry a relatively large uncertainty. When measurements of α was unavailable, a branching ratio was estimated by analogy to a closely related compound [taken from Rosen et al. (2004)]. This values are highlighted with (E). To calculate the production rate for the alkyl nitrates and ozone the OH concentration must be known beside the concentration of the hydrocarbons. The non methane hydrocarbon mixing ratios were measured using GC-FID [10] method from the 15.08.11 til the 04.09.11. Therefore calculation of the production rate can only be made for this period. The biogenic VOCs and and aromatics were measured using TD-GC-MS [11] from the 16.08.11 to the end of the campaign (10.09.11). OH was measured via the LIF technique, but unfortunately with poor data coverage. For the short periods were OH measurements were available a linear correlation to $J(O\,^1D)$ was observed, and was used to determine the OH concentration during the other days. The maximum OH concentrations during the campaign were estimated to be in the order of about $2 \times 10^6 \frac{molec}{cm^3}$ with an associated error of a factor 2.
The anthropogenic, organic precursors for alkyl nitrates and ozone production were typically in the low ppbv range. The daily median values for the complete campaign varied between 14 pptv for cis-2-butene and about 570 pptv for ethane and pentene. In some periods higher concentrations were encountered with propene increased up to 18.5 ppbv and butadiene to about 10 ppbv. The median daytime values of biogenic VOCs varied from about 6pptv for p-cymene to about 85 pptv for toluene. Maximum levels were reached up to 400 pptv for toluene and 16 pptv for p-cymene. Isoprene mixing ratios varied between 1 and 220 pptv which an median value of about 44 pptv. Diel profiles from each hydrocarbon used for this analysis are shown in Appendix C.3. Table 6.1 shows the median mixing ratios for different hydrocarbons for the time period between 11:00 and 13:00 UTC (similar to the analysis shown in Rosen et al. (2004)). This time window was chosen due to the maximum OH concentration during the day with subsequently highest ∑ANs production rates. The averaged data comprise only days with high photochemical activations. For the later analysis the time period from DoY [12] 226 to 246 was chosen with the exception of DoY 230, 238, 239 and 242. These days were not included in the analysed data due to lower insolation. The calculated median OH concentration for this period was about $1.2 \times 10^6 \frac{molec}{cm^3}$.

[10] GC-FID: Gas Chromatography - Flame Ionization Detector
[11] TD-GC-MS:Thermal dissociation - Gas Chromatography - Mass Spectrometer
[12] DoY: Day of Year

Figure 6.16 shows the diurnal profile of the measured AN mixing ratios for the chosen time period. A nighttime background of about 300 pptv was observed with an increase of approximately 300-350 pptv by circa 12:00 UTC.

Table 6.1.: *Calculations of $\sum AN$ and O_3 Production from each the Hydrocarbons measured during the campaign, as described by Equations 6.10 and 6.11. The rate constants, α and γ values are taken from Rosen et al. (2004). Only α values for limonene and myrcene were taken from Pratt et al. (2012). Mixing ratios of the Hydrocarbons are median values from the time period 11-13 UTC. Median OH concentration during that period was about $1.2 \times 10^6 \frac{molec}{cm^3 s}$*

Trace gas	Mix ratio pptv	k_{OH} $\times 10^{11}$ molec/ cm^{-3} s^{-1}	γ	α	$P_{\sum ANs}$ pptv hr^{-1}	P_{O_3} pptv hr^{-1}
Alkenes						
Ethene	246	0.85	2.00	0.0086	0.078	17.94
Propene	105	2.63	2.00	0.015	0.178	23.4
cis2-butene	15	5.60	2.00	0.037 (E)	0.13	6.8
1-pentene	560	3.14	2.00	0.05 (E)	3.77	143.3
1,3 butadiene	240	6.60	2.00	0.07	4.8	128
Isoprene	85	10.1	2.00	0.044	1.63	71
Limonene	28	17.1	2.00	0.28	5.8	30
α - pinene	49	5.37	2.85 (E)	0.18	2.05	26.5
myrcene	20	21.5	2.00 (E)	0.18 (E)	3.36	30.6
p-cymene	5	1.51	2.00 (E)	0.03	0.01	0.62
Aromatics						
Benzene	78	1.23	2.00	0.10 (E)	0.42	7.5
Toluene	126	0.60	2.00	0.10 (E)	0.33	5.89
o-xylene	21	1.37	2.00	0.10 (E)	0.13	2.3
m,p - xylene	46	1.43	2.00	0.10 (E)	0.29	5.1
Ethylbenzene	26	7.10	2.00	0.10 (E)	0.8	14.5
Alkanes						
Ethane	590	0.026	2.00	0.019	0.013	1.3
Propane	330	0.115	2.00	0.036	0.06	3.16
n-butane	265	0.254	2.85	0.077	0.22	7.65
i-butane	131	0.233	2.85 (E)	0.255	0.34	2.8
i-pentane	282	0.390	2.85 (E)	0.35 (E)	1.67	8.8
n-pentane	211	0.394	2.85 (E)	0.105	0.38	9.2
Hexane	56	0.561	2.85 (E)	0.141	0.19	3.32
HCHO	1940	0.85	2.00	0	0	143
CO	116650	0.024	1.00	0	0	121
Total					26.4	807

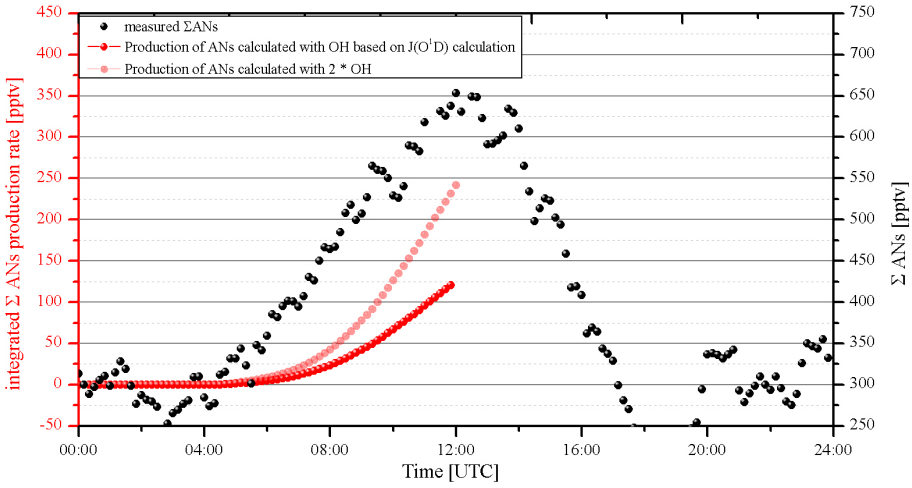

Figure 6.16.: *Averaged AN diurnal profile together with the integrated production rate*

The production rates for the formation of the alkyl nitrates were derived from the measured hydrocarbons, which are listed in Table 6.1. The calculated diurnal profile of the total production rate is shown in Figure 6.17. With sunrise and subsequent increase in OH the production rate increases monotonically til noon.

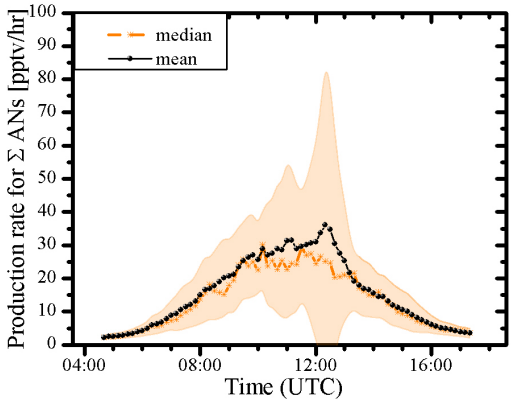

Fig. 6.17.: *Diurnal profile of the total production rate calculated from each measured hydrocarbon*

Interestingly as seen in Figure 6.16 is that the increase in ∑ANs starts slightly earlier than the increase in the calculated OH initiated production of ∑ANs from VOC oxidation. This difference might be explained via two possible reasons. The first reason could be related to the break up of the nocturnal boundary layer in the early morning followed by entrainment of higher ∑ANs mixing ratios which were stored in the residual layer from the day before. A second reason could be related to halogen chemistry. As reported in Phillips et al. (2012b) on most nights significant $ClNO_2$ mixing ratios were present during the campaign. Furthermore they showed that especially between 05:00 and 08:00 UTC the production rate of Cl atoms via the photolysis of $ClNO_2$ is dominant compared to the formation of OH. Assuming that the oxidation of VOCs by Cl atoms is similar to the oxidation by OH this could lead to the formation of ∑ANs during the early morning. As NO increased similarly to the ∑ANs, this supports the possible ∑ANs production by Cl initiated VOC oxidation in the

presence of NO.
The maximum production rate is reached at about 12:00 UTC with about 30 pptv/hr. Assuming that during this period the losses of the alkyl nitrates are very small (which is typically the case), the time profile of the production rate can be integrated to gain an estimate of total alkyl nitrate mixing ratio. The result of this integration (Figure 6.16 (red)) showed an estimated formation of alkyl nitrates of about 120 pptv at about 12:00 UTC, so that about 35-40 % of the measured increase in the alkyl nitrates during the morning can be explained with the estimated OH and the measured hydrocarbons. However, this calculation contains several uncertainties:

- During this campaign a large set of VOC were measured. In total 7 alkanes ($C_2 - C_6$), serveral alkene ($C_2 - C_5$), isoprene, terpenes and aromatics. However still a large set of VOCs, especially alkanes with a high carbon number, which are expected to have large branching ratios for the formation of alkyl nitrates, were not reported. The overall production rate including every hydrocarbon which is present in the atmosphere forming an alkyl nitrate is therefore expected to be larger than that calculated from the measured hydrocarbons.

- Another important aspect in the interpretation of the calculated production rates is the influence of the branching ratio α for each hydrocarbon. As only α values for the most important hydrocarbons are determined via laboratory studies, the branching ratio must be estimated for several other hydrocarbons. These values are marked with 'E' in Table 6.1. But even the branching ratios for the hydrocarbons which are determined via laboratory studies have significant uncertainties. For example the nitrate yield for isoprene varies between 4 and 15 %.

- The third main uncertainty which has to be taken into account in the OH concentrations. OH concentrations were measured occasionally during the campaign but unfortunately not in the period where most of the hydrocarbons were measured. Therefore for this period OH calculations were estimated via a dependence of OH on $J(O^1D)$. Higher OH concentrations would obviously favour the $\sum$ANs production rate as shown also in Figure 6.16. The transparent red curve represents the total alkyl nitrate production rate assuming a doubled OH concentration (maximum of about $2.4 \times 10^6 \frac{molec}{cm^3}$). With this assumption about 70-80 % of the measured increase in the total akyl nitrates could be explained.

Considering the uncertainties the measured increase of the alkyl nitrates during the morning is reasonable well explained by the production rates derived from the measured hydrocarbon. Assuming that the calculated OH concentration is an

lower limit as well the number of measured hydrocarbons the calculation of the production rate can be estimated as an lower limit.
For this calculation no loss terms are included. As already shown in section 2.3.3, alkyl nitrates are very stable. The lifetime due to the reaction with OH is in the order of several weeks to months depending on the class of nitrates. Due to photolysis the lifetime of ∑ANs is reduced to weeks. These are the main loss processes for the alkyl nitrates formed by RO_2 from alkane reactions (mononitrates). The water solubility of hydroxyalkyl nitrates formed by RO_2 from alkene reactions is for many of these hydroxynitrates larger than for the mononitrates and therefore deposition can shorten the lifetime of these nitrates considerably.

6.9.1. Contribution to the ∑ANs Production rate

Since several VOCs were measured during the campaign it is interesting to see which class of VOCs or which individual VOC are the dominant production term for the alkyl nitrates. Therefore the contribution of the different VOCs was calculated using the daily median values. The total median daily production rate was 12.5 pptv/hr. Figure 6.18 shows a composite of three different fractions. Panel a) shows the contribution of all individual measured VOCs. The main single contributor is limonene a biogenic VOC with about 27.4 % (myrcene contributes to 13.5 %). The alkenes pentene and butadiene contribute about 15.5 and 16.6 %, respectively. The only significant contributor from the alkanes was propane with about 9.2%. Panel b) divides the total production rate only into different classes of VOCs. The major contribution is due to the terpenes with about 53.6 % fol-

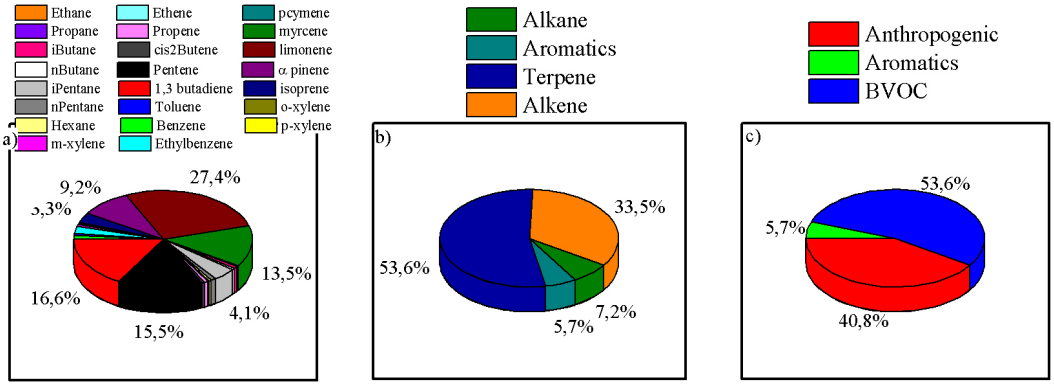

Figure 6.18.: *Composite of three Pie - chart diagrams: a) shows the contribution of each measured hydrocarbon to to the total production rate of alkyl nitrates; b) shows the contribution of the different classes of compounds and c) shows the contribution between anthropogenic and biogenic VOCs*

lowed by the alkenes with about 33.5 %. The alkanes and the aromatics have only a minor influence on the alkyl nitrate production with only about 13 %. Panel

c) shows the distribution between the anthropogenic VOCs and the biogenically emitted ones. The production of alkyl nitrates at Kleiner Feldberg has similar contributions from biogenic and anthropogenic hydrocarbons.
Comparing these daily averaged data with different periods (e.g. early morning, noon, late afternoon) shows that the production rate of $\sum$ANs varied due to the strong diurnal OH profile. Whereas the daily averaged total production rate was about 12.5 pptv/hr, the production rate varied during the day from low values of only 6.4 pptv/hr in the early morning to 27.2 pptv/hr for the midday period and decreased again to about 7.1 pptv/hr in the late afternoon. The contribution between the individual VOCs did not vary so much during the day. The contribution between the anthropogenic and the biogenic precursors to the production rate showed similar values for the early morning and late afternoon as for the averaged day. Only during midday the ratio between the anthropogenic and the biogenic impacts changed slightly. The anthropogenic influence increased from about 41 to about 47 %.The impact of the aromatics was rather constant for all periods.

6.9.2. Link between $\sum$ANs and Ozone

In Day et al. (2003) and Rosen et al. (2004) the correlation of alkyl nitrates and ozone was used to derive the overall branching ratio (α) for an air mass. As introduced in section 6.9 alkyl nitrates and ozone have similar photochemical formation path ways. Therefore a correlation between both can be expected.
The $O_x/\sum ANs$ relationship ($O_x = O_3 + NO_2$)is the result of chemistry and transport, which can be approximate as the time integral

$$\frac{\Delta O_3}{\Delta \sum ANs} = \frac{\int (P_{O_3} - D_{O_3} + E_{O_3})dt}{\int (P_{\sum ANs} - D_{\sum ANs} + E_{\sum ANs})dt} \tag{6.12}$$

where P represents the chemical production rate, D the deposition rate and E the entrainment rate. With the TD-CRDS instrument only the total alkyl nitrates are measured, not specific alkyl nitrates. Therefore reactions that change the identity of the nitrate (but do not remove the nitrate functional group) do not decrease the NO_2 signal measured in the CRD coming from the $\sum$ANs. If this simple analysis would be applied for speciated $\sum$ANs, then chemical loss reactions of that compound would need to be explicitly accounted for. Assuming that the loss due to deposition and the influence of entrainment can be neglected, Equation 6.12 can be reduced only to the production rate. Using Equation 6.10 and 6.11 for the productions rate leads to:

$$\frac{\Delta O_3}{\Delta \sum ANs} = \frac{\int (P_{O_3})dt}{\int (P_{\sum ANs})dt} = \frac{\int (\sum_i \gamma_i (1-\alpha_i) k_{OH+RH_i}[OH][RH_i(t)])dt}{\int (\sum_i \alpha_i k_{OH+RH_i}[OH][RH_i](t))dt} \tag{6.13}$$

this Equation can be approximated in a simpler form

$$\frac{\Delta O_3}{\Delta \sum ANs} \approx \frac{2(1-A)}{A} \approx \frac{2}{A} \tag{6.14}$$

where A is the ∑ANs yield for the mixture of hydrocarbons. The fixed number in the numerator of the simplified Equation is the γ value which is for most of the hydrocarbon in this calculation equal to 2. Therefore if the air sample is uniformly mixed, contained only one hydrocarbon, and the loss terms were negligible, then the relationship between O_3 and ∑ANs observed by TD-CRDS would be compact and linear with a slope of approximately $\frac{2}{\alpha}$. Therefore the slope of this linear correlation is dependent on the hydrocarbon mixture. For n-pentane the slope would be 19, for smaller alkenes like propene e.g. the slope would be about 133. Aldehydes for example are involved in ozone production but not in the production of alkyl nitrates therefore in this case the slope would be infinite. Due to the expected strong correlation between ∑ANs and ozone the following analysis was conducted to estimate the averaged branching ratio for the alkyl nitrate production. Table 6.2 describes a statistic for ∑ANs as a function of O_x mixing ratio. For this statistics the O_x mixing ratios were binned with a 5 ppbv range beginning from 25 ppbv up to 90 ppbv. From each bin the median of the ∑ANs mixing ratio in this bin was calculated.

Tab. 6.2.: *$\sum AN$ measurements within ranges of O_x for all data of the selected data set between 05:00 and 18:00 UTC*

O_x ppbv	Median ∑ANs	σ ∑ANs	N
25-30	0.12	0.055	8
30-35	0.154	0.082	49
35-40	0.23	0.14	83
40-45	0.32	0.21	121
45-50	0.44	0.2	154
50-55	0.58	0.2	183
55-60	0.53	0.25	165
60-65	0.68	0.26	79
65-70	0.61	0.18	92
70-75	0.79	0.18	53
75-80	0.68	0.22	14
80-85	0.65	0.11	8
85-90	0.74	0.02	3

As seen in the Table 6.2 the ∑ANs mixing ratios increased from about 0.12 ppbv in the O_x bin from 25-30 ppbv to about 0.79 ppbv in the 70-75 ppbv O_x bin. The median values for the ∑ANs mixing ratios for the O_x bins higher than 75 ppbv has to be considered carefully due to the low number of data points in these O_x intervals. But a clear correlation between both species is obvious. Due to the fact that the measurement site has no clear meteorological pattern (like e.g. in the publication of Day et al. (2003)) the following analysis has to be considered with care due to the fact that the measured ∑ANs and O_3 concentration might be not have the exact precursor sources. Due to the different lifetime of both species this might be the case. Nevertheless the following analysis can give an approximation for the effective branching ratio. For the correlation analysis O_x ($O_x = O_3 + NO_2$) is used due to the reason that O_3 is formed via photolysis of NO_2, O_3 was however the dominant fraction of O_x. The $\sum ANs$ concentration were averaged dependent on the O_x mixing ratios. Therefore for each 2 ppbv O_x

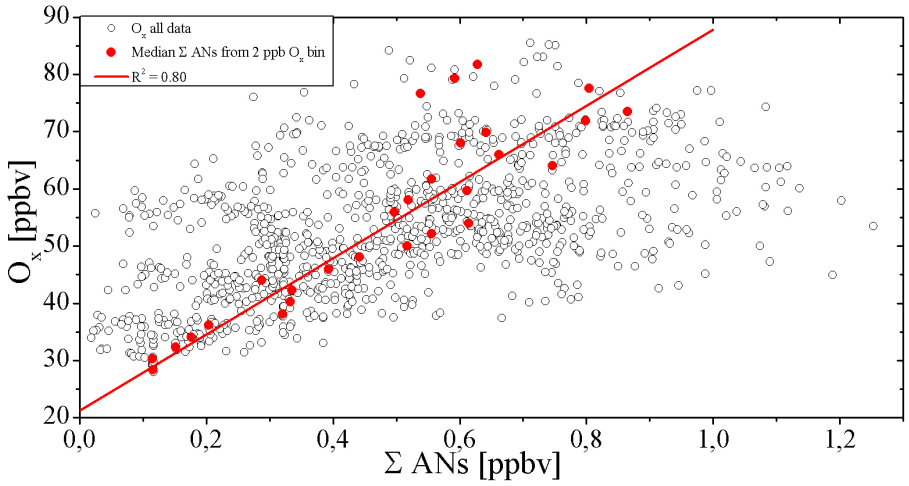

Figure 6.19.: *O_x ($O_x = O_3 + NO_2$) versus $\sum$ANs (ppbv) for data between 05:00 and 18:00 UTC for the selected data set (open circles). The red circles represent the median $\sum$ AN concentration based on a 2 ppbv O_x bin*

bin the $\sum$ANs which belonged to this bin were averaged. Figure 6.19 shows the observed O_x versus $\sum$ANs during 05:00 and 18:00 UTC for the selected data set (open circles). The red circles represent the median $\sum$ANs values derived from the binned O_x data. For both data sets a good correlation is seen but the median $\sum$ANs values show a even better linear dependency. Therefore the rest of the analysis the averaged $\sum$ANs values were used. Using equation 6.14 the slopes from the observed correlation between O_x versus $\sum$ANs can be used to derive the yields for the nitrate formation. Correlations between O_x and $\sum$ANs were studied for different time periods from the data set to try to estimate the yield for the nitrate formation depending on the time of day. Figure 6.20 shows the correlation between O_x versus $\sum$ANs for the time period between 11:00 and 13:00 UTC (to compare with the data of Table 6.1). The Figure shows the complete data for this time period (black circles) with the median $\sum$ANs values (red circles). The red line shows the linear fit for the median values against the binned O_x values. The fit routine which was used for this fits was a bivariante fitting routine which accounts for x and y errors. For the errors the standard deviation from the averaged median values were used. The fit shows a relatively good correlation ($R^2 = 0.76$). The derived slope is 42.7 ± 1.4. Using equation 6.14 this slope leads to an average nitrate yield of $\alpha = 0.047 \pm 0.0016$. Applying this method for other time periods over the day the branching ratios varied between about 0.022 and 0.047 with an averaged value of $\alpha = 0.0337 \pm 0.0075$. The correlation coefficient (R^2) for all chosen time period for the correlation between O_x and the median $\sum$ANs concentration were relatively good and varied between 0.7 and 0.85.

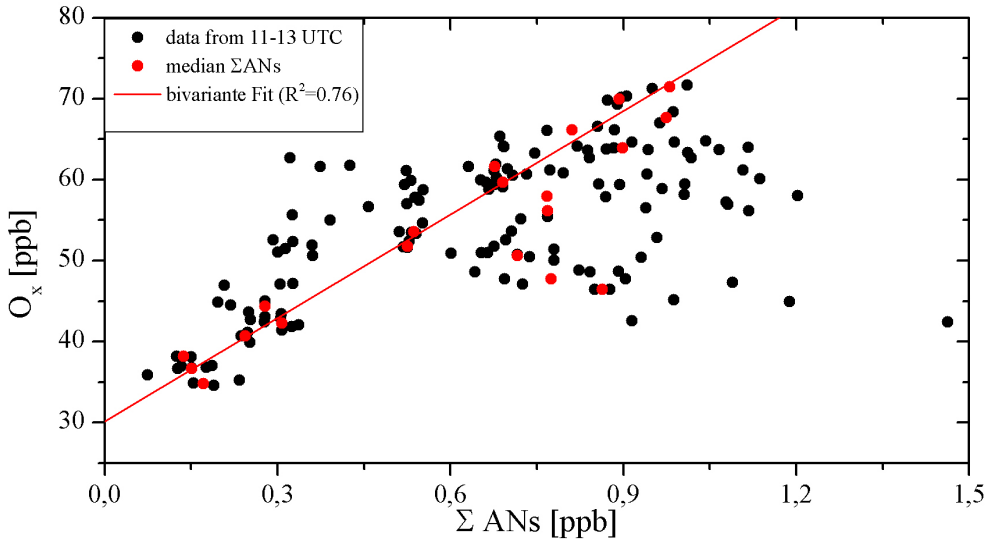

Figure 6.20.: *O_x ($O_x = O_3 + NO_2$) versus ∑ANs (ppbv) for data between 11:00 and 13:00 UTC (black circle). The ed circles represent the median ∑AN. The line is the fit to the median data.*

6.9.2.1. Comparison with calculated branching ratios

The branching ratios derived from the measured ∑ANs can be compared with branching ratios calculated based on the production rates for ∑ANs and ozone from the measured hydrocarbons. To compare these both methods the median values from each hydrocarbon for the specific time period is used. With the known rate constants with OH and the known branching ratios for each individual hydrocarbon a total production rate for the alkyl nitrates and O_3 can be calculated. The ratio of $\frac{\Delta O_3}{\Delta \sum ANs}$ for both production rates determines the branching ratio. In Table 6.1 the median values for the measured hydrocarbon for the time period between 11:00 - 13:00 UTC are shown. During this time period OH concentrations are expected to be at their maximum. On average the calculated OH concentrations during that period were in the order of $1.2 \times 10^6 \frac{molec}{cm^3}$. The total ∑ANs production rate for this period was 26.4 pptv/hr whereas the O_3 production rate was about 807 pptv/hr. For these production rates the calculated branching ratio after Equation 6.13 is 0.065. The branching ratio derived from the observation for this time period is reasonably close at about 0.047. As already mentioned the branching ratio from the observation varied between 0.022 and 0.047 the variation in the branching ratio based on the hydrocarbon sources showed much less variation. The total production rates for ∑ANs and O_3 varied greatly during the day due to the large variation in OH which has a strong diurnal profile. But the calculated branching ratios showed much less variation compared to the observations. Depending on the time period the calculated branching ratios varied between 0.065 and 0.076 with an averaged value of about 0.071.

Whereas the observations of $\sum$ANs and O_3 suggest a branching ratio of about 3.3 %, the branching ratio calculated from the precursor hydrocarbon is about 7 %. The difference can be related to unaccounted sources of O_3, such as aldehyde oxidation, which contribute to O_3 production but not to the production of alkyl nitrates. For example the oxidation of acetaldehyde by OH typically leads to formation of three O_3 molecules. Therefore, e.g. if the acetaldehyde concentration is only half of the HCHO concentration, a large portion of the discrepancy between the branching ratios derived from observed and calculated could be explained by its oxidation. Beside the aldehydes also methane (CH_4) will change the ratio of $\Delta O_3/\Delta \sum ANs$ leading to a slightly lower α. This effect is assumed to be not so important at this site.

On the other hand an overestimated calculated production rates of $\sum$ANs would lead to steeper slope. As shown in section 6.9.1 limonene and myrcene have a significant contribution to the production rate of $\sum$ANs. Both of them have very large branching ratio. If the assumed branching ratio are lower then those used for this calculation this would lead to an overestimation of the $\sum$ANs production rate. In Rosen et al. (2004) a branching ratio for limonene is reported of about 0.1. Using this branching ratio the total production rate calculated from Table 6.1 would decrease to about 22.7 pptv/hr for the $\sum$ANs and increase the O_3 production rate to 815 pptv/hr leading to an decrease of the branching ratio from 6.5 to 5.6 %. Beside the measured hydrocarbon, a huge set of hydrocarbon especially the longer chain hydrocarbons ($C_6 - C_{12}$) were not reported. The branching ratios for the longer chain hydrocarbons are expected to be larger than for the shorter chain hydrocarbons. Depending on the mixing ratios of these compounds this would lead again to an increase in the effective branching ratio.

The derived branching ratios are in the expected range for a semi-rural site. Day et al. (2003) reported slopes in the range of 25 -120 for measurements at Granite Bay (a rural site in California) and La Porte (an urban site close to Houston, Texas) which are dependant on the time of days at both sides. Rosen et al. (2004) measured slopes in the range of 50 also in La Porte.

Beside this relatively good agreement it has to be noticed again, the meteorological situation on top of Mt. Kleiner Feldberg is complex. Although the production is the major term contributing to the observed $\Delta O_x/\Delta \sum ANs$ throughout much of the day, loss processes such as deposition or entrainment could influence the ratio. $\sum$ANs are typically expected to be long lifed with larger lifetimes compared to O_3. But this is dependent on the kind of nitrate. If most of the $\sum$ANs are hydroxyalkyl nitrates, then $\sum$ANs will be lost to deposition faster than O_3 during transport to the measurement site from the source region and the actual branching ratio of the original hydrocarbon mixture would be higher. Indeed the great

diel variability of $\sum$ANs compared to O_3 suggests that this is the case . Entrainment is likely most important during the early morning, as the nocturnal inversion breaks up and there is downward mixing of compounds from aloft. Depending on the lifetime of O_3 and $\sum$ANs, it could be that the $O_3/\sum ANs$ relationship from the previous day is preserved above the nocturnal surface layer, then the actual relationship of $O_3/\sum ANs$ in the early morning can be affected by the chemical composition from the afternoon of the previous day.

6.10. Summary of PARADE

The CRD instrument developed in this thesis was deployed to measure NO_2, total peroxy nitrates and total alkyl nitrates simultaneously, during the PARADE 2011 campaign. The campaign took place on the summit of Mt. Kleiner Feldberg in Central Germany. The performance of the instrument was very good with a typical detection limit of about 50 pptv for NO_2 and about 70 pptv for $\sum PNs$ and $\sum$ANs for 4 sec time resolution. Beside the TD-CRDS instrument seven other instruments operated during the campaign. The good agreement with the other measurements can be considered as a validation for the new instrument.

The TD-CRDS is an important (absolute) tool to characterize calibration sources for other instruments. The TD-CIMS from the same research group measures speciated peroxy nitrates, peracetic acid and chloryl nitrate and was calibrated using synthetic samples of PAN and $ClNO_2$ which were calibrated using TD-CRDS. The comparison between the total peroxy nitrates measured via the TD-CRDS with PAN measured by the TD-CIMS showed a very good agreement with a PAN/$\sum$PNs fraction of about 86 % as reported in several other publications [Roberts (1990)]. The $\sum$PNs showed a clear diurnal profile following the O_3 profile. The measured $\sum$PNs mixing ratios varied between close to the detection limit up to 1.8 ppbv. The performance of the $\sum$PNs measurements was very good over the complete campaign and only minor interferences due to thermal dissociation of N_2O_5 were observed.

The measurements of total alkyl nitrates were performed for the first time at the Taunus Observatory, and it was the first time that the instrument measured NO_2, total peroxy nitrates and alkyl nitrates simultaneously in the field. The performance of the $\sum$PNs and $\sum$ANs measurements were very good, with no significant problems. For $\sum$PNs and $\sum$ANs, there are possible interfering species. N_2O_5 thermally decompose at 90°C. Therefore N_2O_5 can act as interfering species fo the $\sum$PNs measurement. Direct correction for the data set was not possible but an upper limit of N_2O_5 which interfere the $\sum$PNs measurements could be derived. $ClNO_2$ thermally decomposes at $450°C$ to NO_2 like the alkyl nitrates. As $ClNO_2$

was measured with the TD-CIMS a correction could be applied. The diel contribution of $\sum$PNs and $\sum$ANs to total NO_y was about 11-12 % and 8-9%, respectively. The contribution of both to the higher oxidized reactive nitrogen species NO_z was about 27 % for $\sum$PNs and aobut 22 % for $\sum$ANs. From the measured set of hydrocarbon the a contribution to the production rate for the formation of $\sum$ANs could calculated which showed that the importance of anthropogenic and biogenic precursors are in the similar range. From the observed correlation between O_x and $\sum$ANs effective branching ratios for the formation of $\sum$ANs could be derived in the order of 3.3 % which was roughly consistent with the calculation based on the measured hydrocarbons. These derived branching ratios are in good agreement with branching ratios found at other rural or urban sites [Day et al. (2003); Rosen et al. (2004)]

This first deployment of the newly constructed TD-CRDS instrument was very successful and showed that the measurements of NO_2 are very accurate in comparison to other instruments. The possibility to measure nitrogen reservoir species like total peroxy nitrates and total alkyl nitrates was demonstrated. To my knowledge these are the first measurements of total alkyl nitrates in Germany.

Part IV.

Conclusion and Outlook

Chapter 7.

Conclusion

The goal of this thesis was to study atmospheric reactive nitrogen chemistry using cavity ringdown spectroscopy. For this purpose a new cavity ring down spectrometer for the detection of NO_2, $\sum$PNs and $\sum$ANs was developed, constructed and deployed at two different measurement site. A further, pre-existing CRD was also deployed for NO_3/N_2O_5 measurements. Reactive nitrogen chemistry was studied during three campaigns with different chemical and geographical locations. The results of the campaigns are summarized here:

- DOMINO 2008 (Continental/rural but also urban influences):
  - *NO_3/N_2O_5 measurements via CRD and DOAS*
    Ground based measurements of NO_3/N_2O_5 were performed by a CRDS and showed very low NO_3 concentrations and short lifetimes. The deployment of a LP-DOAS allowed vertically distributed NO_3 measurements.
  - *NO_3 lifetime dependence on chemical influence*
    NO_3 lifetimes were generally low and strongly dependent on the chemical influence of the surroundings. Continental and rural influences were associated with longer lifetimes which could be constrained by the calculated NO_3 losses whereas lifetimes influenced by the urban character of Huelva were typically very short and could only be partly explained. The very high reactivity towards NO_3 is potentially caused by emissions of reduced sulphur compounds (RSC) or alkenes from the petrochemical industry around Huelva (see sections 5.4.2 - 5.6).
  - *Comparison between ground based and vertically distributed NO_3 measurements:*
    A clear increase in NO_3 mixing ratios with height was found depending strongly on the meteorological conditions (see sections 5.8.1 - 5.8.4).
    Mean NO_3 concentration for the entire campaign was about 5 times higher in the uppermost layer compared to the ground based measurements (see section 5.8.2).
    Nocturnal removal of NO_x from the atmosphere via gas phase reactions of NO_3 at the ground was calculated to be about 0.1 ppbv/hr which was

in a similar range compared to the diel NO_x removal. The vertical NO_3 gradient suggests that the mean NO_x loss in the nocturnal boundary layer is higher than the results from the ground based measurements (see section 5.9).
The importance of NO_3 as nighttime oxidant and its effect on VOC removal was found to be greater at higher levels compared to the oxidation by OH during the day (see section 5.10).

- HUMPPA 2010 (Boreal forest, remote area):
  - *First deployment of the new developed CRDS based on direct NO_2 measurements.*
  - *Intercomparison at very low NO_2 mixing ratios with a CLD instrument*: The comparison showed a good agreement of both instruments within their accuracies (see section 6.2.2).

- PARADE 2011 (semi rural):
  - *Extended intercomparison between 7 NO_2 instruments*:
    The comparison between all instruments showed a good agreement.(see section 6.2.1).
  - *First measurements of $\sum$PNs and $\sum$ANs with new CRDS*:
    Detection of both nitrates during the campaign was successful with a limit of detection of about 100 pptv for both nitrates. Potential interferences could be determined and corrected for. $\sum$PNs varied between less than 100 pptv and 1.8 ppbv and $\sum$ANs varied up to 1.6 ppbv (see sections 6.3 and 6.4).
    The results of the $\sum$PNs measurements showed good correlation to independent PAN measurements. (see section 6.8).
    A PAN/$\sum$PNs ratio of 0.86 could be derived which is in good agreement to several other publications [Roberts (1990)] (see section 6.3.3).
    $\sum$ANs were measured the first time at Kl. Feldberg.
  - *Characterization of $\sum$ANs and O_3 chemistry:*
    From a correlation study between O_3 and $\sum$ANs an effective branching ratio for the formation of $RONO_2$ via the reaction RO_2+NO $\longrightarrow$ $RONO_2$ of about 3-4 % was derived which was roughly consistent with the calculations based on the measured hydrocarbons (see section 6.9.2).
  - *Contribution of $\sum$PNs and $\sum$ANs to NO_z and NO_y*:
    The diel contribution of $\sum$PNs and $\sum$ANs to NO_y was found to be about 11-12 % and 8-9%, respectively and to the higher oxidized reactive nitrogen compounds NO_z to be about 27 % and 22 %, respectively (see section 6.7 and 6.7.1).

Chapter 8.

Outlook

The results from the DOMINO campaign highlight the importance of understanding the vertical distribution of trace gases especially during the night should be extended. Especially the increase of NO_3 with height indicates that ground based measurements of NO_3 underestimate the importance of NO_3 in the nocturnal oxidation processes. More vertically resolved measurements a LP-DOAS system should be carried out in polluted and also remote areas and more compact in-situ instruments as the CRDS instruments may be deployed on aircraft or on movable elevators to investigate the vertical distribution with a very high spatial resolution. Beside vertical NO_3 measurements during nighttime it would also be helpful to measure several VOCs such as monoterpenes and their vertical distribution to gain an impression of height dependent loss processes for NO_3.

The results from the PARADE campaign showed that organic nitrates are useful indicator of atmospheric processes. Especially the measurements of total alkyl nitrates which are rare over the globe are very important in terms of a better understanding of the nitrogen related chemical processes. Therefore measurements of organic nitrates in particular alkyl nitrates in regions of biogenically and anthropogenically dominated hydrocarbon emissions would provide useful information about the photochemical O_3 production and the partioning to the total NO_y. The branching ratios for the formation of alkyl nitrates via the reaction of RO_2 with NO are only known for a few hydrocarbons which also can impact model calculations of O_3 production on global scale. Therefore also laboratory studies to derive the branching ratios for different types of hydrocarbons should be extended. Detailed chemical modeling of $\sum$ANs and $\sum$PNs would be useful in interpreting the present data and also extrapolate to other regions.

From the instrumental point of view there are also several possibilities to improve the performance of the CRD. The precision of the instrument could be improved approximately by a factor of two by faster acquisition of the measured ring down traces. In this thesis the acquisition time to acquire about 1300 ring down traces was in the order of 3-4 s whereas in Fuchs et al. (2009) which have a similar instrument reports an acquisition time of about 1 s for 1600 traces. The reduction

of the footprint size of the instrument would also be further improvement to deploy it on mobile platforms especially for vertically resolved measurements (lifts, towers and aircraft). Additionally the number of cavities could be increased to about 4 or more to have to opportunity of measuring several traces (like e.g. NO_3, N_2O_5, NO_2, peroxy nitrates and alkyl nitrates) simultaneously and avoid problems associated with interpolation of datasets (e.g. $\sum$ANs). Beside the organic nitrates also nitric acid can thermally decompose to NO_2. Therefore the implementation of a third heater unit would be helpful to extend the measurements by an additional NO_y species.

Appendix

A. Abbreviations

AMS	Aerosol Mass Spectrometer
APS	Aerosol Particle Sizer
ASA	Aerosol Surface Area
BLC	Blue Light Converter
CE-DOAS	Cavity Enhanced Differential Optical Absorption Spectroscopy
CIMS	Chemical Ionization Mass Spectrometer
CLD	ChemiLuminescence Detector
CRDS	Cavity RingDown Spectroscopy
CRM	Comparative Reactivity Method
DMS	DiMethyl Sulfide
DOAS	Differential Optical Absorption Spectroscopy
DoY	Day of Year
DWD	Deutscher Wetter Dienst
FEP	Fluorinated Ethylene Propylene
FMPS	Fast Mobility Particle Sizer
FWHM	Full-Width at Half-Maximum
GC-FID	Gas Chromatograph - Flame Ionization Detector
GC-PID	Gas Chromatograph . Photoionization Detector
HLUG	Hessisches Landesamt für Umwelt und Geologie
HPLC	High Performance Liquid Chromatography
IPCC	Intergovernmental Panel on Climate Change
IUPAC	International Union of Pure and Applied Chemistry
LIF	Laser Induced Fluorescence
LOPAP	LOng Path Absorption Photometer
LP-DOAS	Long Path - Differential Optical Absorption Spectroscopy
MAX-DOAS	Multi Axis - Differential Optical Absorption Spectroscopy
MOLA	MObile LAboratory
MPAN	PeroxyMethacryloyl Nitrate
MVK	Methyl Vinyl Ketone
NBL	Nocturnal Boundary Layer
NDIR	nondispersive infrared sensor

continued on next page

continued from last page

NMHC	Non Methane HydroCarbon
NOAA	National Oceanic and Atmospheric Administration
PAA	PerAcetic Acid
PAN	Peroxyacetyl Nitrate
PeRCA	Peroxy Radical Chemical Amplification
PerCEAS	Peroxy radical Cavity Enhanced Absorption Spectrometers
PFA	PerFluoroAlkoxy
PPN	PeroxyPropionyl Nirate
ppb	parts per billion
ppm	parts per million
ppt	parts per trillion
PTFE	PolyTetraFluoroEthylene
PTRMS	Proton - Transfer - Reaction Mass Spectrometry
PTR-ToF-MS	Proton - Transfer - Time of Flight - Reaction Mass Spectrometry
QCL	Quantum Cascade Laser
RSC	Reduced Sulphur Compounds
SOA	Secondary Organic Aerosol
TD	Thermal Dissociation
TD-GC-MS	Thermal Dissociation - Gas Chromatograph Mass Spectrometry
TUV	Tropospheric Ultraviolet and Visible (TUV) Radiation Model
VOC	Volatile Organic Compounds

B. DOMINO 2008

In the following some more information about the DOMINO campaign will shown. Section B.1 shows the Facsimile Code and the output of the simulation for a 12 h run. This simulation input are the averaged concentration during the nights of the campaign (T=282 K, O_3=26.4 ppb and NO_2=2.7 ppb). For the direct losses for NO_3 (k_x) and the indirect losses from NO_3 over N_2O_5 (k_y) also averaged losses were used calculated from the measurements which accounts for NO_3 losses ($k_x = 0.03s^{-1}$ and $k_y = 0.0002343s^{-1}$). Section B.2 shows an overview of the measured trace gases during the campaign. The time-series also includes information of the air mass origin. Section B.3 shows the comparison between the individual loss terms for NO_3 (stack plot) and the calculated inverse lifetime for each night.

B.1. Steady state calculation

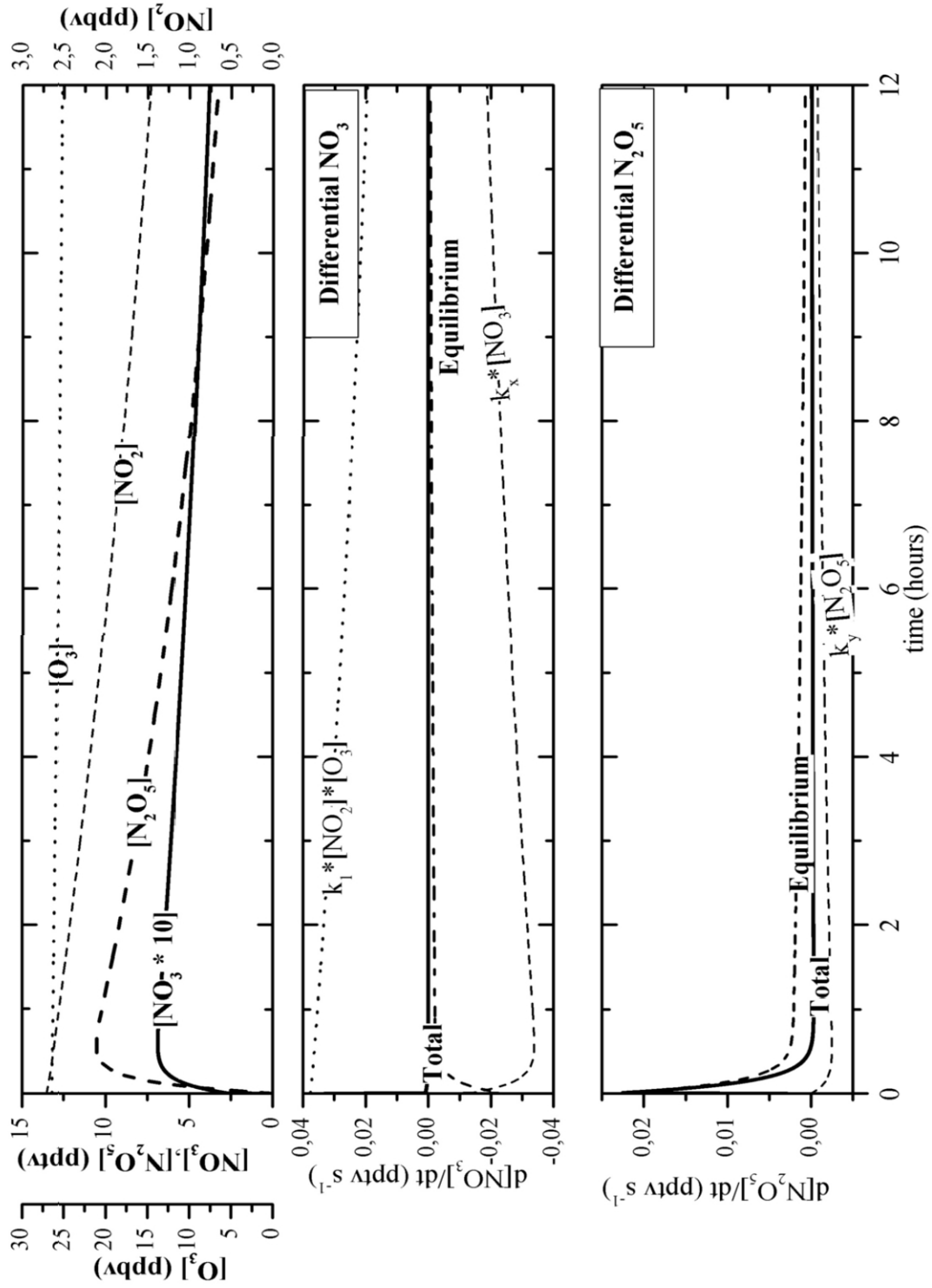

```
*            NO2-NO3-N2O5 steady state                    ;
* ==================================                      ;
variable N2O5 NO2  NO3 NO NOi O3 O3i o2 o f1 f2 NO2i       ;
variable NO3i N2O5i                                        ;
* ------------------------------------------              ;
* INITIAL CONCENTRATIONS                                   ;
* ------------------------------------------              ;
parameter  k1 k2 k2eq k3 k4  k5 k6 k7  HPL2 LPL2   m       ;
* ------------------------------------------------------- ;
parameter p 759.7                                          ;
parameter T 282                                            ;
* ------------------------------------------              ;
*                                                          ;
COMPILE GENERAL                                            ;
**                                                         ;
COMPILE INITIAL                                            ;
M = P * 3.24E16 * 298 /T                                   ;
NO2i = M * 2.70389e-9                                      ;
NOi = M * 0e-9                                             ;
O3i = M * 26.40833e-9                                      ;
NO3i = M * 0e-12                                           ;
N2O5i = M * 0e-12                                          ;
NO = NOi                                                   ;
O3 = O3i                                                   ;
NO3=NO3i                                                   ;
N2O5 = N2O5i                                               ;
**                                                         ;
COMPILE EQUATIONS                                          ;
* ------------------------------------------------        ;
   % k1                 : n2o5 = no3 + no2                 ;
   % k2                 : no2 + no3 = n2o5                 ;
   % k4                 : NO + O3 = NO2                    ;
   % k5                 : NO2 + O3 = NO3                   ;
   % kx               : NO3 =                              ;
   % ky               : N2O5 =                             ;
* ------------------------------------                     ;
*Rate equations                                            ;
LPL2 = 2.0E-30*(T/300)@-4.4                                ;
HPL2 = 1.4E-12*(T/300)@-0.7                                ;
k2 = (LPL2*M/(1+(LPL2*M/HPL2)))                            ;
       *0.6@((1+(LOG10(LPL2*M/HPL2))**2)**-1)              ;
k2eq = 2.7e-27*exp(11000/T)                                ;
k1 = k2 / k2eq                                             ;
k3 = 1.5e-11 * exp(170/T)                                  ;
k4 = 2e-12*exp(-1400/T)                                    ;
k5 = 1.2e-13*exp(-2450/T)                                  ;
k6 = 3.45e-12*exp(270/T)                                   ;
kx = 0.04911                                               ;
ky = 0.00023391                                            ;
**                                                         ;
compile instant                                            ;
 open 7   "SteadyState.sim" new                            ;
 open 8   "oio.fat" new                                    ;
* open 9   "acet.fit" new                                  ;
* open 10  "acet.gr2" new                                  ;
**                                                         ;
COMPILE BLOCK 3                                            ;
PSTREAM 3                                                  ;
**                                                         ;
compile header                                             ;
write 1=7, ".dataset"                                      ;
write 1=7, ".data" %                                       ;
**                                                         ;
PSTREAM 3 7 10                                             ;
time   NO2 NO3 N2O5 O3 k2 M T kx ky                        ;
**                                                         ;
when                                                       ;
1)  time = 0.0 + 1*8000% call block 3                      ;
 **                                                        ;
 *hmax 0.001                                               ;
 BEGIN                                                     ;
 STOP                                                      ;
```

B.2. Timeseries

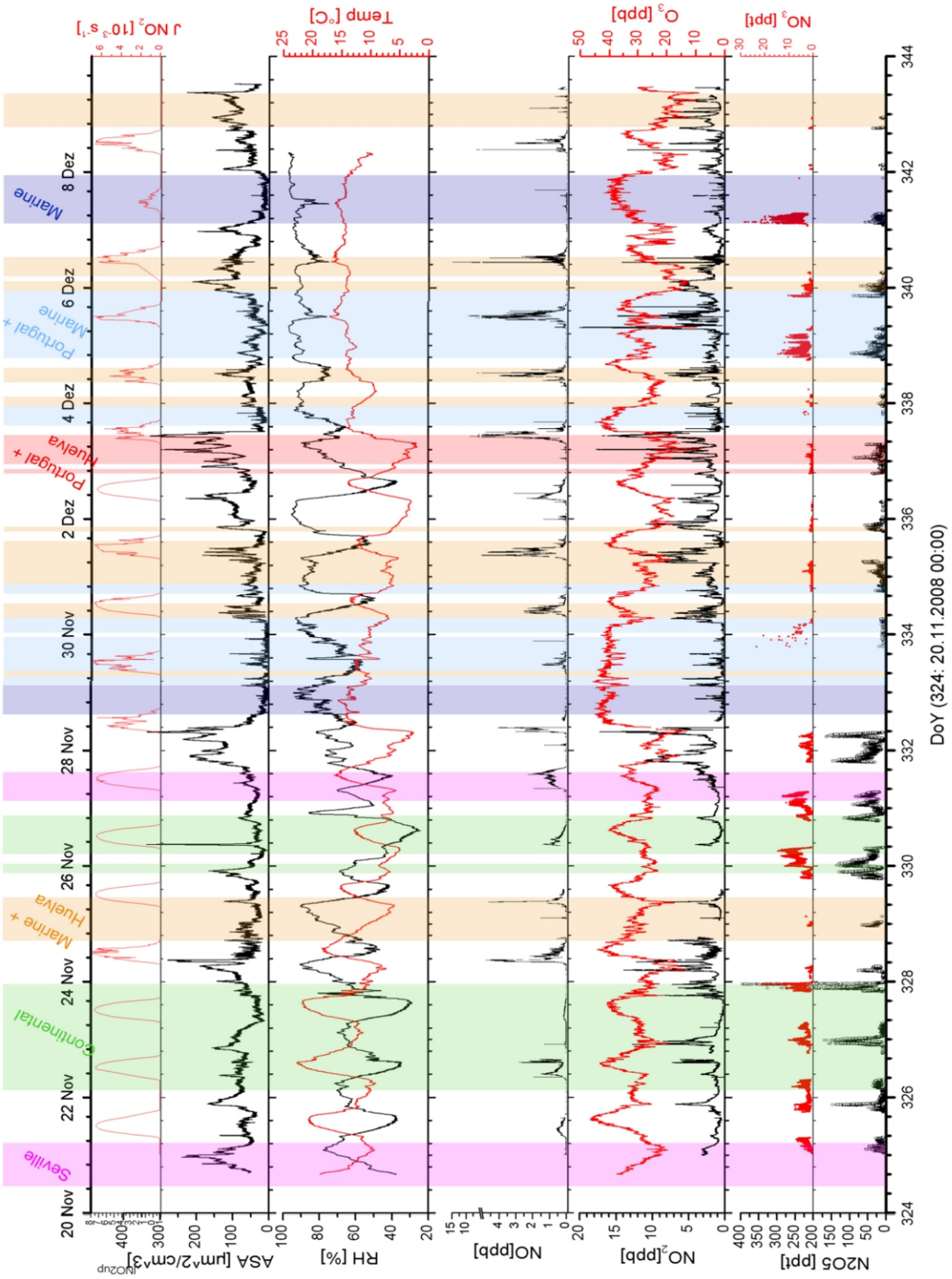

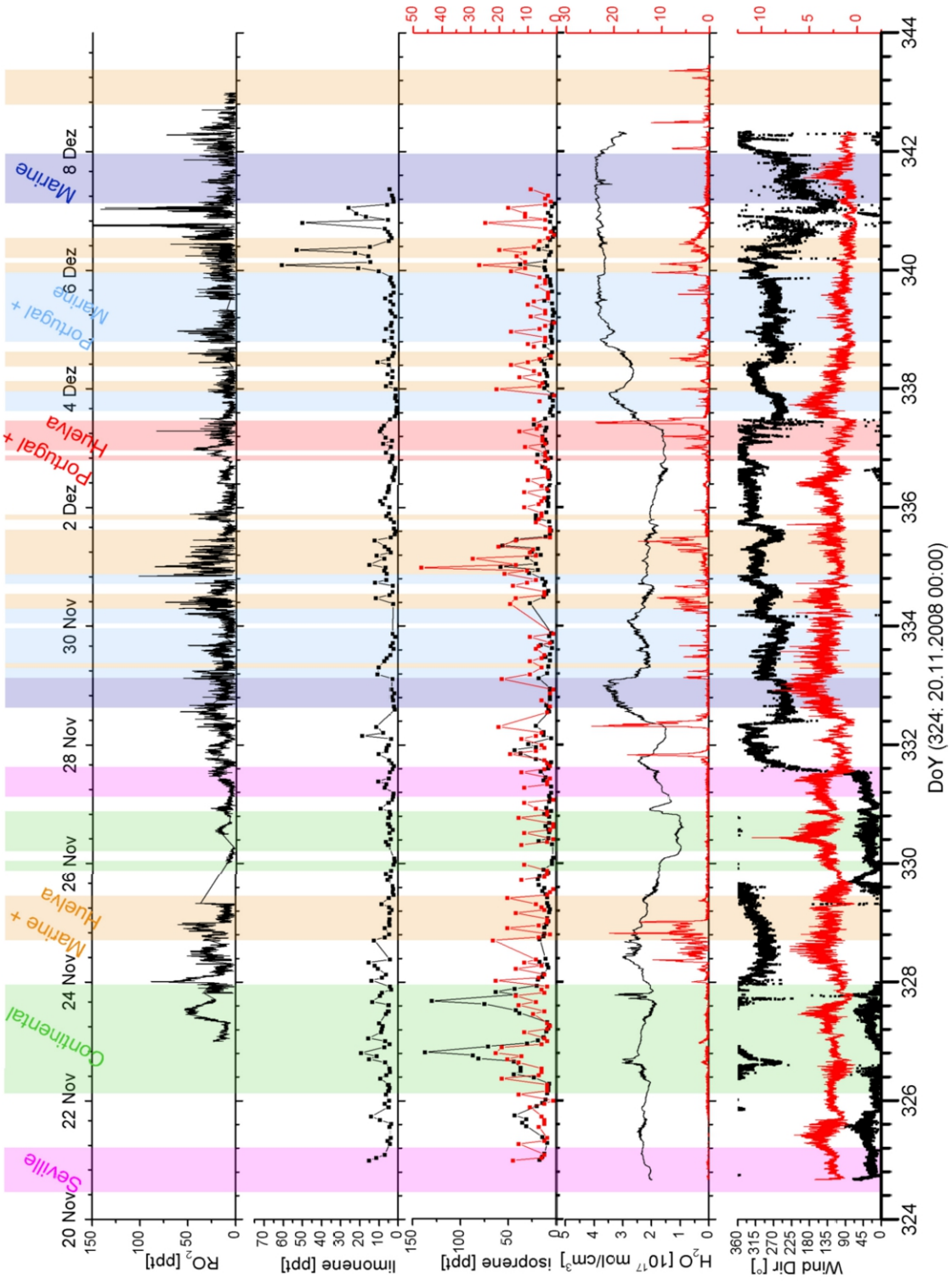
Seville
Continental
Marine + Huelva
Portugal + Huelva
Portugal + Marine
Marine
20 Nov
22 Nov
24 Nov
26 Nov
28 Nov
30 Nov
2 Dez
4 Dez
6 Dez
8 Dez
DoY (324: 20.11.2008 00:00)
RO2 [ppt]
limonene [ppt]
isoprene [ppt]
H2O [10^17 mol/cm^3]
Wind Dir [°]

B.3. Nocturnal losses

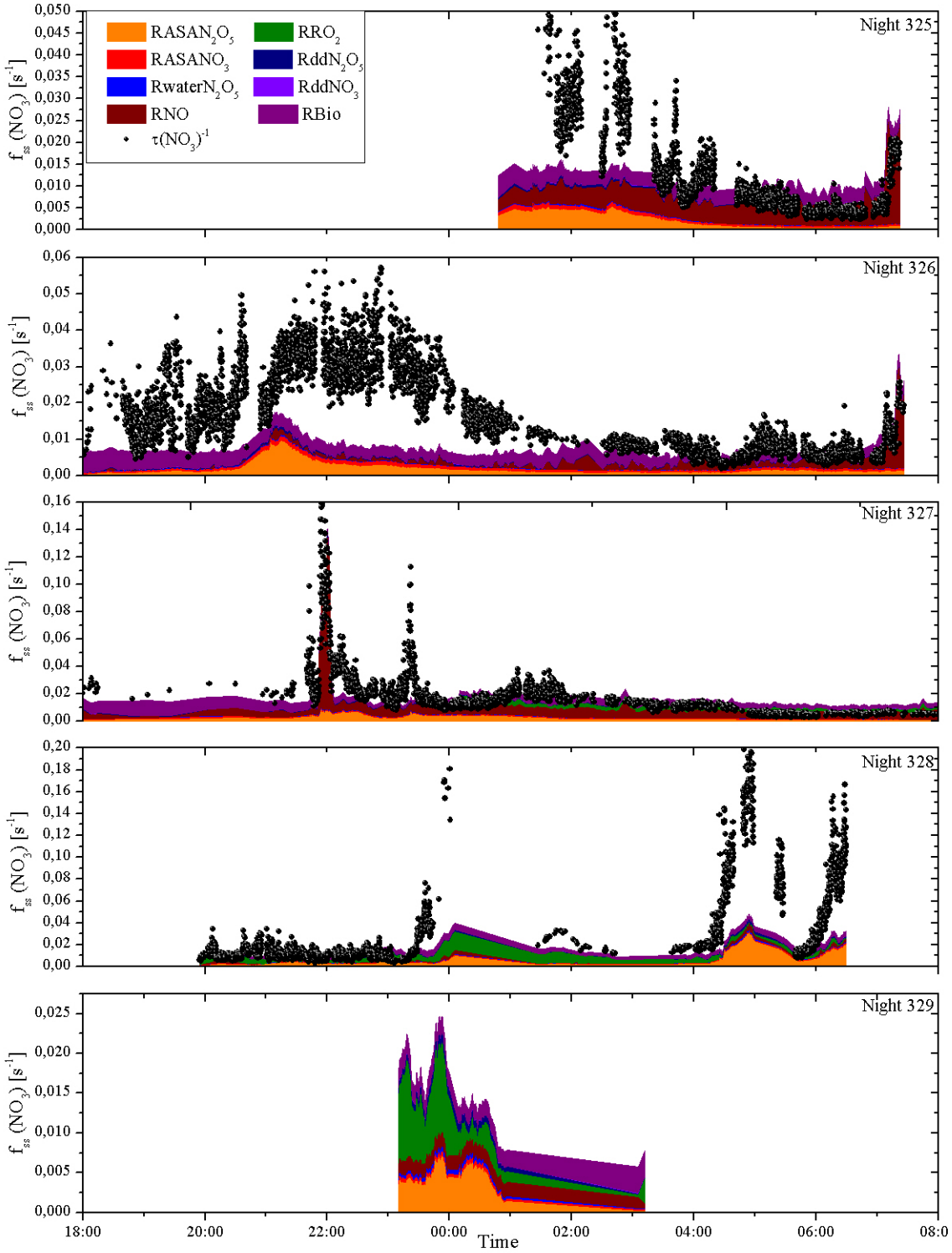

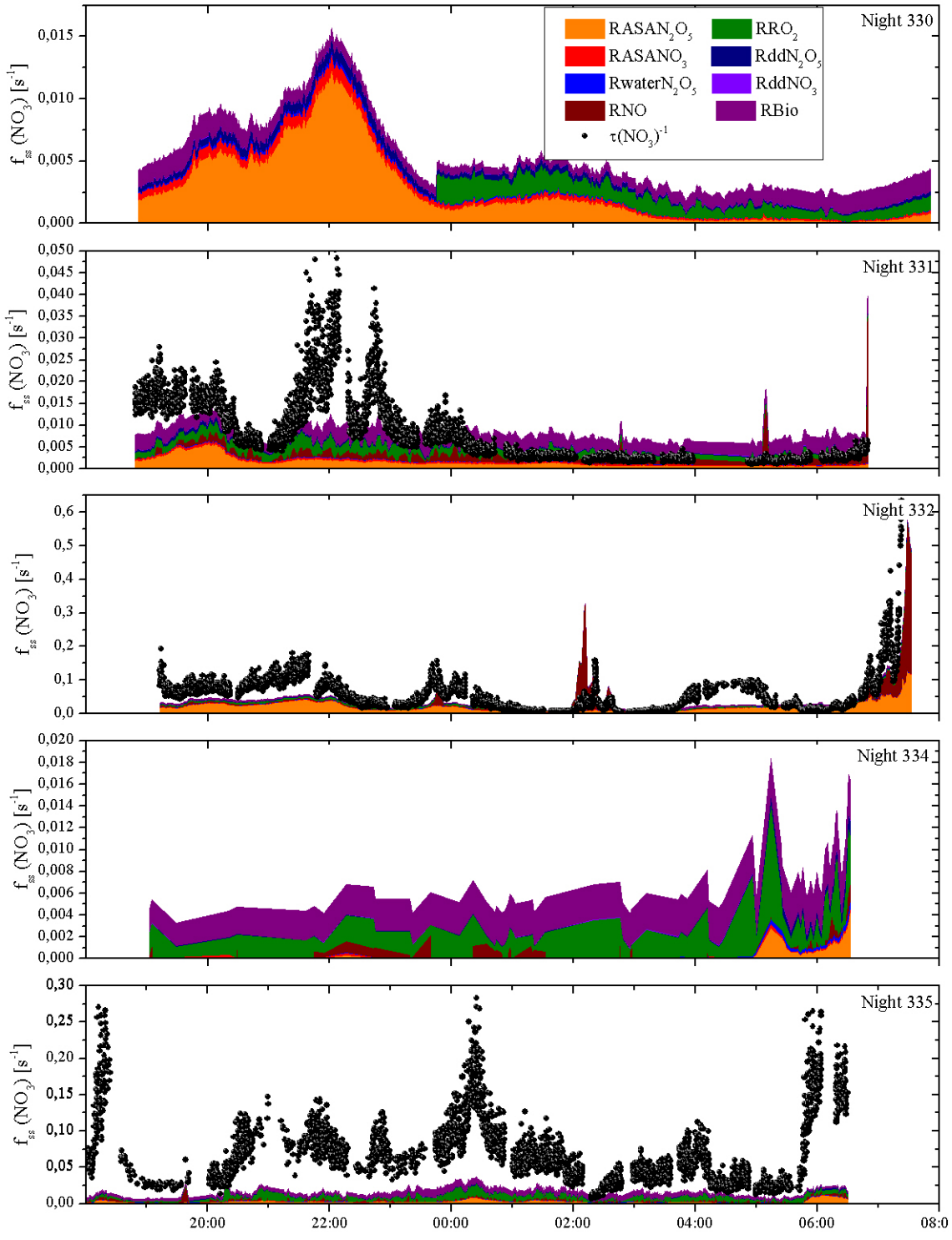
Night 330
Night 331
Night 332
Night 334
Night 335
RASAN2O5
RASANO3
RwaterN2O5
RNO
RRO2
RddN2O5
RddNO3
RBio
τ(NO3)-1
fss (NO3) [s-1]
20:00
22:00
00:00
02:00
04:00
06:00
08:0

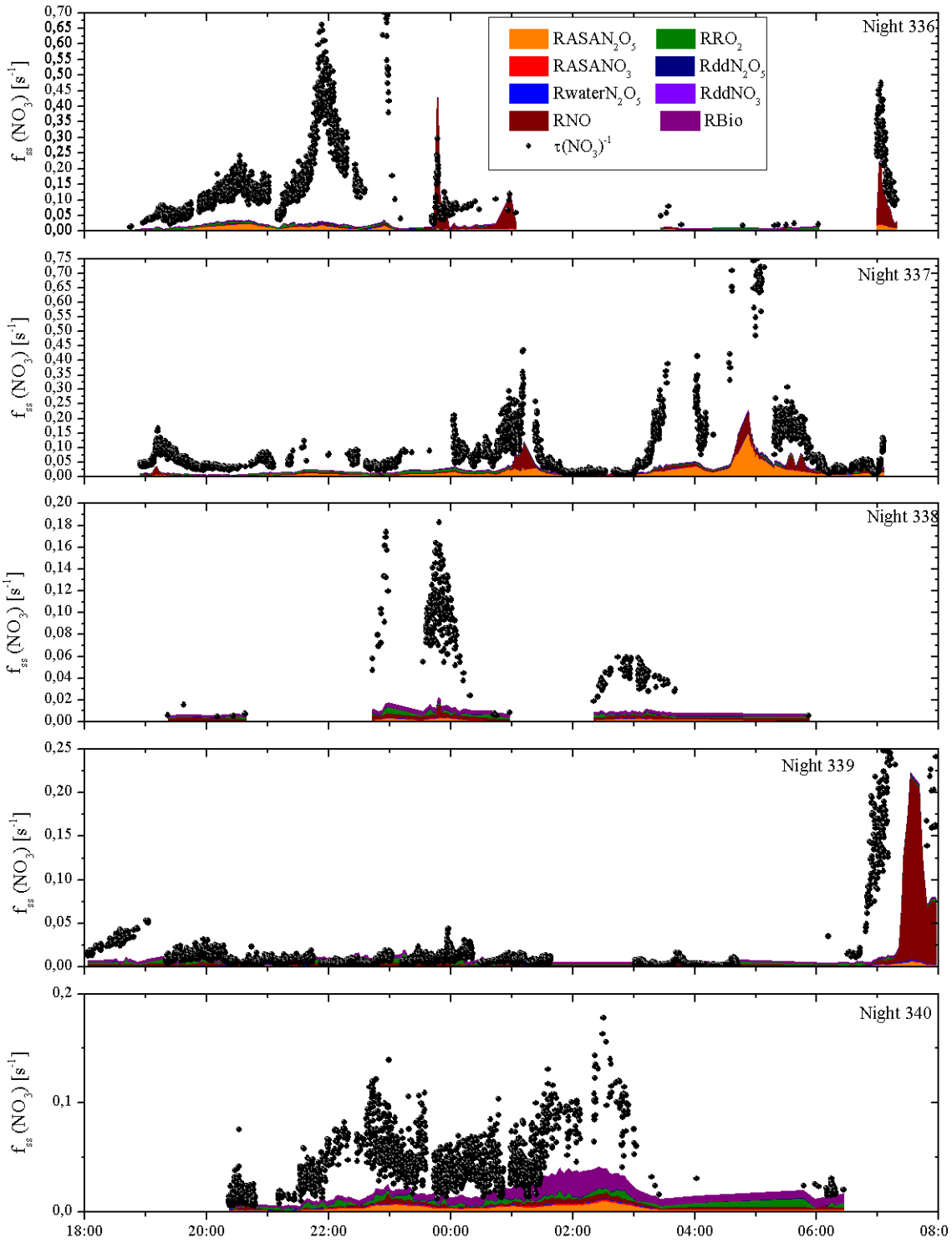
Night 336
Night 337
Night 338
Night 339
Night 340
RASAN2O5
RASANO3
RwaterN2O5
RNO
τ(NO3)-1
RRO2
RddN2O5
RddNO3
RBio
fss (NO3) [s-1]
18:00
20:00
22:00
00:00
02:00
04:00
06:00
08:0

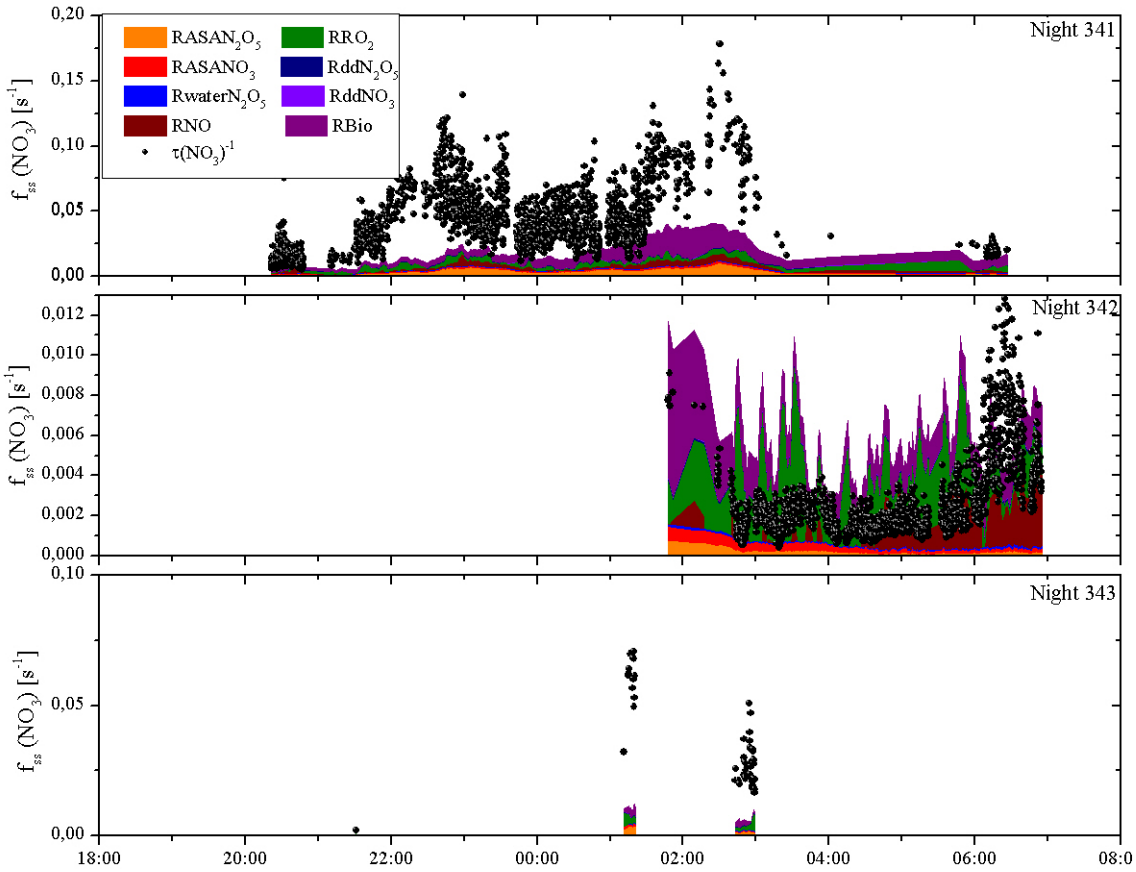
RASAN2O5
RASANO3
RwaterN2O5
RNO
τ(NO3)-1
RRO2
RddN2O5
RddNO3
RBio
Night 341
Night 342
Night 343
fss (NO3) [s-1]
0,20
0,15
0,10
0,05
0,00
0,012
0,010
0,008
0,006
0,004
0,002
0,000
18:00
20:00
22:00
00:00
02:00
04:00
06:00
08:0

C. PARADE 2011

In the following the time series of the measured compounds during the Parade campaign are shown (C.1). Additionally the diel profile are shown from the hydrocarbon used for the calculation of the production rates for the alkyl nitrates (C.2). Section C.4 shows the diel profile of the individual NO_y species which were used to calculate the contribution of each individual species to the total sum of NO_y. In C.4 the observed correlation between O_x and $\sum$ANs are shown for the different time periods which were used to calculate the effective branching ratio for the alkyl nitrate formation.

C.1. Timeseries

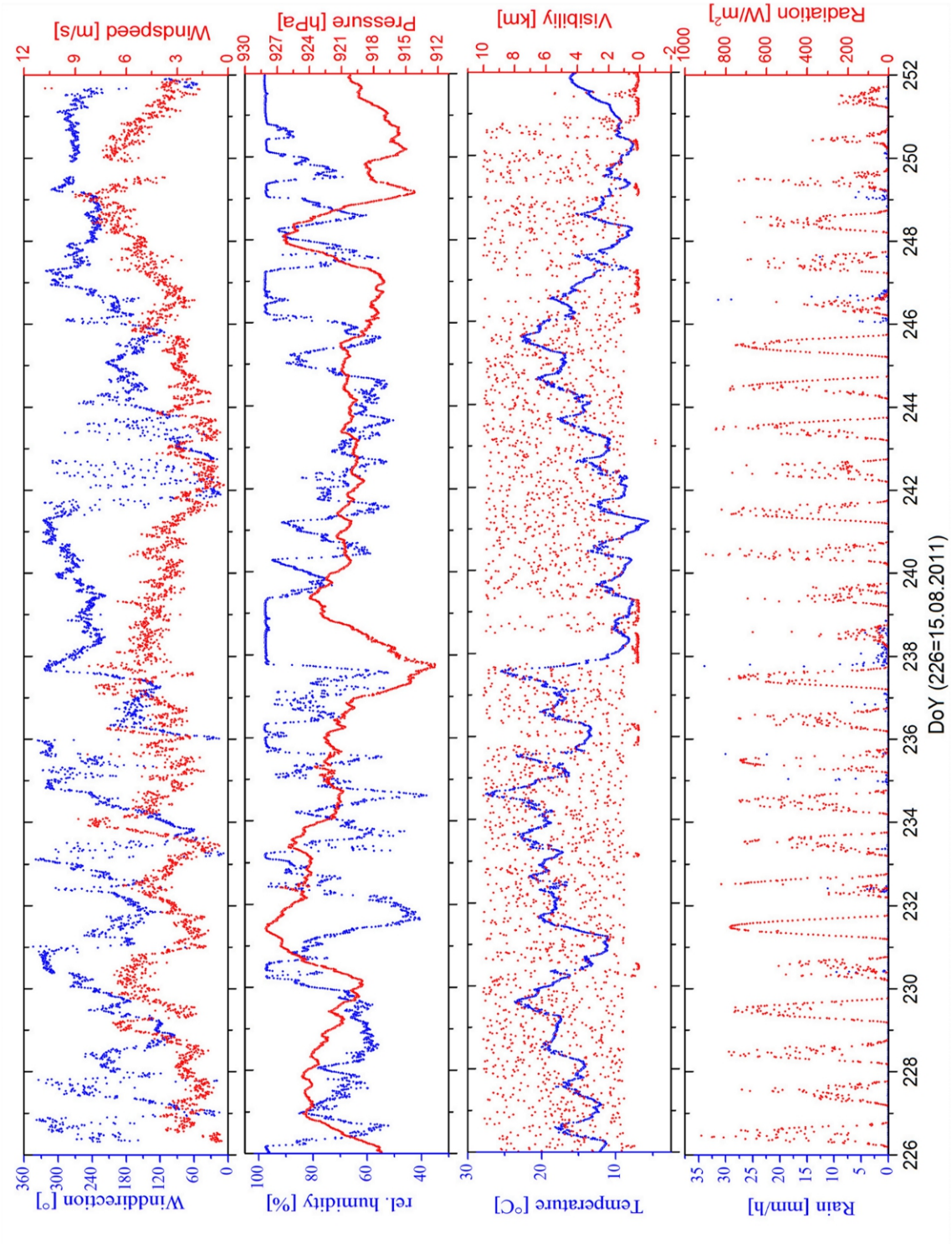

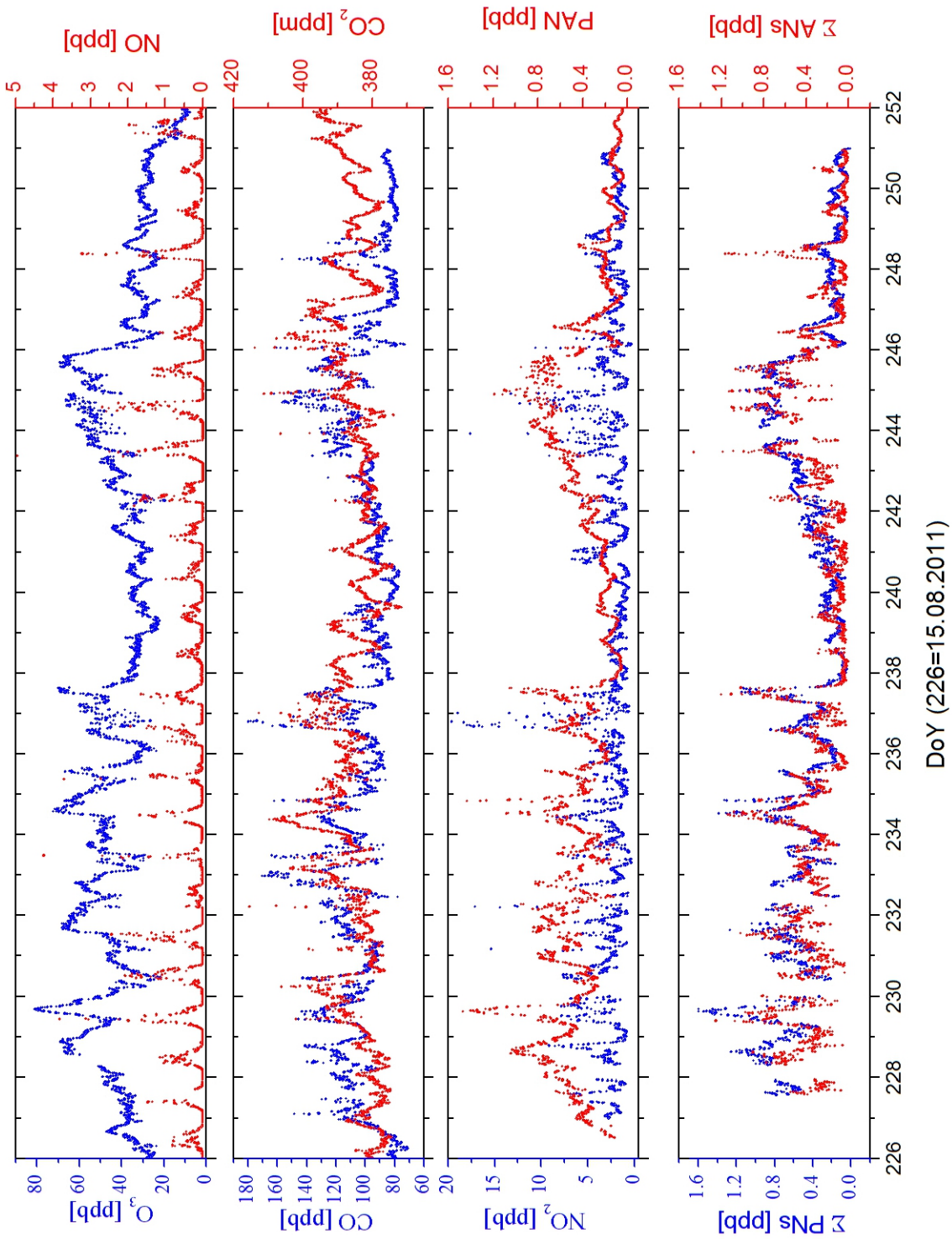
O3 [ppb]
CO [ppb]
NO2 [ppb]
Σ PNs [ppb]
NO [ppb]
CO2 [ppm]
PAN [ppb]
Σ ANs [ppb]
DoY (226=15.08.2011)

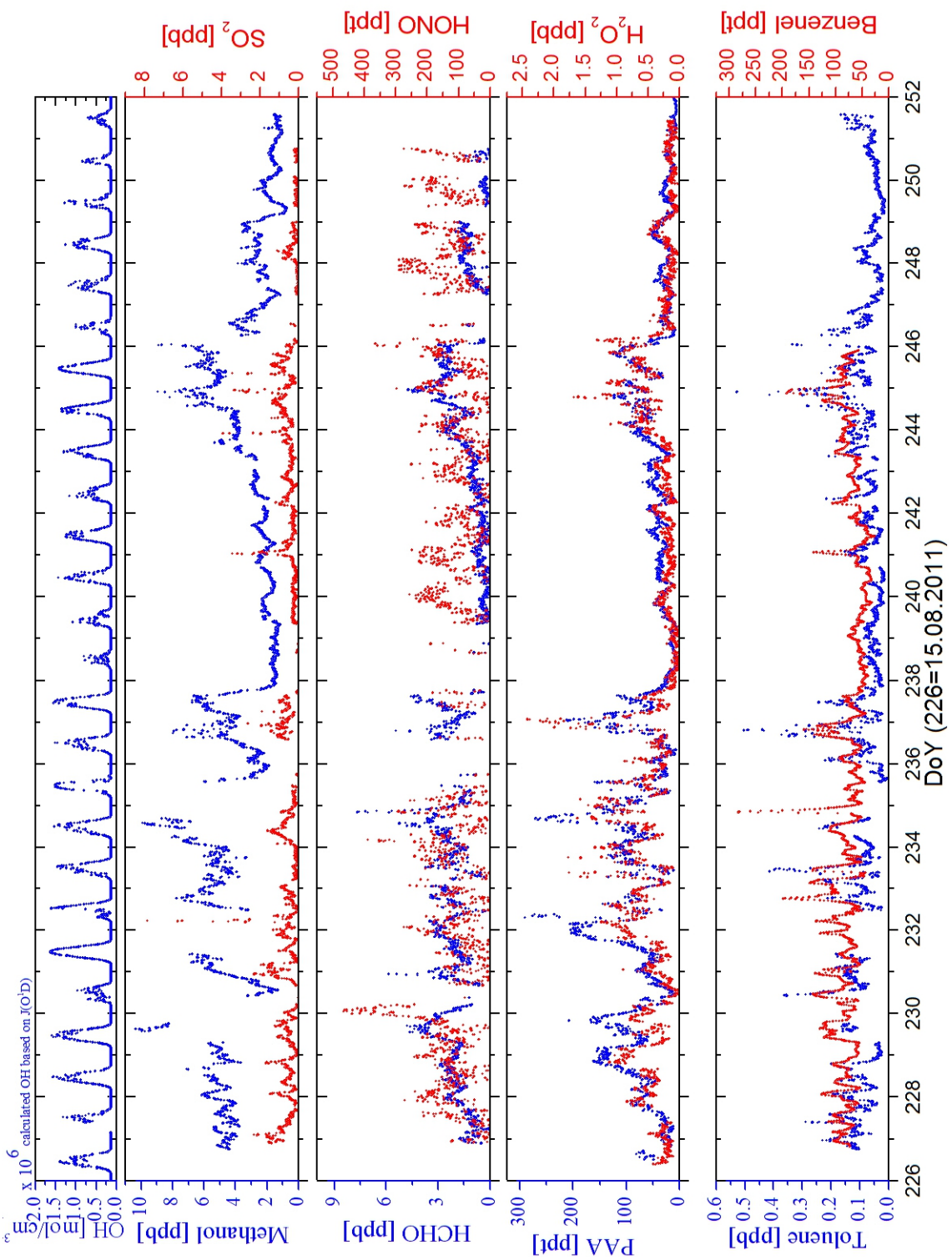
OH [mol/cm³]
x 10⁶ calculated OH based on J(O¹D)
Methanol [ppb]
SO₂ [ppb]
HCHO [ppb]
HONO [ppt]
PAA [ppt]
H₂O₂ [ppb]
Toluene [ppb]
Benzenel [ppt]
DoY (226=15.08.2011)

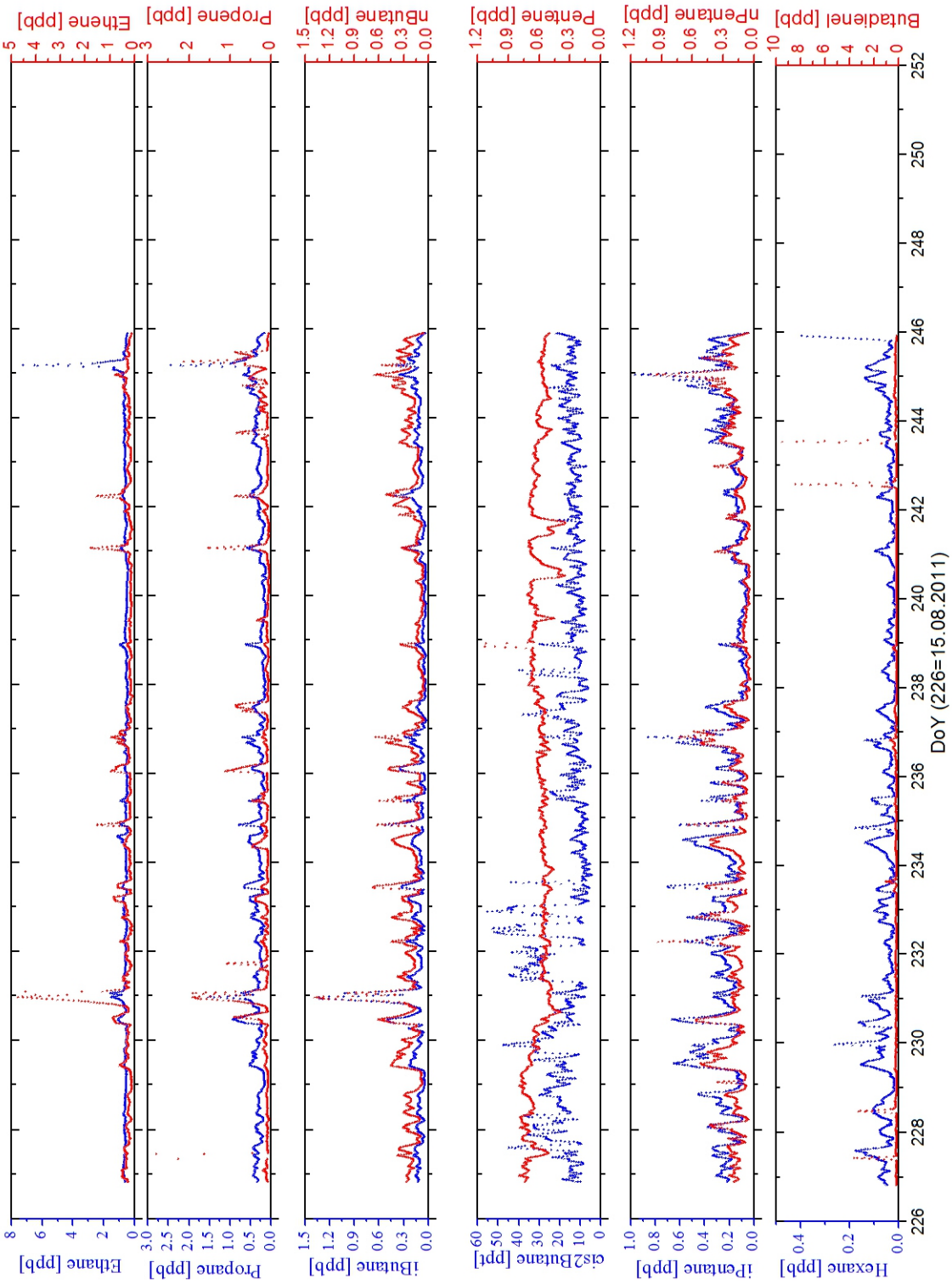
Ethane [ppb]
Propane [ppb]
iButane [ppb]
cis2Butane [ppt]
iPentane [ppb]
Hexane [ppb]
Ethene [ppb]
Propene [ppb]
nButane [ppb]
Pentene [ppb]
nPentane [ppb]
Butadiene [ppb]
DoY (226=15.08.2011)

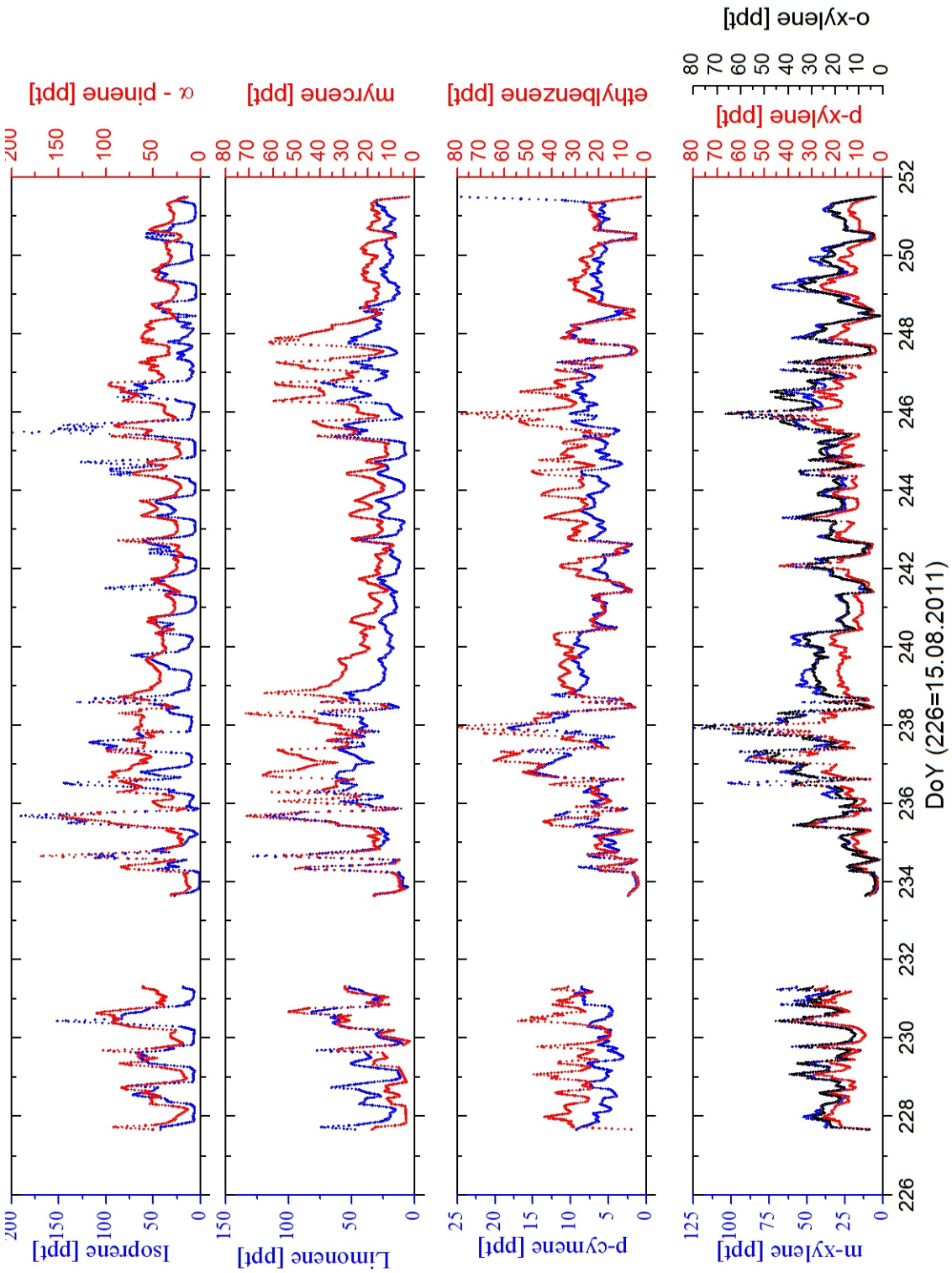
o-xylene [ppt]
p-xylene [ethylbenzene [ppt]
myrcene [ppt]
α - pinene [ppt]
m-xylene [ppt]
p-cymene [ppt]
Limonene [ppt]
Isoprene [ppt]
DoY (226=15.08.2011)

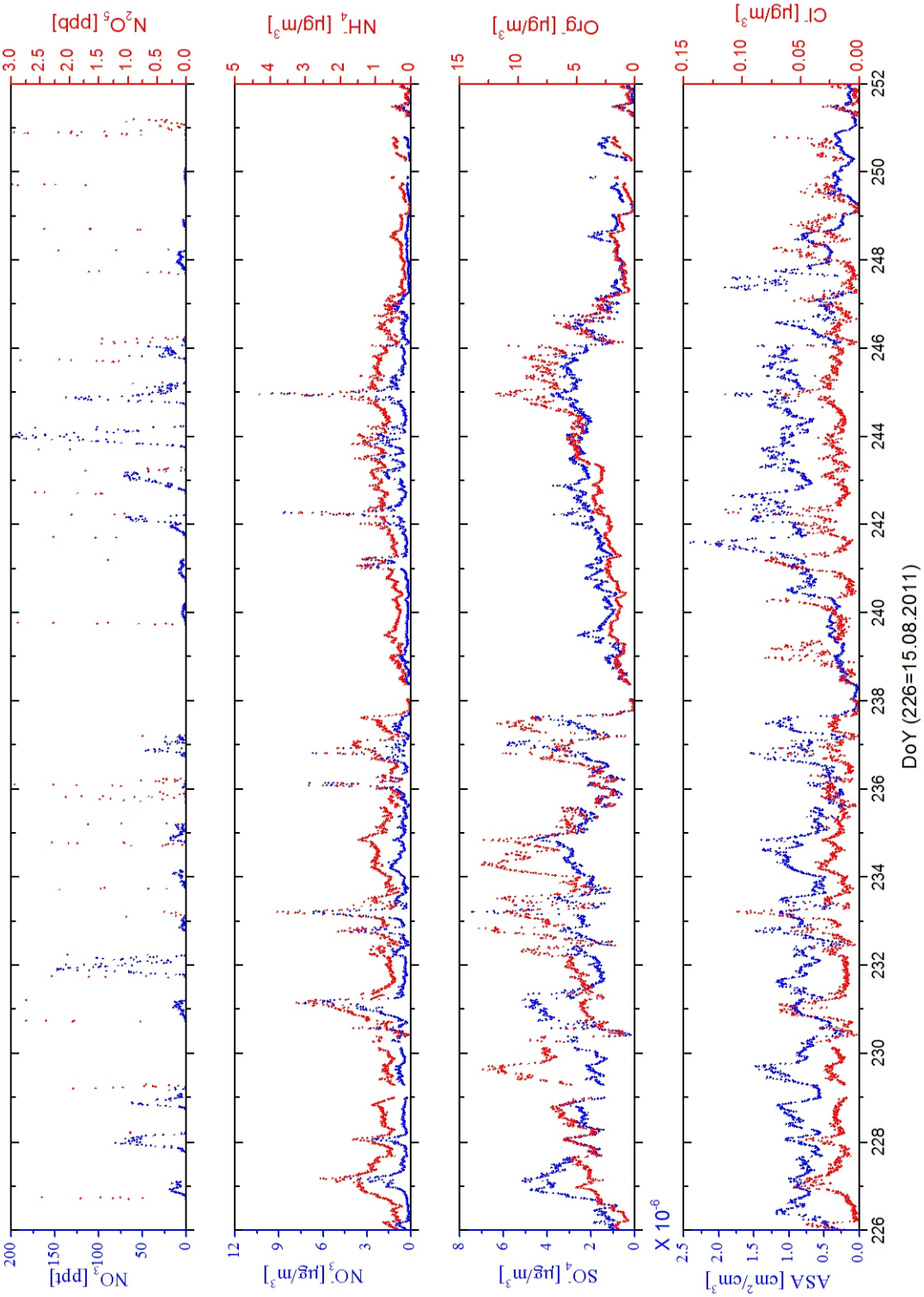
ASA [cm²/cm³]
Cl⁻ [µg/m³]
SO₄²⁻ [µg/m³]
X 10⁻⁶
Org⁻ [µg/m³]
NH₄⁺ [µg/m³]
NO₃⁻ [µg/m³]
NO₃ [ppt]
N₂O₅ [ppb]
DoY (226=15.08.2011)

C.2. Diurnal profile from NO_y contribution

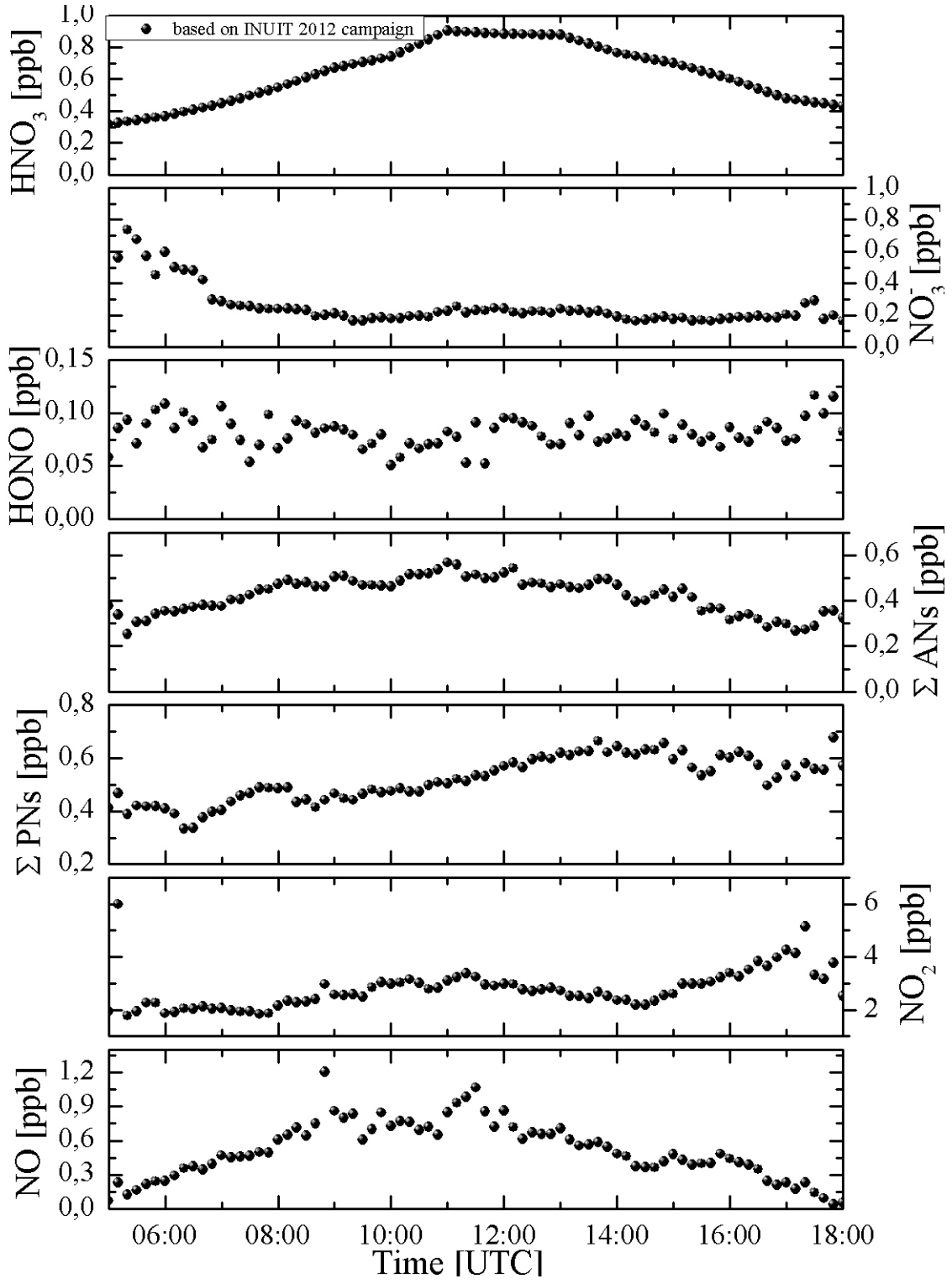

C.3. Diel Profiles

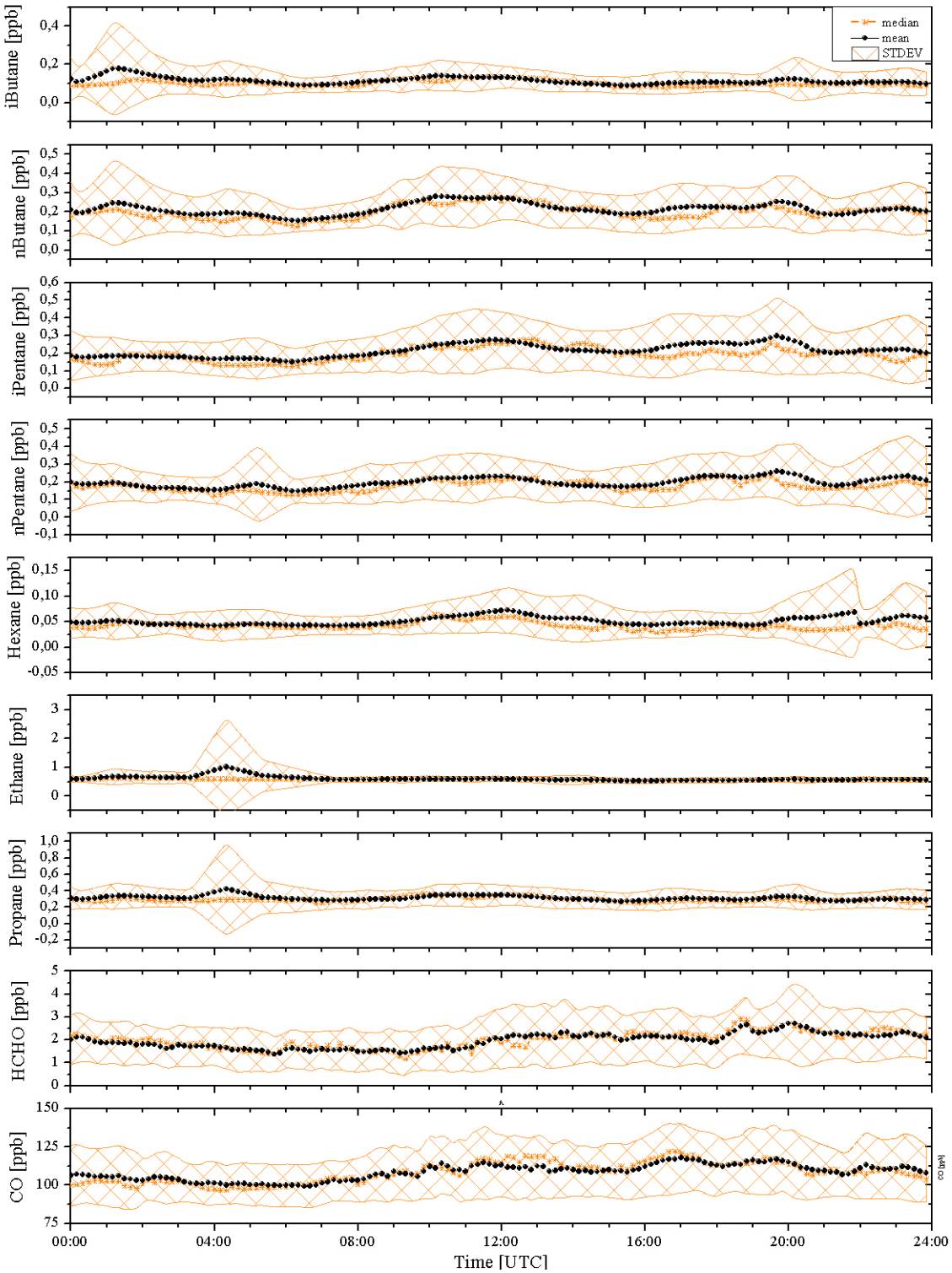

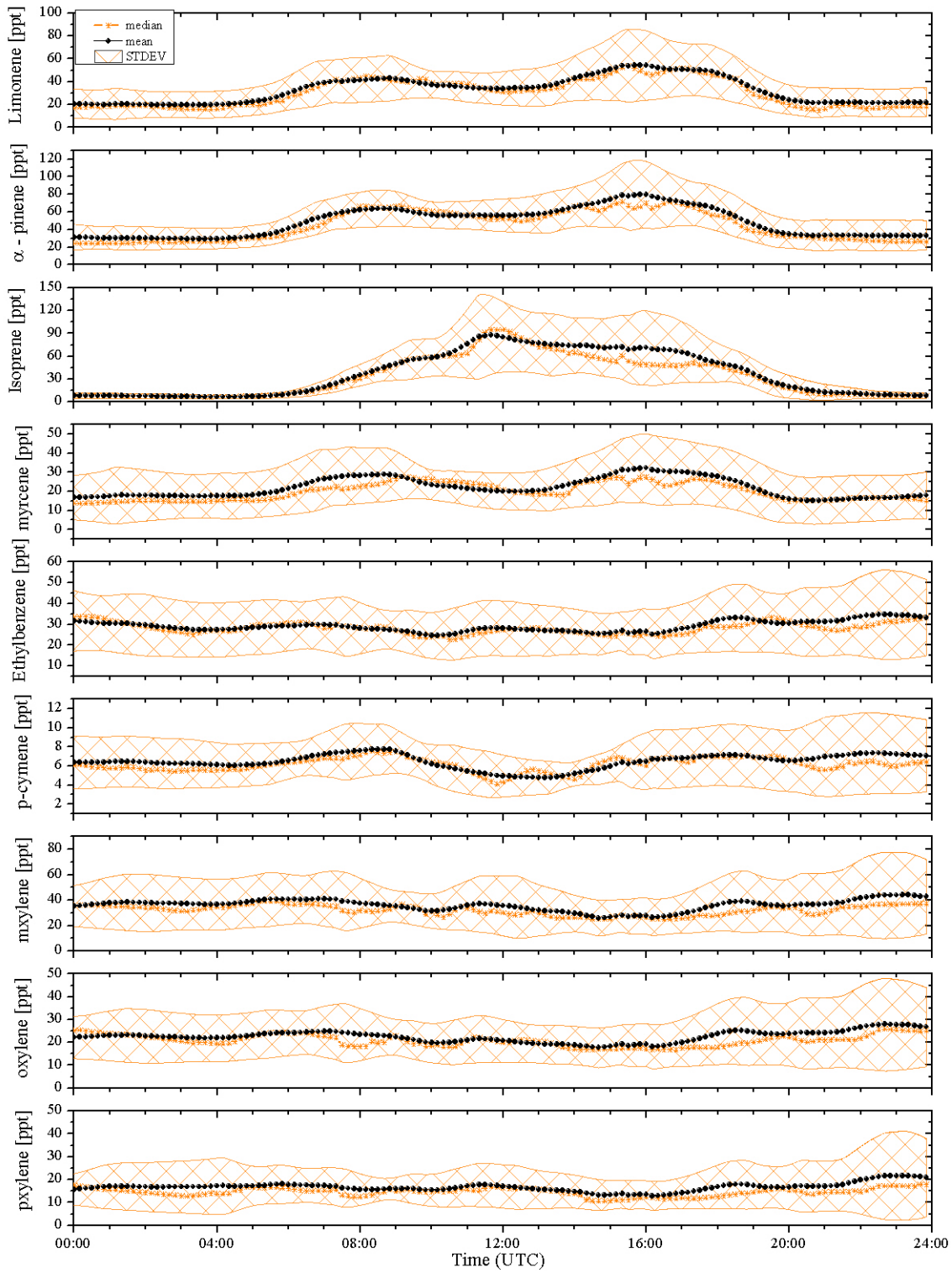
median
mean
STDEV
Limonene [ppt]
α - pinene [ppt]
Isoprene [ppt]
myrcene [ppt]
Ethylbenzene [ppt]
p-cymene [ppt]
mxylene [ppt]
oxylene [ppt]
pxylene [ppt]
00:00
04:00
08:00
12:00
16:00
20:00
24:00
Time (UTC)

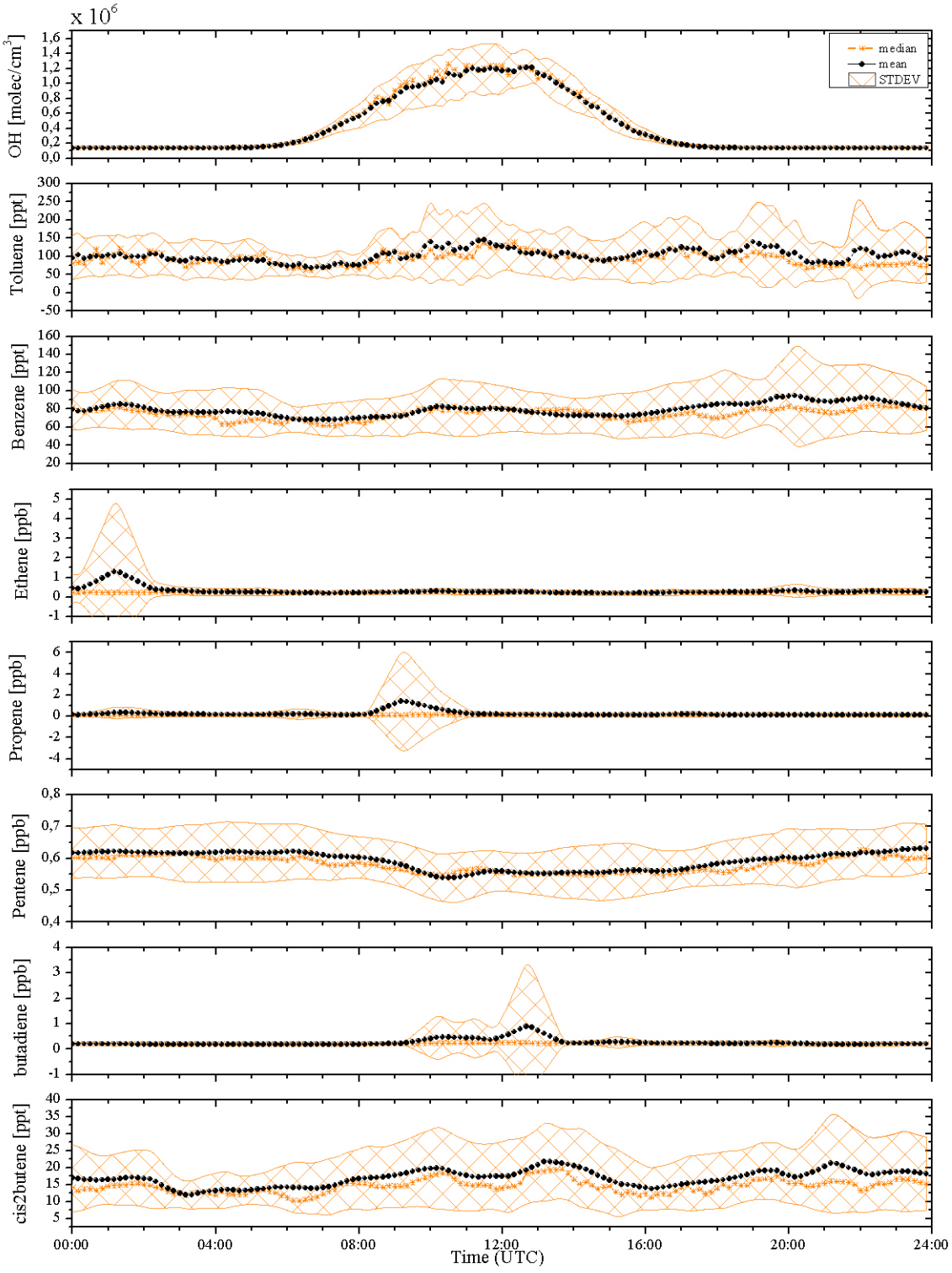
x 10^6
OH [molec/cm^3]
median
mean
STDEV
Toluene [ppt]
Benzene [ppt]
Ethene [ppb]
Propene [ppb]
Pentene [ppb]
butadiene [ppb]
cis2butene [ppt]
00:00
04:00
08:00
12:00
16:00
20:00
24:00
Time (UTC)

C.4. O_x versus $\sum$ANs

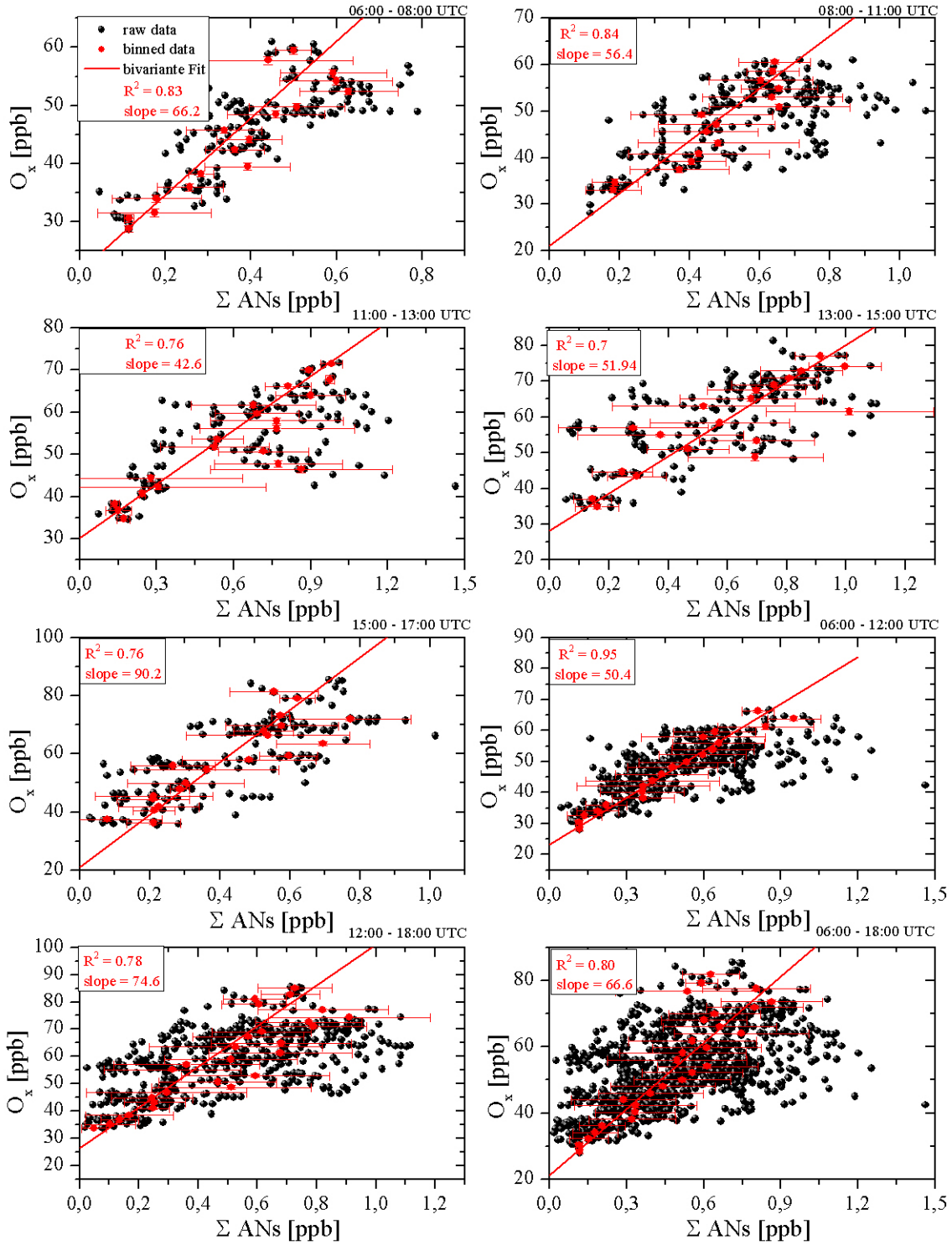

List of Figures

2.1. Tropospheric column NO_2 from (a) satellite measurements (GOME) and (b) atmospheric chemistry models. The maps represent ensemble average annual mean tropospheric NO_2 column density maps for the year 2000. (adapted from van Noije et al. (2006) and IPCC (2007)). 9

2.2. NO_3/N_2O_5 ratio against NO_2 mixing ratios for different temperatures. The temperature dependent equilibrium constant was calculated based on Atkinson et al. (2004) 17

2.3. Loss processes for different types of organic nitrates [Figure adopted from Talukdar et al. (1997, 1995)]. The additional thermal decomposition rates for Methyl - and Isopropyl nitrate are calculated using the Arrhenius Equation after Roberts (1990) (here Temperatures are assumed to be 298 K at Ground and about 227 K at about 11 km height). For the photolysis rate and OH reaction averaged values for actinic flux andOH concentrations are used calculated for summer conditions and 30° N and standard temperature profile. 25

2.4. Schematic overview of day and night time chemistry of NOy in the troposphere adapted from Aldener et al. (2006) 28

3.1. Scheme of a cavity assisted spectrometer. I_0: Incident pulsed light intensity. R: Mirrors with high reflectivity. L_0: mirror distance. L: Effective absorbing path. α: Absorbing and/or scattering species 32

3.2. A schematic of the two-channel CRDS at 662 nm. Ambient air was sampled through the filter and then divided into the two channels. The NO_3 cavity is kept at room temperature, the $NO_3 + N_2O_5$ cavity and inlet is kept at 90 °. PZ: polarizer WP: quarter wavelength plate BS: beam splitter 33

3.3. The cavity emission spectra from the two channels (red line: NO_3 cavity), blue line: NO_3+N_2O_5 cavity, both on left y-axis). Additionally the NO_3 absorption spectra (black line on right y-axis) at 298 K from Yokelson et al. (1994) 34

3.4. Graph of a typical measurement for determination of wall loss rates of the cavities 36

3.5. Typical data set for the determination of the loss rate of NO_3 and N_2O_5 on the filters. In the upper panel a) the measurement of N_2O_5 with and without filter is shown. In the lower panel b) the same measurement is shown for NO_3 37

3.6. The new constructed Cavity Ring Down Spectrometer. Detailed information are explained in the text and in the schematic overview in Figure 3.7 38

3.7. Schematic overview of the TD-CRDS two channel instrument. Details are explained in the text 39

3.8. normalized laser spectra of both channels (red line: NO_2 reference cell, blue line: thermal dissociation channel, both on left y-axis). Additionally on the right y axis the NO_2 cross section from Voigt et al. (2002) is shown as well possible interference species in this wavelength range (H_2O calculated from the HITRAN database, Glyoxal from Volkamer et al. (2005b)) and methylglyoxal from Sander et al. (2006) 40

3.9. Sketch of a typical measurement during a field campaign: the black dots represent the NO_2 reference cavity, the red dots display the $\sum$PNs measurements at 200°C, the blue dots show the measured $\sum$PNs + $\sum$ANs and the green dots show the NO_2 concentration measured over the bypass of the TD cavity. 41
3.10. Ratio of the mirror distance L_0 to the effective absorption path length L depending on the purge flow derived from measurement of a constant amount of NO_2 diluted with a constant flow of zero air at different levels of the purge flow. 43
3.11. calculate effective cross section of a laser diode emission spectrum taken every 20 minutes during a measurement campaign 44
3.12. Dependency of measured equivalent NO_2 mixing ratios on different pressure changes 45
3.13. Dependence of measured extinction on different levels of water vapour. Additionally plotted the equivalent NO_2 mixing ratios on the right hand side. The resulting decrease in extinction with increasing water vapour concentrations is due to smaller Rayleigh scatter cross section of water compared to zero air. 46
3.14. Relation between measured and calculated NO_2 production within in the instrument 47
3.15. Result of a model run according to eq.3.11 and the used values of Table 3.1. The residence time in this simulation is 10ms: IPN is isopropyl nitrate 49
3.16. Temperature distribution of the heater under standard flow condition 50
3.17. Temperature dependency of the thermal dissociation efficiency of peroxy nitrates . 51
3.18. Linearity of instrument and as well of the PAN source. PAN concentration were calculated assuming 90% conversion efficiency of photolytic PAN source (NO mixing ratio of 617 ppb) 52
3.19. Normalized TD signals of PAN, isopropyl nitrate and isobutyl nitrate as function of heater temperature. Dissociation of $\sum$PNs ($\sum$ANs) is quantitative at $\sim$ 200°C ($\sim$ 450°C) with no overlap with the other species 53
3.20. Qualitative measurement of alkyl nitrate: measured alkyl nitrate mixing ratios are plotted against calculated mixing ratios. 54
3.21. Dependence of 1 σ precision on integration time (Allan deviation plot) from a 2 h period of measurement of zero air. The upper panel shows the time series of the equivalent NO_2 mixing ratio. The middle panel shows a period of measurement of a constant alkyl nitrate mixing ratio of 700 pptv. The dependence of the calculated 1 σ precision on the integration time. The dashed line is the precision expected for purely random noise. 55
3.22. Uncertainty of the instrument as function of NO_2 mixing ratio (log scale) from 50 pptv to 100 ppbv including a maximum error for the humidity correction of 6 pptv (black dots: 95 % RH at 22 °C); 4pptv (red dots: 75 % RH at 22°C), 2 pptv(blue dots: 50% RH at 22°C) and 20 pptv of NO_2 possible in synthtetic air 56
3.23. Accuracy of the instrument as function of NO_2 mixing ratio (log scale) from 50 pptv to 100 ppbv including a maximum error for the humidity correction of 6 pptv (black dots: 95 % RH at 22 °C); 4pptv (red dots: 75 % RH at 22°C), 2 pptv(blue dots: 50% RH at 22°C) and no influence of synthetic air for each of them 57

4.1. Map of Europe on which the red stars represents the locations of the different campaigns 59
4.2. Overview of the surrounding area during the DOMINO campaign. Part a) of the figure shows the measurement site in relation to the surrounding with Huelva in the north west and Seville in the north east. Part b) shows a closer look at the measurement site "Base de Arenosillo". Part c) shows a view from the measurement site of the surrounding canopy. 61

4.3. a) Map of Spain. b) is showing the location of the field measurements and the local surroundings. . . . 62
4.4. On the left side, a map of Western Europe with focus on the Iberian Peninsula is shown including 48 h backwards trajectories calculated for every 2 hours using the HYSPLIT model. The zoom-in on the right side shows the transport direction of the classified air mass types at the measurement site. 6 air mass categories corresponding to different source regions were separated: "Seville" (purple), "Continental" (green), "Portugal + Huelva" (red), "Marine + Huelva" (orange), "Portugal + Marine" (light blue) and "Marine" (blue) . . . 63
4.5. Frequency distribution of the actual mean wind direction during the night (18:00 - 06:00) . . . 63
4.6. Meteorological overview during Domino 2008. The upper panel shows the temperature (black) and the pressure (red). The middle panel shows the wind direction colour coded by the wind speed. The regional influenced sectors are highlighted by different colours. The lowest panel shows the radiation during the campaign (blue dots) and the rainfall for each day (red bars) . . . 64
4.7. A huge set of different instrumentations. On the left side the front side of the measurement set up is shown with the different inlet location for each instrument. On the right side the back side of the container are shown with our NO_3/N_2O_5 and APS inlet . . . 65
4.8. Set up of the LP-DOAS instrument. The telescope was mounted on the ESAT building and the retro reflectors are mounted to a Tower at 4.8 km distance . . . 66
4.9. Schematic overview of the different light paths and the layers. The three different light paths are outlined in yellow. The blue boxes display the different layers. The box on the right side of the figure shows the average height of each layer above the ground. . . . 67
4.10. Overview of the surroundings during the PARADE campaign. This figure is a composite of a) a google map figure of the measurement site in relation to the surroundings, b) a closer view of the Taunus Oberservatory of the Uni Frankfurt (google maps) . . . 70
4.11. Meteorological overview during Parade 2011. The upper panel shows the temperature (black) and the pressure (red). The middle panel shows the wind direction colour coded by the wind speed. The regional influenced sectors are highlighted by different colours. The lowest panel shows the radiation during the campaign (blue dots) and the rainfall for each day (red bars) . . . 71
4.12. a) shows the surroundings of the measurement site with the different regional influenced sectors. b) Map of central Europe is shown including 48 hours backwards trajectories calculated for every 3 h using the HYSPLIT model. 5 air mass categories corresponding to different source regions were separated: "UK & I" (red), "English channel" (light blue), "Atlantic" (green), "Continental" (orange) and "mediterian" (purple) . . . 72
4.13. Picture of the Taunus Observatory with additional measurement containers around the observatory. . . . 73

5.1. Timeseries of the NO_3 and N_2O_5 mixing ratios. Additionally the NO_2 and the O_3 mixing ratios are plotted owing to their direct coupling to NO_3 and N_2O_5 . . . 86
5.2. Nocturnal profile of calculated NO_3 (a) and measured N_2O_5 (b) mixing ratios . . . 87
5.3. Timeseries of the NO_3 lifetime . . . 88
5.4. Mean nocturnal profile of the NO_3 lifetime . . . 88
5.5. Mean diel profile of the organic to sulphate fraction of the aerosols . . . 91

5.6. Nocturnal profile of the different loss processes: a) H_2O concentration, b) NO mixing ratio, c) aerosol surface area, d) Isoprene mixing ratio, e) α - pinene mixing ratio and f) limonene mixing ratio 91
5.7. Wind-direction dependency of NO_3 lifetimes (nighttime only). Almost 50% of the airmasses encountered at night came from the Huelva sector or was at least influenced by this sector, and were associated with very short NO_3 lifetimes 92
5.8. Averaged nocturnal profile of the inverse NO_3 lifetime compared with the calculated measured losses divided in four different wind sectors 93
5.10. 48 h Back trajectories calculated every hours using the Hysplit model. 94
5.9. Overview of measurements on the night 23rd - 24th in which the wind direction swung form the continental to the Huelva sector 95
5.11. Dependence of $\tau_{ss}(NO_3)$ on NO_2 and SO_2 mixing ratios and the aerosol surface area (ASA). 96
5.12. Overview of the aerosol content for the night of the 23rd to 24th November. The left plots shows the organic to sulfate ratio. The plot on the right site showed the organic fraction of the aerosol (left y-axis) and the sulphate to sulphate + nitrate ratio (right y-axis) 97
5.13. Apportioned NO_3 loss rates on the night 23-24 November. The various contribution are: $RASAN_2O_5$ = uptake of N_2O_5 to aerosol, $RASANO_3$ = reaction of NO_3 to aerosol, $RwaterN_2O_5$ = homogeneous hydrolysis of N_2O_5 with water, RNO = reaction of NO_3 with NO, RRO_2 = reaction of NO_3 with RO_2, $RddNO_3$ and $RddN_2O_5$ = Dry deposition of NO_3 and N_2O_5, RBio = reaction of NO_3 with isoprene, limonene and α - pinene, RSO_2 is the missing reactivity which has been scaled to correlate with SO_2 mixing ratios. The black dots are the calculated loss frequency of NO_3. 98
5.14. 48 h back trajectories for the night 26th to 27th of November calculated with the Hysplit model 101
5.15. Overview of measurements on the night 26-27 November 102
5.16. 26-27 November: Dependency of $\tau_{ss}(NO_3)$ on NO_2, the aerosol surface area (ASA) and the wind direction. Additionally the dependency of NO_2 on the aerosol surface area is shown. 103
5.17. Apportioned NO_3 loss rates on the night 26-27 November. The various contribution are: $RASAN_2O_5$ = uptake of N_2O_5 to aerosol (using $\gamma = 0.04$), $RASANO_3$ = uptake of NO_3 to aerosol (using $\gamma = 0.1$), $RwaterN_2O_5$ = homogeneous hydrolysis of N_2O_5 with water, RRO_2 = reaction of NO_3 with RO_2, $RddNO_3$ and $RddN_2O_5$ = Dry deposition of NO_3 and N_2O_5, RBio = reaction of NO_3 with isoprene, limonene and α - pinene. The black dots are the calculated loss frequency of NO_3. 104
5.18. verview of the aerosol content for the night of the 26-27 November. The left plots shows the organic to sulfate ratio. The plot on the right site showed the organic fraction of the aerosol (left y-axis) and the sulphate to sulphate + nitrate ratio (right y-axis) 105
5.19. Temperature dependence of the N_2O_5 and NO_3 concentrations. The left shows the correlation between ground temperature and NO_3/N_2O_5 mixing ratios. Right shows the anti correlation of both species against temperature difference of 50m and ground level 106
5.20. Overview of the nocturnal median lifetimes and loss processes with their different portioning to the entire measured losses (left site) and a comparison of the entire campaign median values with the median values for the different sectors. Appendix B.3 the nocturnal profiles for each night. 107

5.21. Relationship between NO_3 lifetimes, $\tau_{ss}(NO_3)$ and the mixing ratios of NO_2, SO_2 and aerosol surface area (ASA) during the entire campaign. 108
5.22. Extract of the time series of calculated daytime NO_3 levels including the measured NO_3 levels during night, ... 109
5.23. Comparison of the relative contribution of NO_3, OH and O_3 to the oxidation capacity. The oxidation capacity was calculated dor the oxidation of VOCs and methane (left), VOCs (middle) and terpenes (right). 110
5.24. Overview of the measured profile from the LP-DOAS measurements and the in-situ measurements. Each panel shows the comparison of the in-situ measurement (black) with the the three layers from the LP-DOAS measurements (red: Layer 1, blue: Layer 2 and orange: Layer 3). Shown are the calculated NO_3 lifetime (upper panel) followed by N_2O_5, NO_3, NO_2 and O_3 113
5.25. Averaged nocturnal profile (18:00 - 08:00) of NO_3, N_2O_5, NO_2, O_3 and the steady state lifetime τ_{NO_3}. In-situ measurements are shown in black, Layer 1 is in red, Layer 2 in blue and Layer 3 in orange. 114
5.26. Height dependency of NO_3 and τ_{NO_3} for the different wind sectors. a) shows an example for NO_3 and τ_{NO_3} profil at 04:00. 116
5.27. Comparison of the temperature change with height to the change of NO_3 mixing ratios in respect to height. Temperature changes were calculated from the temperature measurements on a 100 m Tower. The black line shows the temperature change from 25 m to 100 m whereas the red line shows the change from 25m to 50m due to no available 100 m measurements during this time period. For the change in NO_3 mixing ratios (blue) the LP-DOAS measurements from Layer 1 and 3 were used in respect to their averaged height above ground (a.g.l.) 117
5.28. Example of a balloon launch on midnight of the 3rd December. The red dots illustrate the potential temperature measured at the 100 m Tower. 117
5.29. Timeseries of the partionioning depending on the measurement height. The upper panel shows the nocturnal profile of the partioning 119
5.30. Daytime and nocturnal LNO_x calculated using Equation 5.16 and 5.17. The upper panel shows the mean daily profile for both (nocturnal losses in black and daytime losses in red). The lower panel shows the entire time series for both losses 120
5.31. LNO_x-timeseries shown for ground based and all LP DOAS Layer. The upper panel shows the nocturnal mean for each Layer compared with the mean average of the daytime loss and the average of the ground based and all Layer is also displayed in the upper and as well in the lower panel. The lower panel shows additionally the 1 hours averages of all data. 121
5.32. Planetary boundary evolution adapted from Stull (1988) 122
5.33. Overview of the Oxidation capacity depending on the vertical NO_3 concentration and different classes. 123
5.34. Comparison of different vertical NO_3 profiles.The different figures are taken or adapted from: a)Aliwell and Jones (1998), b) Stutz et al. (2004), c) Allan et al. (2002), d) Brown et al. (2007b), e) von Friedeburg et al. (2002), f) Stutz et al. (2009), g) Brown et al. (2007a), h) this thesis 126

6.1. Correlation plots of the 10 min averaged data between 7 different instruments. Each panel shows the correlation of one instrument against the CRD instrument: a) LP-DOAS, b) LIF, c) CLD (AG Fischer), d) CE-DOAS, e) CLD (Mola), f) CLD (HLUG). 131
6.2. Stacked column plot of the relative frequency distribution of the NO_2 concentration collected in 0.5 ppbv bins 132

6.3. Composite of the time series of the NO_2 measurements from the CRD and CLD instruments (lower panel) and a) unexpected behaviour during the campaign and c) possible interference by Glyoxal or Methylgloxal . . . 134
6.4. Relative frequency distribution of the NO_2 concentration summarized in 0.1 ppbv bins . . . 135
6.5. Comparison of a CLD instrument against CRD instrument during the HUMPPA-COPEC campaign 2010. Panel a) shows the the correlation of the entire data set except periods of instrumental problems and b) only for values lower than 400 pptv 136
6.6. Correlationplot between NO_2 mixing ratio of the TD-Channel using the bypass and the NO_2 reference channel . . . 137
6.7. Correlationplot between PAN measurements made by the MPI-CIMS and the sum of peroxy nitrates measured by the TD-CRDS . . . 138
6.8. Timeseries of 10 min average of the NO_2, $\sum$PNs, $\sum$ANs, Temperature and relative humidity . . . 139
6.9. Diel profile of NO_2, $\sum$PNs, $\sum$ANs, O_3 and Temperature for an average of 26 days 142
6.10. Frequency distribution of the actual mean wind direction during the campaign . . 143
6.11. Frequency distribution for NO_2, CO, $\sum$PNs and $\sum$ANs during the campaign . . . 144
6.12. Averaged diurnal profile of total NO_y (upper panel) and the relative fraction of individual NO_y species to the total amount of NO_y (lower panel). HNO_3 data are an estimate based on measurements in 2012. Orange represent the NO fraction, red: NO_2, blue: total peroxy nitrates, brown: total alkyl nitrates, navy blue: aerosol NO_3 and purple: HONO . . . 146
6.13. Time series of total calculated NO_y (bottom) and the contribution of the different measured individual $NO_{y\,i}$ (e.g. FNO: Contribution of NO). . . . 147
6.14. Averaged diurnal profile of total NO_z (upper panel) and the relative fraction of individual NO_z species to the total amount of NO_y (lower panel). HNO_3 data are an estimate based on measurements in 2012. blue: fraction of total peroxy nitrates, brown: total alkyl nitrates, navy blue: aerosol NO_3 and purple: HONO . 149
6.15. Diurnal profile of total peroxy nitrates druing PARADE (upper panel) and the profile of PAN from measurements during summer 1998 and 1999 [bottom panel] . 150
6.16. Averaged AN diurnal profile together with the integrated production rate 154
6.17. Diurnal profile of the total production rate calculated from each measured hydrocarbon . . . 154
6.18. Composite of three Pie - chart diagrams: a) shows the contribution of each measured hydrocarbon to to the total production rate of alkyl nitrates; b) shows the contribution of the different classes of compounds and c) shows the contribution between anthropogenic and biogenic VOCs . . . 156
6.19. O_x ($O_x = O_3 + NO_2$) versus $\sum$ANs (ppbv) for data between 05:00 and 18:00 UTC for the selected data set (open circles). The red circles represent the median $\sum AN$ concentration based on a 2 ppbv O_x bin . . . 159
6.20. O_x ($O_x = O_3 + NO_2$) versus $\sum$ANs (ppbv) for data between 11:00 and 13:00 UTC (black circle). The ed circles represent the median $\sum AN$. The line is the fit to the median data. . . . 160

List of Tables

2.1. Estimate of global tropospheric nitrogen oxides emissions in Tg N yr^{-1} [from IPCC (2007) AR4] . . . 8
2.2. NO_3 rate constants at room temperature for selected VOCs and their lifetimes at a fixed NO_3 mixing ratio [taken from Brown and Stutz (2012)] . . . 15
2.3. Summary of uptake coefficients of NO_3 and N_2O_5 on different kinds of aerosols [adapted from Brown and Stutz (2012)] . . . 19

3.1. Arrhenius parameters [$k = A\ exp(-E_a/(RT))$] for TD of selected molecules. R is the universal gas constant (8.314 J mol^{-1} K^{-1}) . . . 48

4.1. Properties of layers . . . 67
4.2. Overview of the in - situ measured gas phase species, measurement technique, precision, accuracy and detection limit according to the time resolution. Abbreviations see Appendix A . . . 68
4.3. Overview of the in - situ measured gas phase species, measurement technique, precision, accuracy and detection limit according to the time resolution. Abbreviations shown in Appendix A . . . 74

5.1. Measured trace gases with their reaction constant towards NO_3 and their mean, median and maxima measured values . . . 90

6.1. Calculations of $\sum$AN and O_3 Production from each the Hydrocarbons measured during the campaign, as described by Equations 6.10 and 6.11. The rate constants, α and γ values are taken from Rosen et al. (2004). Only α values for limonene and myrcene were taken from Pratt et al. (2012). Mixing ratios of the Hydrocarbons are median values from the time period 11-13 UTC. Median OH concentration during that period was about $1.2 \times 10^6 \frac{molec}{cm^3 s}$ . . . 153
6.2. $\sum AN$ measurements within ranges of O_x for all data of the selected data set between 05:00 and 18:00 UTC . . . 158

Bibliography

Aldener, M., Brown, S. S., Stark, H., Williams, E. J., Lerner, B. M., Kuster, W. C., Goldan, P. D., Quinn, P. K., Bates, T. S., Fehsenfeld, F. C., and Ravishankara, A. R. (2006). Reactivity and loss mechanisms of NO_3 and N_2O_5 in a polluted marine environment: Results from in situ measurements during New England Air Quality Study 2002. *Journal of Geophysical Research-Atmospheres*, 111, art. D23S73, doi 10.1029/2006JD007252(D23):–.

Aliwell, S. R. and Jones, R. L. (1998). Measurements of tropospheric NO_3 at midlatitude. *Journal Of Geophysical Research-Atmospheres*, 103(D5):5719–5727.

Allan, B. J., Carslaw, N., Coe, H., Burgess, R. A., and Plane, J. M. C. (1999). Observations of the nitrate radical in the marine boundary layer. *Journal of Atmospheric Chemistry*, 33(2):129–154.

Allan, B. J., McFiggans, G., Plane, J. M. C., Coe, H., and McFadyen, G. G. (2000). The nitrate radical in the remote marine boundary layer. *Journal of Geophysical Research-atmospheres*, 105(D19):24191–24204.

Allan, B. J., Plane, J. M. C., Coe, H., and Shillito, J. (2002). Observations of NO_3 concentration profiles in the troposphere. *Journal Of Geophysical Research-Atmospheres*, 107(D21).

Ambrose, J. L., Mao, H., Mayne, H. R., Stutz, J., Talbot, R., and Sive, B. C. (2007). Nighttime nitrate radical chemistry at Appledore island, Maine during the 2004 international consortium for atmospheric research on transport and transformation. *Journal Of Geophysical Research-Atmospheres*, 112.

Andrés-Hernández, M. D., Kartal, D., Growley, J. N., Sinha, V., Regelin, E., Martínez-Harder, M., Nenakhov, V., Williams, J., Harder, H., Bozem, H., Song, W., Thieser, J., Tang, M.-J., Hosaynali Beygi, Z., and Burrows, J. P. (2012). Diel peroxy radicals in a semi industrial coastal area: nighttime formation of free radicals. *Atmospheric Chemistry and Physics Discussions*, 12(8):19529–19570.

Asaf, D., Pedersen, D., Matveev, V., Peleg, M., Kern, C., Zingler, J., Platt, U., and Luria, M. (2009). Long-Term Measurements of NO_3 Radical at a Semiarid Urban Site: 1. Extreme Concentration Events and Their Oxidation Capacity. *Environmental Science & Technology*, pages –.

Atherton, C. S. and Penner, J. E. (1988). The Transformation of Nitrogen Oxides In the Polluted Troposphere. *Tellus Series B Chemical and Physical Meteorology*, 40(5):380–392.

Atkinson, R. and Arey, J. (2003). Atmospheric degradation of volatile organic compounds. *Chemical Reviews*, 103(12):4605–4638.

Atkinson, R., Aschmann, S. M., Carter, W. P., and Winer, A. M. (1982). Kinetics of the gas-phase reactions of OH radicals with alkyl nitrates at $298 \pm 2K$. *International Journal of Chemical Kinetics*, 14:919–926.

Atkinson, R., Baulch, D. L., Cox, R. A., Crowley, J. N., Hampson, R. F., Hynes, R. G., Jenkin, M. E., Rossi, M. J., and Troe, J. (2004). Evaluated kinetic and photochemical data for atmospheric chemistry: Volume I - gas phase reactions of O_x, HO_x, NO_x and SO_x species. *Atmospheric Chemistry and Physics*, 4(6):1461–1738.

Atkinson, R., Baulch, D. L., Cox, R. A., Crowley, J. N., Hampson, R. F., Hynes, R. G., Jenkin, M. E., Rossi, M. J., Troe, J., and Subcommittee, I. (2006). Evaluated kinetic and photochemical data for atmospheric chemistry: Volume II ; gas phase reactions of organic species. *Atmospheric Chemistry and Physics*, 6(11):3625–4055.

Atlas, E. (1988). Evidence for $> C3$ alkyl nitrates in rural and remote atmosphere. *Nature*, 331426-248.

Ayers, J. D., Apodaca, R. L., Simpson, W. R., and Baer, D. S. (2005). Off-axis cavity ring-down spectroscopy: application to atmospheric nitrate radical detection. *Applied Optics*, 44(33):7239–7242.

Baer, D. S., Paul, J. B., Gupta, J. B., and O'Keefe, A. (2002). Sensitive absorption measurements in the near-infrared region using off-axis integrated-cavity-output spectroscopy. *Applied Physics B-lasers and Optics*, 75(2-3):261–265.

Barnes, I., Hjorth, J., and Mihalopoulos, N. (2006). Dimethyl Sulfide and Dimethyl Sulfoxide and Their Oxidation in the Atmosphere. *Chemical Reviews*, 106(3):940–975.

Beaver, M. R., Clair, J. M. S., Paulot, F., Spencer, K. M., Crounse, J. D., LaFranchi, B. W., Min, K. E., Pusede, S. E., Wooldridge, P. J., Schade, G. W., Park, C., Cohen, R. C., and Wennberg, P. O. (2012). Importance of biogenic precursors to the budget of organic nitrates: observations of multifunctional organic nitrates by CIMS and TD-LIF during BEARPEX 2009. *Atmospheric Chemistry and Physics*, 12(13):5773–5785.

Berntsen, T. K., Karlsdóttir, S., and Jaffe, D. A. (1999). Influence of Asian emissions on the composition of air reaching the north western United States. *Geophys. Res. Lett.*, 26(14):2171–2174.

Bertram, T. H. and Thornton, J. A. (2009). Toward a general parameterization of N_2O_5 reactivity on aqueous particles: the competing effects of particle liquid water, nitrate and chloride. *Atmospheric Chemistry and Physics*, 9(21):8351–8363.

Bertram, T. H., Thornton, J. A., and Riedel, T. P. (2009a). An experimental technique for the direct measurement of N_2O_5 reactivity on ambient particles. *Atmospheric Measurement Techniques*, 2(1):231–242.

Bertram, T. H., Thornton, J. A., Riedel, T. P., Middlebrook, A. M., Bahreini, R., Bates, T. S., Quinn, P. K., and Coffman, D. J. (2009b). Direct observations of N_2O_5 reactivity on ambient aerosol particles. *Geophys. Res. Lett.*, 36(19):L19803–.

Bridier, I., Caralp, F., Loirat, H., Lesclaux, R., Veyret, B., Becker, K. H., Reimer, A., and Zabel, F. (1991). Kinetic and Theoretical-studies of the Reactions $CH_3C(O)O_2 + NO_2 + M \longleftrightarrow CH_3C(O)NO_2 + M$ between 248 K and 393 K and Between 30-torr and 760-torr. *Journal of Physical Chemistry*, 95(9):3594–3600.

Brown, S. S., deGouw, J. A., Warneke, C., Ryerson, T. B., DubÃ©, W. P., Atlas, E., Weber, R. J., Peltier, R. E., Neuman, J. A., Roberts, J. M., Swanson, A., Flocke, F., McKeen, S. A., Brioude, J., Sommariva, R., Trainer, M., Fehsenfeld, F. C., and Ravishankara, A. R. (2009a). Nocturnal isoprene oxidation over the Northeast United States in summer and its impact on reactive nitrogen partitioning and secondary organic aerosol. *Atmospheric Chemistry and Physics*, 9(9):3027–3042.

Brown, S. S., Dube, W. P., Fuchs, H., Ryerson, T. B., Wollny, A. G., Brock, C. A., Bahreini, R., Middlebrook, A. M., Neuman, J. A., Atlas, E., Roberts, J. M., Osthoff, H. D., Trainer, M., Fehsenfeld, F. C., and Ravishankara, A. R. (2009b). Reactive uptake coefficients for N_2O_5 determined from aircraft measurements during the Second Texas Air Quality Study: Comparison to current model parameterizations. *Journal Of Geophysical Research-Atmospheres*, 114.

Brown, S. S., Dube, W. P., Osthoff, H. D., Stutz, J., Ryerson, T. B., Wollny, A. G., Brock, C. A., Warneke, C., De Gouw, J. A., Atlas, E., Neuman, J. A., Holloway, J. S., Lerner, B. M., Williams, E. J., Kuster, W. C., Goldan, P. D., Angevine, W. M., Trainer, M., Fehsenfeld, F. C., and Ravishankara, A. R. (2007a). Vertical profiles in NO_3 and N_2O_5 measured from an aircraft: Results from the NOAA P-3 and surface platforms during the New England Air Quality Study 2004. *Journal of Geophysical Research-Atmospheres*, 112(D22):–.

Brown, S. S., Dube, W. P., Osthoff, H. D., Wolfe, D. E., Angevine, W. M., and Ravishankara, A. R. (2007b). High resolution vertical distributions of NO_3 and N_2O_5 through the nocturnal boundary layer. *Atmospheric Chemistry and Physics*, 7:139–149–.

Brown, S. S., Ryerson, T. B., Wollny, A. G., Brock, C. A., Peltier, R., Sullivan, A. P., Weber, R. J., Dube, W. P., Trainer, M., Meagher, J. F., Fehsenfeld, F. C., and Ravishankara, A. R. (2006). Variability in nocturnal nitrogen oxide processing and its role in regional air quality. *Science*, 311(5757):67–70.

Brown, S. S., Stark, H., Ciciora, S. J., McLaughlin, R. J., and Ravishankara, A. R. (2002). Simultaneous in situ detection of atmospheric NO_3 and N_2O_5 via cavity ring-down spectroscopy. *Review of Scientific Instruments*, 73(9):3291–3301.

Brown, S. S., Stark, H., and Ravishankara, A. R. (2003). Applicability of the steady state approximation to the interpretation of atmospheric observations of NO_3 and N_2O_5. *Journal of Geophysical Research-Atmospheres*, 108, Art. 4539, doi:10.1029/2003JD003407(D17):–.

Brown, S. S. and Stutz, J. (2012). Nighttime radical observations and chemistry. *Chem. Soc. Rev.*, pages –.

Buhr, M. P., Parrish, D. D., Norton, R. B., Fehsenfeld, F. C., Sievers, R. E., and Roberts, J. M. (1990). Contribution of Organic Nitrates to the Total Reactive Nitrogen Budget at a Rural Eastern U.S. Site. *J. Geophys. Res.*, 95(D7):9809–9816.

Burrows, J. P., Dehn, A., Deters, B., Himmelmann, S., Richter, A., Voigt, S., and Orphal, J. (1998). Atmospheric remote-sensing reference data from GOME: Part I. Temperature-dependent absorption cross-sections of NO_2 in the 231-794 nm range. *Journal of Quantitative Spectroscopy & Radiative Transfer*, 60(6):1025–1031.

Butkovskaya, N. I. and LeBras, G. (1994). Mechanism of the $NO_3 + DMS$ Reaction By Discharge Flow Mass-spectrometry. *Journal of Physical Chemistry*, 98(10):2582–2591.

Calvert, J. G. and Madronich, S. (1987). Theoretical-study of the Initial Products of the Atmospheric Oxidation of Hydrocarbons. *Journal of Geophysical Research-atmospheres*, 92(D2):2211–2220.

Cantrell, C., Shetter, R., Calvert, J., Eisele, F., Williams, E., Baumann, K., Brune, W., Stevens, S., and Mather, J. (1997). Peroxy radicals from photostationary state deviations and steady state calculations during the Tropospheric OH Photochemistry Experiment at Idaho Hill, Colarado, 1993. *J. Geophys. Res.-Atmos.*, 102:6369–6378.

Cantrell, C. A., Shetter, R. E., and Calvert, J. (1996). Peroxy radical chemistry during FIELD-VOC 1993 in Brittany, France. *Atmospheric Environment*, 30(23):3947–3957.

Carbajo, P. G. and Orr-Ewing, A. J. (2010). NO_2 quantum yields from ultraviolet photodissociation of methyl and isopropyl nitrate. *Physical Chemistry Chemical Physics*, 12(23):6084–6091.

Carpenter, L., Clemitshaw, K., Burgess, R., Penkett, S., Cape, J., and McFadyen, G. (1998). Investigation and evaluation of the NO_x / O_3 photochemical steady state. *Atmospheric Environment*, 32:3353–3365–.

Carslaw, N., Carpenter, L. J., Plane, J. M. C., Allan, B. J., Burgess, R. A., Clemitshaw, K. C., Coe, H., and Penkett, S. A. (1997). Simultaneous observations of nitrate and peroxy radicals in the marine boundary layer. *Journal Of Geophysical Research-Atmospheres*, 102(D15):18917–18933.

Clemitshaw, K. C., Williams, J., Rattigan, O. V., Shallcross, D. E., Law, K. S., and Anthony Cox, R. (1997). Gas-phase ultraviolet absorption cross-sections and atmospheric lifetimes of several C2 - C5 alkyl nitrates. *Journal of Photochemistry and Photobiology A: Chemistry*, 102:117–126.

Crowley, J. N., Schuster, G., Pouvesle, N., Parchatka, U., Fischer, H., Bonn, B., Bingemer, H., and Lelieveld, J. (2010). Nocturnal nitrogen oxides at a rural mountain-site in south-western Germany. *Atmospheric Chemistry and Physics*, 10(6):2795–2812.

Curtis, A. R. and Sweetenham, W. P. (1987). Facsimile, AERE, Report R-12805.

Day, D. A., Dillon, M. B., Wooldridge, P. J., Thornton, J. A., Rosen, R. S., Wood, E. C., and Cohen, R. C. (2003). On alkyl nitrates, O_3, and the "missing NO_y". *Journal of Geophysical Research-atmospheres*, 108(D16):4501.

Day, D. A., Farmer, D. K., Goldstein, A. H., Wooldridge, P. J., Minejima, C., and Cohen, R. C. (2009). Observations of NOx,$\sum$ PN′s, $\sum$ AN′s, HNO_3 at a Rural Site in the California Sierra Nevada Mountains: summertime diurnal cycles. *Atmospheric Chemistry and Physics*, 9(14):4879–4896.

Day, D. A., Wooldridge, P. J., Dillon, M. B., Thornton, J. A., and Cohen, R. C. (2002). A thermal dissociation laser-induced fluorescence instrument for in situ detection of NO_2, peroxy nitrates, alkyl nitrates, and HNO_3. *J. Geophys. Res.*, 107(D6):4046–.

Dentener, F. J. and Crutzen, P. J. (1993). Reaction Of N_2O_5 On Tropospheric Aerosols - Impact On The Global Distributions of NOx, O_3, and OH. *Journal Of Geophysical Research-Atmospheres*, 98(D4):7149–7163.

Diesch, J.-M., Drewnick, F., Zorn, S. R., von der Weiden-ReinmÃ¼ller, S.-L., Martinez, M., and Borrmann, S. (2012). Variability of aerosol, gaseous pollutants and meteorological characteristics associated with changes in air mass origin at the SW Atlantic coast of Iberia. *Atmos. Chem. Phys.*, 12(8):3761–3782.

Draxler, R. R. and Rolph, G. D. (2011). HYSPLIT (HYbrid Single-Particle Lagrangian Integrated Trajectory) Model access via NOAA ARL READY Website (http://ready.arl.noaa.gov/HYSPLIT.php). NOAA Air Resources Laboratory, Silver Spring, MD.

Emmerson, K. M. and Carslaw, N. (2009). Night-time radical chemistry during the TORCH campaign. *Atmospheric Environment*, 43(20):3220–3226.

Emmerson, K. M., Carslaw, N., and Pilling, M. J. (2005). Urban atmospheric chemistry during the PUMA campaign 2: Radical budgets for OH, HO_2 and RO_2. *Journal of Atmospheric Chemistry*, 52(2):165–183.

Escorcia, E. N., Sjostedt, S. J., and Abbatt, J. P. D. (2010). Kinetics of N_2O_5 Hydrolysis on Secondary Organic Aerosol and Mixed Ammonium Bisulfate Secondary Organic Aerosol Particles. *J. Phys. Chem. A*, 114(50):13113–13121.

Evans, M. J. and Jacob, D. J. (2005). Impact of new laboratory studies of N_2O_5 hydrolysis on global model budgets of tropospheric nitrogen oxides, ozone, and OH. *Geophysical Research Letters*, 32(9).

Fahey, D. W., Hübler, G., Parrish, D. D., Williams, E. J., Norton, R. B., Ridley, B. A., Singh, H. B., Liu, S. C., and Fehsenfeld, F. C. (1986). Reactive Nitrogen Species in the Troposphere: Measurements of NO, NO_2, ceHNO3, Particulate Nitrate, Peroxyacetyl Nitrate (PAN), O_3, and Total Reactive Odd Nitrogen (NO_y) at Niwot Ridge, Colorado. *J. Geophys. Res.*, 91(D9):9781–9793.

Farman, J. C., Gardiner, B. G., and Shanklin, J. D. (1985). Large losses of total ozone in Antarctica reveal seasonal ClO_x/NO_x interaction. *Nature*, 315(6016):207–210.

Farmer, D. K., Perring, A. E., Wooldridge, P. J., Blake, D. R., Baker, A., Meinardi, S., Huey, L. G., Tanner, D., Vargas, O., and Cohen, R. C. (2011). Impact of organic nitrates on urban ozone production. *Atmospheric Chemistry and Physics*, 11(9):4085–4094.

Fenter, F. F. and Rossi, M. J. (1997). Heterogeneous Reaction of NO_3 with Ice and Sulfuric Acid Solutions: Upper Limits for the Uptake Coefficients. *The Journal of Physical Chemistry A*, 101(22):4110–4113.

Finlayson-Pitts, B., Ezell, M., and Pitts, J. J. (1989). Formation of chemically active chlorine compounds by reactions of atmospheric NaCl particles with gaseous N_2O_5 and $ClONO_2$. *Nature*, 337:241–244.

Finlayson-Pitts, B. and James N. Pitts, J. (1999). *Chemistry of the Upper and Lower Atmosphere: Theory, Experiments, and Applications*. Academic Press.

Fischer, E. V., Jaffe, D. A., Reidmiller, D. R., and Jaeglé, L. (2010). Meteorological controls on observed peroxyacetyl nitrate at Mount Bachelor during the spring of 2008. *J. Geophys. Res.*, 115(D3):D03302–.

Fish, D., Shallcross, D., and Jones, R. (1999). The vertical distribution of NO_3 in the atmospheric boundary layer. *Atmospheric Environment*, 33(5):687–691.

Flocke, F., Volz-Thomas, A., and Kley, D. (1991). Measurements of alkyl nitrates in rural and polluted air masses. *Atmospheric Environment. Part A. General Topics*, 25(9):1951–1960.

Flocke, F. M., Weinheimer, A. J., Swanson, A. L., Roberts, J. M., Schmitt, R., and Shertz, S. (2005). On the measurement of PANs by gas chromatography and electron capture detection. *Journal of Atmospheric Chemistry*, 52(1):19–43.

Folkers, M., Mentel, T. F., and Wahner, A. (2003). Influence of an organic coating on the reactivity of aqueous aerosols probed by the heterogeneous hydrolysis of N_2O_5. *Geophysical Research Letters*, 30(12).

Fry, J. L., Kiendler-Scharr, A., Rollins, A. W., Brauers, T., Brown, S. S., Dorn, H.-P., Dubé, W. P., Fuchs, H., Mensah, A., Rohrer, F., Tillmann, R., Wahner, A., Wooldridge, P. J., and Cohen, R. C. (2011). SOA from limonene: role of NO_3 in its generation and degradation. *Atmospheric Chemistry and Physics*, 11(8):3879–3894.

Fry, J. L., Kiendler-Scharr, A., Rollins, A. W., Wooldridge, P. J., Brown, S. S., Fuchs, H., Dube, W., Mensah, A., dal Maso, M., Tillmann, R., Dorn, H.-P., Brauers, T., and Cohen, R. C. (2009). Organic nitrate and secondary organic aerosol yield from NO_3 oxidation of isopinene evaluated using a gas-phase kinetics/aerosol partitioning model. *Atmospheric Chemistry and Physics*, 9(4):1431–1449.

Fuchs, H., Dubé, W. P., Lerner, B. M., Wagner, N. L., Williams, E. J., and Brown, S. S. (2009). A Sensitive and Versatile Detector for Atmospheric NO_2 and NOx Based on Blue Diode Laser Cavity Ring-Down Spectroscopy. *Environmental Science & Technology*, 43(20):7831–7836.

Fuchs, N. and Sutugin, A. (1970). *Highly dispersed aerosols*. Ann Arbor Science Publishers.

Fuzzi, S., Facchini, M. C., Schell, D., Wobrock, W., Winkler, P., Arends, B. G., Kessel, M., Mols, J. J., Pahl, S., Schneider, T., Berner, A., Solly, I., Kruisz, C., Kalina, M., Fierlinger, H., Hallberg, A., Vitali, P., Santoli, L., and Tigli, G. (1994). Multiphase Chemistry and Acidity of Clouds at Kleiner-Feldberg. *Journal of Atmospheric Chemistry*, 19(1-2):87–106.

Galloway, J. N., Dentener, F. J., Capone, D. G., Boyer, E. W., Howarth, R. W., Seitzinger, S. P., Asner, G. P., Cleveland, C. C., Green, P. A., Holland, E. A., Karl, D. M., Michaels, A. F., Porter, J. H., Townsend, A. R., and Vorosmarty, C. J. (2004). Nitrogen cycles: past, present, and future. *Biogeochemistry*, 70(2):153–226.

Galmarini, S., Duynkerke, P. G., and deArellano, I. V. G. (1997). Evolution of nitrogen oxide chemistry in the nocturnal boundary layer. *Journal of Applied Meteorology*, 36(7):943–957.

George, C., Ponche, J. L., Mirabel, P., Behnke, W., Scheer, V., and Zetzsch, C. (1994). Study of the Uptake of N_2O_5 by Water and NaCl Solutions. *Journal of Physical Chemistry*, 98(35):8780–8784.

Geyer, A., Ackermann, R., Dubois, R., Lohrmann, B., Muller, T., and Platt, U. (2001a). Long-term observation of nitrate radicals in the continental boundary layer near Berlin. *Atmospheric Environment*, 35(21):3619–3631.

Geyer, A., Alicke, B., Konrad, S., Schmitz, T., Stutz, J., and Platt, U. (2001b). Chemistry and oxidation capacity of the nitrate radical in the continental boundary layer near Berlin. *Journal of Geophysical Research-Atmospheres*, 106(D8):8013–8025.

Geyer, A., Alicke, B., Mihelcic, D., Stutz, J., and Platt, U. (1999). Comparison of tropospheric NO_3 radical measurements by differential optical absorption spectroscopy and matrix isolation electron spin resonance. *Journal Of Geophysical Research-Atmospheres*, 104(D21):26097–26105.

Geyer, A., Bachmann, K., Hofzumahaus, A., Holland, F., Konrad, S., Klupfel, T., Patz, H. W., Perner, D., Mihelcic, D., Schafer, H. J., Volz-Thomas, A., and Platt, U. (2003). Nighttime formation of peroxy and hydroxyl radicals during the BERLIOZ campaign: Observations and modeling studies. *Journal of Geophysical Research-atmospheres*, 108(D4):8249.

Geyer, A. and Stutz, J. (2004). Vertical profiles of NO_3, N_2O_5, O_3, and NOx in the nocturnal boundary layer: 2. Model studies on the altitude dependence of composition and chemistry. *Journal Of Geophysical Research-Atmospheres*, 109(D16).

Gölz, C., Senzig, J., and Platt, U. (2001). NO_3-initiated oxidation of biogenic hydrocarbons. *Chemosphere - Global Change Science*, 3(3):339–352.

Griffiths, P. T., Badger, C. L., Cox, R. A., Folkers, M., Henk, H. H., and Mentel, T. F. (2009). Reactive Uptake of N_2O_5 by Aerosols Containing Dicarboxylic Acids. Effect of Particle Phase, Composition, and Nitrate Content. *Journal Of Physical Chemistry A*, 113(17):5082–5090.

Griffiths, P. T. and Cox, R. A. (2009). Temperature dependence of heterogeneous uptake of N_2O_5 by ammonium sulfate aerosol. *Atmospheric Science Letters*, 10(3):Natl Ctr Atmospher Sci.

Guenther, A., Hewitt, C. N., Erickson, D., Fall, R., Geron, C., Graedel, T., Harley, P., Klinger, L., Lerdau, M., McKay, W. A., Pierce, T., Scholes, B., Steinbrecher, R., Tallamraju, R., Taylor, J., and Zimmermann, P. (1995). A global model of natural volatile organic compound emission. *J. Geophys. Res.*, 100(8873-8892).

Guenther, A., Karl, T., Harley, P., Wiedinmyer, C., Palmer, P. I., and Geron, C. (2006). Estimates of global terrestrial isoprene emissions using MEGAN (Model of Emissions of Gases and Aerosols from Nature). *Atmospheric Chemistry and Physics*, 6(11):3181–3210.

Hallquist, M., Stewart, D. J., Baker, J., and Cox, R. A. (2000). Hydrolysis of N_2O_5 on submicron sulfuric acid aerosols. *Journal Of Physical Chemistry A*, 104(17):3984–3990.

Hallquist, M., Stewart, D. J., Stephenson, S. K., and Cox, R. A. (2003). Hydrolysis of N_2O_5 on sub-micron sulfate aerosols. *Physical Chemistry Chemical Physics*, 5(16):3453–3463.

Hallquist, M., Wangberg, I., Ljungstrom, E., Barnes, I., and Becker, K. H. (1999). Aerosol and product yields from NO_3 radical-initiated oxidation of selected monoterpenes. *Environmental Science & Technology*, 33(4):553–559.

Handisides, G. M. (2001). *The influence of Peroxy Radicals on Ozone Production*. PhD thesis, Johann Wolfgang Goethe - Universität in Frankfurt am Main.

Hao, C. S., Shepson, P. B., Drummond, J. W., and Muthuramu, K. (1994). Gas-chromatographic Detector For Selective and Sensitive Detection of Atmospheric Organic Nitrates. *Analytical Chemistry*, 66(21):3737–3743.

Hargrove, J., Wang, L., Muyskens, K., Muyskens, M., Medina, D., Zaide, S., and Zhang, J. (2006). Cavity Ring-Down Spectroscopy of Ambient NO_2 with Quantification and Elimination of Interferences. *Environmental Science & Technology*, 40(24):7868–7873.

Hargrove, J. and Zhang, J. (2008). Measurements of NO_x, acyl peroxynitrates, and NO_y with automatic interference corrections using a NO_2 analyzer and gas phase titration. *Review of Scientific Instruments*, 79(4):046109.

Haugen, D. (1973). *Workshop on Micrometeorology*. American Meteorological Society.

Hauglustaine, D. A., Madronich, S., Ridley, B. A., Flocke, S. J., Cantrell, C. A., Eisele, F. L., Shetter, R. E., Tanner, D. J., Ginoux, P., and Atlas, E. L. (1999). Photochemistry and budget of ozone during the Mauna Loa Observatory Photochemistry Experiment (MLOPEX 2). *Journal of Geophysical Research-atmospheres*, 104(D23):30275–30307.

Hauglustaine, D. A., Madronich, S., Ridley, B. A., Walega, J. G., Cantrell, C. A., Shetter, R. E., and Hubler, G. (1996). Observed and model-calculated photostationary state at Mauna Loa observatory during MLOPEX 2. *Journal of Geophysical Research-atmospheres*, 101(D9):14681–14696.

Hautefeuille, P. and Chappuis, J. (1881). De la recherche des composés gazeaux et de l'étude de quelques-unes de leurs proprietés à l'aide du spectroscope. *C. R. Acad. Sci. Paris*, 92(80-83).

Heintz, F., Platt, U., Flentje, H., and Dubois, R. (1996). Long-term observation of nitrate radicals at the tor station, Kap Arkona (Rugen). *Journal of Geophysical Research-Atmospheres*, 101(D17):22891–22910–.

Hendry, D. G. and Kenley, R. A. (1977). Generation of Peroxy Radicals From Peroxy Nitrates (RO_2NO_2) - Decomposition of Peroxyacyl Nitrates. *Journal of the American Chemical Society*, 99(9):3198–3199.

Hendry, D. G. and Kenley, R. A. (1979). Atmospheric Chemistry of Peroxy Nitrates. *Grosjean, D. (ed.). Nitrogenous Air Pollutants: Chemical and Biological Implications. X+349p. Ann Arbor Science Publishers, Inc.: Ann Arbor, Mich.,usa. Illus*, pages P137–148.

Heue, K. P., Richter, A., Bruns, M., Burrows, J. P., von Friedeburg, C., Platt, U., Pundt, I., Wang, P., and Wagner, T. (2005). Validation of SCIAMACHY tropospheric NO_2 -columns with AMAXDOAS measurements. *Atmospheric Chemistry and Physics*, 5:1039–1051.

Holland, E. A., Dentener, F. J., Braswell, B. H., and Sulzman, J. M. (1999). Contemporary and pre-industrial global reactive nitrogen budgets. *Biogeochemistry*, 46(1-3):7–43.

Holloway, A. and Wayne, R. (2010). *Atmospheric Chemistry*. Royal Society of Chemistry.

Horowitz, L. W., Fiore, A. M., Milly, G. P., Cohen, R. C., Perring, A., Wooldridge, P. J., Hess, P. G., Emmons, L. K., and Lamarque, J.-F. (2007). Observational constraints on the chemistry of isoprene nitrates over the eastern United States. *J. Geophys. Res.*, 112(D12):D12S08–.

Hu, J. H. and Abbatt, J. P. D. (1997). Reaction probabilities for N_2O_5 hydrolysis on sulfuric acid and ammonium sulfate aerosols at room temperature. *JPC-A*, 101(5):871–878.

Huff, D. M., Joyce, P. L., Fochesatto, G. J., and Simpson, W. R. (2011). Deposition of dinitrogen pentoxide, N_2O_5 , to the snowpack at high latitudes. *Atmospheric Chemistry and Physics*, 11(10):4929–4938.

Huisman, A. J., Hottle, J. R., Coens, K. L., DiGangi, J. P., Galloway, M. M., Kammrath, A., and Keutsch, F. N. (2008). Laser-Induced Phosphorescence for the in Situ Detection of Glyoxal at Part per Trillion Mixing Ratios. *Analytical Chemistry*, 80(15):5884–5891. PMID: 18593190.

IPCC (2007). *Climate Change 2007: The Physical Science Basis. Contribution of Working Group I to the Fourth Assessment Report of the Intergovernmental Panel on Climat Change.* Cambridge University Press.

Ito, A., Sillman, S., and Penner, J. E. (2007). Effects of additional nonmethane volatile organic compounds, organic nitrates, and direct emissions of oxygenated organic species on global tropospheric chemistry. *J. Geophys. Res.*, 112(D6):D06309–.

IUPAC (2010). IUPAC Subcommittee for gas kinetic data evaluation. Evaluated kinetic data: http://www.iupac-kinetic.ch.cam.ac.uk/. u.

Jensen, N. R., Hjorth, J., Lohse, C., Skov, H., and Restelli, G. (1992a). Products and Mechanisms of the Gas-phase Reactions of NO_3 with CH_3SCH_3, CD_3SCD_3, CH_3SH and CH_3SSCH_3. *Journal of Atmospheric Chemistry*, 14(1-4).

Jensen, N. R., Hjorth, J., Lohse, C., Skov, H., and Restelli, G. (1992b). Reactions of the Nitrate Radical With A Series of Reduced Organic Sulfur-compounds In Air. *International Journal of Chemical Kinetics*, 24(10):839–850.

Johnston, H. S., Davis, H. F., and Lee, Y. T. (1996). NO_3 photolysis product channels: Quantum yields from observed energy thresholds. *Journal of Physical Chemistry*, 100(12):4713–4723.

Kamm, S., O., M., Naumann, K. H., Saathoff, H., and Schrath, U. (1999). Heterogeneous Interaction of Ozone, NO_2 and N_2O_5 with Soot Aerosol. *Transactions on Ecology and the Environment*, 28.

Kane, S. M., Caloz, F., and Leu, M. T. (2001). Heterogeneous uptake of gaseous N_2O_5 by $(NH_4)_2SO_4$, NH_4HSO_4, and H_2SO_4 aerosols. *J. Phys. Chem. A*, 105(26):6465–6470–.

Karagulian, F. and Rossi, M. J. (2007). Heterogeneous chemistry of the NO_3 free radical and N_2O_5 on decane flame soot at ambient temperature: Reaction products and kinetics. *Journal Of Physical Chemistry A*, 111(10):1914–1926.

Kastler, J. and Ballschmiter, K. (1998). Bifunctional alkyl nitrates - trace constituents of the atmosphere. *Fresenius Journal of Analytical Chemistry*, 360(7-8):812–816.

Kirchner, F., Mayer-Figge, A., Zabel, F., and Becker, K. H. (1999). Thermal stability of peroxynitrates. *International Journal of Chemical Kinetics*, 31(2):127–144.

Kotchenruther, R. A., Jaffe, D. A., and Jaeglé, L. (2001). Ozone photochemistry and the role of peroxyacetyl nitrate in the springtime northeastern Pacific troposphere: Results from the Photochemical Ozone Budget of the Eastern North Pacific Atmosphere (PHOBEA) campaign. *J. Geophys. Res.*, 106(D22):28731–28742.

Krause, H., Eisenreich, N., and Pfeil, A. (1989). Kinetics of evaporation and decomposition of isopropyl nitrate by rapid scan IR spectroscopy. *Thermochimica Acta*, 149(0):349–356.

LaFranchi, B. W., Wolfe, G. M., Thornton, J. A., Harrold, S. A., Browne, E. C., Min, K. E., Wooldridge, P. J., Gilman, J. B., Kuster, W. C., Goldan, P. D., de Gouw, J. A., McKay, M., Goldstein, A. H., Ren, X., Mao, J., and Cohen, R. C. (2009). Closing the peroxy acetyl nitrate budget: observations of acyl peroxy nitrates (PAN, PPN, and MPAN) during BEARPEX 2007. *Atmospheric Chemistry and Physics*, 9(19):7623–7641.

Lamarque, J. F., Kiehl, J. T., Brasseur, G. P., Butler, T., Cameron-Smith, P., Collins, W. D., Collins, W. J., Granier, C., Hauglustaine, D., Hess, P. G., Holland, E. A., Horowitz, L., Lawrence, M. G., McKenna, D., Merilees, P., Prather, M. J., Rasch, P. J., Rotman, D., Shindell, D., and Thornton, P. (2005). Assessing future nitrogen deposition and carbon cycle feedback using a multimodel approach: Analysis of nitrogen deposition. *Journal of Geophysical Research-atmospheres*, 110(D19):D19303.

Lamb, B., Gay, D., Westberg, H., and Pierce, T. (1996). A biogenic hydrocarbon emission inventory for the U.S.A. using a simple forest canopy model. *Atmos. Environ. 27A*, 27A(1673-1690).

Leighton, P. (1961). *Photochemistry of air pollution*. Physical chemistry. Academic Press.

Lenner, M. (1987). Nitrogen-dioxide In Exhaust Emissions From Motor-vehicles. *Atmospheric Environment*, 21(1):37–43.

Leue, C., Wenig, M., Wagner, T., Klimm, O., Platt, U., and Jahne, B. (2001). Quantitative analysis of NO_x emissions from Global Ozone Monitoring Experiment satellite image sequences. *Journal of Geophysical Research-atmospheres*, 106(D6):Amer Geophys Union.

Logan, J. A. (1983). Nitrogen oxides in the Troposphere:Global and Regional Budgets. *Journal Of Geophysical Research*, 88:10785–10807.

Luke, W. T., Dickerson, R. R., and Nunnermacker, L. J. (1989). Direct Measurements of the Photolysis Rate Coefficients and Henry's Law Constants of Several Alkyl Nitrates. *J. Geophys. Res.*, 94(D12):14905–14921.

Mannschreck, K., Gilge, S., Plass-Duelmer, C., Fricke, W., and Berresheim, H. (2004). Assessment of the applicability of NO-NO_2-O_3 photostationary state to long-term measurements at the Hohenpeissenberg GAW Station, Germany. *Atmospheric Chemistry and Physics*, 4:1265–1277.

Martinez, M., Perner, D., Hackenthal, E. M., Kulzer, S., and Schutz, L. (2000). NO_3 at Helgoland during the NORDEX campaign in October 1996. *Journal of Geophysical Research-atmospheres*, 105(D18):22685–22695.

Mentel, T., Bleilebens, D., and Wahner, A. (1996). A study of nighttime nitrogen oxide oxidation in a large reaction chamber at the fate of NO_2, N_2O_5, HNO_3, and O_3 at different humidities. *Atmospheric Environment*, 30(23):4007–4020.

Mentel, T. F., Sohn, M., and Wahner, A. (1999). Nitrate effect in the heterogeneous hydrolysis of dinitrogen pentoxide on aqueous aerosols. *Physical Chemistry Chemical Physics*, 1(24):5451–5457.

Merten, A., Tschritter, J., and Platt, U. (2011). Design of differential optical absorption spectroscopy long-path telescopes based on fiber optics. *Applied Optics*, 50(5):738–754.

Middleton, J., Kendrick, J. J., and Schwalm, H. W. (1950). Injury to herbaceous plants by smog or air pollution (in California.). *Plant Dis Reporter*, 34((9)):245–252.

Mihelcic, D., Holland, F., Hofzumahaus, A., Hoppe, L., Konrad, S., Musgen, P., Patz, H. W., Schafer, H. J., Schmitz, T., Volz-Thomas, A., Bachmann, K., Schlomski, S., Platt, U., Geyer, A., Alicke, B., and Moortgat, G. K. (2003). Peroxy radicals during BERLIOZ at Pabsthum: Measurements, radical budgets and ozone production. *Journal of Geophysical Research-atmospheres*, 108(D4):8254.

Mihelcic, D., Klemp, D., Muesgen, P., Paetz, H. W., and Volz-Thomas, A. (1993). Simultaneous measurements of peroxy and nitrate radicals at Schauinsland. *Journal of Atmospheric Chemistry*, 16:313–335. 10.1007/BF01032628.

Murphy, J. G., Day, D. A., Cleary, P. A., Wooldridge, P. J., and Cohen, R. C. (2006). Observations of the diurnal and seasonal trends in nitrogen oxides in the western Sierra Nevada. *Atmospheric Chemistry and Physics*, 6(12):5321–5338.

Ng, N. L., Kwan, A. J., Surratt, J. D., Chan, A. W. H., Chhabra, P. S., Sorooshian, A., Pye, H. O. T., Crounse, J. D., Wennberg, P. O., Flagan, R. C., and Seinfeld, J. H. (2008). Secondary organic aerosol (SOA) formation from reaction of isoprene with nitrate radicals (NO_3). *Atmospheric Chemistry and Physics*, 8(14):4117–4140.

Nielsen, T., Pilegaard, K., Egelov, A. H., Granby, K., Hummelshoj, P., Jensen, N. O., and Skov, H. (1996). Atmospheric nitrogen compounds: Occurrence, composition and deposition. *Science of the Total Environment*, 189:WHO European Off.

Noxon, J. F., Norton, R. B., and Henderson, W. R. (1978). Observation of atmospheric NO_3. *Geophys. Res. Lett.*, 5(675-678).

Noxon, J. F., Norton, R. B., and Marovich, E. (1980). NO_3 in the troposphere. *Geophys. Res. Lett.*, 7(125-128).

Nunes, L. S. S., Tavares, T. M., Dippel, J., and Jaeschke, W. (2005). Measurements of atmospheric concentrations of reduced sulphur compounds in the All Saints Bay area in Bahia, Brazil. *Journal of Atmospheric Chemistry*, 50(1):79–100.

Okeefe, A. and Deacon, D. A. G. (1988). Cavity Ring-down Optical Spectrometer For Absorption-measurements Using Pulsed Laser Sources. *Review of Scientific Instruments*, 59(12):2544–2551.

Orlando, J. J., Tyndall, G. S., Bertman, S. B., Chen, W. C., and Burkholder, J. B. (2002). Rate coefficient for the reaction of OH with CH_2=C(CH_3)C(O)ONO_2 (MPAN). *Atmospheric Environment*, 36(11):PII S1352–2310(02)00090–0.

Orlando, J. J., Tyndall, G. S., Moortgart, G. K., and Calvert, J. G. (1993). Quantum Yields for NO_3 Photolysis Between 570 and 635 nm. *Journal of Physical Chemistry*, 97(42):10996–11000.

Orphal, J., Fellows, C. E., and Flaud, P. M. (2003). The visible absorption spectrum of NO_3 measured by high-resolution Fourier transform spectroscopy. *Journal of Geophysical Research-atmospheres*, 108(D3):4077.

Osthoff, H. D., Pilling, M. J., Ravishankara, A. R., and Brown, S. S. (2007). Temperature dependence of the NO_3 absorption cross-section above 298 K and determination of the equilibrium constant for NO_3+NO_2 $\longleftrightarrow$ N_2O_5 at atmospherically relevant conditions. *Phys. Chem. Chem. Phys.*, 9(43):5785–5793.

Osthoff, H. D., Roberts, J. M., Ravishankara, A. R., Williams, E. J., Lerner, B. M., Sommariva, R., Bates, T. S., Coffman, D., Quinn, P. K., Dibb, J. E., Stark, H., Burkholder, J. B., Talukdar, R. K., Meagher, J., Fehsenfeld, F. C., and Brown, S. S. (2008). High levels of nitryl chloride in the polluted subtropical marine boundary layer. *Nature Geosci*, 1(5):324–328.

Pal, R., Kim, K.-H., Jeon, E.-C., Song, S.-K., Shon, Z.-H., Park, S.-Y., Lee, K.-H., Hwang, S.-J., Oh, J.-M., and Koo, Y.-S. (2009). Reduced sulfur compounds in ambient air surrounding an industrial region in Korea. *Environmental Monitoring and Assessment*, 148(1-4):109–125.

Parrish, D. D. and Buhr, M. P. (1993). Measurement Challenges of Nitrogen Species in the Atmosphere. In *Advances in Chemistry*, volume 232, pages 243–273–. American Chemical Society.

Parrish, D. D., Trainer, M., Williams, E. J., Fahey, D., Hubler, G., Eubank, C., Liu, S., Murphy, P., Albritton, D., and Fehsenfeld, F. (1986). Measurements of the NO_x - O_3 Photostationary State At Niwot Ridge, Colorado. *Journal of Geophysical Research-atmospheres*, 91(D5):5361–5370.

Paul, D., Furgeson, A., and Osthoff, H. D. (2009). Measurements of total peroxy and alkyl nitrate abundances in laboratory-generated gas samples by thermal dissociation cavity ring-down spectroscopy. *Review Of Scientific Instruments*, 80(11):114101.

Paul, D. and Osthoff, H. D. (2010). Absolute Measurements of Total Peroxy Nitrate Mixing Ratios by Thermal Dissociation Blue Diode Laser Cavity Ring-Down Spectroscopy. *Analytical Chemistry*, 82(15):6695–6703.

Paulot, F., Crounse, J. D., Kjaergaard, H. G., Kroll, J. H., Seinfeld, J. H., and Wennberg, P. O. (2009). Isoprene photooxidation: new insights into the production of acids and organic nitrates. *Atmospheric Chemistry and Physics*, 9(4):1479–1501.

Paulot, F., Henze, D. K., and Wennberg, P. O. (2012). Impact of the isoprene photochemical cascade on tropical ozone. *Atmospheric Chemistry and Physics*, 12(3):1307–1325.

Penkett, S., Burgess, R., Coe, H., Coll, I., Hov, ., Lindskog, A., Schmidbauer, N., Solberg, S., Roemer, M., Thijsse, T., Beck, J., and Reeves, C. (2007). Evidence for large average concentrations of the nitrate radical NO_3 in Western Europe from the HANSA hydrocarbon database. *Atmospheric Environment*, 41(16):3465 – 3478.

Penkett, S. A., Blake, N. J., Lightman, P., Marsh, A. R. W., Anwyl, P., and Butcher, G. (1993). The Seasonal Variation of Nonmethane Hydrocarbons in the Free Troposphere Over the North Atlantic Ocean: Possible Evidence for Extensive Reaction of Hydrocarbons With the Nitrate Radical. *J. Geophys. Res.*, 98(D2):2865–2885.

Perring, A. E., Bertram, T. H., Wooldridge, P. J., Fried, A., Heikes, B. G., Dibb, J., Crounse, J. D., Wennberg, P. O., Blake, N. J., Blake, D. R., Brune, W. H., Singh, H. B., and Cohen, R. C. (2009a). Airborne observations of total $RONO_2$: new constraints on the yield and lifetime of isoprene nitrates. *Atmospheric Chemistry and Physics*, 9(4):1451–1463.

Perring, A. E., Wisthaler, A., Graus, M., Wooldridge, P. J., Lockwood, A. L., Mielke, L. H., Shepson, P. B., Hansel, A., and Cohen, R. C. (2009b). A product study of the isoprene+NO_3 reaction. *Atmospheric Chemistry and Physics*, 9(14):4945–4956.

Phillips, G. J., Makkonen, U., Schuster, G., Sobanski, N., Hakola, H., and Crowley, J. (2012a). The detection of nocturnal N_2O_5 as HNO_3 by alkali- and aqueous-denuder techniques. *Atmospheric Measurement Techniques Discussions*, 5(5):7489–7505.

Phillips, G. J., Tang, M. J., Thieser, J., Brickwedde, B., Schuster, G., Bohn, B., Lelieveld, J., and Crowley, J. N. (2012b). Significant concentrations of nitryl chloride observed in rural continental Europe associated with the influence of sea salt chloride and anthropogenic emissions. *Geophys. Res. Lett.*, 39(10):L10811–.

Platt, U., Alicke, B., Dubois, R., Geyer, A., Hofzumahaus, A., Holland, F., Martinez, M., Mihelcic, D., Klupfel, T., Lohrmann, B., Patz, W., Perner, D., Rohrer, F., Schafer, J., and Stutz, J. (2002). Free radicals and fast photochemistry during BERLIOZ. *Journal of Atmospheric Chemistry*, 42(1):359–394.

Platt, U. and Heintz, F. (1994). Nitrate Radicals In Tropospheric Chemistry. *Israel Journal of Chemistry*, 34(3-4):289–300.

Platt, U. and Janssen, C. (1995). Observation and role of the free radicals NO_3, CLO, BrO and IO in the troposphere. *Faraday Discussions*, 100:175–198.

Platt, U., Le Bras, G., Poulet, G., Burrows, J. P., and Moortgat, G. K. (1990). Peroxy radicals from night-time reaction of NO_3 with organic compounds. *Nature*, 348(147-149).

Platt, U. and LeBras, G. (1997). Influence of DMS on the O_x - NO_y partitioning and the NO_x distribution in the marine background atmosphere. *Geophysical Research Letters*, 24(15):1935–1938.

Platt, U., Perner, D., Harris, G. W., Winer, A. M., and Pitts, J. M. (1980). Detection of NO_3 in the polluted troposphere by differential optical absorption. *Geophys. Res. Lett.*, 7(89-92):o.

Platt, U., Perner, D., and Patz, H. W. (1979). Simultaneous Measurement of Atmospheric CH_2O, O_3, and NO_2 By Differential Optical-absorption. *Journal of Geophysical Research-oceans and Atmospheres*, 84(NC10):6329–6335.

Platt, U., Perner, D., Schröder, J., Kessler, C., and Toennissen, A. (1981). The diurnal variation of NO_3. *JGR*, 86:11965–11970–.

Platt, U. and Stutz, J. (2008). *Differential Optical Absorption spectrosopy, Principles and Applications*. Springer, Heidelberg.

Poehler, D., Vogel, L., Frieß, U., and Platt, U. (2010). Observation of halogen species in the Amundsen Gulf, Arctic, by active long-path differential optical absorption spectroscopy. *Proceedings of the National Academy of Sciences*, 107(15):6582–6587.

Pratt, K. A., Mielke, L. H., Shepson, P. B., Bryan, A. M., Steiner, A. L., Ortega, J., Daly, R., Helmig, D., Vogel, C. S., Griffith, S., Dusanter, S., Stevens, P. S., and Alaghmand, M. (2012). Contributions of individual reactive biogenic volatile organic compounds to organic nitrates above a mixed forest. *Atmospheric Chemistry and Physics*, 12(21):10125–10143.

Ravishankara, A. R. and Lovejoy, E. R. (1994). Atmospheric Lifetime, Its Application and Its Determination - Cfc-substitutes As A Case-study. *Journal of the Chemical Society-faraday Transactions*, 90(15):2159–2169.

Richter, A. and Burrows, J. P. (2002). Tropospheric NO_2 from GOME measurements. *Remote Sensing of Trace Constituents In the Lower Stratosphere, Troposphere and the Earth's Surface: Global Observations, Air Pollution and the Atmospheric Correction*, 29(11):Comm Space Res.

Ridley, B. A., Shetter, J. D., Walega, J. G., Madronich, S., Elsworth, C. M., Grahek, F. E., Fehsenfeld, F. C., Norton, R. B., Parrish, D. D., Hübler, G., Buhr, M., Williams, E. J., Allwine, E. J., and Westberg, H. H. (1990). The Behavior of Some Organic Nitrates at Boulder and Niwot Ridge, Colorado. *J. Geophys. Res.*, 95(D9):13949–13961.

Riemer, N., Vogel, H., Vogel, B., Anttila, T., Kiendler-Scharr, A., and Mentel, T. F. (2009). Relative importance of organic coatings for the heterogeneous hydrolysis of N_2O_5 during summer in Europe. *J. Geophys. Res.*, 114(D17):D17307–.

Riemer, N., Vogel, H., Vogel, B., Schell, B., Ackermann, I., Kessler, C., and Hass, H. (2003). Impact of the heterogeneous hydrolysis of N_2O_5 on chemistry and nitrate aerosol formation in the lower troposphere under photosmog conditions. *Journal of Geophysical Research-atmospheres*, 108(D4):4144.

Roberts, J. M. (1990). The atmospheric chemistry of organic nitrates. *Atmospheric Environment. Part A. General Topics*, 24(2):243–287.

Roberts, J. M., Bertman, S. B., Parrish, D. D., Fehsenfeld, F. C., Jobson, B. T., and Niki, H. (1998). Measurement of alkyl nitrates at Chebogue Point, Nova Scotia during the 1993 North Atlantic Regional Experiment (NARE) intensive. *Journal of Geophysical Research-atmospheres*, 103(D11):13569–13580.

Roberts, J. M. and Fajer, R. W. (1989). UV absorption cross sections of organic nitrates of potential atmospheric importance and estimation of atmospheric lifetimes. *Environ. Sci. Technol.*, 23(8):945–951.

Roberts, J. M., Flocke, F., Chen, G., de Gouw, J., Holloway, J. S., Hubler, G., Neuman, J. A., Nicks, D. K., Nowak, J. B., Parrish, D. D., Ryerson, T. B., Sueper, D. T., Warneke, C., and Fehsenfeld, F. C. (2004). Measurement of peroxycarboxylic nitric anhydrides (PANs) during the ITCT 2K2 aircraft intensive experiment. *Journal of Geophysical Research-atmospheres*, 109(D23):D23S21.

Roberts, J. M., Flocke, F., Stroud, C. A., Hereid, D., Williams, E., Fehsenfeld, F., Brune, W., Martinez, M., and Harder, H. (2002). Ground-based measurements of peroxycarboxylic nitric anhydrides (PANs) during the 1999 Southern Oxidants Study Nashville Intensive. *J. Geophys. Res.*, 107(D21):4554–.

Roberts, J. M., Jobson, B. T., Kuster, W., Goldan, P., Murphy, P., Williams, E., Frost, G., Riemer, D., Apel, E., Stroud, C., Wiedinmyer, C., and Fehsenfeld, F. (2003). An examination of the chemistry of peroxycarboxylic nitric anhydrides and related volatile organic compounds during Texas Air Quality Study 2000 using ground-based measurements. *J. Geophys. Res.*, 108(D16):4495–.

Roberts, J. M., Osthoff, H. D., Brown, S. S., and Ravishankara, A. R. (2008). N_2O_5 Oxidizes Chloride to Cl_2 in Acidic Atmospheric Aerosol. *Science*, 321(5892):1059–1059.

Roberts, J. M., Osthoff, H. D., Brown, S. S., Ravishankara, A. R., Coffman, D., Quinn, P., and Bates, T. (2009). Laboratory studies of products of N_2O_5 uptake on Cl^- containing substrates. *Geophys. Res. Lett.*, 36(20):L20808–.

Rollins, A. W., Kiendler-Scharr, A., Fry, J. L., Brauers, T., Brown, S. S., Dorn, H.-P., Dube, W. P., Fuchs, H., Mensah, A., Mentel, T. F., Rohrer, F., Tillmann, R., Wegener, R., Wooldridge, P. J., and Cohen, R. C. (2009). Isoprene oxidation by nitrate radical: alkyl nitrate and secondary organic aerosol yields. *Atmospheric Chemistry and Physics*, 9(18):6685–6703.

Rosen, R. S., Wood, E. C., Wooldridge, P. J., Thornton, J. A., Day, D. A., Kuster, W., Williams, E. J., Jobson, B. T., and Cohen, R. C. (2004). Observations of total alkyl nitrates during Texas Air Quality Study 2000: Implications for O_3 and alkyl nitrate photochemistry. *J. Geophys. Res.*, 109(D7):D07303–.

Rothman, L. S., Jacquemart, D., Barbe, A., Benner, D. C., Birk, M., Brown, L. R., Carleer, M. R., Chackerian, C., Chance, K., Coudert, L. H., Dana, V., Devi, V. M., Flaud, J. M., Gamache, R. R., Goldman, A., Hartmann, J. M., Jucks, K. W., Maki, A. G., Mandin, J. Y., Massie, S. T., Orphal, J., Perrin, A., Rinsland, C. P., Smith, M. A. H., Tennyson, J., Tolchenov, R. N., Toth, R. A., Vander Auwera, J., Varanasi, P., and Wagner, G. (2005). The HITRAN 2004 molecular spectroscopic database. *Journal of Quantitative Spectroscopy & Radiative Transfer*, 96(2):139–204.

Rudich, Y., Talukdar, R., Ravishankara, A., and Fox, R. (1996). Reactive uptake of NO_3 on pure water and ionic solutions. *J. Geophys. Res.*, 101:21023–21031–.

Russell, A. G., Winner, D. A., Harley, R. A., Mccue, K. F., and Cass, G. R. (1993). Mathematical-modeling and Control of the Dry Deposition Flux of Nitrogen-containing Air-pollutants. *Environmental Science & Technology*, 27(13):2772–2782.

Sander, S. P., Friedl, R., Golden, D., Kurylo, M., Huie, R., Orkin, V., Moortgat, G., Ravishankara, A. R., Kolb, C. E., Molina, M. J., and Finlayson-Pitts, B. (2006). Chemical kinetics and photochemical data for use in atmospheric studies: Evaluation Number 17. Technical report, National Aeronautics and Space Administration / Jet Propulsion Laboratory / California Institute of Technology, Pasadena, CA.

Schneider, M. and Ballschmiter, K. (1999). C3 - C14 alkyl nitrates in remote South Atlantic air. *Chemosphere*, 38(1):233–244.

Schuster, G., Labazan, I., and Crowley, J. N. (2009). A cavity ring down/cavity enhanced absorption device for measurement of ambient NO_3 and N_2O_5. *Atmospheric Measurement Techniques*, 2(1):1–13.

Seinfeld, J. and Pandis, S. (2006). *Atmospheric chemistry and physics: from air pollution to climate change*. A Wiley-Intersciencie publications. Wiley.

Shon, Z. H. and Kim, K. H. (2006). Photochemical oxidation of reduced sulfur compounds in an urban location based on short time monitoring data. *Chemosphere*, 63(11):1859–1869.

Singh, H. B., Herlth, D., Kolyer, R., Salas, L., Bradshaw, J. D., Sandholm, S. T., Davis, D. D., Crawford, J., Kondo, Y., Koike, M., Talbot, R., Gregory, G. L., Sachse, G. W., Browell, E., Blake, D. R., Rowland, F. S., Newell, R., Merrill, J., Heikes, B., Liu, S. C., Crutzen, P. J., and Kanakidou, M. (1996). Reactive nitrogen and ozone over the western Pacific: Distribution, partitioning, and sources. *J. Geophys. Res.*, 101(D1):1793–1808.

Singh, H. B. and Salas, L. J. (1989). Measurements of peroxyacetyl nitrate (pan) and peroxypropionyl nitrate (ppn) at selected urban, rural and remote sites. *Atmospheric Environment (1967)*, 23(1):231–238.

Slusher, D. L., Huey, L. G., Tanner, D. J., Flocke, F. M., and Roberts, J. M. (2004). A thermal dissociation chemical ionization mass spectrometry (TD-CIMS) technique for the simultaneous measurement of peroxyacyl nitrates and dinitrogen pentoxide. *J. Geophys. Res.*, 109:–.

Smith, N., Plane, J. M. C., Nien, C. F., and Solomon, P. A. (1995). Nighttime Radical Chemistry In the San-joaquin Valley. *Atmospheric Environment*, 29(21).

Sneep, M. and Ubachs, W. (2005). Direct measurement of the Rayleigh scattering cross section in various gases. *Journal of Quantitative Spectroscopy & Radiative Transfer*, 92(3):293–310.

Sommariva, R., Osthoff, H. D., Brown, S. S., Bates, T. S., Baynard, T., Coffman, D., de Gouw, J. A., Goldan, P. D., Kuster, W. C., Lerner, B. M., Stark, H., Warneke, C., Williams, E. J., Fehsenfeld, F. C., Ravishankara, A. R., and Trainer, M. (2009). Radicals in the marine boundary layer during NEAQS 2004: a model study of day-time and night-time sources and sinks. *Atmospheric Chemistry and Physics*, 9(9):3075–3093.

Sommariva, R., Pilling, M. J., Bloss, W. J., Heard, D. E., Lee, J. D., Fleming, Z. L., Monks, P. S., Plane, J. M. C., Saiz-Lopez, A., Ball, S. M., Bitter, M., Jones, R. L., Brough, N., Penkett, S. A., Hopkins, J. R., Lewis, A. C., and Read, K. A. (2007). Night-time radical chemistry during the NAMBLEX campaign. *Atmospheric Chemistry and Physics*, 7(3):587–598.

Song, W., Williams, J., Yassaa, N., Martinez, M., Adame Carnero, J. A., Hidalgo, P. J., Bozem, H., and Lelieveld, J. (2011). Winter and summer characterization of biogenic enantiomeric monoterpenes and anthropogenic BTEX compounds at a Mediterranean Stone Pine forest site. *Journal of Atmospheric Chemistry*, 68(3):233–250.

Stull, R. (1988). *An Introduction to Boundary Layer Meteorology*. Atmospheric Sciences Library. Springer.

Stutz, J., Alicke, B., Ackermann, R., Geyer, A., White, A., and Williams, E. (2004). Vertical profiles of NO_3, N_2O_5, O_3, and NO_x in the nocturnal boundary layer: 1. Observations during the Texas Air Quality Study 2000 (vol 109, art no D12306, 2004). *Journal Of Geophysical Research-Atmospheres*, 109(D16).

Stutz, J., Wong, K. W., Lawrence, L., Ziemba, L., Flynn, J. H., Rappenglück, B., and Lefer, B. (2009). Nocturnal NO_3 radical chemistry in Houston, TX. *Atmospheric Environment*, In Press, Corrected Proof:–.

Sutton, J. A. and Driscoll, J. F. (2004). Rayleigh scattering cross sections of combustion species at 266, 355, and 532 nm for thermometry applications. *Optics Letters*, 29(22):2620–2622.

Talukdar, K. R., B. Burkholder, J., Hunter, M., K. Gilles, M., M. Roberts, J., and R. Ravishankara, A. (1997). Atmospheric fate of several alkyl nitrates Part 2: UV absorption cross-sections and photodissociation quantum yields. *J. Chem. Soc., Faraday Trans.*, 93(16):2797–2805.

Talukdar, R. K., Burkholder, J. B., Schmoltner, A. M., Roberts, J. M., Wilson, R. R., and Ravishankara, A. R. (1995). Investigation of the Loss Processes For Peroxyacetyl Nitrate In the Atmosphere - UV Photolysis and Reaction With OH. *Journal of Geophysical Research-atmospheres*, 100(D7):14163–14173.

Tang, M. J., Thieser, J., Schuster, G., and Crowley, J. N. (2010). Uptake of NO_3 and N_2O_5 to Saharan dust, ambient urban aerosol and soot: a relative rate study. *Atmospheric Chemistry and Physics*, 10(6):2965–2974.

Tang, M. J., Thieser, J., Schuster, G., and Crowley, J. N. (2012). Kinetics and mechanism of the heterogeneous reaction of N_2O_5 with mineral dust particles. *Phys. Chem. Chem. Phys.*

Thaler, R. D., Mielke, L. H., and Osthoff, H. D. (2011). Quantification of Nitryl Chloride at Part Per Trillion Mixing Ratios by Thermal Dissociation Cavity Ring-Down Spectroscopy. *Analytical Chemistry*, 83(7):2761–2766.

Thomas, K., Volz-Thomas, A., Mihelcic, D., Smit, H. G. J., and Kley, D. (1998). On the exchange of NO_3 radicals with aqueous solutions: Solubility and sticking coefficient. *Journal of Atmospheric Chemistry*, 29(1):17–43.

Thompson, C. R., Kats, G., and Lennox, R. W. (1979). Phytotoxicity of Air-pollutants Formed By High Explosive Production. *Environmental Science & Technology*, 13(10):1263–1268.

Thornton, J. A., Kercher, J. P., Riedel, T. P., Wagner, N. L., Cozic, J., Holloway, J. S., DubÃ©, W. P., Wolfe, G. M., Quinn, P. K., Middlebrook, A. M., Alexander, B., and Brown, S. S. (2010). A large atomic chlorine source inferred from mid-continental reactive nitrogen chemistry. *Nature*, 464(7286):271–274.

Thornton, J. A., Wooldridge, P. J., Cohen, R. C., Martinez, M., Harder, H., Brune, W. H., Williams, E. J., Roberts, J. M., Fehsenfeld, F. C., Hall, S. R., Shetter, R. E., Wert, B. P., and Fried, A. (2002). Ozone production rates as a function of NO_x abundances and HO_x production rates in the Nashville urban plume. *Journal of Geophysical Research-Atmospheres*, 107(D12):–.

Toda, K., Obata, T., Obolkin, V. A., Potemkin, V. L., Hirota, K., Takeuchi, M., Arita, S., Khodzher, T. V., and Grachev, M. A. (2010). Atmospheric methanethiol emitted from a pulp and paper plant on the shore of Lake Baikal. *Atmospheric Environment*, 44(20):2427–2433.

Trainer, M., Buhr, M. P., Curran, C. M., Fehsenfeld, F. C., Hsie, E. Y., Liu, S. C., Norton, R. B., Parrish, D. D., Williams, E. J., Gandrud, B. W., Ridley, B. A., Shetter, J. D., Allwine, E. J., and Westberg, H. H. (1991). Observations and Modeling of the Reactive Nitrogen Photochemistry at a Rural Site. *J. Geophys. Res.*, 96(D2):3045–3063.

Turberg, M., Giolando, D., Tilt, C., Soper, T., Mason, S., Davies, M., Klingensmith, P., and Takacs, G. (1990). Atmospheric photochemistry of alkyl nitrates. *Journal of Photochemistry and Photobiology A: Chemistry*, 51(3):281–292.

Turnipseed, A. A., Huey, L. G., Nemitz, E., Stickel, R., Higgs, J., Tanner, D. J., Slusher, D. L., Sparks, J. P., Flocke, F., and Guenther, A. (2006). Eddy covariance fluxes of peroxyacetyl nitrates (PANs) and NO_y to a coniferous forest. *Journal of Geophysical Research-atmospheres*, 111(D9):D09304.

van Aardenne, J. A., Carmichael, G. R., Levy II, H., Streets, D., and Hordijk, L. (1999). Anthropogenic NO_x emissions in Asia in the period 1990-2020. *Atmospheric Environment*, 33(4):633–646.

van Noije, T. P. C., Eskes, H. J., Dentener, F. J., Stevenson, D. S., Ellingsen, K., Schultz, M. G., Wild, O., Amann, M., Atherton, C. S., Bergmann, D. J., Bey, I., Boersma, K. F., Butler, T., Cofala, J., Drevet, J., Fiore, A. M., Gauss, M., Hauglustaine, D. A., Horowitz, L. W., Isaksen, I. S. A., Krol, M. C., Lamarque, J. . F., Lawrence, M. G., Martin, R. V., Montanaro, V., Mueller, J. . F., Pitari, G., Prather, M. J., Pyle, J. A., Richter, A., Rodriguez, J. M., Savage, N. H., Strahan, S. E., Sudo, K., Szopa, S., and van Roozendael, M. (2006). Multi-model

ensemble simulations of tropospheric NO_2 compared with GOME retrievals for the year 2000. *Atmospheric Chemistry and Physics*, 6:2943–2979.

van Stratum, B. J. H., VilÃ -Guerau de Arellano, J., Ouwersloot, H. G., van den Dries, K., van Laar, T. W., Martinez, M., Lelieveld, J., Diesch, J.-M., Drewnick, F., Fischer, H., Hosaynali Beygi, Z., Harder, H., Regelin, E., Sinha, V., Adame, J. A., Sörgel, M., Sander, R., Bozem, H., Song, W., Williams, J., and Yassaa, N. (2012). Case study of the diurnal variability of chemically active species with respect to boundary layer dynamics during DOMINO. *Atmos. Chem. Phys.*, 12(12):5329–5341.

Veitel, H., Kromer, B., Mossner, M., and Platt, U. (2002). New techniques for measurements of atmospheric vertical trace gas profiles using DOAS. *Environmental Science and Pollution Research*, pages 17–26.

Voigt, S., Orphal, J., and Burrows, J. P. (2002). The temperature and pressure dependence of the absorption cross-sections of NO_2 in the 250-800 nm region measured by Fourier-transform spectroscopy. *Journal of Photochemistry and Photobiology A-chemistry*, 149(1-3):PII S1010–6030–(01)00650–5.

Volkamer, R., Molina, L. T., Molina, M. J., Shirley, T., and Brune, W. H. (2005a). DOAS measurement of glyoxal as an indicator for fast VOC chemistry in urban air. *Geophys. Res. Lett.*, 32(8):L08806–.

Volkamer, R., Spietz, P., Burrows, J., and Platt, U. (2005b). High-resolution absorption cross-section of glyoxal in the UV-VIS and IR spectral ranges. *Journal of Photochemistry and Photobiology A-chemistry*, 172(1):35–46.

Volz-Thomas, A., Patz, H. W., Houben, N., Konrad, S., Mihelcic, D., Klupfel, T., and Perner, D. (2003). Inorganic trace gases and peroxy radicals during BERLIOZ at Pabstthum: An investigation of the photostationary state of NO_x and O_3. *Journal of Geophysical Research-atmospheres*, 108(D4):8248.

von Friedeburg, C., Wagner, T., Geyer, A., Kaiser, N., Vogel, B., Vogel, H., and Platt, U. (2002). Derivation of tropospheric NO_3 profiles using off-axis differential optical absorption spectroscopy measurements during sunrise and comparison with simulations. *Journal Of Geophysical Research-Atmospheres*, 107(D13).

Vrekoussis, M., Liakakou, E., Mihalopoulos, N., Kanakidou, M., Crutzen, P. J., and Lelieveld, J. (2006). Formation of HNO_3 and NO_3 - in the anthropogenically-influenced eastern Mediterranean marine boundary layer. *Geophysical Research Letters*, 33(5):L05811.

Wagner, C., Hanisch, F., de Coninck, H., Holmes, N. S., Schuster, G., and Crowley, J. N. (2008). The interaction of N_2O_5 with mineral dust: Aerosol flow tube and Knudsen reactor studies. *ACP*, 8:91–109–.

Wahner, A., Mentel, T. F., and Sohn, M. (1998a). Gas-phase reaction of N_2O_5 with water vapor: Importance of heterogeneous hydrolysis of N_2O_5 and surface desorption of HNO_3 in a large teflon chamber. *Geophysical Research Letters*, 25(12):2169–2172.

Wahner, A., Mentel, T. F., Sohn, M., and Stier, J. (1998b). Heterogeneous reaction of N_2O_5 on sodium nitrate aerosol. *Journal of Geophysical Research-atmospheres*, 103(D23):31103–31112.

Wang, S., Ackermann, R., and Stutz, J. (2006). Vertical profiles of O_3 and NOx chemistry in the polluted nocturnal boundary layer in Phoenix, AZ: I. Field observations by long-path DOAS. *Atmospheric Chemistry and Physics*, 6(9):2671–2693.

Warneck, P. and Zerbach, T. (1992). Synthesis of Peroxyacetyl Nitrate In Air By Acetone Photolysis. *Environmental Science & Technology*, 26(1):74–79.

Washenfelder, R. A., Langford, A. O., Fuchs, H., and Brown, S. S. (2008). Measurement of glyoxal using an incoherent broadband cavity enhanced absorption spectrometer. *Atmos. Chem. Phys.*, 8(24):7779–7793.

Wayne, R. P., Barnes, I., Biggs, P., Burrows, J. P., Canosamas, C. E., Hjorth, J., Lebras, G., Moortgat, T, G. K., Perner, D., Poulet, G., Restelli, G., and Sidebottom, H. (1991). The Nitrate Radical - Physics, Chemistry, and the Atmosphere. *Atmospheric Environment Part A-general Topics*, 25(1):1–203.

Williams, J., Crowley, J., Fischer, H., Harder, H., Martinez, M., Petäjä, T., Rinne, J., Bäck, J., Boy, M., Dal Maso, M., Hakala, J., Kajos, M., Keronen, P., Rantala, P., Aalto, J., Aaltonen, H., Paatero, J., Vesala, T., Hakola, H., Levula, J., Pohja, T., Herrmann, F., Auld, J., Mesarchaki, E., Song, W., Yassaa, N., Nölscher, A., Johnson, A. M., Custer, T., Sinha, V., Thieser, J., Pouvesle, N., Taraborrelli, D., Tang, M. J., Bozem, H., Hosaynali-Beygi, Z., Axinte, R., Oswald, R., Novelli, A., Kubistin, D., Hens, K., Javed, U., Trawny, K., Breitenberger, C., Hidalgo, P. J., Ebben, C. J., Geiger, F. M., Corrigan, A. L., Russell, L. M., Ouwersloot, H. G., Vila -Guerau de Arellano, J., Ganzeveld, L., Vogel, A., Beck, M., Bayerle, A., Kampf, C. J., Bertelmann, M., Köllner, F., Hoffmann, T., Valverde, J., Gonzalez, D., Riekkola, M.-L., Kulmala, M., and Lelieveld, J. (2011). The summertime Boreal forest field measurement intensive (HUMPPA-COPEC-2010): an overview of meteorological and chemical influences. *Atmos. Chem. Phys.*, 11(20):10599–10618.

Williams, J., Roberts, J. M., Fehsenfeld, F. C., Bertman, S. B., Buhr, M. P., Goldan, P. D., Hubler, G., Kuster, W. C., Ryerson, T. B., Trainer, M., and Young, V. (1997). Regional ozone from biogenic hydrocarbons deduced from airborne measurements of PAN, PPN, and MPAN. *Geophysical Research Letters*, 24(9):1099–1102.

Wolfe, G. M., Thornton, J. A., McNeill, V. F., Jaffe, D. A., Reidmiller, D., Chand, D., Smith, J., Swartzendruber, P., Flocke, F., and Zheng, W. (2007). Influence of trans-Pacific pollution transport on acyl peroxy nitrate abundances and speciation at Mount Bachelor Observatory during INTEX-B. *Atmospheric Chemistry and Physics*, 7(20):5309–5325.

Wu, S., Mickley, L. J., Jacob, D. J., Logan, J. A., Yantosca, R. M., and Rind, D. (2007). Why are there large differences between models in global budgets of tropospheric ozone? *J. Geophys. Res.*, 112(D5):D05302–.

Yokelson, R. J., Burkholder, J. B., Fox, R. W., Talukdar, R. K., and Ravishankara, A. R. (1994). Temperature-dependence of the NO_3 Absorption-spectrum. *Journal of Physical Chemistry*, 98(50):13144–13150.

Zel'dovich, Y. and Raizer, Y. (1966). *Physics of Shock Waves and High-Temperature Hydrodynamic Phenomena*. Academic Press.

Zetzsch, C. and Behnke, W. (1992). Heterogeneous Photochemical Sources of Atomic Cl In the Troposphere. *Berichte Der Bunsen-gesellschaft-physical Chemistry Chemical Physics*, 96(3).

Acknowledgements - Danksagung

Nach gut 4 Jahren ist es endlich geschafft. Da eine Arbeit von solchem Umfang nicht alleine auf die Beine gestellt werden kann, möchte ich mich an dieser Stelle bei allen recht herzlich bedanken, die mich während dieser Zeit unterstützt haben:

* Zuallererst möchte ich mich ganz besonders bei Prof. Ulrich Platt bedanken, dass er sich bereit erklärt hat, meine Doktorarbeit zu betreuen, und trotz der räumlichen Distanz immer Interesse an meiner Arbeit gezeigt hat.

* Ich möchte mich auch bei Prof. Thomas Wagner bedanken, der sich bereit erklärt hat, mein Zweitgutachten zu übernehmen.

* Mein ganz besonderer Dank gilt Dr.John N. Crowley. John hat alle Eigenschaften, die ich mir von einem perfekten Chef wünsche! Er hat es mir ermöglicht, diese interessante und abwechslungsreiche Arbeit am MPIC durchzuführen. Bei vielen ertragreichen Diskussionen hat er mir die Welt der Atmosphären-Forschung noch näher gebracht. Er hat es mir auch ermöglicht, an vielen internationalen Konferenzen und Workshops teilzunehmen. Auch neben der wissenschaftlichen Seite hatte John immer ein offenes Ohr für jegliche Art von Fragen. Die 4 Jahre in seiner Arbeitsgruppe waren eine sehr schöne Zeit, die ich nicht missen möchte.

* Ein ganz besonderes Dankeschön geht an Dipl.-Ing. Gerhard Schuster. Ohne seine große Unterstützung wäre das neuentwickelte Instrument nicht das, was es jetzt ist. Neben seinen tollen Ingenieursfähigkeiten hatte er auch immer ein offenes Ohr für alle Belange des Lebens. Von seinem großem Engagement, Ideenreichtum und Optimismus konnte ich sehr viel lernen. Danke auch dafür.

* Ich möchte mich auch bei Prof.Bender und Prof.Weidemüller bedanken, dass sie sich bereit erklärt haben als weitere Prüfer an meiner Disputation teil--zunehmen.

* Elmar Uherek und Agnes Heinemann danke ich für die Unterstützung seitens der International Max Planck Research School (IMPRS).

* Vielen Dank an die Mitarbeiter der Werkstatt, Elektronik, Verwaltung und Haustechnik für die gute Unterstützung während meiner Arbeit.

* Ich möchte mich auch bei den Organisatoren der drei Kampagnen, Monica Martinez (DOMINO), Jonathan Williams (HUMPPA) und John Crowley (PARADE), an denen ich teilgenommen habe, bedanken. Nur durch die gute Organisation war es möglich diese tollen Messergebnisse zu erzielen.

* Für die Finanzierung meiner Arbeit bedanke ich mich bei der Deutschen Forschungsgemeinschaft (DFG) sowie der IMPRS.

* Meinen Bürokollegen, Abraham, Bernard, Christoph, Gerhard und Nicolas möchte ich ganz besonders für die angenehme Zeit danken. Nicht immer stand dabei die Arbeit im Vordergrund.

* Ein besonderer Dank gilt auch der gesamten AG Crowley über die gesamten vier Jahre. Danke an Abraham, Bernard, Christoph, Gavin, Gerhard, Geert, Jan, Maria, Matthias, Mingjin, Nicolas P., Nicolas S., Stefan, Terry, Victor und John für die schöne gemütliche Arbeitsatmosphäre und natürlich auch für die vielen Freizeitaktivitäten, wie unser traditionelles Weihnachtsbowling!

* Es ist toll, während einer so langen Zeit in einer neuen Stadt nicht nur sehr nette Arbeitskollegen zu haben, sondern auch viele neue Freunde zu gewinnen. Die netten Kaffeerunden am Institut und auch die anderen schönen Freizeitaktivitäten wie das Pubquiz (Kopfsalat rules) werden mir fehlen. Daher bedanke ich mich von ganzen Herzen für die tolle gemeinsame Zeit bei Alex, Anke, Claudia, Daniel, Eliza, Ellen, Julia, Matthias, Mingjin, Robert und Christoph.

* Danke Kathrin, dass du mich in den letzten 3 Jahren so gut unterstützt hast, immer für mich da warst und dass wir alles so gut hinbekommen haben während dieser Zeit!

* Zu guter Letzt gilt mein ganz besonderer Dank meinen Eltern und meiner Familie. Danke, dass ihr mich in den letzten Jahren so toll unterstützt habt. Ihr habt mir mein Studium ermöglicht und sonst auch sehr viele andere Dinge. Danke für Alles!!!